Metal-organic framework thin films for microelectronic chemical and biological sensor applications

Von der Fakultät für Elektrotechnik und Informationstechnik der Rheinisch-Westfälischen Technischen Hochschule Aachen zur Erlangung des akademischen Grades eines Doktors der Naturwissenschaften genehmigte Dissertation

vorgelegt von

Huijie Jiang, M. Sc.

aus Shangqiu, China

Berichter: Universitätsprofessor Dr. Sven Ingebrandt

Universitätsprofessor Dr. Joachim Knoch

Tag der mündlichen Prüfung: 11.03.2025

Dedicated to my father

Abstract

This thesis explores the potential of metal-organic framework (MOF) thin-film-based microelectronic devices in chemical and bio-sensing applications. Specifically, one section focuses on optimizing the MOF thin films for detecting phthalates in aqueous and non-aqueous media. Another section examines the dynamics of the cell-substrate interaction and cellular proliferation on MOF thin-film substrates. Electrochemical impedance spectroscopy (EIS) technique is involved in both applications. Two highly controllable platforms, a microfluidics platform and a dip coater, were developed in-house for the controlled growth of high-quality MOF thin films on solid surfaces, employing a layer-by-layer liquid-phase epitaxy (LbL-LPE) approach. The process parameters for the microfluidics platform were optimized to demonstrate scalability for larger-scale dip coating processes. Subsequently, the optical and electrical characteristics of the MOF thin films were elucidated using different approaches. To aid such characterisations, three lithographic techniques were developed to pattern MOF thin films using various sacrificial layers, enhancing on-chip integration. Furthermore, a unique optical characterisation method was developed to leverage the optical contrast of MOF thin films on Si/SiO_2 substrates for the rapid assessment of film quality, including homogeneity and thickness. Owing to their dynamic inherent characteristics reported in the literature, three different MOF-thin-films, namely $Cu_3(HHTP)_2$ (HHTP = 2,3,6,7,10,11-hexahydroxytriphenylene), Ni-(BDC-NH_2) (BDC-NH_2 = 2-aminoterephthaleic acid), and Fe-(BDC-NH_2), were investigated.

Firstly, a systematic investigation was conducted into the fundamental electrical properties of semiconducting $Cu_3(HHTP)_2$ thin-film devices, including an examination of the effects of rapid thermal annealing treatment. Additionally, the electrical characteristics of electrolyte-gated field-effect transistors (EG-FETs) based on $Cu_3(HHTP)_2$ thin films were studied in phosphate buffer solutions, revealing an ambipolar transport behaviour dominated by capacitive gating. The MOF EG-FETs show a very high potential for ion-sensing in liquid environments. Furthermore, $Cu_3(HHTP)_2$ thin-film devices were utilized to investigate the interaction mechanisms between $Cu_3(HHTP)_2$ and various phthalates and phthalate derivatives, indicating that the observed responses were influenced by factors such as molecular size, weight, structure, and charge.

Abstract

Secondly, the detection of phthalates in liquids using EIS with a two-electrode configuration was demonstrated with Ni-(BDC-NH_2) thin-film devices, which exhibited dose-dependent responses to diisobutyl phthalate, a crucial pollutant in water streaming from the polymer industry.

Finally, Fe-(BDC-NH_2) thin-film devices were employed to study the cellular dynamics on MOF substrates using Electric Cell-substrate Impedance Sensing (ECIS). This technique enabled the observation of cell dynamics, including attachment, spreading, and proliferation, over extended periods, allowing for comparisons between different cell lines, such as PC-12 and MDCK.

In summary, the novel sensor concepts and sensors based on MOF materials exhibit highly promising properties for chemical and biological sensor system applications. The production of thin, crystalline films with low roughness is highly reproducible over a large area, and integration into a microsystems manufacturing process has been achieved. The first sensors demonstrate very promising properties for the sensitive and selective detection of phthalates. Additionally, the layers can be utilized as active substrates for the electronic detection of cell properties. In both the domains of biosensorics and bio- and neuroelectronics, considerable potential exists for the future development of novel applications for this emerging class of materials.

Zusammenfassung

Diese Dissertation untersucht die Eignung von speziellen organisch-metallischen Funktionsschichten, sogenannten MOFs (metal-organic frameworks), als Signalwandlermaterialien in mikroelektronischen Sensoren für chemische und biosensorische Anwendungen. Der erste Teil konzentriert sich auf die Herstellung und Optimierung der MOF-Dünnfilme zur Detektion von Phthalaten (verschiedene Weichmacher aus der Kunststoffindustrie) in wässrigen und nicht wässrigen Medien. Der zweite Teil untersucht die Dynamik der Adhäsion und Proliferation von Zellen auf MOF-Dünnfilmen. In beiden Anwendungen wurde die Methode der elektrochemischen Impedanzspektroskopie (EIS) genutzt. Um ein kontrolliertes Wachstum von ultra-dünnen und qualitativ hochwertigen MOF-Dünnfilmen auf festen Oberflächen zu ermöglichen, wurden zwei präzise kontrollierbare Plattformen, eine Mikrofluidik-Plattform und ein System zum automatisierten Dip-Coating, entwickelt, die beide die Methode der schichtweisen Flüssigphasen-Epitaxie (LbL-LPE) ausnutzen. Die Prozessparameter wurden mit Hilfe der Mikrofluidik-Plattform optimiert und danach die Skalierbarkeit der Methode für großflächige Dip-Coating Prozesse demonstriert. Anschließend wurden die optischen und elektrischen Eigenschaften der MOF-Dünnfilme mithilfe verschiedener Methoden untersucht. Um die Charakterisierungen zu unterstützen, wurden drei verschiedene lithografische Techniken zur Strukturierung der MOF-Dünnfilme entwickelt, wodurch auch eine spätere Prozess-Integration ermöglicht wurde. Darüber hinaus wurde eine neue Charakterisierungsmethode entwickelt, die den optischen Kontrast der MOF-Dünnfilme auf Si/SiO_2-Substraten für eine schnelle Bewertung der Filmqualität, Homogenität und Dicke ausnutzt. Aufgrund ihrer dynamischen inhärenten Eigenschaften, die bereits in der Literatur beschrieben wurden, wurden drei verschiedene MOF-Materialien, nämlich $Cu_3(HHTP)_2$ (HHTP = 2,3,6,7,10,11-He-xahydroxytriphenylen), Ni-(BDC-NH_2) (BDC-NH_2 = 2-Aminoterephthalsäure) und Fe-(BDC-NH_2) intensiv untersucht.

Zunächst wurden die grundlegenden elektrischen Eigenschaften von halbleitenden $Cu_3(HHTP)_2$-Dünnfilmen systematisch untersucht, insbesondere im Hinblick auf einen schnellen Temperschritt bei der Herstellung. Darüber hinaus wurden nach erfolgreicher Prozessintegration der MOF-Dünnfilme die elektrischen Eigenschaften von elektrochemisch gesteuerten Transistoren (EG-FETs) auf Basis von $Cu_3(HHTP)_2$-Dünnfilmen in Phosphatpufferlösungen untersucht: Dabei wurde ein ambipolares elektrisches Transportverhalten festgestellt, das von kapazitiven Steuereffekten dominiert wird. Die MOF EG-FETs zeigten eine sehr gute Eignung

Abstract

für die Ionendetektion in flüssigen Umgebungen. Darüber hinaus wurden $Cu_3(HHTP)_2$-Dünnfilme verwendet, um die Interaktionsmechanismen zwischen $Cu_3(HHTP)_2$ und verschiedenen Phthalaten sowie Phthalatderivaten zu untersuchen, wobei die beobachteten Sensorantworten von Faktoren wie molekulare Größe, Gewicht, Struktur und Ladung der Analyten beeinflusst wurden.

Die sensitive Detektion von Phthalaten in Flüssigkeiten wurde unter Verwendung von EIS in einer Zwei-Elektroden-Konfiguration mit Ni-(BDC-NH_2)-Dünnfilmen demonstriert. Die Sensoren zeigten sehr gute, dosisabhängige Reaktionen auf Diisobutylphthalat, einen bedeutenden Schadstoff in Trinkwasser, der aus den Herstellungsprozessen der Polymerindustrie stammt.

Abschließend wurden Fe-(BDC-NH_2)-Dünnfilme eingesetzt, um die zellulären Dynamiken auf MOF-Substraten mit Hilfe der Electric Cell-substrate Impedance Sensing (ECIS) Technik zu untersuchen. Diese Technik ermöglichte über längere Zeiträume die elektrische Detektion der Zell-Dynamik, einschließlich Adhäsion, Ausbreitung und Proliferation, wobei zwei verschiedene Zelllinien (PC-12 und MDCK) verglichen wurden.

Zusammenfassend zeigen die neuartigen Sensorkonzepte und Sensoren auf Basis von MOF-Materialien sehr vielversprechende Eigenschaften für chemische und biologische Sensorsystemanwendungen. Eine sehr reproduzierbare Herstellung von dünnen, kristallinen Filmen mit geringer Rauhigkeit ist großflächig möglich und eine Integration in einem mikrosystemtechnischen Herstellungsprozess ist gelungen. Die ersten Sensoren zeigen sehr vielversprechende Eigenschaften zur sensitiven und selektiven Detektion von Phthalaten. Darüber hinaus können die Schichten als aktive Substrate für die elektronische Detektion von Zelleingenschaften genutzt werden. In beiden Anwendungsbereichen, der Biosensorik und der Bio- und Neuroelektronik, bleibt noch sehr viel Raum für zukünftig neue Anwendungen dieser neuartigen Materialklasse.

Acknowledgements

As my doctoral journey draws to a close, I would like to express my deepest gratitude to everyone who offered their guidance, help, and support during my time at IWE1.

First and foremost, I am deeply thankful to my supervisor, Prof. Dr. Sven Ingebrandt, for giving me the opportunity to conduct my research at IWE1 and for his invaluable guidance throughout my doctoral study. Your lectures on 'Bioelectronics' greatly enhanced my understanding of the phenomena observed in my transistors and sparked my interest in bio-related research. It was an honour to serve as a tutor for the 'Bioelectronics' course, an experience I thoroughly enjoyed. Thank you!

I am also grateful to Prof. Dr. Joachim Knoch for agreeing to be the second examiner of my thesis and for granting me access to the tools at IHT to characterize my MOF thin films and devices. The knowledge I gained from your 'Nanoelectronic Devices' lectures was instrumental in helping me comprehend the behaviours observed in my transistors. Thank you!

My sincere thanks go to Dr. Vivek Pachauri for his direct supervision. Without your invaluable suggestions and our countless scientific discussions, completing my thesis within four years would not have been possible. I am also grateful for the opportunities you provided to attend national and international conferences, which broadened my horizons and allowed me to connect with experts from both academia and industry. Thank you!

I would like to extend my appreciation to Prof. Dr. Francesca Santoro and Dr. Ziyu Gao for their assistance in conducting cell-related studies. Your help was invaluable. Thank you!

I am also thankful to Prof. Dr. Akash Deep for assisting with TEM characterizations of MOF samples, which significantly contributed to my manuscript. Thank you!

A special thank you goes to all the members of IWE1 for their scientific, technological, administrative, and moral support. In particular, I would like to thank Prof. Dr.-Ing. Uwe Schnakenberg, Dr. Xuan Thang Vu, Hartmut Pütz, Patrick Borycka, Lisa Hertje, Lea Baumann, Jochen Heiss, Dorothee Breuer, Eva-Janina Sekula, Esra Camkerten, Dagmar Noetzel, Nicola Gelhausen, Piriyangka Pushparani, and Melanie Kaesler.

Acknowledgements

I am also grateful to my colleagues and former colleagues: Divagar Murugan, Dibyendu Khan, Animesh Singh, Hesam Amiri, Hocine Bahri, Sota Hirokawa, Aidin Nikookhesal, Ahmed Ben Romdhane, Daniele Storelli, Andrea Kauth, Felix Jiang, Chunling Li, Yuan Cao, Eashika Ghosh, Jan Wagner, Milad Eyvazi Hesar, and Roman Deubel. Thank you for making my time at IWE1 truly unforgettable!

I would also like to thank my project, thesis, and Hiwi students for their contributions to my research projects: Bo Stäglich, Shiqi Zhang, Tianyu Wei, Isil Berfin Sönmez, Henning Bommes, Minju Kim, Ahmed Zacky Mohomed Yoosuf, Maria Anastasia Sinarso, Ming Li, Meriam Mrad, and Zakaria N'Sairia.

My heartfelt thanks go to the Chinese Scholarship Council for their crucial financial support, which made it possible for me to pursue my doctoral studies in Germany.

I would also like to express my appreciation to my friends for the wonderful times we shared.

To my girlfriend, thank you for your unwavering mental support and companionship.

I am immensely grateful to my younger brother for taking care of our mother and managing all the little things back home.

Finally, my deepest gratitude goes to my mother for her selfless support over the past four years. Thank you, Mom!

Thank you all!

Table of Contents

Introduction

A microelectronic sensor functions as a bridge between the environment and microelectronics, much like conventional sensors. Its primary role is to convert non-electrical input variables, such as physical, chemical, or biological stimuli, into electrical signals that are compatible with readout systems. [1-4] For example, chemical sensors quantitatively detect the presence or concentration of chemical substances such as neurotransmitters, pesticides, and volatile organic compounds and produce corresponding electrical outputs, [5-7] while biosensors detect biological analytes such as enzymes, antibodies, or DNA, and generate electrical signals accordingly. [8, 9] Such a sensor is composed of three principal functional components: a converter or so-called receptor, a transducer, and a signal processor. The transducer is the core component, responsible for converting non-electrical signals into electrical outputs. The receptor and signal processor facilitate the communication between the environment and the transducer, as well as between the transducer and the readout system. As the term "microelectronic" suggests, the fabrication of these sensors utilizes techniques derived from microelectronics and semiconductor manufacturing, enabling the creation of devices that are extremely small and capable of integration with other electronic components. This miniaturization capability allows for their use in compact, portable devices with low power consumption.

The transducer, which serves as the core of a microelectronic sensor, has undergone significant advancements over the past decades since the 1940s. [10] These advancements have seen transducers evolving from conventional elemental semiconductors (e.g., Si, Ge, and Te) [11, 12] to III-V compound semiconductors (e.g., GaN, GaAs, and GaP), [13, 14] wide bandgap semiconductors (e.g., SiC, ZnO, and CdS), [15, 16] organic semiconductors, [17, 18] low-dimensional semiconductors (e.g., carbon nanotube and transition metal dichalcogenides, TMDCs), [19, 20] and more recently, emerging porous semiconductors (e.g., metal-organic frameworks, MOFs and covalent-organic frameworks, COFs). [21-24] The superior electrical properties and enhanced sensitivity for chemical and biological sensing make these novel materials promising candidates for transducers in sensor applications. This potential is further supported by technological developments in the microfabrication, packaging, and characterization of microelectronic devices. [5-9] However, the integration of emerging semiconducting materials, such as MOFs, with contemporary semiconductor technologies is still in its early stages. Current efforts are primarily focused on the fabrication of high-quality thin films and the optimization of on-chip integration processes. [21-24]

Introduction

The receptor, in a microelectronic chemical/biosensor is as crucial as the transducer. [25, 26] In such sensors, the receptor is responsible for detecting the presence of specific molecules/analytes. For example, a shift in the threshold voltage of a silicon-based ion-sensitive field-effect transistor (ISFET) has been observed when exposed to electrolytes with varying pH levels. This shift can be attributed to alterations in the surface potential due to the protonation or deprotonation of surface hydroxyl groups. [27] Thus, a well-designed or carefully selected receptor is essential for facilitating specific binding with targeted analytes, such as DNA-DNA coupling or antigen-antibody interactions. However, a significant limitation of semiconducting transducers in microelectronic chem/biosensors is the lack of inherent functional groups that can specifically bind to analytes. This challenge is particularly pronounced when detecting small molecules, where their small size, low molecular weight, and minimal charge, result in limited sensitivity and selectivity. [28, 29] Moreover, introducing external functional groups to the surfaces of transducers through post-synthetic modification might alter their intrinsic electrical properties. [30] Therefore, it is critical to discover or develop new semiconducting materials that can actively interact with their surroundings and effectively convert these interactions into electrical signals.

Metal-organic frameworks (MOFs), a class of crystalline porous materials, have recently garnered significant attention from researchers across various fields, including chemistry, materials science, physics, and biology. As organic-inorganic hybrid materials, MOFs are composed of metal nodes (either individual metal ions or complexed metal clusters) and multidentate organic ligands, connected through coordination linkages. [31-34] Compared to conventional porous materials, MOFs offer several distinctive features, including tuneable structures and functionalities, ordered channels, high porosity, abundant binding sites, and a high specific surface area. These novel materials demonstrate tremendous potential in a variety of applications, including gas separation and storage, energy conversion and storage, catalysis, sensing, and biomedicine. [35-48] Recently, their applicability in electronics and optoelectronics has gained recognition, particularly with the successful synthesis of electrically conductive MOFs (c-MOFs). [49-53] The exceptional electrical properties of c-MOFs make them as effective signal transducers, while their abundant binding sites, such as open metal sites and organic functional groups, can serve as receptors to specifically interact with external analytes. [54-56] This ideal combination of tuneable compositions, structures, and diverse electrical properties positions c-MOFs as highly promising candidates for applications in microelectronic sensors, particularly in chemical and biosensing.

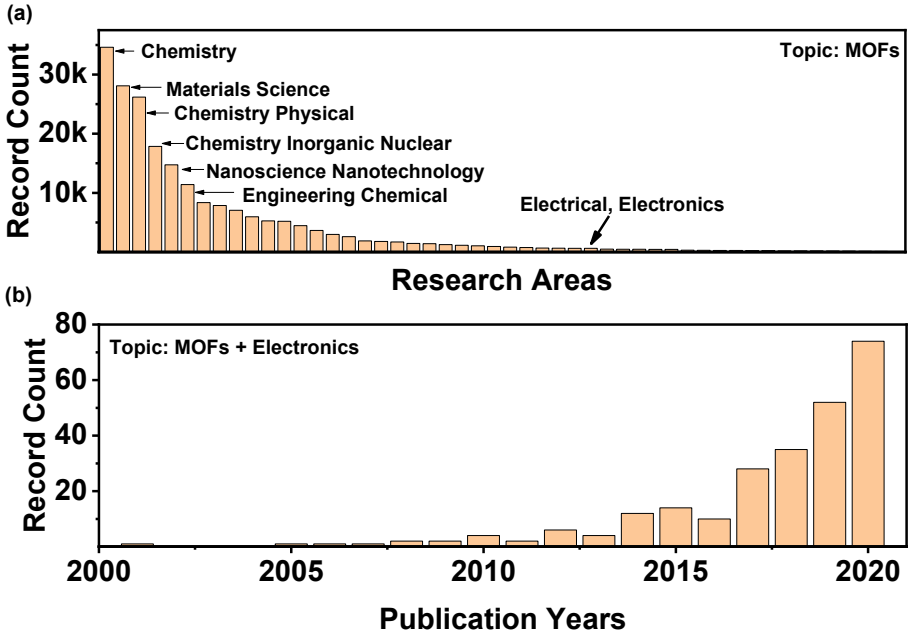

Figure 0.1: Current research areas of MOFs. (a) Publication records of top 50 research areas of MOFs. The majority of research is focused on Chemistry and Materials Science, while the application of MOF-based electronics is still in the early stages of development. (b) The development of MOF-based electronics over the past two decades. The successful synthesis of electrically conductive MOFs in 2012 marked a turning point, leading to a period of rapid growth in the application of MOFs in electronics.

During my doctoral studies, the focus was on the investigation of two insulating MOFs and one semiconducting MOF, with the aim of developing advanced microelectronic sensors for detecting small molecules, such as phthalates, and studying cell-substrate interactions. The overall research comprised the growth of high-quality MOF thin films, the development of lithographic patterning techniques, and the integration of these thin films into microelectronic devices for electrical characterization and sensor applications. Chapter 1 provides an overview of the theories that underpin the thesis, including the fundamental chemistry and electrical properties of MOFs, current strategies for the growth and patterning of MOF thin films, and the potential applications of MOF-based microelectronic sensors. Chapter 2 describes two platforms designed for the liquid-phase epitaxial growth of MOF thin films using a layer-by-layer strategy: (i) an automated microfluidics platform and (ii) an automated dip coater. This chapter explores how synthetic parameters, such as precursor concentrations, solvents, and temperatures, influence the growth of MOF thin films. Additionally, the correlation between microfluidic depositions and dip coating was discussed. Chapter 3 presents three lithographic patterning methods developed for thin-film characterization and on-chip integration. The application of these methods was evaluated in the context of the stability of the MOFs and the synthetic parameters used. Furthermore, an optical approach based on the optical contrast of MOF thin films on Si/SiO_2 substrates is introduced for rapid quality assessment of patterned MOF thin films, including

their homogeneity and thickness. Chapter 4 focuses on the on-chip integration of semiconducting MOF thin films through microfabrication, in conjugation with the liquid-phase epitaxial growth and lithographic patterning techniques developed earlier. This chapter also discusses the use of rapid thermal processing technology to enhance the quality of MOF thin films, including improvements in crystallinity and conductivity, and to optimize the electrical contact between metal microelectrodes and MOF thin films. Ultimately, an electrolyte-gated field-effect transistor was constructed and systematically studied in phosphate buffers with varying ionic strengths. Chapter 5 marks the first application of MOF-based microelectronic chemical sensors for detecting small molecules, with a particular focus on phthalates due to growing concerns regarding water safety. Eleven types of phthalates were tested to evaluate the sensing performance of the developed microelectronic sensors using electrochemical impedance spectroscopy and to elucidate the underlying host-guest interactions. The findings provide valuable insights for the further optimization of MOF-based microelectronic sensors for small molecule detection. Chapter 6 introduces the second application of these microelectronic sensors: the study of cell-substrate interactions using Electric Cell-substrate Impedance Sensing, in which MOF thin films serve as novel functional substrates in contact with cells. The excellent biocompatibility of MOF thin films enables the long-term monitoring of cell dynamics. Finally, Chapter 7 summarizes the main achievements of my doctoral research and offers an outlook on the future of MOF-based microelectronic sensors.

1 Theory

Metal-organic frameworks (MOFs), also known as porous coordination polymers, are a class of crystalline porous solids, constructed of metal nodes and organic ligands through coordination chemistry (**Figure 1.1**). [57-59] With advancements made over the past 30 years, MOFs demonstrate great potential in a variety of applications, including gas separation and storage, energy conversion and storage, catalysis, sensing, electronics, optoelectronics, and biomedicine. [35-48] Such advanced applications rely on the unique structure features (e.g., high specific surface area and porosity, tunable structures and functionalities), and superior chemical, optical, and electrical properties. In particular, the combination of porosities, functionalities and electrical conductivities enable MOFs promising candidates for microelectronic sensor applications. [60, 61]

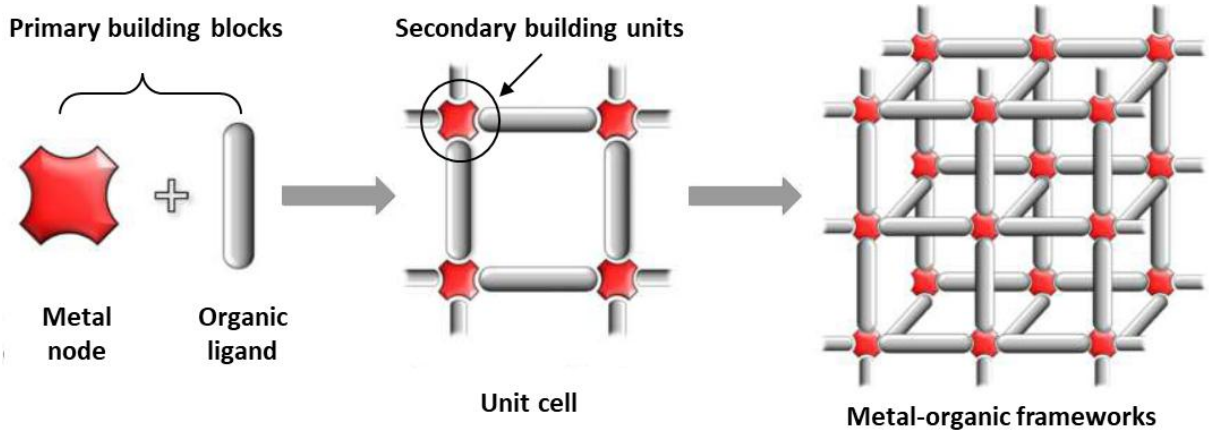

Figure 1.1: Schematic illustration of typical synthetic route and structure of MOFs. [62] The design of MOFs are driven by both metal-containing building blocks and organic building blocks.

This chapter begins with a theoretical discussion that introduces the fundamentals of MOFs, including secondary building units (SBUs) used in the construction of MOFs, the corresponding structural classifications of MOFs (one-dimensional, two-dimensional and three-dimensional lattices) and the approaches for the design and discovery of novel MOFs (reticular chemistry, post-synthetic modification, template-based synthesis, theoretical simulation and machine learning). The subsequent discussion focuses on the electrical properties of MOFs, including electrical transport pathways and electrical characterization approaches, as well as their applications in electronics, specifically in transistors, where MOFs serve as functional or channel layers). Finally, the chapter addresses the fabrication and patterning of MOF thin films are introduced, which is crucial for realizing such advanced applications.

1.1 Secondary building units

In the context of design and discovery of novel MOFs, the concept of reticular chemistry is employed. [63, 64] This strategy has been utilized to guide the design and synthesis of porous framework materials (e.g., MOFs and COFs) over the past two decades. [65, 66] Reticular chemistry represents a generic methodology for forming extended crystalline frameworks through the application of strong bonds to connect SBUs, which are metal cluster entities comprising metal ions and the corresponding coordination groups from organic ligands . This approach has been instrumental in advancing the development of MOFs in structural design and target applications. To achieve rational reticular design of MOFs, three primary prerequisites must be fulfilled: (i) SBUs, (ii) topological networks, and (iii) isoreticular chemistry. [65] Based on isoreticular chemistry, numerous MOFs have been synthesized with the same or similar topological networks but exhibit varying properties. Examples include the isoreticular MOFs (IRMOF) series and the Matériaux de l′Institut Lavoisier (MIL) series. [67, 68] Among these, the structural characteristics of the SBUs for the design and synthesis of MOFs are of particular importance, including the number of nodes and the geometries involved. The abundance of available SBUs allows for the rational design and discovery of numerous novel MOFs through the strategic assembly of diverse SBUs. Within the context of MOFs, SBUs consist of two primary building blocks: metal-containing building blocks (MBBs) and organic building blocks (OBBs), which will be discussed in greater detail subsequently. The following section will focus on the structures of MOFs that can be assembled from these primary building blocks through coordination bonds, including one-dimensional (1-D) linear structures, two-dimensional (2-D) planar structures, and three-dimensional (3-D) complex structures.

1.1.1 Metal-containing building blocks

In keeping with the rapid development of the MOFs community, MBBs have evolved from simple single-metal nodes (SMNs) to complex multiple-metal nodes (MMNs) or metal clusters, as illustrated in **Figure 1.2**. In comparison to SMNs, which possess known coordination numbers (CNs) and coordination geometries (CGs), MMNs exhibit a broader range of potential coordination numbers (e.g., CN=12, 18, and 24) and a markedly more intricate array of CGs (e.g., cuboctahedron and snub square antiprism). In this context, SBUs with connectivity n are designated as n-connected (n-c) SBUs, where $n \geq 2$. Additionally, the concept of the dimensionality of MBBs (rod-like (1-D) and sheet-like (2-D) MBBs) has recently emerged as a distinct category, rather than being subsumed under zero-dimensional (0-D) or dot-like SMNs/MMNs.

This section will examine metal-containing SBUs in terms of their CNs, CGs, and dimensional characteristics.

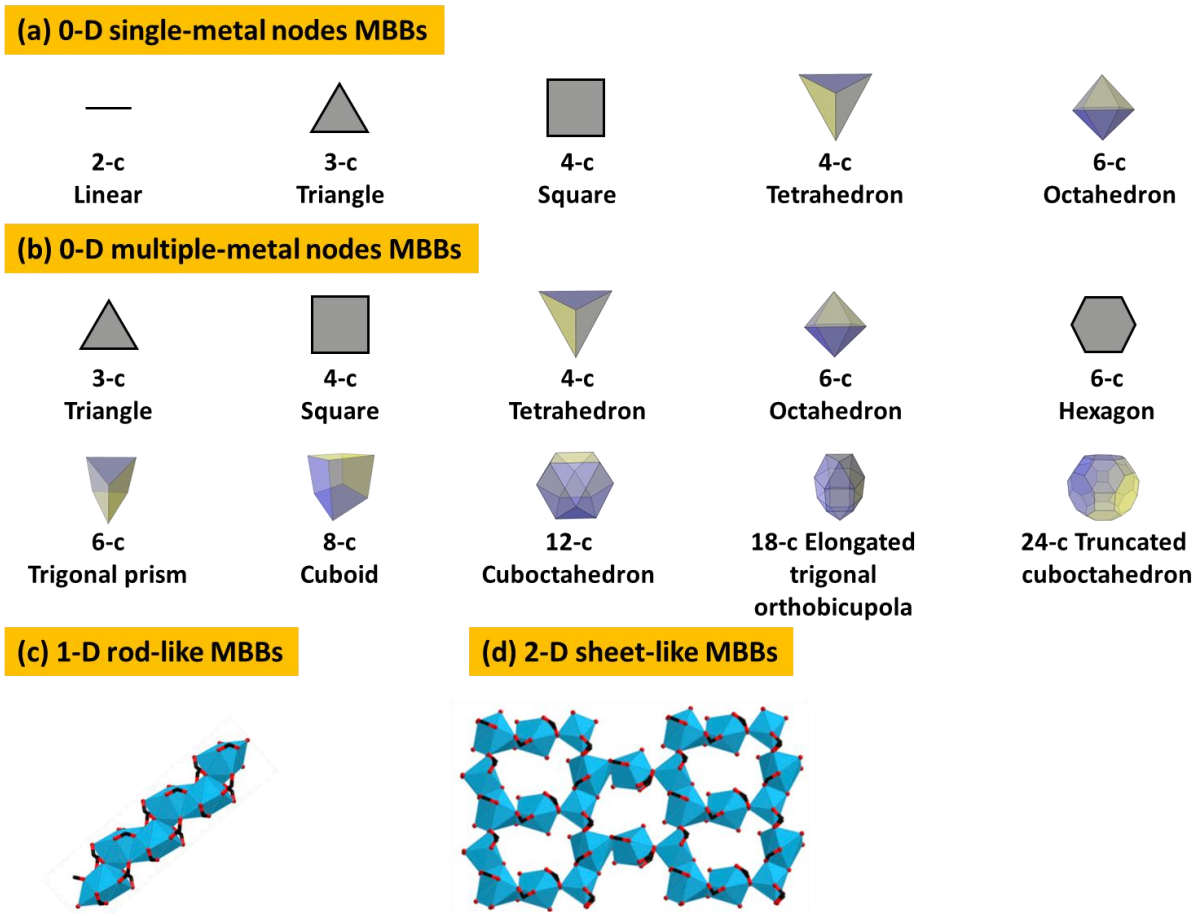

Figure 1.2: Classification of MBBs. Polyhedrons in (a) and (b) are resourced from https://www.mathsisfun.com/. Polyhedrons in (c) and (d) are resourced from Ref 69. [69]

Dot-like MBBs. MBBs with a dot-like morphology are classified into two categories based on their complexity. SMNs and MMNs. As widely recognized, SMNs represent a class of indispensable components utilized in the formation of molecular complexes with primitive CGs, as illustrated in **Figure 1.2**. These complexes take the form of 3-c triangles, 4-c squares/tetrahedrons, and 6-c octahedrons. In the construction of MOFs, SMNs are frequently employed in zeolitic imidazolate frameworks (ZIFs), which constitute a subclass of MOFs with zeolite-like structures. [70, 71] In order to simplify the crystal structures, metal ions are regarded as SMNs only when the number of coordinated linkers is identical to the CG of the metal ions, which delineate the target topological nets, shown in **Figure 1.2a**. For instance, a Zn^{2+} ion with a 4-c tetrahedron CG could coordinate with four imidazolate (im) linkers, resulting in a $Zn(im)_4$ tetrahedron SBU. This SBU could then be extended along the xyz axes toform a 3-D framework. Additionally, an Ag^{+} ion with a 3-c triangle CG can react with three tricyanomethide to form a triangular SBU, resulting in a 2-D extended structure. [72] However, greater attention should be paid to linkers

capable of forming chelation with metal ions, whereby the number of linkers is not identical to the CG of the metal ions. Subsequently, when simplified as topological nets, the CG would be unambiguous and would not be ignored. To illustrate, when Cu^{2+} ions with a 6-c octahedral CG react with 2,3,6,7,10,11-hexahydroxytriphenylene (HHTP) molecules, only two HHTP molecules coordinate with one Cu^{2+} ion, forming a planar geometry. Concurrently, two solvent molecules, such as H_2O, coordinate perpendicular to the square. Upon examination of the resulting MOF structure, $Cu_3(HHTP)_2$, it can be observed that each HHTP molecule contributes two adjacent -OH groups, which react with one Cu^{2+} ion to form a square configuration. As previously stated, two H_2O molecules obstruct the remaining two coordination sites. Therefore, Cu^{2+} ions in $Cu_3(HHTP)_2$ can only be considered 2-c linear SBUs in the ultimate topological net. [73] In contrast, the representative examples of SMNs as 6-c octahedron building blocks are SIFSIX MOFs, a series of materials based on square grid layers constructed by connecting M^{2+} cations (such as Cu^{2+}, Ni^{2+}) and linear organic linkers (e.g., bipyridine). [74, 75] These materials are pillared with inorganic $[SiF_6]^{2-}$ anions. However, if the pillar molecules are replaced by solvent molecules, the central metal would present a 4-c square CG, resulting in 2-D layers. To date, the majority of reported MOFs have been constructed using first- or second-row transition metal ions with low CNs and known CGs. Despite the use of rare-earth metal ions (e.g., Eu and Tb) with higher CNs in the construction of MOFs, the CNs and CGs of rare-earth metal ions remain constrained. It is imperative to underscore that the CNs and CGs of SMNs are unambiguous. [76]

Consequently, when MMNs function as MBBs, the intrinsic CNs and CGs of each metal ion are typically disregarded in order to simplify the ultimate topological nets. It should be noted, however, that this does not imply that these components are unimportant; they are essential for the construction of MOFs. As has been documented, MMNs possess a greater abundance and intricacy of CN and CG, encompassing not only the 3-c triangles, 4-c squares/tetrahedrons, and 6-c octahedrons, but also the 6-c hexagons/trigonal prisms and 8-c cuboids. These include the icosahedron, the 12-c cuboctahedron, the 16-c snub square antiprism, the 18-c elongated trigonal orthobicupola, and the 24-c, and even higher CNs and more complex CGs, shown in **Figure 1.2b**. Consequently, MMNs afford researchers a greater scope for the design and synthesis of versatile MOFs with enhanced stability and additional functionalities. Among inorganic materials, the periodic structure comprising 3-c triangles represents the chiral 3-D Si network observed in $SrSi_2$ and has been regarded as a structural model for reticular synthesis. [77] For example, a representative MOF with the same topological net was constructed using 1,3,5-benzenetricarboxylate (BTC) linkers and Zn-based MMNs with a propeller-shaped binuclear $Zn_2(CO_2)_3$. [78] Consequently, the synthesis of a Cu-based MOF with the same topology was

achieved by replacing Zn^{2+} with Cu^{2+}. [79] However, MMNs with a 3-c triangle CG are less prevalent than SMNs. The most prevalent 4-c MMNs typically exhibit 4-c squares with a binuclear metal paddlewheel (M_2L_4), where M represents a divalent metal ion such as Cu^{2+}, Ni^{2+}, Co^{2+}, etc. L denotes the linker, which may be a bridging ligand such as terephthalic acid (BDC). [80, 81] For example, MOF-2 is assembled from Zn^{2+} paddlewheels with a 4-c square CG and 2-c linear BDC linkers. In this configuration, the additional two open sites perpendicular to the square are occupied by solvent molecules, such as H_2O or other capping reagents, resulting in 2-D frameworks. [80] If the aforementioned two open sites are connected to two additional linear linkers, thereby forming a second linker, a 6-c octahedral MMN is produced. In this structure, the second linear linkers serve the function of pillars, facilitating the joining of adjacent 2-D layers. Furthermore, other MOFs with 6-c octahedral MMNs are IRMOF series, such as MOF-5, in which each Zn-O cluster connects six BDC linkers, thereby forming a 3-D framework with a cubic topology. In addition to the octahedral CG, a hexagonal CG of MMNs is also a possibility. For example, Schröder's research group reported the discovery of a MOF, $[Zn_3(1,4\text{-}BDC)_3(DEF)_2]\cdot DEF$ (DEF = N,N-Diethylformamide), which exhibits 6-c MMNs. [82] In the structure, six BDC^{4-} anions are associated with a building block, forming links with six separate building blocks, which together give the honeycomb-like 2-D net. The aforementioned MMNs are often employed in the construction of MOFs due to their straightforward and well-characterized CGs and CNs. Furthermore, in order to enhance the diversity of MOF systems and provide additional potential for MOFs, MMNs with higher CNs and more intricate CGs have been developed, including those with 8-c, 12-c, 16-c, and 24-c MMNs. In general, they are utilized in the construction of complex MOFs with 3-D structures.

Rod-like MBBs. As previously stated, the CGs and CNs of 0-D metal-containing SBUs are clearly defined, whereas those of 1-D rod-like metal-containing SBUs are infinite. [83, 84] Consequently, the structural design and prediction of MOFs derived from 1-D metal-containing SBUs is more challenging than that of 0-D dot-like metal-containing SBUs. This is due to the fact that the ultimate topological nets based on 1-D metal-containing SBUs are vague, which in turn makes it difficult to predict. Nevertheless, the analytical methodology for the structural and topological characterization of MOFs based on 1-D metal-containing SBUs has been well-established. Furthermore, while the prediction of target nets remains challenging, some MOFs, designated as rod-MOFs based on 1-D metal-containing SBUs, can be reliably synthesized through reticular chemistry, as exemplified by the MOF-74 series. [85] The MOF-74 series, also known as CPO-27 (coordination polymer of Oslo), is constructed from 1-D metal-containing SBUs, namely metal oxide chains and 2,5-dioxido-1,4-benzenedicarboxylate ($DOBDC^{4-}$). By

modifying the metal ions, including Zn^{2+}, Cu^{2+}, Mg^{2+}, Fe^{2+}, and organic linkers, a variety of MOFs with analogous frameworks to MOF-74 have been synthesized through reticular chemistry. [85] The successful synthesis of MOF-74-type frameworks is contingent upon the fulfilment of the following requirements: (1) Metal ions with similar CGs, and (2) –OH groups included in linkers are postulated to be at the ortho-position of carboxyl groups. However, MOFs based on 1-D metal-containing SBUs are typically 3-D frameworks, and thus far, no 2-D MOFs have been obtained from 1-D rod-like metal-containing SBUs.

Sheet-like MBBs. Similarly, as with 1-D metal-containing SBUs, metal-containing SBUs with 2-D infinite frameworks have also been synthesized, although they remain relatively uncommon. Metal-containing SBUs constructed into 2-D sheet-like structures are also referred to as "sheet-MOFs", though they possess 3-D frameworks. [86] Moreover, sheet-MOFs are anticipated to exhibit enhanced stability, including thermal and solvent stability, based on the findings that rod-MOFs are more stable than MOFs constructed from 0-D metal-containing SBUs. For example, ULMOF-1, one of the sheet-MOFs, exhibited remarkable thermal stability up to 610°C under an N_2 atmosphere. [87] Furthermore, a Ce-based MOF comprising 2-D metal-containing SBUs was synthesized and designated as CTH-15. [86] In this compound, an infinite 2-D metal-containing SBU is formed, and the 2-D metal-containing SBUs are connected by benzene-1,2,4,5-tetracarboxylic acid linkers, designated as H_4BTEC. The authors demonstrated that rod-MOFs and sheet-MOFs are more stable than MOFs constructed from 0-D metal-containing SBUs.

1.1.2 Organic secondary building blocks

In contrast to MBBs, OBBs exhibit significantly simpler CNs and reduced CGs. However, the enhanced structural flexibility and diversity inherent to these units render the design and prediction of target MOFs more challenging. A recent review paper discussed the flexible characteristics of organic linkers. [32] Eight fundamental operations are employed to describe the changes in position of the end groups in OBBs. These are the identity operation, four in-plane operations (expansion, contraction, in-plane rotation, and in-plane translation), and three out-of-plane operations (torsion, out-of-plane rotation, and out-of-plane translation). For further details, please refer to the aforementioned review. Nevertheless, the structural flexibility and diversity of MOFs have led to the emergence of new categories, which continue to expand the field. A number of strategies are commonly employed for the classification of organic SBUs. For example, organic linkers are classified according to the coordinated groups present, including carboxyl, hydroxyl, amino, thiol, and even halogens. [88, 89] In this study, the organic SBUs

are categorized based on their CNs and CGs in accordance with reticular chemistry. Similarly, organic SBUs exhibit comparable CGs and CNs values to those observed in simple 0-D metal-containing SBUs, including the 2-c sticks, 3-c triangles, 4-c squares, 4-c tetrahedrons, and 6-c hexagonal structures. The diverse geometries of OBBs offer a multitude of possibilities for the construction of novel and versatile MOFs. Nevertheless, the development of linkers with specific geometries, particularly those with high connectivity, is a pressing necessity. Consequently, there is imperative for organic chemists to synthesize the requisite organic molecules.

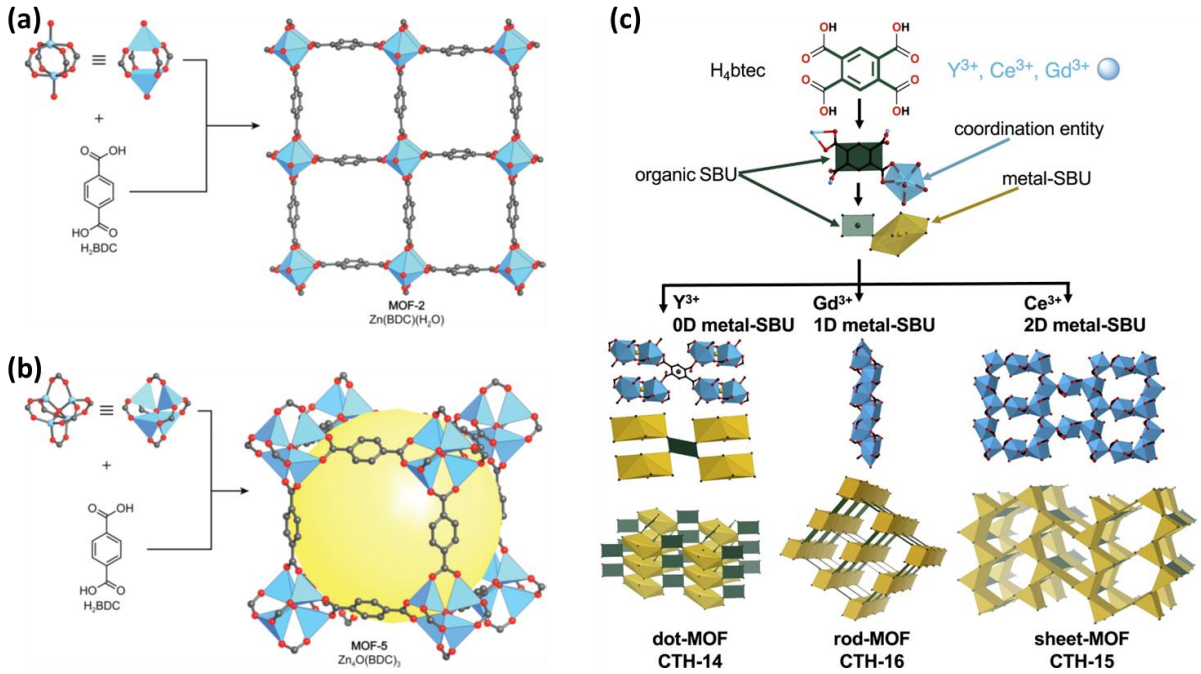

Figure 1.3: The application of reticular chemistry for the synthesis of MOFs. Crystal structures of (a) MOF-2, $Zn(BDC)(H_2O)$ [80] and (b) MOF-5, [90] $Zn_4O(BDC)_3$. (c) Overview of the three different MOFs, CTH-14, CTH-15, and CTH-16 constructed from dot-, rod-, and sheet-like MBBs. [86]

1.2 Structures of MOFs

This section presents an introduction to the structures of MOFs, based on the dimensions of the constructed lattices. The combination of MBBs and OBBs allows for the formation of 1-D, 2-D, and 3-D lattices through the assembly of SBUs based on the principles of reticular chemistry. For example, a combination of 2-c organic OBBs with 3-c triangles, 4-c squares, or 6-c hexagons MBBs, could result in the formation of 2-D lattices. Furthermore, it should be noted that 2-c linear OBB with 2-c linear OBBs result in 1-D coordination polymers rather than MOFs. The corresponding lattices of MOFs constructed of SBUs with varying connectivity are summarized in **Table 1-1**.

As illustrated in **Figure 1.3a**, MOF-2, a 2-D lattice constructed by Zn^{2+} ions, features a 6-c octahedral CG and 2-c BDC linkers. [80] In MOF-2, Zn^{2+} ions coordinate with BDC linkers to

form a planar 2-D square net, resulting from the combination of 4-c square metal-containing SBUs and 2-c linear organic SBUs. The remaining two coordination sites are perpendicular to the 2-D lattice and are capped by solvent molecules, such as H_2O. Subsequently, MOF-2 with a 2-D structure is constructed by extending the structure across the 2-D plane. Moreover, the adjacent monolayers are held together by van der Waals forces. However, by slight modification of the reaction conditions, MOF-5 with a 3-D lattice can be synthesized, as illustrated in **Figure. 1.3b**. [90] The MBBs in MOF-5 are more complex than those in MOF-2. They coordinate with six BDC linkers to form a 3-D lattice comprising 6-c octahedron metal-containing SBUs and 2-c linear organic SBUs, where the Zn-O clusters adopt an octahedral CG.

In the construction of 2-D MOFs, the starting components can be either 2-c linear building blocks or 3-c triangles, 4-c squares, or 6-c hexagons with planar geometries. For example, 2-c linear BDC linkers, 3-c triangular HHTP linkers, and 4-c planar Tetrakis(4-carboxyphenyl)porphyrin (TCPP) linkers may be employed. In accordance with reticular chemistry, the formation of 2-D lattices is contingent upon the connection of 2-c building blocks with 3-c triangles, 4-c squares, and 6-c hexagons. Given the inherent limitations in the electrical conductivities of most MOFs, this discussion will focus on a select class of MOFs that exhibit enhanced electrical conductivity, designated as electrically conductive MOFs (c-MOFs). This topic will be elaborated upon in greater detail in **Section 1.4**. A review of the lattices of c-MOFs reveals that the majority are constructed from pi-conjugated organic SBUs, including HHTP, hexaiminotriphenylene (HITP), and hexathiotriphenylene (HTTP). [48] To the best of my knowledge, $Ni_3(HITP)_2$ is one of the most conductive c-MOFs, with a conductivity of 40 S cm^{-1}. [91] The employment of HHTP, HITP, or HTTP as organic SBUs and Cu^{2+}, Ni^{2+}, or other metal ions with planar CGs as metal-containing SBUs allows for the formation of honeycomb-like 2D lattices. In $Ni_3(HITP)_2$, the HITP linkers serve as 3-c triangular organic SBUs, while the Ni^{2+} ions are 2-c linear MBBs, in contrast to the 4-c squares or 6-c octahedrons that would be expected. In light of the above, it is worth reiterating that when employing the concept of reticular chemistry to extract topological nets and to inform the design and synthesis of MOFs, the intrinsic CGs and CNs are, to some extent, set aside. However, it is important to bear in mind that the individual CG of single ions is a crucial factor in the discovery of new MOFs.

In comparison 2-D lattices, 3-D lattices such as MOF-5 series and ZIF series offer a greater range of design and synthesis options. One of the most prevalent strategies is the utilisation of MBBs or OBBs in conjunction with 3-D CGs. The ZIF series represents a typical example of this category, featuring SMNs with porous structures analogous to those observed in zeolites.

For instance, ZIF-8 is constructed from 4-c tetrahedral Zn^{2+} ions and 2-c linear imidazole linkers. Similarly, the synthesis of ZIF-7 and ZIF-90 was achieved by replacing the imidazole linkers with their derivatives. [92, 93] Consequently, the pore sizes can be modified, and the channels functionalized by altering the organic linkers, without affecting the final topological structure. Another frequently employed strategy is to link 2-D layers with 2-c linear linkers, such as 4,4'-bipyridine. Conversely, the distance between layers can be modified by utilising linkers of varying length.

Furthermore, I would like to introduce an outstanding piece of work reported by Amombo Noa et al. [86] The researchers obtained three distinct types of MOFs (termed dot-MOFs, rod-MOFs, and sheet-MOFs) by controlling the dimensions of the metal-containing SBUs, which were discussed in **Section 1.1** and illustrated in **Figure 1.3c**. The formation of dot-like, rod-like, and sheet-like metal-containing SBUs was typically achieved by utilizing Y^{3+}, Ce^{3+}, and Gd^{3+} as metal sources, respectively. Subsequently, the metal-containing SBUs are linked by an organic SBU, H^4BTEC, with a 4-c planar geometry, resulting in the formation of a dot-MOF in $H_2NMe_2[Y(BTEC)(H_2O)]$, denoted as CTH-14, a sheet-MOF in $[Ce_3(BTEC)(HBTEC)(OAc)(HCO_2)]$, denoted as CTH-15, and a rod-MOF in 4,4-azopyridinium$[Gd_2(BTEC)_2]$, denoted as CTH-16. In this study, the stability of the materials was also investigated, with the results indicating a trend from dot-MOFs to rod-MOFs to sheet-MOFs. Consequently, the sheet- and rod-MOFs exhibit enhanced thermal stability. Accordingly, an alternative approach would be to increase the dimensions of the MBBs in order to prepare more robust MOFs. However, the design of MOFs from rod-like MBBs or sheet-like MBBs is less reliable than that from well-established dot-like MBBs, in part due to the difficulty in predicting targeted nets. Nevertheless, the construction of some rod-MOFs from multi-functional groups can be achieved with a high degree of reliability through the application of reticular chemistry.

Table 1-1: Structures of MOFs assembled of SBUs based on reticular chemistry. In bolds are the MOFs synthesized in this thesis work.

Organic SBUs / *Metal-containing SBUs*		Linear (2-c)	Triangle (3-c)	Square (4-c)	Tetrahedron (4-c)	Octahedron (6-c)	Hexagon (6-c)
0-D	Linear (2-c)	1D	2D	2D	3D	3D	2D
	Triangle (3-c)	2D	2D	2D/3D	3D	2D	3D
	Square (4-c)	2D	2D/3D	2D/3D	3D	3D	3D
	Tetrahedron (4-c)	3D	3D	3D	3D	3D	3D
	Octahedron (6-c)	3D	3D	3D	3D	3D	3D
	Hexagon (6-c)	2D	2D	3D	3D	2D	3D
	Trigonal prism (6-c)	3D	3D	3D	3D	3D	3D
	Higher CNs (8, 12, 18, 24)	3D	3D	3D	3D	3D	3D
1-D		3D	3D	3D	3D	3D	3D
2-D		3D	3D	3D	3D	3D	3D

1.3 Design and discovery of novel MOFs

This section aims to present an overview of the general and recently emerging strategies employed in the design and discovery of novel MOFs. These include reticular chemistry, post-synthetic modification, template synthesis, theoretical simulation, and the application of machine learning. [63, 92, 94-98] Reticular chemistry represents the most popular strategy, which has been subjected to a systematic discussion in the preceding sections. The following section will discuss post-synthesis modification and template synthesis. Post-synthesis modification refers to the introduction of new functionalities after the synthesis of host MOFs. Template synthesis employs the use of soft or hard templates. The aforementioned strategies are primarily conducted through experimental means. Furthermore, this section will examine the applications of first-principles simulation and machine learning in the screening of optimal MOF structures and the optimization of suitable synthetic conditions for the preparation of targeted MOFs.

1.3.1 Post-synthetic modification

To some extent, post-synthetic modification (PSM) represents a complementary strategy for the synthesis of novel MOFs, given that the reticular chemistry of some MOF structures is constrained by steric hindrance associated with organic molecules or coordination affinity between metal ions and coordination groups. Consequently, the PSM of MOFs represents a valuable approach for the synthesis of novel MOFs with enhanced properties, thereby facilitating their potential applications in practical settings. PSM of MOFs has been employed in a multitude of fields, including gas adsorption and storage, catalysis, chemical and gas sensors, and numerous others. Furthermore, the structural stability of the resulting material can be enhanced through PSM.

By looking into MOF structures, which are constructed of metal clusters and organic linkers giving rise to porous solids. Consequently, there is sufficient flexibility to modify MOF compounds. For example, modifications may be made to the metal-containing SBUs, organic SBUs, a combination of both, or to the guest. In addition, the individual modification method comprises a series of more detailed approaches. I will refrain from discussing the details further. For further information, please refer to the recently published paper discussing the post-synthetic modification of metal–organic frameworks toward applications. [94] It should be noted that the structural stability of post-synthetically modified MOFs must be considered due to the potential solvent instability and harsh conditions for chemical reactions, including the use of strong acidic or basic solutions.

1.3.2 Template-based synthesis

As previously stated, reticular chemistry and PSM strategies are commonly utilized to design and synthesize new MOF structures with novel properties. Despite the high intrinsic specific surface area (1000–10000 $m^2 \cdot g^{-1}$) of MOFs, which is considerably higher than that of most other porous materials, such as zeolites and porous polymers, the pore sizes are relatively narrow, typically less than 2 nm. [99, 100] Consequently, the internal space of MOFs is inaccessible for bulk molecules, such as polymers and proteins, which are predominantly confined to the external surface of MOF particles. Furthermore, it is crucial to engineer the optimal shapes and morphologies (e.g., hollow or mesoporous structures) to increase and optimize the utilization of MOFs' accessible surface area and enhance the efficiency of MOF-based applications.

Two principal strategies have been employed to direct the synthesis of MOFs, namely soft-templated synthesis and hard-templated synthesis. In the context of soft-templated synthesis of MOFs, the most commonly utilized templates encompass surfactant micelles, DNA-like polymers, copolymers, and ionic liquids, among others. Hard templates are typically comprised of sacrificial templates (e.g., polymers, silica, MOFs, metal oxides, and layered materials), semi-sacrificial templates (e.g., MOFs), and non-sacrificial templates (e.g., polymers, silica, noble metals, MOFs, metal oxides, zeolites, and layered materials). This suggests that there are numerous potential avenues for regulating MOF morphologies and pore sizes through the use of templates. In summary, hard templates are typically employed to synthesize ordered nanomaterials (e.g., arrays) with well-defined shapes. Soft templates are typically employed to prepare nanomaterials with specific shapes (e.g., nanowires, nanorods) by leveraging the properties of micelles. In hard-templated synthesis, the shapes or morphologies of the resulting materials are dependent on the specific shapes of the hard templates employed. In contrast, the shapes or morphologies of soft-templated MOFs are determined by the self-assembly of micelles. Moreover, the removal of soft templates is relatively straightforward; however, it may result in the residual presence of the templates. The use of hard templates in MOF synthesis carries the risk of damaging the resulting nano-structured materials during template removal.

The template-confined growth strategy is an efficient, universal, and feasible approach among various synthetic strategies. The growth direction is contingent upon key parameters, including the adsorption energy barrier, catalytic activity, and hydrophilicity. In general, growth is constrained in the z-direction. Accordingly, in order to manufacture the target materials, it is necessary that the template possess a high dimension, in order to prevent chemical reactions from occurring. It can be reasonably deduced that templates with lower dimensions, such as nan-

owires and quantum dots, are unlikely to facilitate the formation of 2-D structures. Consequently, templates utilized for the synthesis of confined 2-D materials are typically available in 2-D or 3-D forms. As a confined template, 2-D materials such as graphene and its derivatives, TMDCs, MOFs, and other 2-D materials (e.g., 2-D metal oxides and hydroxides) are optimal for the growth of 2-D configurations due to their imposition of a z-direction restriction on growth. Furthermore, 2-D materials can be synthesized from 3-D textured materials, including 3-D salt crystals, 3-D metal foams, and 3-D liquid metal alloys. This differs from the process of 2-D templating, in which confined growth can only occur at the tops of 3-D templates. Subsequently, 3-D structures can be disintegrated via an emulsion process, thereby producing 2-D layers.

1.3.3 Novel strategies to discover MOFs

MOFs are highly versatile and can be nano-engineered in a multitude of hierarchical forms and material combinations. The controlled synthesis of MOFs is typically based on the metal-containing SBUs and organic SBUs involved and their respective properties, with the objective of achieving the desired applications. The use of computational tools such as Vienna Ab initio Simulation Package is beneficial for the targeted modelling of functional MOF architectures based on first-principles simulation. A number of theoretical reports on the sorption mechanism of MOFs are based on studies employing Density Functional Theory (DFT) and Grand Canonical Monte Carlo (GCMC) simulations. These studies investigate variations in electronic potentials, enthalpies, and dispersion interactions upon the adsorption of guest moieties. While there have been a few recent computational studies on the adsorption behaviours of MOFs for different adsorbates, the majority of these studies have yet to be practically applied and require further investigation. Furthermore, there is a paucity of theoretical modelling on coordination unsaturated sites (CUS) or surface functionalization-based adsorption in MOFs. In light of the aforementioned circumstances, a joint computational and experimental approach is recommended, whereby the potential for strong molecular interactions between the adsorbent (MOF) and adsorbate is initially evaluated through theoretical analysis. Such explorations will primarily focus on the CUS of the MOF in conjunction with the adsorbent, as well as the assessment of the diverse functional groups (amine, carboxylate, etc.) of MOFs in relation to the adsorbent. Subsequently, the theoretically feasible combinations can be evaluated through experimentation, thereby providing insights that can inform further refinements in MOF design.

Chapter 1: Theory

Theoretical modelling

The synthesis of innovative MOF structures using a variety of metal nodes and organic ligands has been the subject of investigation in order to fully realize their potential for optimum attributes. However, the potential number of MOF structures is infinite, given the numerous possibilities for ligand alteration and topology. Consequently, the experimental selection and optimization of suitable MOFs for specific applications has proven to be a significant challenge. The number of MOF types in the Cambridge Structural Database, which is updated and maintained by the Cambridge Crystallographic Data Centre, has increased to approximately 110000, from approximately 70000 in 2017. The preceding labour-intensive methodology is no longer a viable option in light of the accelerated expansion in research and development activities pertaining to diverse forms of MOFs.

The theoretical calculation can effectively address the shortcomings of experimental detection methods as a novel approach to material research, facilitating a more profound comprehension of chemical reaction mechanisms and the prediction of theoretical spectra for the purpose of identifying spectrum peaks. In recent years, theoretical calculations have become an increasingly significant aspect of material research and development, as evidenced by the growing number of theoretical calculations that have contributed to advancements in material research operations. The data-driven research approach for materials based on theoretical calculation is becoming increasingly prevalent with the development of supercomputers. The “computing first” approach has been employed in a growing number of research projects. In contrast to the synthesis-test research mode, the theoretical calculation-based approach enables the direct prediction and acquisition of diverse properties and structure-activity relations of materials from a theoretical perspective. This approach offers invaluable guidance for material development, potentially reducing the material development cycle and subsequent research costs. It is beyond doubt that the future of material discovery will be shaped by directional screening technology for materials with structural diversity, such as MOFs. Over the past decade, research on theoretical computations related to MOFs has seen a dramatic increase in activity. In order to anticipate the structures and properties of MOFs with extremely high accuracy, a variety of calculation theories, methods, and models are continuously developed, modified, and validated. However, there is currently no comprehensive analysis available that provides an overview of the theoretical advancements in MOF calculation methods and their practical applications.

Machine learning

The advent of enhanced molecular simulation methodologies and comprehensive MOF databases has rendered large-scale computational screening of MOFs for a multitude of applications

a realistic prospect. The application of high-throughput screening with GCMC simulations has been demonstrated to be an invaluable tool in the identification of optimal materials and the investigation of the theoretical performance limits of MOFs in gas storage and separation applications. The combination of large-scale structural screening and high-throughput DFT calculations represents a powerful approach for identifying novel MOFs with promising catalytic properties in the field of MOF-based catalysis. Furthermore, computational screening may also consider structural alterations that could be conducted on MOFs. The advent of robust computational tools has precipitated a significant shift in the research landscape for MOFs. Molecular simulations with reasonable precision can be used to obtain performance data for tens of thousands of MOFs. The exploration of MOFs for various applications is no longer limited to empirically synthesized structures, as the potential for constructing an almost limitless number of materials has been unlocked. These modifications, however, have introduced new challenges, as the collection of vast amounts of simulated data for MOFs indicates that straightforward interpretation and analysis are no longer a viable approach. Moreover, even with the most advanced computing resources currently available, exhaustively exploring all potential combinations and conducting exhaustive analysis to identify a few select top-performing MOFs is an inefficient approach.

The application of machine learning (ML) represents a potential solution to the aforementioned challenges. ML is a subfield of computer science that involves training computer systems to learn from given data and make predictions or judgments based on automated analysis. As part of our endeavour to identify uncertainty within a vast array of materials for a given application, ML offers a straightforward approach to comprehend the design and discovery of materials. It is important to note that ML is not the primary focus of scientific inquiry; rather, it is a valuable tool that enhances the process of scientific investigation. ML has begun to play a significant role in scientific research, with applications ranging from natural language processing and image analysis to drug discovery and genomics. ML has been employed in the field of materials science for a range of applications, including the design and optimization of organic semiconductors, metal oxides, conductive 2-D materials, and others. In the case of MOFs, ML approaches can be employed to identify latent trends in copious data sets that may not be immediately apparent but are crucial for comprehending material performance. Moreover, ML can effectively identify the structures that would demonstrate the highest performance for specific applications among an unlimited number of hypothetical MOFs. It is therefore essential to gain an understanding of how different ML methods have been used in the context of MOFs, as well as to identify potential avenues for the future integration of ML in MOF research. The advent

of this novel approach to material design and discovery will usher in a new era of materials, characterised by unprecedented opportunities and challenges.

1.4 Electrical properties

Electrical conductivity quantifies how well a material can transport electrical charge. It depends on two factors: the concentration of charge carriers, n, and the mobility of these carriers, μ. Manipulating either of these factors is complex and necessitates a thorough understanding of the material's electronic structure and the mechanisms behind charge transport. Fundamentally, charge transport in solids can occur via two general mechanisms: hopping transport and band-like transport, as illustrated in **Figure 1.4a**. In hopping transport, charges move between discrete, non-bonded sites where the carriers are localized. This mechanism is typical in disordered materials, glasses, and organic semiconductors. Conversely, in ballistic transport, strong interactions between sites create continuous energy bands with delocalized charge carriers, commonly seen in crystalline inorganic materials.

The primary distinction between these two mechanisms is the temperature dependence of conductivity. Hopping-type conductivity increases with temperature and follows an exponential law, as described by **Equation 1-1**:

$$\sigma = \sigma_0 * \exp\left[-\frac{T_0}{T} * \frac{1}{d}\right] \quad \text{1-1}$$

Where σ is the conductivity, T is the temperature, T_0 and σ_0 are constants specific to the material, and d is the dimensionality of the sample.

In contrast to hopping transport, band-like transport can be influenced by temperature in both positive and negative ways. In metallic materials with high carrier concentrations, conductivity is hindered by various scattering processes that become more pronounced at higher temperatures, resulting in less efficient transport. In semiconductors, conductivity is typically limited by the charge carrier concentration. Higher temperatures generate more free holes or electrons, leading to increased conductivities. The conductivity of semiconductors often follows an Arrhenius dependence, as shown in **Equation 1-2**:

$$\sigma = \sigma_0 * \exp\left[-\left(\frac{E_a}{kT}\right)\right] \quad \text{1-2}$$

Where E_a is the activation energy. The value of E_a is tied to the width of the band gap, as well as the energy levels of dopants.

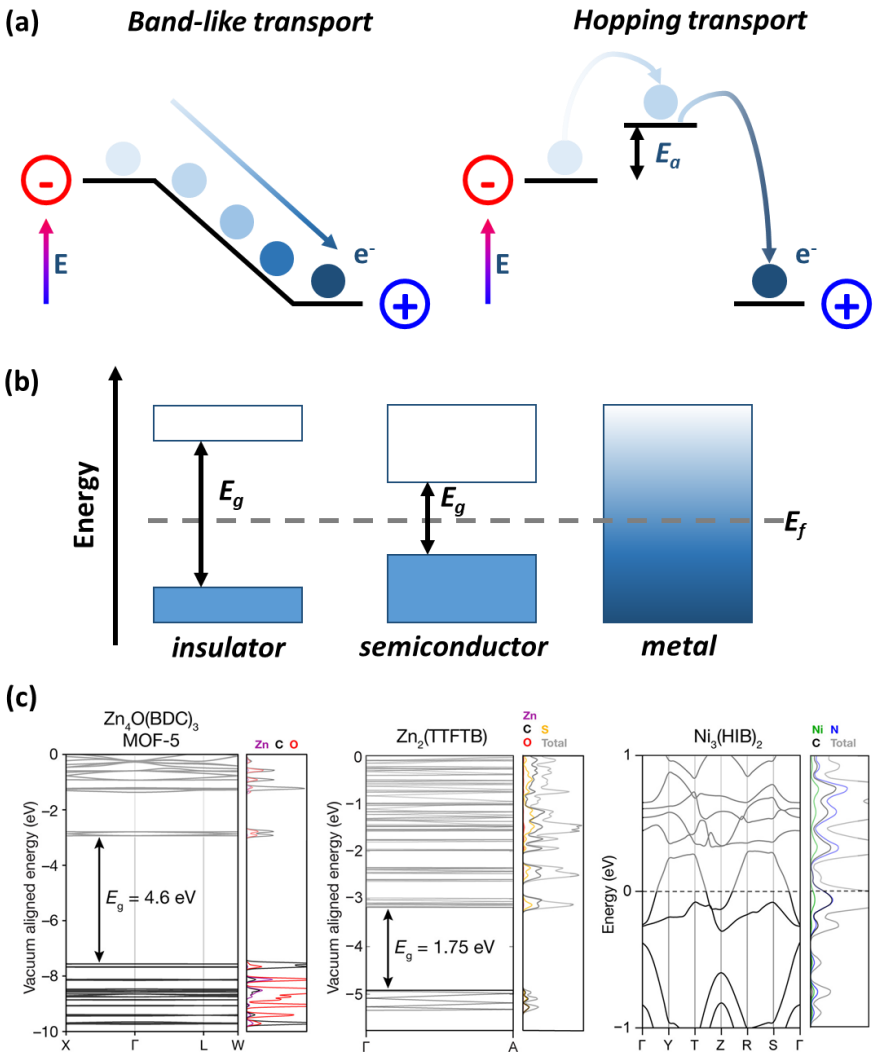

Figure 1.4: Electrical properties of MOF. (a) Two primary charge transport mechanisms: band-like transport and hopping transport. (b) Electronic structures of a typical insulator, semiconductor, and metal, where E_g is the band gap and E_f is the Fermi level. (c) Calculated electronic band structures and densities of states for an insulating MOF (MOF-5), a semiconducting MOF (Zn_2(TTFTB), where TTFTB is tetrathiafulvalene tetrabenzoate), and a metallic MOF ($Ni_3(HIB)_2$, where HIB is hexaiminobenzene). [101]

The generalized electronic band structures of an insulator, semiconductor, and metal are depicted in **Figure 1.4b**. An insulator is characterized by a large band gap (E_g), typically greater than 4 eV, resulting in a very low population of the conduction band. A semiconductor has an intermediate E_g that allows the promotion of free charge carriers to the conduction band through thermal or optical excitation. A metal has at least one band crossing the Fermi level (E_f), providing a continuum of allowed electronic states and leading to high conductivities. **Figure 1.4c** illustrates examples of a typical insulating MOF (MOF-5), a semiconducting MOF (Zn_2(TTFTB)), and a metallic MOF ($Ni_3(HIB)_2$).

In practice, determining charge transport mechanisms is complicated by several factors. Specifically for conductive MOFs, two key issues arise. First, most measurements in the literature

have been performed on polycrystalline pellets rather than single crystals. This introduces an inherent thermally activated resistance due to hopping between different grains of the material. Second, significant disorder or defects can create trap states, where charge carriers become localized and must hop between these states. For instance, a missing linker defect could disrupt a charge transport pathway, creating a barrier to transport, with other types of defects having similar effects. To definitively determine the charge transport mechanism in a material, a combination of variable temperature single-crystal conductivity studies, electronic structure calculations, and optical spectroscopy is required.

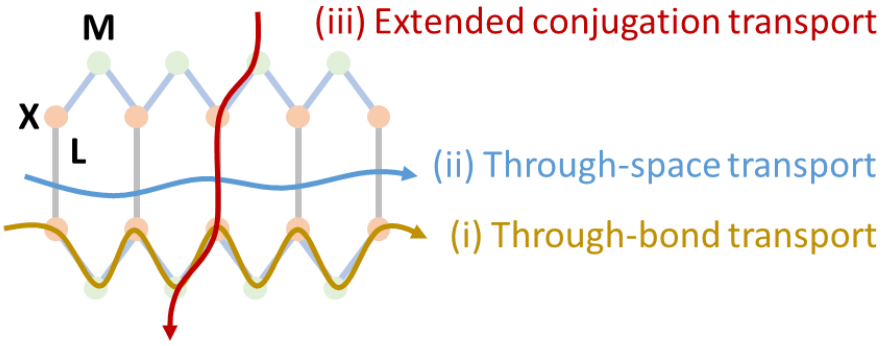

Figure 1.5: Three charge transport pathways have been proposed in c-MOFs, although it should be noted that this is not an exhaustive list. (i) through-bond transport (brown), ii through-space transport (blue), and (iii) extended conjugation transport (red). M, L and X represent metal centre, organic linker and coordination atom, respectively.

1.4.1 Electrical transport pathways

In designing conductive MOFs, manipulating charge transport pathways is still under exploration. These include the through-bond pathway, the through-space pathway and extended conjugation pathways, which are intrinsic charge transport mechanisms. [101] Guest-induced charge transport pathways will not be discussed here. **Figure 1.5** illustrates the above-mentioned charge transport pathways, which will be discussed with details in following sections.

Through-bond pathways. Here we define the ···M-X-M-X··· chain (brown curve) where the charge carries flow through as through-bond charge transport pathway. Therefore, to facilitate charge flow, well-matched energy levels and proper orbital overlap between metal centres and coordination atoms are paramount, which result in small band gaps and high charge mobilities. In this case, the main skeleton of organic ligands is not involved in transporting charge carrier. The representative MOFs with through-bond pathways are Mn_2(DSBDC), Fe_2(DSBDC) (DSBDC = 2,5-disulfhydrylbenzene-1,4-dicarboxylic acid), Fe_2(DOBDC), Fe_2(DOBDC) (DOBDC = 2,5-dihydroxybenzene-1,4-dicarboxylic acid), $K_xFe_2(BDP)_3$ ($0 \leq x \leq 2$;

BDP^{2-} = 1,4-benzenedipyrazolate), and $Fe_2(BDT)_3$ (H_2BDT = 5,5′-(1,4-phenylene)bis(1H-tetrazole)). [102-105] From these reported highly conductive MOFs, it is approved that softer and more electroactive linkers with coordinating sulphur or nitrogen atoms is favourable for charge carrier flow through ···M-X-M-X··· chains resulting from the energy matching and improved metal-ligand orbital overlap.

Through-space pathways. In contrast to though-bond pathways, the organic ligands are involved in transporting charge carriers. In this case, these organic ligands are featured with large π systems with free electrons. Then charge carrier could be transported through organic linkers or through space by π-π interactions. Such phenomenon with through-space pathways is pronounced in TTFTB- and HHTP-based conductive MOFs, such as M_2(TTFTB) (M = Mn, Zn, and Cd) and LnHHTP (Ln = La, Nd, Ho and Yb). [106, 107] Based the this concept for designing electrically conductive MOFs, more organic ligands with larger π systems were synthesized and employed for the synthesis of MOFs, such as 1,2,3,4,5,6,7,8,9,10,11,12-perthiolated coronene, 2,3,9,10,16,17,23,24-octahydroxyphthalocyanine, and metal(II) 2,3,9,10,16,17,23,24-octaaminophthalocyanine. [108-111]

Extended-conjugation pathways. Such an extended-conjugation pathway is a combination of through-bond pathway and through-space pathway. Therefore, the requisites for both charge carrier transport pathways need to be met in one MOF: (i) energy matching and orbital overlap between metal centres and coordination atoms from ligands and (ii) ligands with π-conjugated systems. Such a combination allows for efficient delocalization of charge carriers within the plane, resulting in extended π-d conjugation and high electrical conductivities. The representative examples are HHTP-, HITP-, and HTTP-based 2-D MOFs, such as $Cu_3(HHTP)_2$, $Ni_3(HITP)_2$, and $Fe_3(HHTP)_2$. [91, 112, 113]

1.4.2 Electrical characterizations

Electrical characterizations including the determination of conductivity and contact resistance. As shown in **Figure 1.6a**, there are four commonly utilized techniques to characterize the electrical conductivity of MOFs, including two-contact method, four-contact method, four-probe method and Van der Pauw (VdP) method. The applications of such measurement techniques depend on the morphology of the samples, (e.g., single crystals, thin films and pressed pellets) as well as the conductivity.

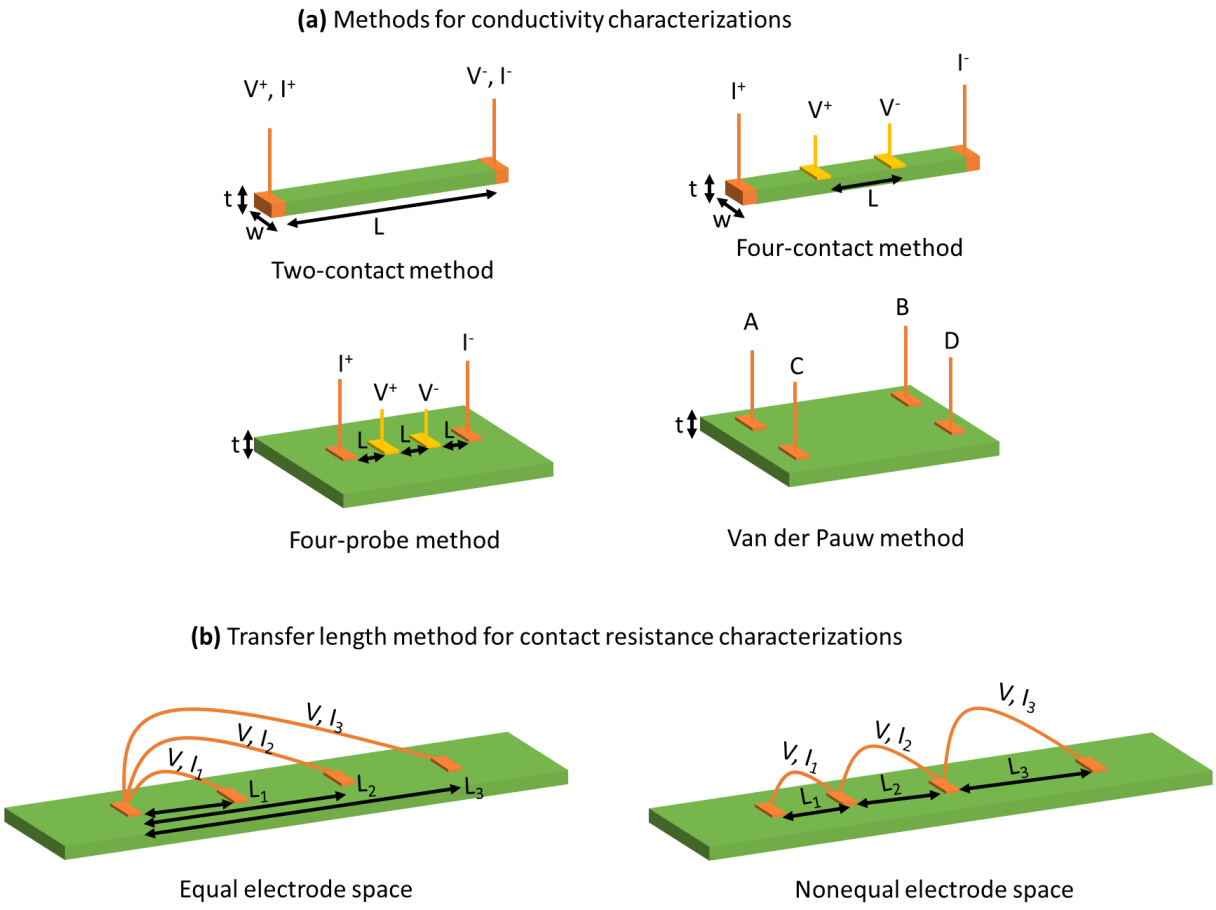

Figure 1.6: Techniques for electrical characterization of c-MOFs. (a) Measurement techniques employed for determining the electrical conductivity of MOFs (single crystals, thin films or pellets). (b) Transfer length methods for the characterizations of contact resistance between MOFs and metal electrodes.

For two-contact method, a constant voltage or current is applied on two electrodes. Current flowing through the sample or the voltage between two electrodes is measured. Then, the conductivity value can be calculated using **Equation 1-3** with known dimensions. Nevertheless, if the resistance of the measured sample is at the same level or lower than contact resistance, four-contact method or four-probe method would be the best. Because both methods exclude the contribution of contact resistance while measuring the resistance. Typically, a constant current is applied to the measured sample through two outer electrodes, the voltage is measured between two inner electrodes. However, the determination of conductivity values depends on the samples. For instance, four-contact configuration is more favourable while measuring large single crystals. Two metal electrodes are attached along the direction where is the conductivity is being evaluated. It is important that the contacts cover the full width of the crystal in the orthogonal direction to allow good estimates of the cross-section area through which current is passed. Then, **Equation 1-3** can be used to calculate conductivity values. In terms of thin films or pressed pellets, four small contacts are attached to the surface, equally spaced along a line.

The conductivity can be calculated from **Equation 1-4**. The VdP method is generally less sensitive to the shape of the sample and should be preferred to the linear four-probe configuration when working with non-rectangular samples. For VdP measurements, four small contacts are attached to four corners of the sample. Then, two resistances are estimated, with current applied along one side, and voltage measured along the opposite. Then, the conductivity of the sample is estimated with **Equation 1-5**. It is worth noting that all the electrical contacts between the measured samples and metal electrodes need to be ohmic contact because ohm's law is employed while calculating conductivity.

Contact resistance can be characterized using transfer length methods (TLM), shown in **Figure 1.6b**. It involves measuring the resistance through a test structure with different gap spacings between the two ohmic contacts and plotting it as a function of the gap spacing. Then the contact resistance can be calculated using **Equation 1-6**. **Figure 1.6b** illustrates two generic configurations to determine contact resistance: (i) equally spaced electrodes and (ii) non-equally spaced electrodes.

$$\sigma = \frac{I}{V} * \frac{L}{w * t} \tag{1-3}$$

$$\sigma = \frac{I}{V} * \frac{1}{2\pi * L * f_1} \tag{1-4}$$

$$\sigma = \frac{ln2}{\pi * t * R_{avg} * f_2} \tag{1-5}$$

$$R_{total}(L) = 2 * R_c + R_{sh} * \frac{L}{w} \tag{1-6}$$

Where σ denotes electrical conductivity. I and V are current and voltage. L, w, and t are the dimensions of the measured samples. f_1 and f_2 are the correction factors depending on the geometry of the sample. R_{avg} is averaged resistance. R_{total}, R_c and R_{sh} are total resistance, contact resistance and sheet resistance, respectively.

1.5 MOF-based electronics for sensor applications

With the advancement of conductive MOFs in recent years, the application of such novel materials in electronics has been extended from serving as functional layers to transducer layers. These conductive MOF-based electronics were for the first time named as MOFtronics by Feng et al., such as electronics, optoelectronics, spintronics, and energy devices. [48] According to my interest and doctoral research, MOF-based transistors are introduced here with details as well

as the sensor applications, including insulating MOFs as functional layers, dielectrics-gated MOF transistors, and electrolyte-gated transistors, shown in **Figure 1.7**.

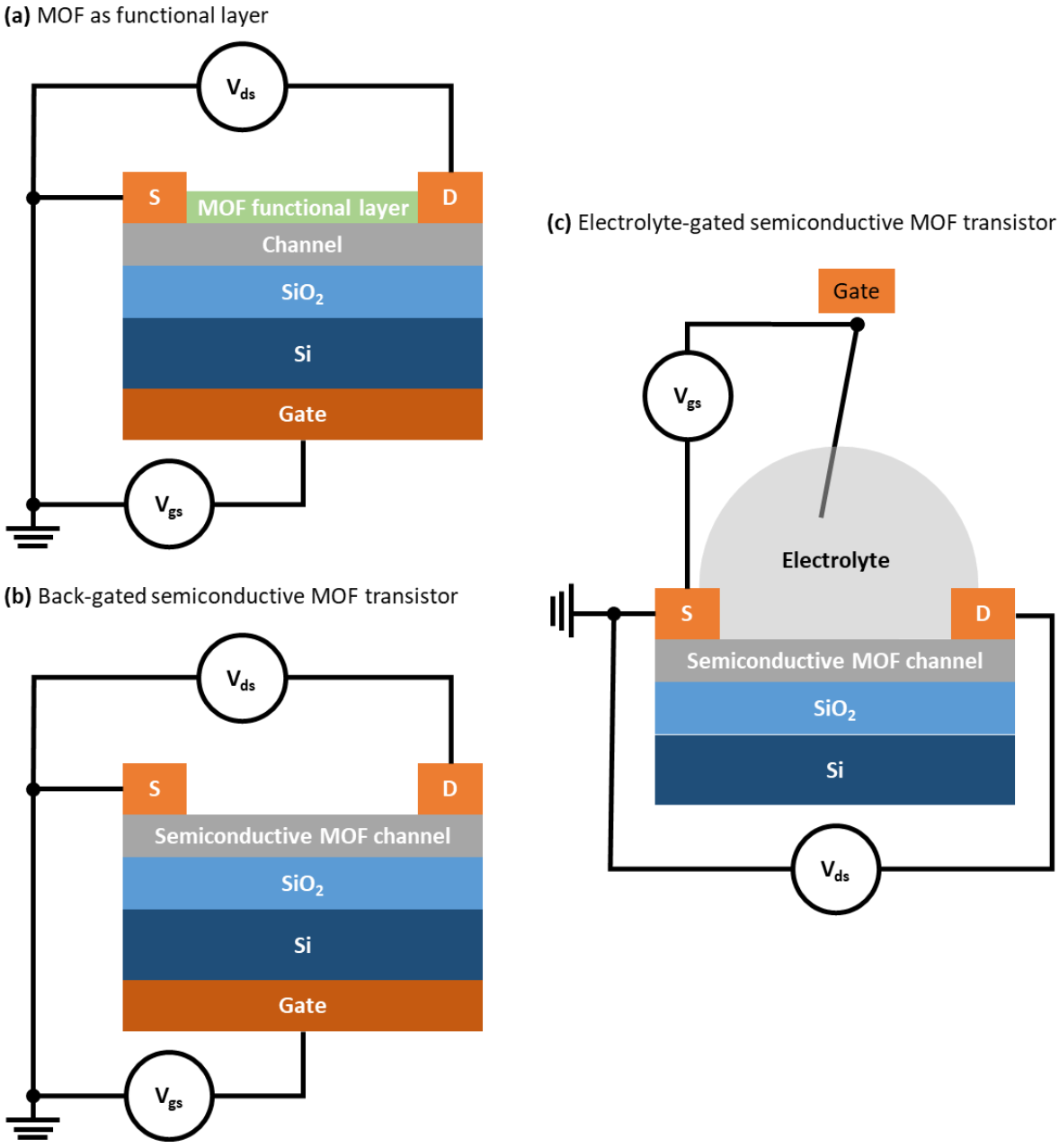

Figure 1.7: Schematic illustration of device configurations of MOF-based field-effect transistors. (a) Insulating MOF functionalized transistor. (b) Dielectrics-gated semiconductive MOF transistor. (c) Electrolyte-gated semiconductive MOF transistor.

1.5.1 Insulating MOFs as functional layers

Among the known MOFs, most of them are insulating, showing very low electrical conductivities ($\sigma < 10^{-9}$ S·cm^{-1}). Nevertheless, such insulating MOFs have shown the capability of improving the performance of the well-studied electronics due to the high specific surface area and porosities, tailorable structures and functionalities, and abundant binding sites. For instance,

one of the typical applications is serving as functional layer on the top of transistor channel, illustrated in **Figure 1.7a**. The channel layers have found to be organic semiconductors (e.g., small molecules and polymers), carbon materials (e.g., carbon nanofibers, graphene), TMDCs (e.g., Molybdenum disulfide), and so on. [114-120] For instance, the intrinsic sensitivity of graphene to vicinal dielectrics and local charge distributions can be probed by examining the position of the Dirac point in graphene FETs. However, to exploit this as a useful sensing principle, it is necessary to achieve selectivity, which is challenging given that graphene itself exhibits no molecule-specific interaction. To solve this problem, Kumar et al. demonstrated an ethanol sensor based on graphene transistors with a MOF layer (Cu-BDC) through liquid phase epitaxial growth. Such a MOF functionalized graphene transistor exhibited a good selectivity to isopropanol, methanol, and other interfering species in air, including water, which can be ascribed to the specific binding of ethanol on Cu-BDC layer. [116] The diversity of insulating MOFs makes them suitable for use as functional layers or receptors, and further research into their applications is warranted.

1.5.2 Back-gated MOF transistors

Semiconductive MOFs are emerging as a class of promising materials, which integrate conductivities and porosities. Therefore, semiconductive MOFs themselves could function as channel layers to construct electronic devices with inherent functionalities, shown in **Figure 1.7b**. [121-123] For instance, Wu et al. for the first time reported a semiconductive MOF based transistor. [123] The channel layer, $Ni_3(HHTP)_2$ membrane, was transferred to Si/SiO_2 substrates after forming an entire layer on air-liquid interfaces. Such a $Ni_3(HHTP)_2$-based transistor exhibited a p-type characteristic with a decent on/off ratio ($> 10^3$). The hole mobility was calculated to be 48.6 $cm^2 \cdot V^{-1} \cdot s^{-1}$. Besides, Lu et al. reported a flexible transistor based on $Ni_3(HHTP)_2$, showing a typical p-type characteristic in air. [121] Nevertheless, the on/off ratio of current was approximately 1.1, indicating poor field-effect regulation of the semiconductive MOF channel. Even though, such a flexible transistor based on $Ni_3(HHTP)_2$ exhibited a good sensing performance (e.g., low limit of detection of 56 ppb and superior selectivity) towards NO_2 in a mixed atmosphere. The exploration of semiconductive-based transistors is still in its infancy, constrained by the limited varieties of semiconductive MOFs.

1.5.3 Electrolyte-gated transistors

In addition to the characterization of semiconductive MOF-based transistors with a solid dielectric in dry conditions, the promising semiconductive MOFs were also characterized in liquids. This type of transistor is classified as an electrolyte-gated transistor, wherein an electrolyte

serves as the dielectric layer and an external gate electrode is required (e.g., an Ag/AgCl reference electrode or a Pt wire). In contrast to dielectrics-gated transistors, the channel conductance of electrolyte-gated transistors can be modified by the gate voltage through ion migration from the electrolyte, which is known as field-effect doping or electrochemical doping. The capacity to function in an aqueous setting and the direct coupling of ions and electrons bestow upon electrolyte-gated transistors a low operational voltage of less than 1 V. To date, nevertheless, only a few research reported semiconductive MOF-based electrolyte-gated transistors. [124-127] For instance, Song et al. reported a $Cu_3(HHTP)_2$-based electrolyte-gated transistor, which exhibited a n-type characteristic in 0.1 M $CaCl_2$ electrolyte solution. The carrier mobility was found to be 4.0 $cm^2 \cdot V^{-1} \cdot s^{-1}$, which was first time to fabricate an ideal n-type electrolyte-gated transistors. [126] Furthermore, the capability of detecting dopamine in liquid was demonstrated, showing high selectivity and sensitivity. However, an ambipolar characteristic of $Cu_3(HHTP)_2$-based electrolyte-gated transistors was reported by the same group, implying that more systematic studies are needed to evaluate the device characteristics and performance. [125]

1.6 MOF thin films

In the above section, the application of MOFs in electronics was discussed with examples, particularly in transistors. To achieve such advanced applications, therefore, it is of great importance to scale down bulk MOFs into thin layers, namely thin films, which facilitates the on-chip integration of MOFs using conventional techniques, such as micro-/nanofabrication and thin-film technologies. In terms of fabrication of MOF thin films, the main routine approaches are categorized into (i) top-down and (ii) bottom-up strategies. [128] For top-down strategy, typically MOF crystals or microcrystals are synthesized in advance, and then dispersed into proper solvents forming MOF suspension. Eventually, MOF films or membranes are deposited onto substrates by drop-casting, spin-coating and so forth. Nevertheless, the formed MOF layers are quite rough and not homogeneous. Besides, the adhesion of MOF layers with substrates also is weak resulting in detachment. Therefore, the integration and applications of MOFs using top-down approaches are limited. In contrast, the bottom-up strategy enables us to construct MOF layers from atomic or molecular levels, such as interfacial synthesis, gas-phase synthesis, and electrosynthesis. Such bottom-up strategy has numerous advantages including thickness controllability, homogeneity, scalability, and ease to integrate with semiconductor processing techniques.

Here, I would like to introduce the approach employed throughout my doctoral study. Layer-by-layer liquid-phase epitaxy (LbL-LPE) based on self-terminating surface reactions, one of

the well-established approaches for the growth of MOF thin films on solid substrates, was for the first time introduced by Wöll and his coworkers in 2007. [129] **Figure 1.8a** illustrates the typical procedures of using LbL-LPE to grow MOF thin films. The precursors are dissolved into separate containers. Initially, the growth substrates (e.g., Au, glass, and Si/SiO_2) are functionalized through different methods depending on the surface functionalities. For instance, oxygen plasma or piranha cleaning treatment is sufficient to generate hydrophilic surfaces with hydroxyl groups, which is beneficial for the nucleation steps. Instead, thiol chemistry is applied to functionalize Au surfaces with desired groups. Step i: the functionalized substrates are submerged into metal precursor solution for a certain period of time (e.g., 10 minutes). Step ii: the substrates from Step i are cleaned with rinsing solvent for a certain period of time (e.g., 2 minutes) to remove unreacted metal precursors, which is typically the same as the solvent for dissolving both precursors. Step iii, the cleaned substrates from Step ii are immersed into organic precursor solution for a certain period of time (e.g., 10 minutes). Step iv: same as step ii, the organic ligand residues are washed away to ensure homogeneous growth of MOF thin films. These four steps are called one LbL cycle. By repeating such LbL cycles, MOF thin films with varying thickness can be obtained. In addition, by varying the surface functionalities, it is possible to regulate the crystallinity and crystallographic orientation of the grown MOF thin films.

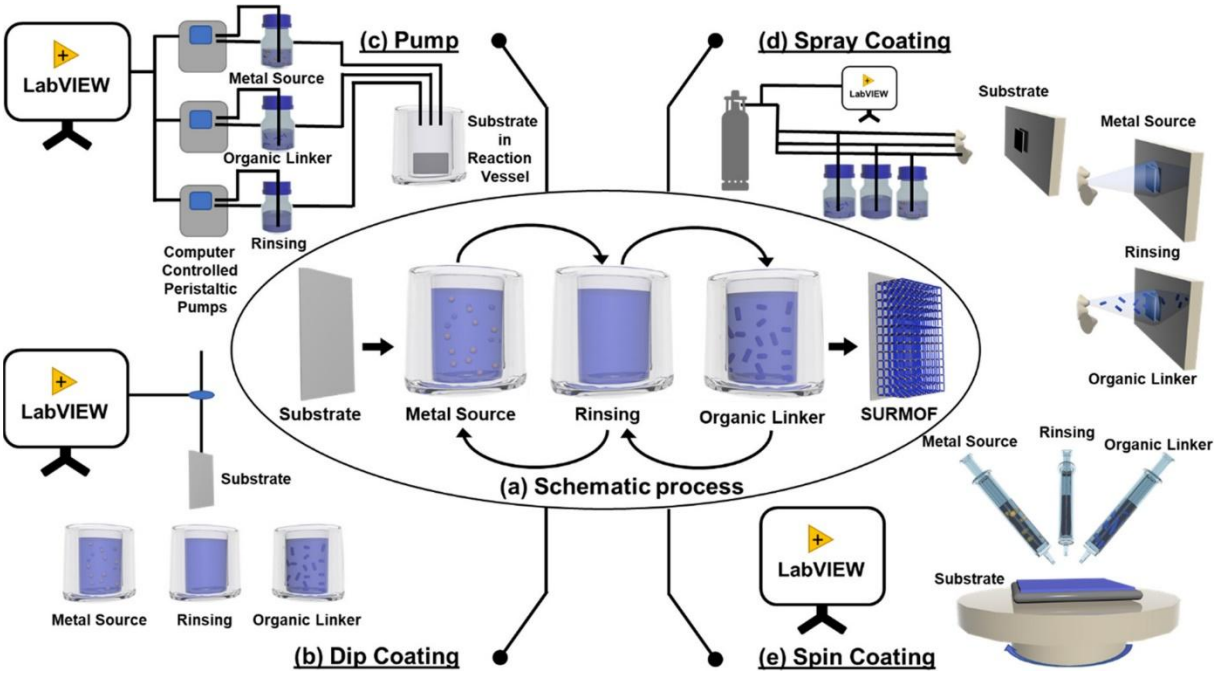

Figure 1.8: Growth of MOF thin films. Schematic illustration of (a) layer-by-layer liquid-phase epitaxy approach for the growth of MOF thin films, (b) dip-coating system, (c) pump-based system, (d) spray-coating system and (e) spin-coating system. [130]

1.6.1 Automated platforms

To perform LbL-LPE for the growth of MOF thin films, four automated techniques were developed, shown in **Figure 1.8b-e**, including dip coating, spin coating, spray coating and pump-based system. [130] The first LbL-LPE process was introduced by Wöll et al. in 2007 to grow $Cu_3(BTC)_2$ thin films with a manual dip coating manner. [129] In 2015, the same research group reported an automated dip coater or so-called dipping robot (**Figure 1.8b**), resulting in easier operation and higher reproducibility of the grown MOF thin films. [131] Instead of moving and submersing substrates into precursor solutions, an automated pump system (**Figure 1.8c**) was achieved in 2011 to perform LbL-LPE for the growth of MOF thin films. [132] Typically, the growth substrates are placed in a cell with temperature control. Then precursor solutions and cleaning solutions are alternatively introduced into the cell. Such an automated pump system has been applied to grow MOF thin films at an elevated temperature instead of room temperature, such as $Zn_2(BDC)_2(H_2O)_2$ and $Cu_2(BDC)_2(H_2O)_2$. Nevertheless, both techniques consume large amount of chemicals and solvents, which don't meet the requirements of atomic economy and green chemistry. Therefore, to reduce solvent and chemical waste, automated spray-coating system and spin-coating system were developed to perform the same LbL-LPE process for the growth of MOF thin films. [133] Regarding the spray-coating method (**Figure 1.8d**), an aerosol is produced from the precursor solutions in the nozzle, which contains tiny droplets with sizes down to the 10 μm region. Then these tiny droplets impact the substrate and form a thin film of reactants on the substrate surface. The material is then deposited at the solid/liquid interface in a manner similar to that observed in the LPE process. There are several critical parameters of the spray coating-assisted LbL-LPE growth, including carrier gas pressure, liquid pressure, flow rate, and distance between the nozzle and the targets. Typical values of these parameters are 1.5 bar, 0.2 bar, 0.25 mL/s and 0.1 m. In 2016, another high-throughput approach was developed by Eddaoudi et al, which a combination of spin coating method with LbL-LPE growth, as shown in **Figure 1.8e**. [134] Compared with the conventional LbL-LPE process (e.g., dipping, pumping), this approach provides a great potential to grow MOF thin films with low cost, significantly reduced preparation time and less chemicals and solvents consumption. The dominant parameters for the successful spin coating procedure include the spin coating speed, spinning time and injection volume/concentration.

As discussed above, each technique has its own advantages and disadvantages, such as the dip coating process is capable of growing MOF thin films on different scales, from small chips to wafer size while it consumes lots of chemicals and solvents. Though pump-based process has

the same disadvantages, the growth of MOF thin films can be conducted at elevated temperatures, which is favourable of the crystallinity of grown layers. Spray-coating and spin-coating systems both can minimize the usage of chemicals and solvents, however, the homogeneity of grown of MOF thin films is not as good as that grown through dip coating process, which is limited by the spray nozzles or spin stages. Accordingly, a compromise must be reached when preparing MOF thin films for a variety of applications.

1.6.2 Patterning methods

The patterning or structuring of MOF thin films is a critical step in the integration of these materials on chips, as it ensures precise positioning. [135, 136] Both bottom-up and top-down strategies have been developed to structure MOF thin films, shown in **Figure 1.9**. In bottom-up methods, molecular building blocks self-assemble into a desired arrangement. However, precise control over the localization of the self-assembly sites is a challenging task. [137] In contrast, top-down approaches employ external stimuli to eliminate the undesired components of a larger area, thereby creating the desired shapes in the preferred location. [138]

Bottom-up patterning

There are two common methods for bottom-up patterning of MOF thin films. (i) micro-contact printing of self-assembly monolayer (SAM) followed with thin-film growth and (ii) conversion of patterned precursor layer. [139-146] For instance, Zhuang et al. reported patterned HKUST-1 films by spin coating on patterned SAMs, which was achieved by creating alternative hydrophilic/hydrophobic patterns using 11-mercaptoundecanoic acid (MUDA) and 1-hexadecanethiol (HDT) with the implementation of microcontact printing. [144] Due to the different surface properties of patterned SAMs, following the spin coating process, the precursor solution was observed to remain predominantly in the hydrophilic areas, thereby restricting crystal nucleation and growth to these regions upon exposure to the alkanol vapor. Stassen et al. reported the conversion of ZnO into ZIF-8 thin films. [139] Typically, a thin layer of ZnO was deposited on a photoresist-patterned substrate through atomic layer deposition. Then, ZIF-8 thin film can be transformed by exposing patterned ZnO layer to 2-methylimidazole (HmIM) vapor. Eventually, the patterned ZIF-8 thin films were completed by removing sacrificial photoresist layer with a simple lift-off process.

Top-down patterning

In contrast to bottom-up patterning, top-down approaches involve the fabrication of MOF thin films on the entire surface, which is followed by lithography process (e.g. photolithography,

electron-beam lithography and X-ray lithography) to structure MOF thin films. [147-149] For instance, Lu et al. reported the top-down patterning of ZIF-8 thin films. In this example, a 200 nm ZIF-8 thin film was deposited on a silicon platform and a layer of photoresist was subsequently spin coated on the ZIF-8 thin film. Because of the excellent chemical stability of ZIF-8 in aqueous base, a dilute aqueous NaOH solution was used to develop the photoresist after exposure. The exposed areas of the ZIF-8 thin film were etched away by immersing the sample in a dilute basic solution. It is of paramount importance to highlight the necessity of considering the stability of MOF thin films in developer solutions, given the diverse stability of MOFs in solvents.

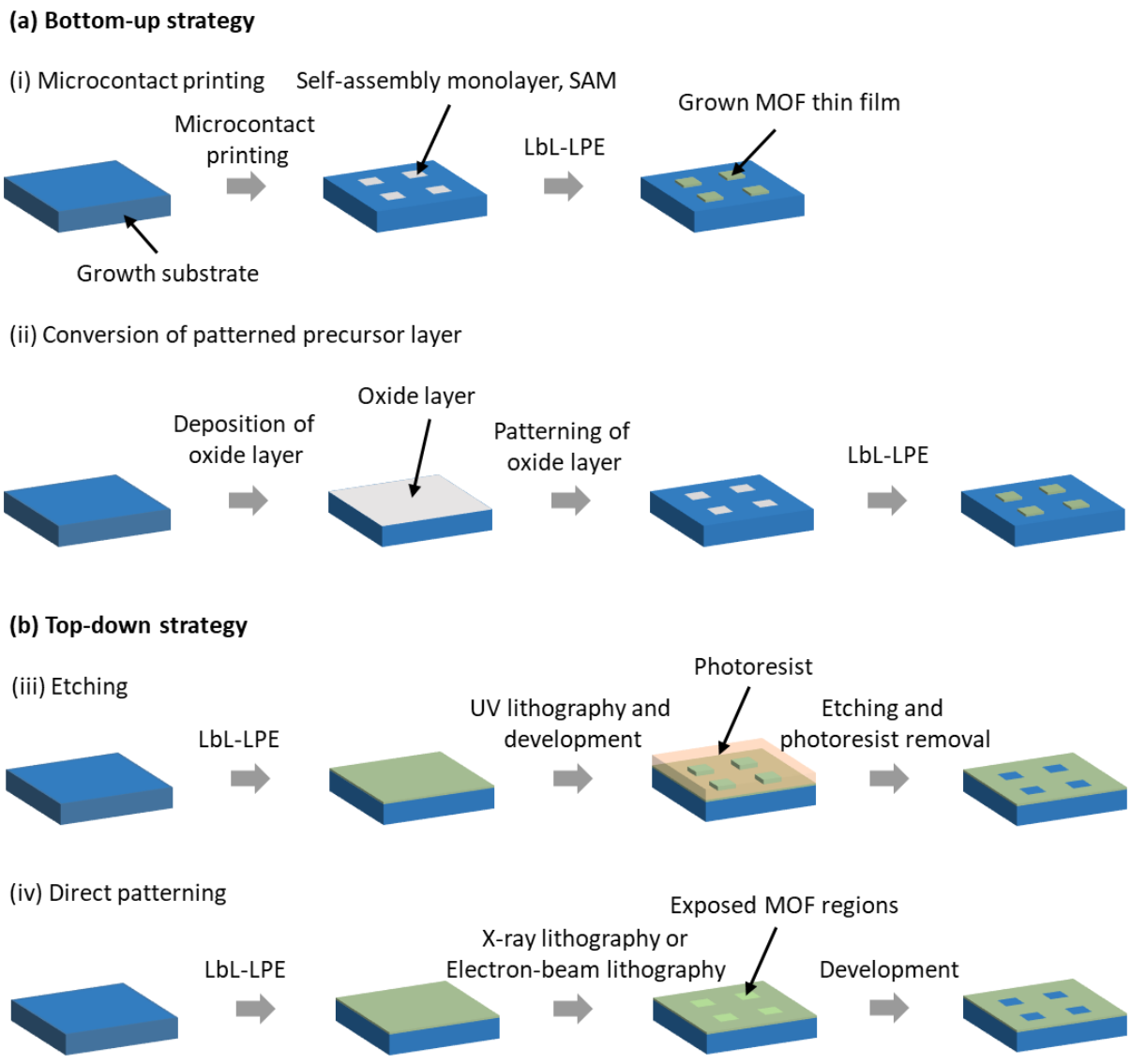

Figure 1.9: Schematic illustration of patterning techniques for MOF thin films. (a) Bottom-up strategy includes (i) micro-contact printing and (ii) conversion of precursor layer. (b) Top-down strategy includes (iii) UV lithography followed by etching process and (iv) direct patterning using X-ray lithography and electron-beam lithography followed by development.

To address this issue, Tu et al. proposed a solution involving resist-free, direct X-ray and electron-beam lithography, which circumvents the use of photoresists and developers. [147] Besides, this process avoids etching damage and contamination and preserves the porosity and crystallinity of the patterned MOFs. In X-ray lithography, a mask is employed to pattern an X-ray-sensitive layer with a resolution of 100 nm or less. In contrast, electron-beam lithography is a maskless technique based on direct writing in an electron-beam-sensitive material, with a resolution extending below 10 nm. In this study, they screened the X-ray or electron-beam sensitivity of a variety of ZIFs (e.g., ZIF-71, ZIF-71-Co, ZIF-72 and ZIF-8). For instance, pristine halogenated ZIFs are entirely insoluble in dimethylsulfoxide (DMSO), they readily dissolve in this solvent after X-ray irradiation. Thus, the direct patterning is achieved. Nevertheless, to date only patterning of ZIF thin films have been studied using X-ray lithography or electron-beam lithography, which is probably due to (a) less accessibility to these techniques and (b) less sensitivity of MOFs to X-ray or electron beam.

As discussed above, these top-down patterning approaches are only applicable in specific cases. While the application of conversing precursor layers to MOF thin films and microcontact printing are also limited. Therefore, it is of great importance to develop a generic method that can be applied to most MOFs.

2 Liquid-phase epitaxial growth of MOF thin films

This chapter outlines two automated configurations for the production of MOF thin films through LbL-LPE. The fabrication of MOF thin films can be achieved using two automated setups: a microfluidics platform and a dip coater. These setups are capable of producing MOF thin films at different scales, including localized deposition (microfluidics-assisted LbL-LPE) and large-scale integration (LbL-LPE coupled with dip coating). With regard to the microfluidics platform, an automated configuration that integrates microfluidics with the LbL epitaxial growth strategy enables the deposition of miniaturized MOF thin films in a confined space with minimal chemical and solvent consumption. The use of programmable syringes and valves allows for the variation of parameters, thereby enabling the investigation of the impact of initial conditions on the growth of MOF thin films. These conditions include, but are not limited to, concentration, solvent, flow rate, and temperature. A database is ultimately established by linking the initial parameters with the properties of the resulting MOF thin films (e.g., thickness, roughness, morphology, and crystallinity). This database will be utilized for the discovery of new materials or novel properties through materials informatics. However, its scope is constrained by the dimensions of the microfluidic channel, which are in the micrometer range. To fabricate MOF thin films on a large scale and integrate them onto chips, an automated dip coater has been constructed to perform LbL-LPE. This apparatus is capable of growing MOF thin films on different scales, from chips to wafers. It should be noted that the current setup is only operational at room temperature, with the limitation of opening containers. Finally, the correlation between microfluidic deposition and dip coating for the fabrication of MOF thin films is discussed. To some extent, localized microfluidic deposition can direct the large-scale dip coating.

2.1 Preparation of precursor solutions

2.1.1 EtOH as solvent

1 mM $NiCl_2 \cdot 6H_2O$ and 1 mM BDC-NH_2 solutions are prepared by dissolving corresponding amount of chemical in EtOH. Prior to performing the growth of MOF thin films, a certain

amount of triethylamine (TEA) is added to deprotonate ligand molecules. Both precursor solutions are stored in fridge for future use.

1 mM $Cu(OAc)_2 \cdot H_2O$ and 0.1 mM HHTP solutions are prepared by dissolving corresponding amount of chemical in EtOH. Both precursor solutions are stored in fridge for future use.

2.1.2 DMF mixture as solvent

1 mM $NiCl_2 \cdot 6H_2O$ and 1 mM BDC-NH_2 solutions are prepared by dissolving corresponding amount of chemical in DMF mixture (DMF:EtOH:H_2O = 16:1:1). Prior to performing the growth of MOF thin films, a certain amount of TEA is added to deprotonate ligand molecules. Both precursor solutions are stored in fridge for future use.

2.1.3 H_2O as solvent

1 mM $NiCl_2 \cdot 6H_2O$ and 1 mM BDC-NH_2 solutions are prepared by dissolving corresponding amount of chemical in DI H_2O. To assure the proper dissolution of BDC-NH_2 in DI H_2O, a certain amount of TEA is added to deprotonate ligand molecules. Both precursor solutions are stored in fridge for future use.

2.2 Pretreatment of growth substrates

2.2.1 Bare Si/SiO_2 substrates

Bare Si/SiO_2 substrates with a dimension of 1 x 1.5 cm^2 are consecutively cleaned by ultrasound in acetone and isopropanol for 10 minutes, respectively to remove photoresist and other organic contaminants. Then dried by N_2 gas. Prior to conducting the growth of MOF thin films, plasma treatment is applied to generate a hydrophilic surface (100 w, 25 sccm, 60 s).

2.2.2 Patterned Si/SiO_2 substrates

The details for the lithographic patterning of Si/SiO_2 substrates are discussed in **section 3.1**. In these cases, the patterned Si/SiO_2 substrates are only treated using oxygen plasma with aforementioned parameters.

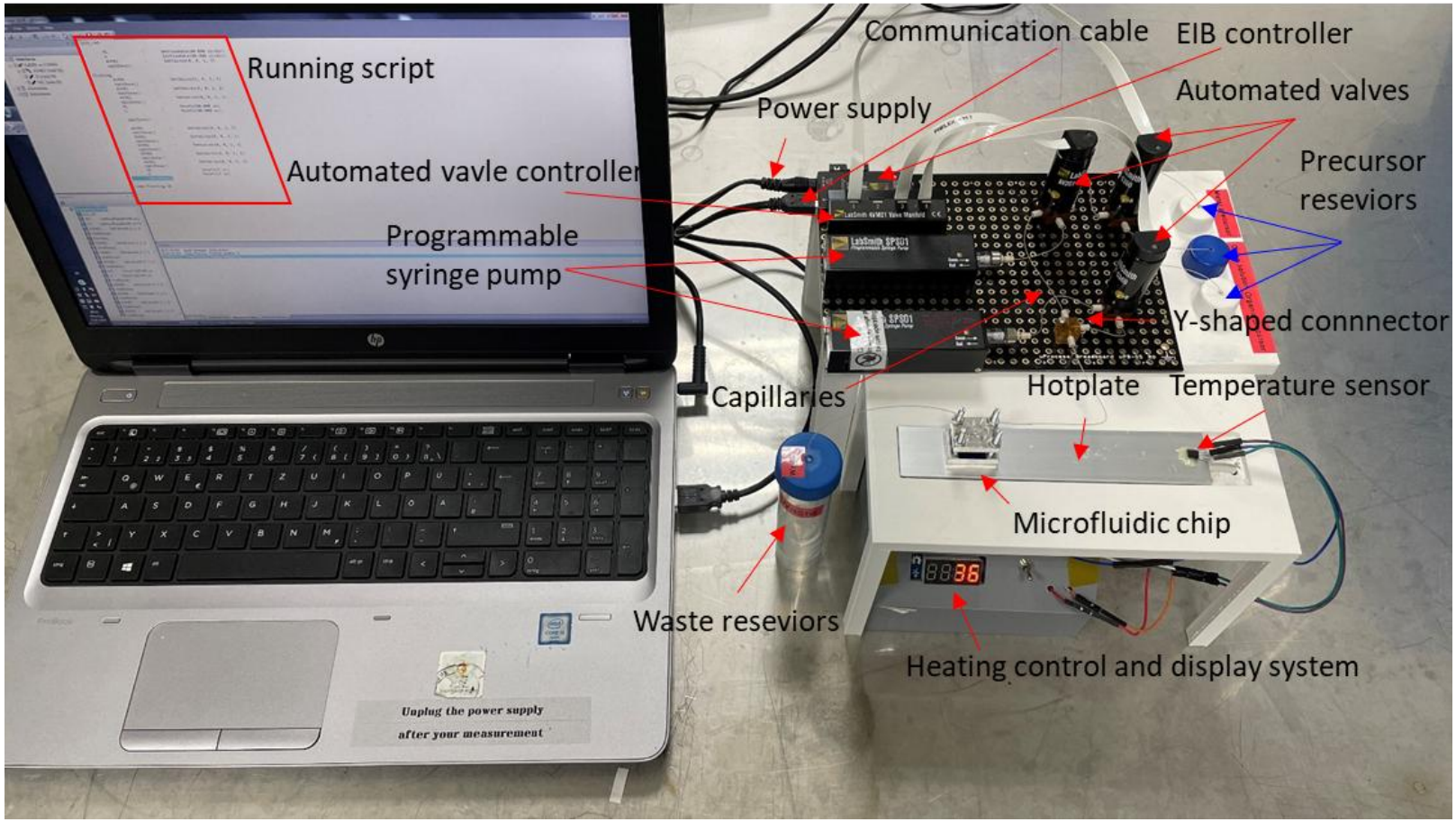

Figure 2.1: Photograph of microfluidics system for the growth of MOF thin films through LbL-LPE, including control system, microfluidic circuit and heating system.

2.3 Automated microfluidic deposition

The term "microfluidics" is used to describe a system that manipulates a relatively small quantity of fluids, typically in the range of 10^{-9} to 10^{-18} liters, through the use of narrow channels with dimensions ranging from ten to hundreds of micrometers. [150] It is a multidisciplinary field that encompasses molecular analysis, molecular biology, and microelectronics. Since 2012, microfluidics technology has been employed for MOF synthesis, primarily for the production of crystals, which can facilitate high-throughput synthesis and produce monodisperse crystals. [151, 152] Moreover, it has been successfully employed for the growth of MOF membranes on the interfaces of polymeric fibers or MOF thin films onto reactive substrates (e.g., $Cu(OH)_2$). [153] Nevertheless, the combination of microfluidics technology and the LbL-LPE strategy has yet to be widely documented. The use of microfluidics for MOF thin film growth on planar substrates offers numerous advantages, including ease of automation and reduced chemical and solvent consumption. This microfluidics-assisted LbL epitaxial growth approach is a promising platform for MOF thin film synthesis, particularly for parameter optimization, including precursor concentrations, solvents, and temperatures. Additionally, it can serve as a prototyping platform for the large-scale synthesis of MOF thin films. The microfluidic system is comprised of three principal components: (i) the hardware, which includes the microfluidic circuitry; (ii) the microfluidic chip; and (iii) the software, which is responsible for issuing commands to the microfluidic circuit.

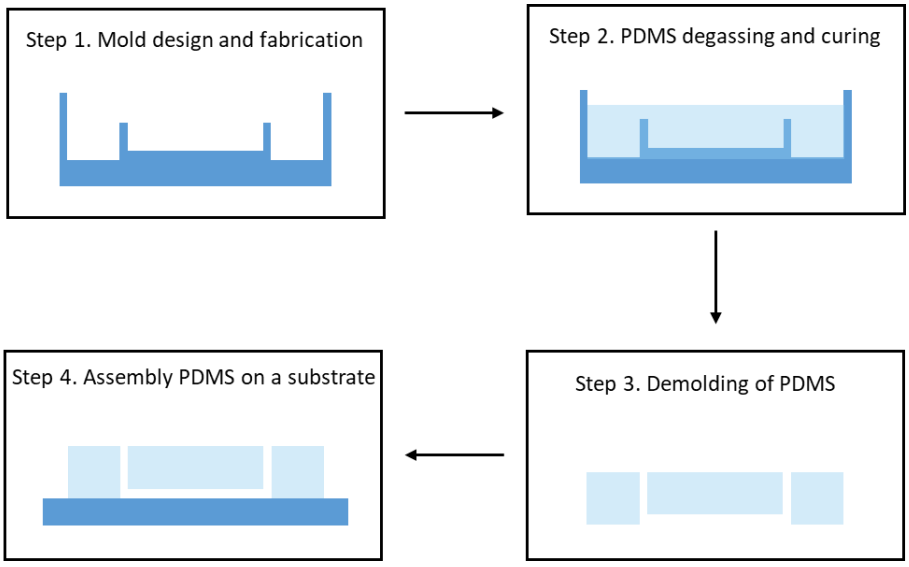

Figure 2.2: Fabrication of PDMS-based microfluidic channels.

2.3.1 Microfluidic circuit

In order to facilitate the growth of MOF thin films using LbL-LPE on a microfluidic platform, three reservoirs are prepared for two precursor solutions and one cleaning solvent. To regulate the liquid flow, two programmable syringe pumps and three automated valves are mounted on a breadboard, as illustrated in **Figure 2.1**. Moreover, a valve controller is employed to regulate the valves, and an EIB controller is mounted to facilitate communication with uProcess software. In addition to the microfluidic circuit, a heating control unit was constructed for the growth of MOF thin films at elevated temperatures.

2.3.2 Microfluidic chips

Polydimethylsiloxane (PDMS) is a polymeric material that is used to create microfluidic channels. [154] These channels are prepared by demolding from 3-D printed molds. The fabrication procedure of PDMS microfluidic channels is illustrated in **Figure 2.2**. Master molds are typically designed using 3-D modeling software (Fusion 360, Autodesk) and 3-D printed using a resin printer. Subsequently, the surfaces of the master mold are passivated through the deposition of a layer of Parylene C (PaC) at room temperature via chemical vapor deposition. A solution of silicone elastomer and curing agent in a 10:1 ratio is prepared by mixing the two components together and degassing the solution using a vacuum desiccator. The transparent mixture is then poured into the master mold and cured at 80°C for a period of two hours. Subsequently, the PDMS blocks with microfluidic channels are removed from the mold, cleaned in isopropanol, and dried with N_2 gas in preparation for future use. To construct the microfluidic apparatus for MOF thin-film growth, the PDMS microfluidic channel is positioned on the Si/SiO_2 substrate (1 x 1.5 cm^2) following oxygen plasma treatment (100 W, 25 sccm, 60 s) and secured between two 3-D-printed clamps fastened by screws, as illustrated in **Figure 2.3**. The weak mechanical bonding of PDMS on the Si/SiO_2 substrate ensures the ease of removal of the PDMS after the growth of MOF thin films.

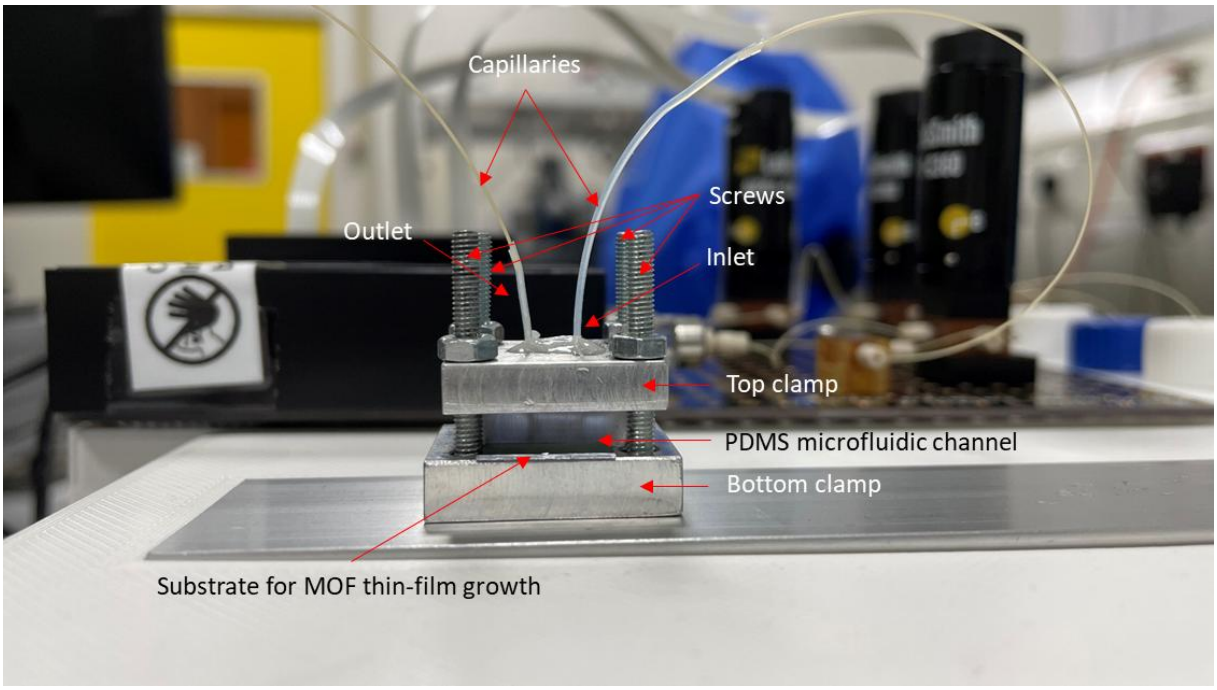

Figure 2.3: Photograph of microfluidic chip, including clamps, PDMS microfluidic channel, and MOF thin-film growth substrate

2.3.3 Software

The scripts are coded using the embedded language of uProcess software (LabSmith) to control liquid flows, including flow rates and flow sequences. The diagram of the automated microfluidic system is shown in **Figure 2.4**. The following code represents the typical sequence for a single LbL cycle.

1. Injection of metal precursor solution:

    a) Turning Val_MC & Val_S to connect SP_MC to the metal reservoir

    b) Loading the metal precursor solution into SP_MC

    c) Turning Val_MC to connect SP_MC to the PDMS fluidic

    d) Injecting the metal precursor into the PDMS fluidic, waiting for 10 minutes

2. Injection of cleaning solutions:

    a) Turning Val_MC & Val_S to connect SP_MC to the cleaning reservoir

    b) Loading the cleaning solution into SP_MC

    c) Turning Val_MC to connect SP_MC to the PDMS fluidic

    d) Injecting the cleaning solution into the PDMS fluidic, waiting for 2 minutes

    e) The above steps are repeated three times

3. Injection of organic precursor solution:

    a) Turning Val_O to connect SP_O to the organic reservoir

    b) Loading the organic precursor solution into SP_O

    c) Turning Val_O to connect SP_O to the PDMS fluidic

    d) Injecting the organic precursor into the PDMS fluidic, waiting for 10 minutes

4. Injection of cleaning solutions:

    a) Turning Val_MC & Val_S to connect SP_MC to the cleaning reservoir

    b) Loading the cleaning solution into SP_MC

    c) Turning Val_MC to connect SP_MC to the PDMS fluidic

    d) Injecting the cleaning solution into the PDMS fluidic, waiting for 2 minutes

    e) The above steps are repeated 3 times

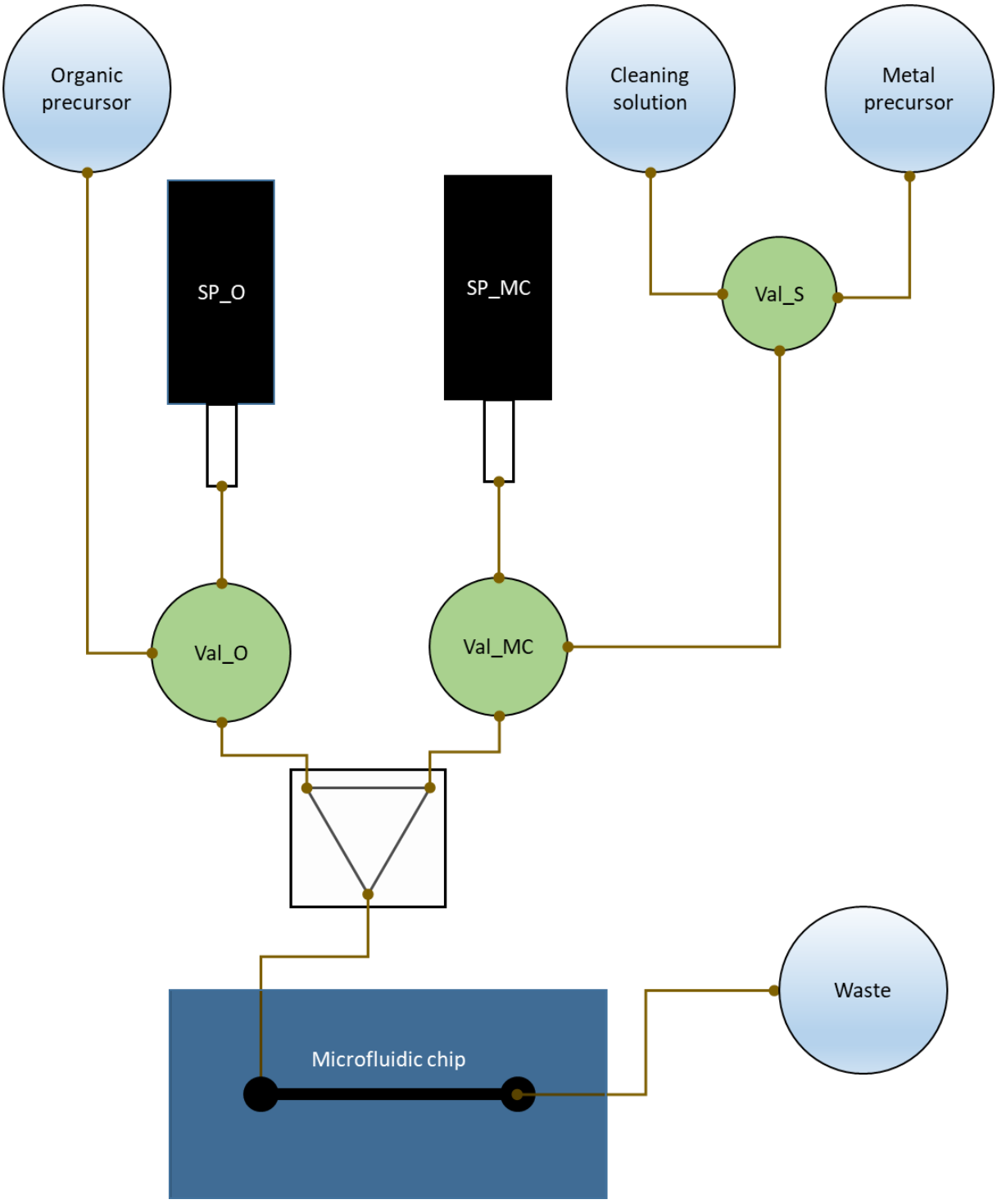

Figure 2.4: Diagram of the automated microfluidic system.

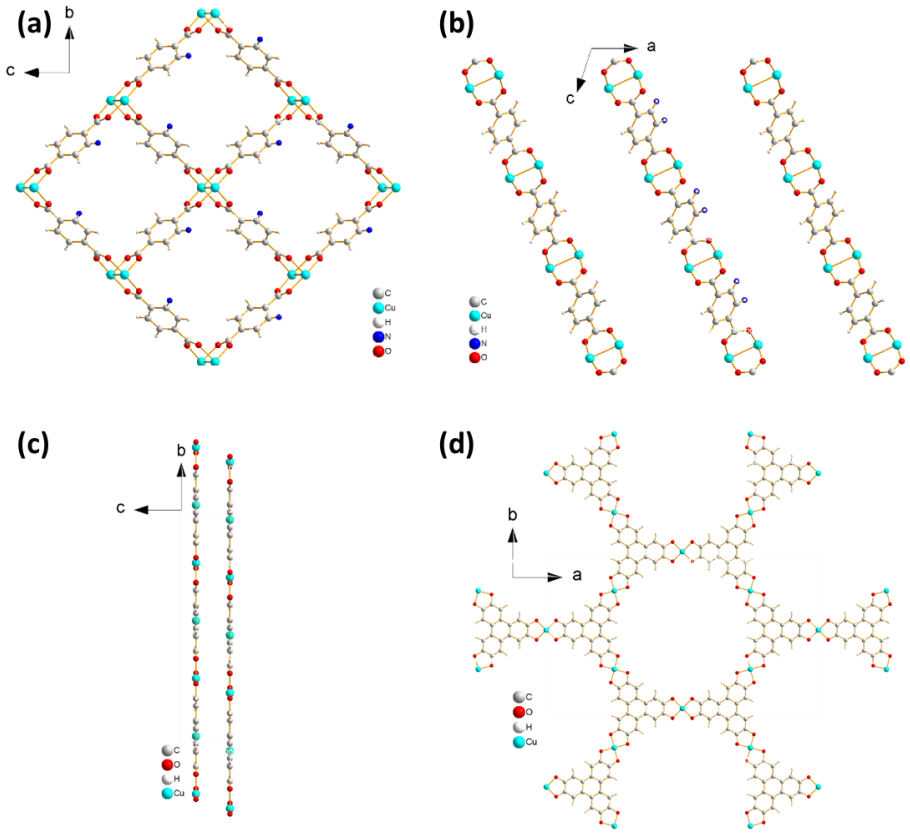

Figure 2.5: Crystallographic structures of Cu-(BDC-NH_2) and $Cu_3(HHTP)_2$. (a, b) Crystallographic structures of Cu-(BDC-NH_2) viewed along a and b axes, respectively. (c, d) Crystallographic structures of $Cu_3(HHTP)_2$ viewed along a and c axes, respectively.

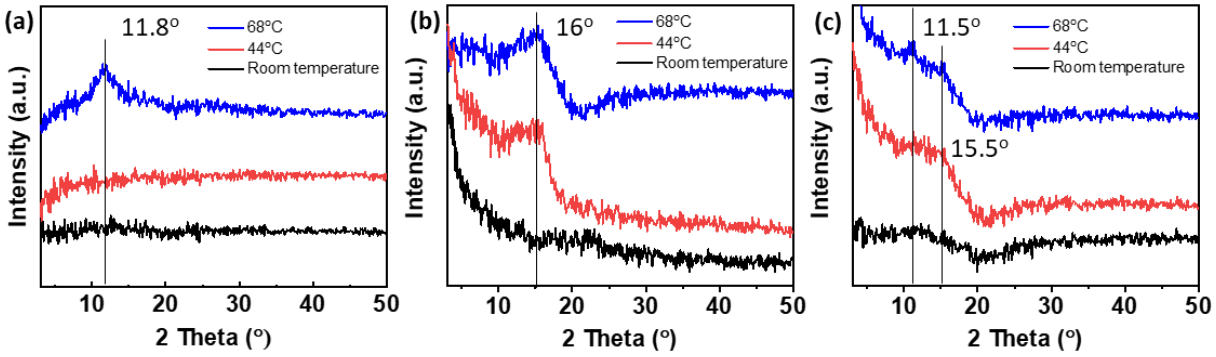

Figure 2.6: GIXRD of Ni-(BDC-NH_2) thin films prepared under different conditions. (a) Ethanol as solvent at room temperature, 44°C and 68°C. (b) DMF mixture (DMF:H_2O:EtOH = 16:1:1) as solvent at room temperature, 44°C and 68°C. (c) DI H_2O as solvent at room temperature, 44°C and 68°C.

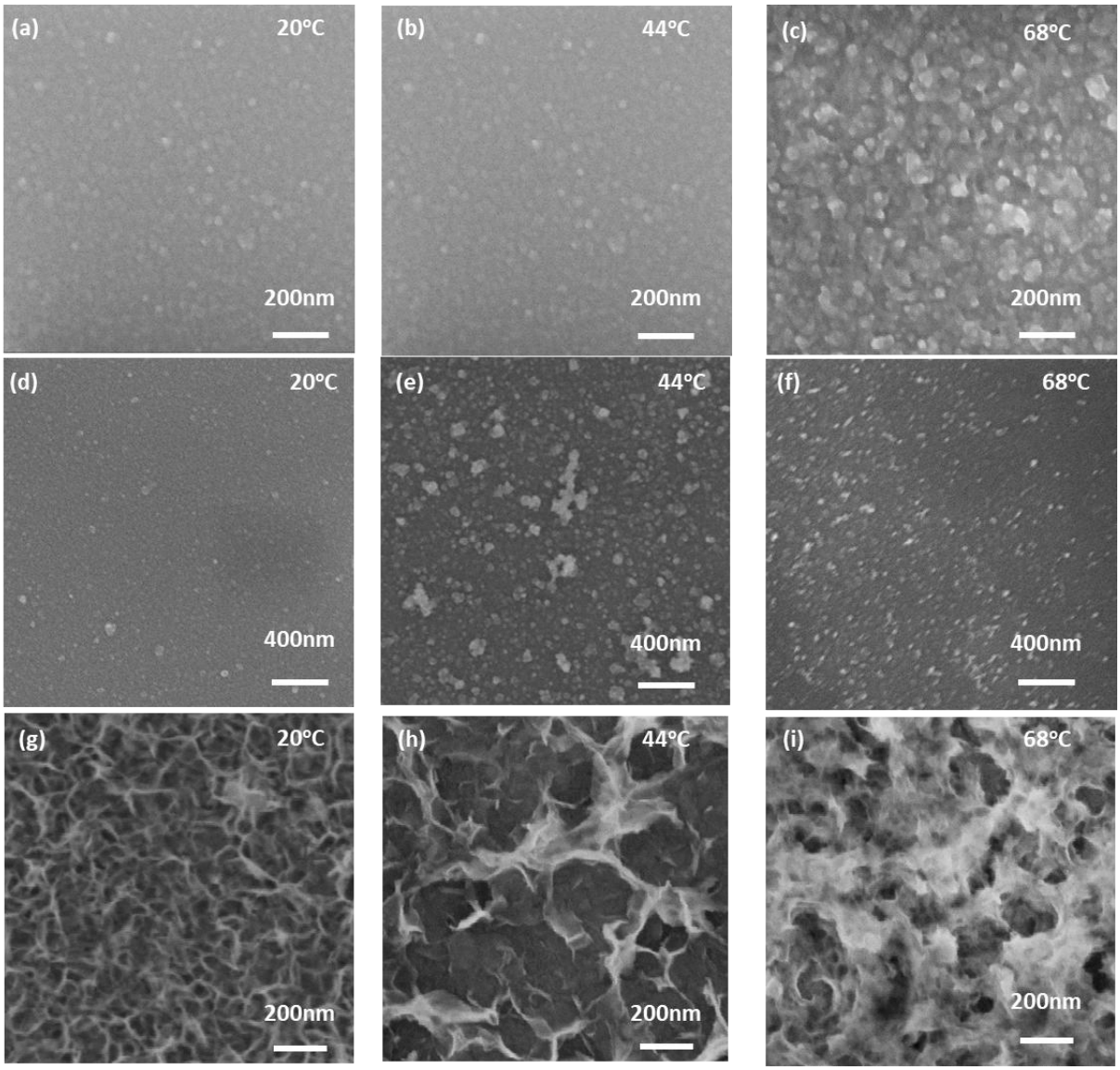

Figure 2.7: High-resolution SEM images of Ni-(BDC-NH_2)-20c thin films prepared under different conditions. (a) Ethanol as solvent at room temperature, 44°C and 68°C. (b) DMF mixture (DMF:H_2O:EtOH = 16:1:1) as solvent at room temperature, 44°C and 68°C. (c) DI H_2O as solvent at room temperature, 44°C and 68°C.

2.3.4 Results

This study demonstrates the application of microfluidics-assisted LbL-LPE for the growth of MOF thin films. Two MOF candidates were investigated: (i) Ni-(BDC-NH_2) and (ii) $Cu_3(HHTP)_2$. **Figure 2.5** illustrates the crystallographic structures of Cu-(BDC-NH_2) and $Cu_3(HHTP)_2$. It is postulated that Ni-(BDC-NH_2) will exhibit a similar structure to that of Cu-(BDC-NH_2), given the analogous coordination geometry of Cu^{2+} and Ni^{2+} ions. [155] In this case, Ni-(BDC-NH_2) exhibits insulating electrical properties, whereas $Cu_3(HHTP)_2$ displays semi-conducting characteristics. [156] This section is dedicated to the study of Ni-(BDC-NH_2). The discussion of $Cu_3(HHTP)_2$ will be presented in the subsequent discussion section. A systematic investigation was conducted on the synthetic parameters, including temperature, precursor ratio,

flow rate, and deposition cycles. The findings are presented in **Table 2-1**. To evaluate the samples, the surface roughness and thickness of the obtained MOF thin films were characterized by atomic force microscopy (AFM). The crystallinity of the samples was determined by conducting grazing-incidence X-ray diffraction (GIXRD) characterization. In all deposition experiments, an intermittent flow method was employed, whereby solutions were introduced into the microfluidic channel at a specific flow rate and retained within the channel. Subsequently, the aforementioned solutions are flushed out with the same flow rate. The rationale behind the use of an intermittent flow is to emulate the process of dip coating, which occurs in a stationary environment. In regard to Ni-(BDC-NH_2), the initial objective was to ascertain the optimal temperature for crystallization by investigating the effects of varying synthetic temperatures (20°C, 44°C, and 68°C). In this study, the concentration ratio was set at 1:1 (1 mM for both precursors), and the flow rate was maintained at 80 μL·min^{-1} for 20 LbL cycles. As illustrated in **Figure 2.6a**, the GIXRD results demonstrate that the synthesized Ni-(BDC-NH_2) thin film exhibits enhanced crystallinity at elevated temperatures. This is corroborated by the augmented grain sizes, as evidenced by high-resolution (SEM), depicted in **Figure 2.7a-c**. Furthermore, the thickness of the synthesized Ni-(BDC-NH_2) thin film increases at elevated temperatures, as illustrated in **Figure 2.8a**. **Figure 2.8d** demonstrates that the fabricated Ni-(BDC-NH_2) thin film at high temperature exhibits minimal surface roughness, indicating that 68°C is the optimal temperature for investigating the other parameters. Consequently, all subsequent experiments were conducted at 68°C with 20 LbL cycles. As shown in **Table 2-1** and **Figure 2.9a**, the precursor ratio or concentration exerts a significant influence on the resultant products. At a lower ratio (C_M:C_O = 1:2, C_M = 0.5 mM), the resulting Ni-(BDC-NH_2) thin film is thinner with a relatively lower surface roughness (R_a = 2.3 nm). Upon reducing the concentration of the organic precursor solution to 2:1 (C_O = 0.5 mM), the thickness of the Ni-(BDC-NH_2) thin film remains unaltered. However, a slight change in surface roughness is observed, shown in **Figure 2.9d**. From these results, it can be concluded that the seeding step of metal ions on the substrate surface has a predominant influence on the overall growth process. [157] In this instance, the ratio of the precursor is maintained at 1:1. Similarly, the introduction of precursor solutions at varying flow rates exerts a comparable influence on the growth of the Ni-(BDC-NH_2) thin film, as observed with varying precursor ratios, shown in **Figure 2.9b** and **Figure 2.9e**. The seeding step is also slower at a lower flow rate, due to the reduced efficiency of mass transport at lower flow rates. However, when the flow rate exceeds 80 μL·min^{-1}, its influence is negligible. Accordingly, the flow rate of 80 μL·min^{-1} was determined to be the optimal value. With all opti-

mized parameters, depositions were carried out on multiple occasions, with the number of cycles varying from 5 to 10, 20, and 40. As illustrated in **Figure 2.9c** and **Figure 2.9f**, the thicknesses of Ni-(BDC-NH_2) thin films demonstrate a linear correlation with deposition cycles, exhibiting a growth rate of approximately 2.6 nm per cycle.

Furthermore, two additional solvent systems were investigated for the growth of Ni-(BDC-NH_2) thin films. The DMF mixture (DMF:DI H_2O:EtOH = 16:1:1) employed for the bulk synthesis of Ni-(BDC-NH_2) was examined at varying temperatures. The remaining parameters were maintained at their optimal values. **Figure 2.6b** illustrates the GIXRD patterns of Ni-(BDC-NH_2) thin films synthesized in a DMF mixture. At 44°C and 68°C, a distinctive peak is evident at approximately 16°. As illustrated in **Figure 2.7d-f**, the SEM images reveal no discernible alteration in the surface morphology of the Ni-(BDC-NH_2) thin films grown in ethanol when compared to those grown in DMF. As illustrated in **Figure 2.8b** and **Figure 2.8e**, the thickness and surface roughness of the Ni-(BDC-NH_2) thin films grown in the DMF mixture at relatively low temperatures exhibit minimal variation, whereas those of the Ni-(BDC-NH_2) thin films synthesized at elevated temperatures demonstrate a significant increase, from ~25 nm to > 200 nm for thickness and from ~3 nm to >25 nm for surface roughness. This suggests a markedly higher reaction rate. In order to comply with the requisite environmental standards, the use of DI H_2O as a synthetic solvent is always a favorable option. Moreover, photoresist can be employed as a passivation and sacrificial layer to structure MOF thin films while the growth is conducted in an aqueous system. **Figure 2.6c** illustrates the GIXRD patterns of Ni-(BDC-NH_2) thin films synthesized in DI H_2O. In contrast to the aforementioned organic solvent systems, the final products synthesized using DI H_2O exhibit a markedly different morphology, as illustrated in **Figure 2.7g-i**. As evidenced by these SEM images, the formation of a nanoflake-shaped array is observed under varying temperatures, a phenomenon that differs from the synthesis of nanoparticles in ethanol or a DMF mixture. Additionally, a slight reduction in the thickness of the Ni-(BDC-NH_2) thin films was observed at elevated temperatures, as illustrated in **Figure 2.8c** and **Figure 2.8f**. It should be noted, however, that all the products exhibit considerably higher surface roughness values (R_a > 25 nm) in comparison to those synthesized under organic conditions.

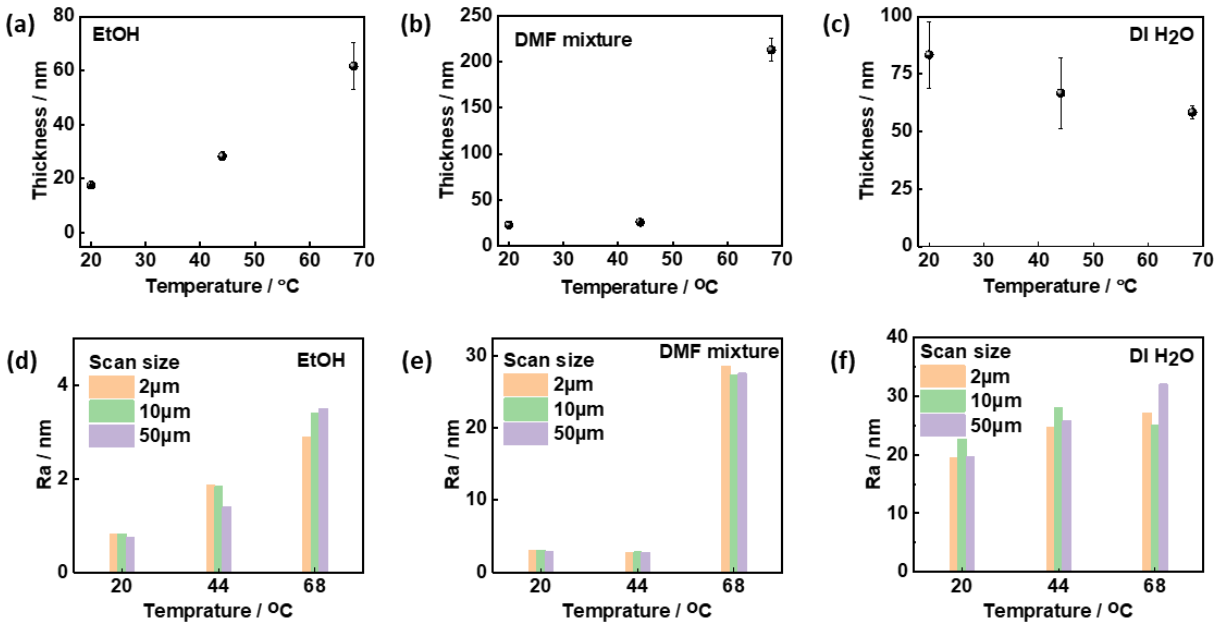

Figure 2.8: Thickness and roughness evaluation of Ni-(BDC-NH_2) thin films prepared under different conditions. (a, d) Ethanol as solvent at room temperature, 44°C and 68°C. (b, e) DMF mixture (DMF:H_2O:EtOH = 16:1:1) as solvent at room temperature, 44°C and 68°C. (c, f) DI H_2O as solvent at room temperature, 44°C and 68°C.

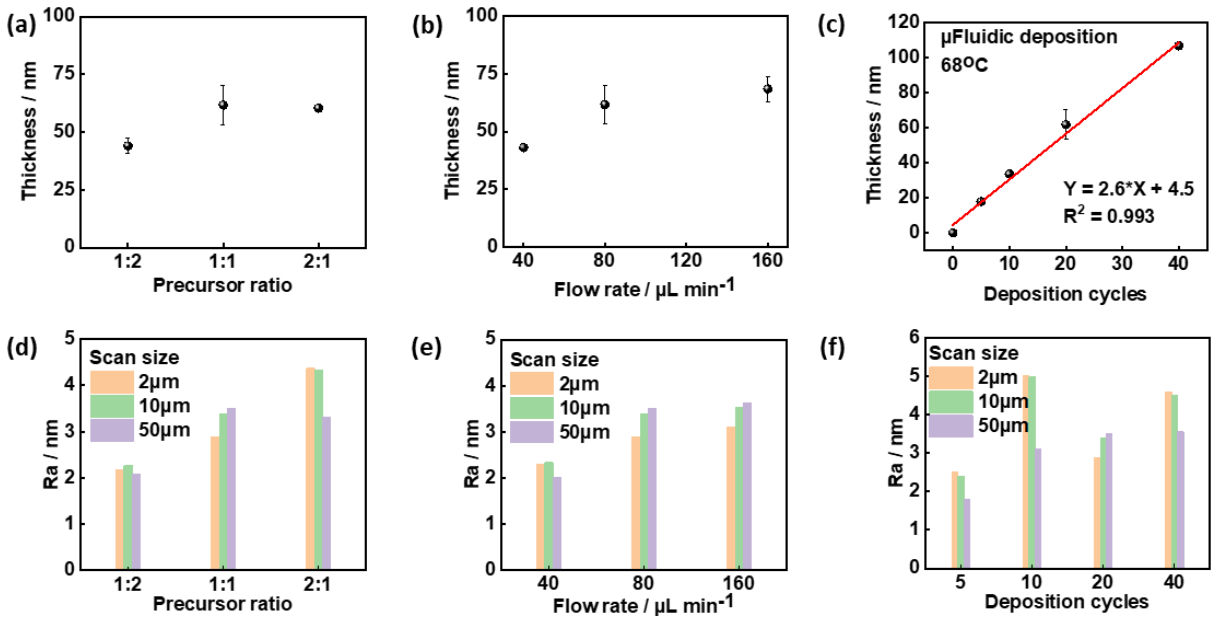

Figure 2.9: Influence of synthetic parameters on MOF thin films prepared using EtOH as solvent. (a, d) Precursor ratios. (b, d) Flow rates. (c, f) Deposition cycles.

Table 2-1: Parameters optimization for the growth of Ni-(BDC-NH_2) thin films on microfluidics platform.

Solvents	Parameters	Temperature (°C)	Precursor ratio (C_M:C_O)	Flow rate (μL·min^{-1})	Deposition cycles	Thickness (nm)	Roughness R_a (nm)	Morphology	Crystallinity
EtOH	Temperature (°C)	20	1:1	80	20	17.7±0.2	0.8	Nanoparticles	x
		44				28.2±1.5	1.8		x
		68				61.7±8.5	3.4		∨
	Precursor ratio (C_M:C_O)	68	1:2	80	20	44±3.5	2.3	Nanoparticles	-
			1:1			61.7±8.5	3.4		
			2:1			60.3±1.5	4.3		
	Flow rate (μL·min^{-1})	68	1:1	40	20	43±1.7	2.3	Nanoparticles	-
				80		61.7±8.5	3.4		
				160		68.5±5.4	3.5		
	Deposition cycles	68	1:1	80	5	17.8±0.3	2.4	Nanoparticles	-
					10	33.5±2.2	5.0		
					20	61.7±8.5	3.4		
					40	106.7±1.5	4.5		
		20	1:1	80	5	4.5±0.5	1.4	Nanoparticles	-
					10	10.8±0.3	1.0		
					20	17.7±2	1.2		
					40	35.3±0.6	1.6		
DMF:H_2O:EtOH (16:1:1)	Temperature (°C)	20	1:1	80	20	22.3±2.5	3.1	Nanoparticles	x
		44				25.3±0.6	2.8		∨
		68				213.3±12.6	27.4		∨
DI H_2O		20	1:1	80	20	83.3±14.4	22.7	Nanoflakes	x
		44				66.7±15.3	25.7		∨
		68				58.3±2.9	32		∨

2.4 Automated dip coating

In comparison to microfluidics-assisted LbL-LPE for the growth of MOF thin films, a considerably larger coating area can be achieved through automated dip coating, spanning from chip size to wafer scale. It is important to note that microfluidics technology is advantageous for the optimization of MOF thin films in a targeted manner, as demonstrated in the aforementioned examples. However, the deposition of MOF thin films is observed to be relatively inhomogeneous due to the variation of the liquid flow profile and the mass transport across the microfluidic channel, as illustrated in **Figure 2.10**. While dip coating conducted in a truly stationary condition is an appropriate method for growing homogeneous MOF thin films with good reproducibility, an alternative approach is to alternatively immerse the substrates into the precursor solutions instead of introducing the fluid onto the substrate surface. All the dip coating processes are performed at room temperature due to the absence of a heating function in the current version of the dip coater.

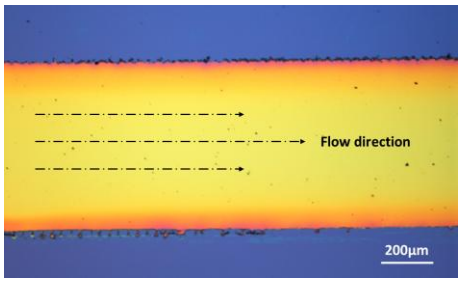

Figure 2.10: An optical image of one of the Ni-(BDC-NH_2)-40c thin films synthesized in EtOH through microfluidics-assisted LbL-LPE.

2.4.1 Automated dip coater

As illustrated in **Figure 2.11**, the dip coater, constructed from readily available materials, comprises several essential components. The motors numbered 1, 2, and 3 are responsible for the vertical and horizontal movements. The fourth component is the sample holder. Beakers 5, 6, and 7 are utilized for the storage of precursors and rinsing solvents. The default positions, 8, 9, and 10, are utilized for calibration purposes. The control unit is item 11.

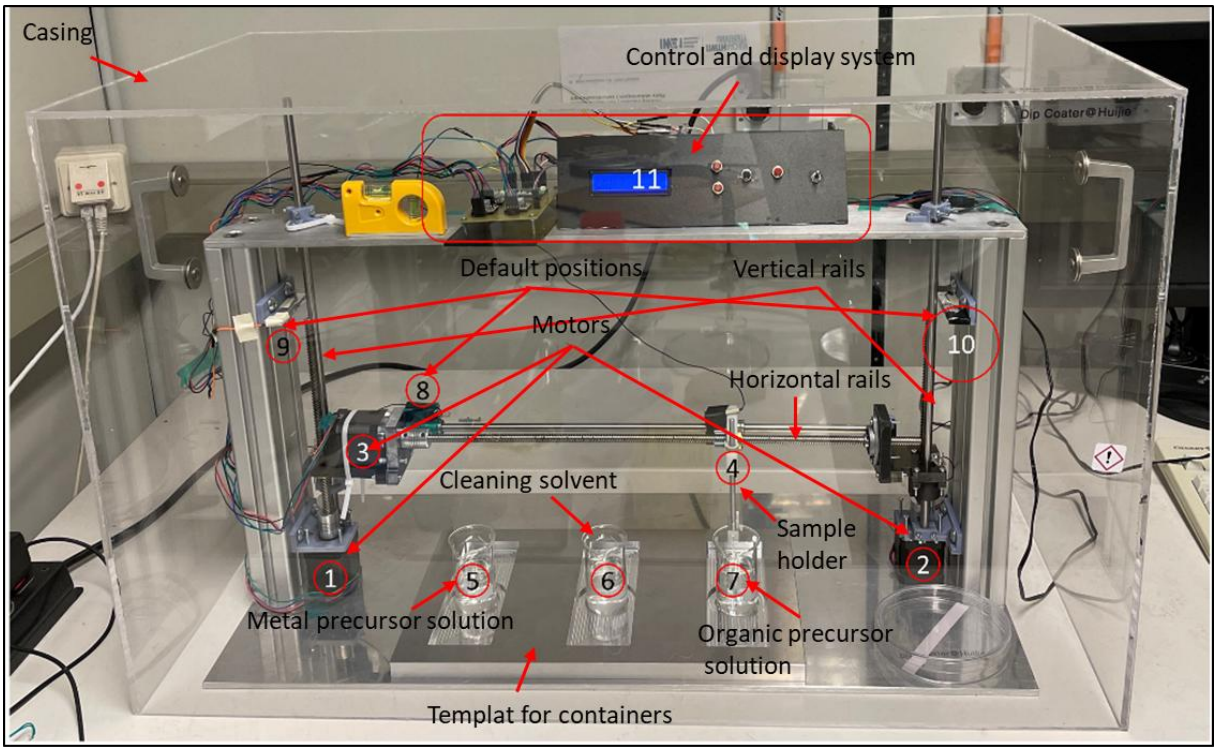

Figure 2.11: Automated dip coater for the growth of MOF thin films through LbL-LPE. [158]

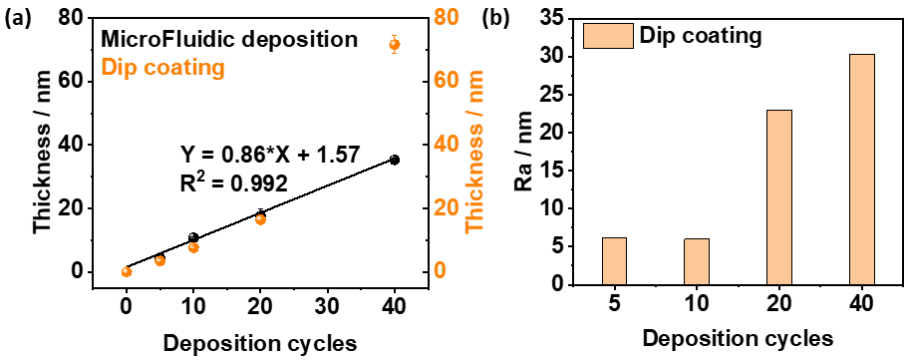

Figure 2.12:Thickness and surface roughness characterization of Ni-(BDC-NH_2) thin films with different number of deposition cycles prepared by automated dip coating in EtOH. (a) Thickness comparison of thin-film samples synthesized using microfluidic deposition and dip coating, (b) Surface roughness of thin-film samples synthesized using dip coating with varying LbL cycles.

2.4.2 Results

In order to compare the quality of Ni-(BDC-NH_2) thin films prepared through microfluidic deposition and dip coating, the same parameters were adopted, with the exception of the investigation of flow rates and temperatures, which are summarized in **Table 2-2**. Initially, the growth of Ni-(BDC-NH_2) thin films with different numbers of deposition cycles in ethanol was conducted. The linear growth of Ni-(BDC-NH_2) thin films was observed up to 20 LbL cycles, with a similar growth rate of ~0.9 nm per cycle, as illustrated in **Figure 2.12**. The surface roughness of the dip-coated samples was found to be significantly higher than that of the microfluidic

deposited samples. This is attributed to the extensive cleaning steps employed in the microfluidic deposition process. These findings illustrate the effectiveness of microfluidic deposition in producing high-quality MOF thin films. Furthermore, the influence of precursor solution concentration was investigated, yielding comparable outcomes to those observed during microfluidic deposition, shown in **Figure 2.13**. In a DMF mixture, the Ni-(BDC-NH_2) thin film obtained after 20 LbL cycles exhibited a comparable thickness but a relatively elevated surface roughness. Notably, the deposition of a Ni-(BDC-NH_2) thin film was essentially absent after 20 cycles, shown in **Figure 2.14**.

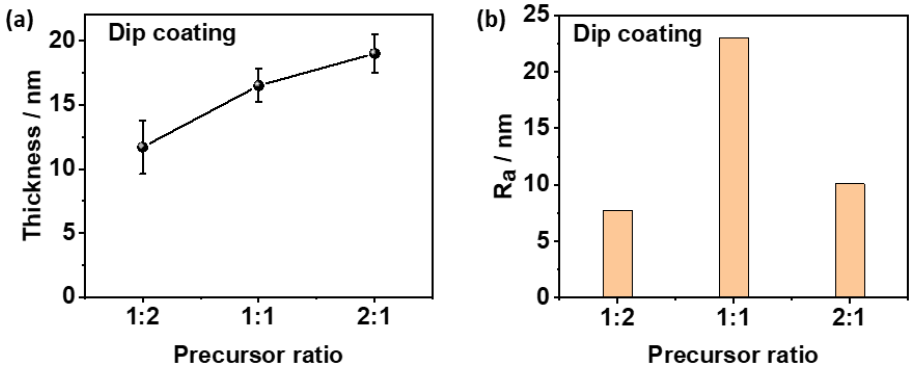

Figure 2.13: Comparison of Ni-(BDC-NH_2)-20c thin films synthesized with different precursor ratios through dip coating. (a) Thickness, and (b) surface roughness.

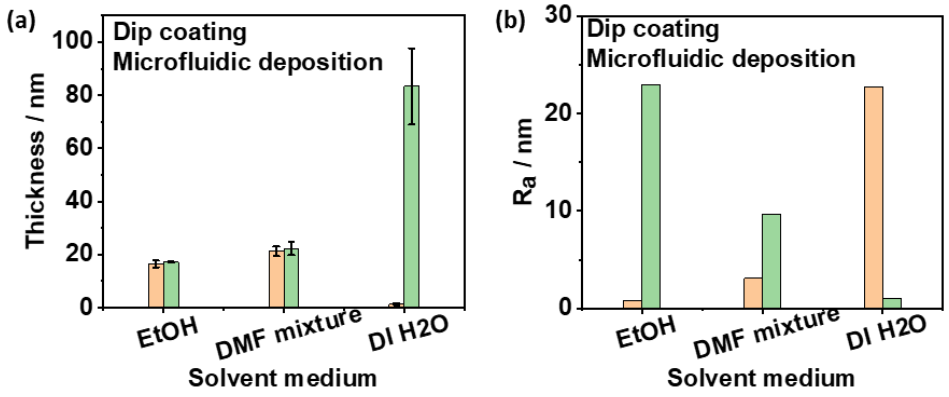

Figure 2.14: Comparison of Ni-(BDC-NH_2)-20c thin films synthesized in EtOH, DMF mixture and DI H_2O under optimal conditions through microfluidic deposition and dip coating. (a) Thickness, and (b) surface roughness.

Table 2-2: Parameters optimization for the growth of Ni-(BDC-NH_2) thin films on dip coater.

Solvents	Parameters	Temperature (°C)	Precursor ratio (C_M:C_O)	Deposition cycles	Thickness (nm)	Roughness R_a (nm)	Morphology	Crystallinity
EtOH	Precursor ratio (C_M:C_O)	20	1:2	20	11.7±2.1	7.7	Nanoparticles	-
			1:1		16.5±1.3	4.8		
			2:1		19.0±1.5	10.1		
	Deposition cycles	20	1:1	5	3.5±0.7	6.1	Nanoparticles	-
				10	7.7±0.8	6.0		
				20	16.5±1.3	4.8		
				40	38.2±5.2	6.6		
DMF:H_2O:EtOH (16:1:1)	Temperature (°C)	20	1:1	20	21.2±1.8	9.7	Nanoparticles	-
DI H_2O		20	1:1	20	1.3±0.4	1.0	-	-

2.5 Discussions

In the context of microfluidic deposition, a comprehensive investigation was conducted to ascertain the influence of five key parameters (temperature, concentration, solvent, flow rate, and deposition cycle) on the growth of Ni-(BDC-NH_2) thin films. While three of the five parameters (concentration, solvent, and deposition cycle) were studied by dip coating due to certain limitations. For example, the investigation of the flow rate in dip coating is not applicable in this case. All dip coating for the growth of Ni-(BDC-NH_2) thin films were conducted at room temperature due to the absence of a heating function. The synthesis temperature has a positive effect on the quality of Ni-(BDC-NH_2) thin films, as evidenced by GIXRD. The nucleation step is of great consequence for the subsequent growth of Ni-(BDC-NH_2) thin films, as evidenced by the studies of flow rates and precursor concentrations. The growth of Ni-(BDC-NH_2) thin films in different solvents exhibits disparate behaviors, which may be attributed to the orientation of the formed nucleation sites. Furthermore, the linear growth of Ni-(BDC-NH_2) thin films in ethanol at RT and 68°C was observed, with a growth rate of approximately 0.9 nm and 2.6 nm per cycle, respectively.

A comparable impact of the aforementioned parameters on the quality of Ni-(BDC-NH_2) thin films was also discerned in the dip coating process. The thicknesses of the Ni-(BDC-NH_2) thin films prepared by both setups are comparable, while the Ni-(BDC-NH_2) thin films prepared by dip coating exhibit significantly higher surface roughness than those prepared by microfluidic deposition. This discrepancy may be attributed to the dynamic cleaning steps incorporated during microfluidic deposition. Moreover, to ascertain the growth rate of Ni-(BDC-NH_2) thin films in ethanol at room temperature, four samples with LbL cycles of 5, 10, 20, and 40 were prepared through microfluidic deposition. A similar relationship was observed at 68°C, whereby the thickness of the Ni-(BDC-NH_2) thin films exhibited a linear correlation with the deposition cycles, with a lower growth rate of 0.9 nm per cycle. Nevertheless, the growth of Ni-(BDC-NH_2) thin films in ethanol at room temperature through dip coating only shows a linear curve until 20 LbL cycles with a similar growth rate. Therefore, the growth of MOF thin films in microscale on microfluidic platforms may provide insights for large-scale device integration on dip coating platforms.

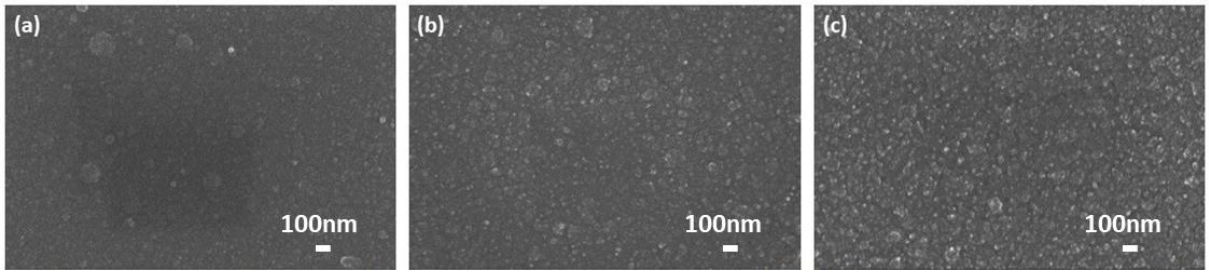

Figure 2.15: Microfluidic deposition of $Cu_3(HHTP)_2$-10c in EtOH at (a) RT, (b) 50°C and (c) 80°C.

Apart from the growth of Ni-(BDC-NH_2) thin films using both microfluidic deposition and dip coating, both systems are also employed for the growth of $Cu_3(HHTP)_2$ thin films.

In this case, using microfluidic deposition we studied the influence of solvents and temperatures on the morphology of $Cu_3(HHTP)_2$ thin films. Initially, the growth of $Cu_3(HHTP)_2$ thin films was conducted in pure ethanol at 20, 50 and 80°C, using 1 mM $Cu(OAc)_2$ and 0.1 mM HHTP as precursor solutions. From high-resolution SEM images shown in **Figure 2.15**, $Cu_3(HHTP)_2$ thin films with smooth surfaces are observed. Besides, the sizes of the crystallites are getting larger at elevated temperatures, which may result in better crystallinity. Solvents also play a significant role while growing MOFs. Gu et al. reported that the orientation of $Cu_3(HHTP)_2$ thin films can be regulated by using water as solvent instead of pure ethanol. Therefore, the influence of water content in ethanol on the growth of $Cu_3(HHTP)_2$ thin films was consequently investigated with 50% (1:1), 80% (4:1) and 90% (9:1) volumetric ratios at 80°C. As observed from high-resolution SEM images, $Cu_3(HHTP)_2$ thin films grown with a 1:1 ratio of DI H_2O to EtOH, show the same morphology as those synthesized in pure ethanol. While in the $Cu_3(HHTP)_2$ thin films grown with a 4:1 ration of DI H_2O to EtOH, the coexistence of nano-particles and nanoflakes were observed, which seems like a transition state from nanoparticles to nanoflakes. With the further increase of water content in ethanol to 90% (v:v), nanoparticles are absent in the final $Cu_3(HHTP)_2$ thin films while with pure nanoflakes. From the cross-section SEM images, the grown $Cu_3(HHTP)_2$ thin films under different conditions have a thickness of approximately 150 nm.

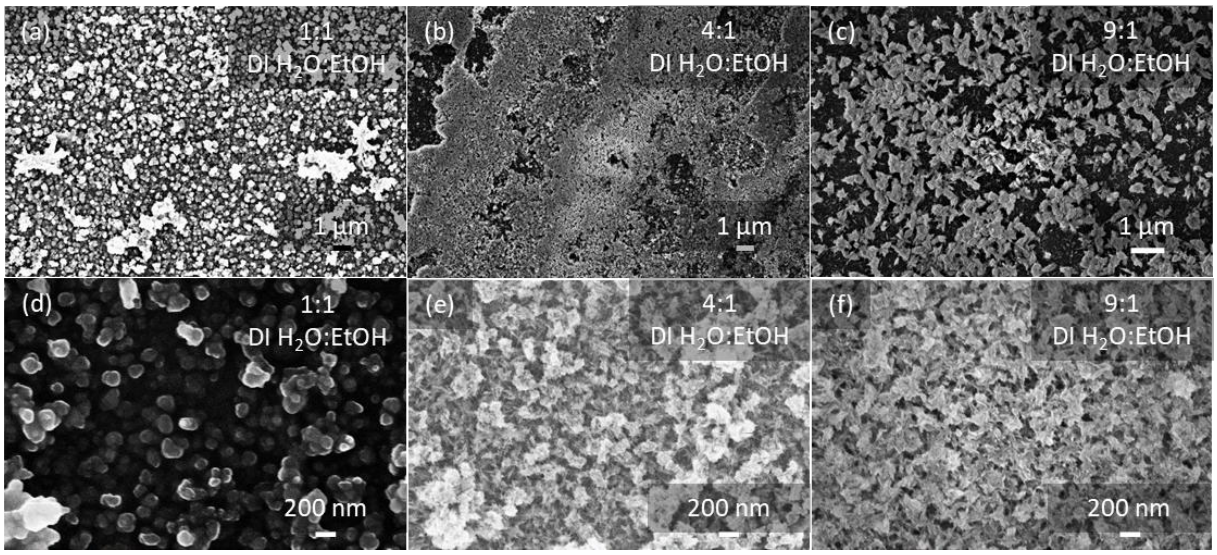

Figure 2.16: High-resolution SEM images of $Cu_3(HHTP)_2$-10c thin films fabricated through microfluidic deposition at 80°C in mixed solvent solution of DI H_2O and EtOH (a and c) 1:1, (b and e) 4:1, and (c and f) 9:1.

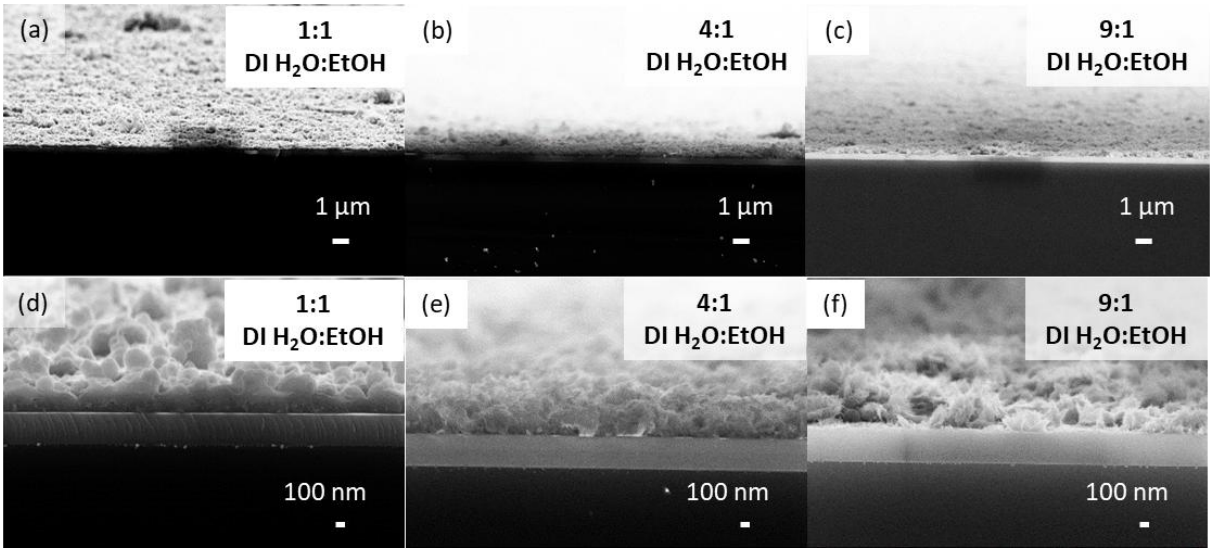

Figure 2.17: Cross-section high-resolution SEM images of $Cu_3(HHTP)_2$-10c thin films fabricated through microfluidic deposition at 80°C in mixed solvent solution of DI H_2O and EtOH (a and c) 1:1, (b and e) 4:1, and (c and f) 9:1.

In terms of the growth of $Cu_3(HHTP)_2$ thin films by dip coating, we only studied the growth rate in pure ethanol at room temperature using 1 mM $Cu(OAc)_2$ and 0.1 mM HHTP as precursor solutions. Therefore, $Cu_3(HHTP)_2$ thin films were prepared by conducting different LbL cycles, 5c, 10c, 15c and 20c. Optical images are shown in **Figure 3.18**. Corresponding SEM images are shown in **Figure 3.19**. These $Cu_3(HHTP)_2$ thin films are very smooth and uniform. In addition, we could see the very clean edges and increased optical contrast with more LbL cycles. Both lithographic patterning of MOF thin films and optical contrast will be discussed with more

details in the following chapter. The thicknesses were measured using AFM and plotted in **Figure 3.20.** There, a linear growth of $Cu_3(HHTP)_2$ thin films was observed with a growth rate of approximately 10 nm per LbL cycle.

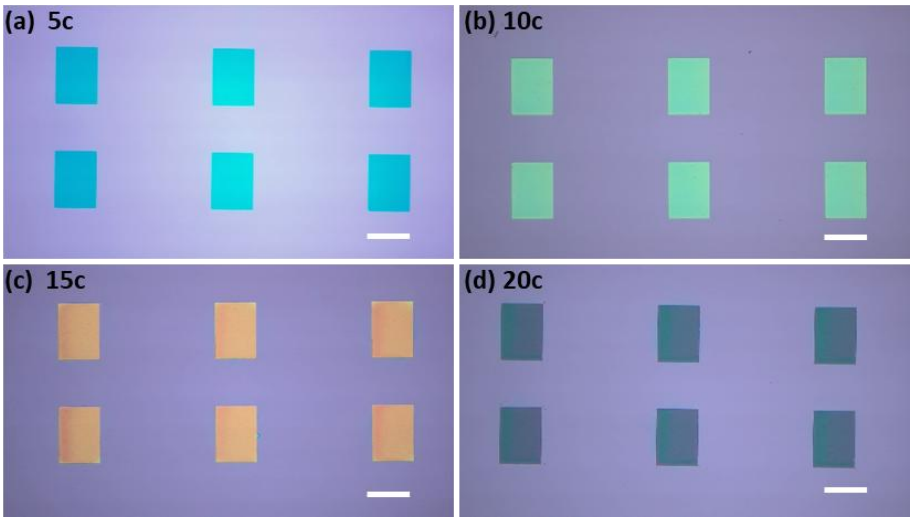

Figure 2.18: Optical images of $Cu_3(HHTP)_2$ thin films captured on a reflected light microscope with white light source. These samples were prepared through dip coating at room temperature with different LbL cycles, 5c, 10c, 15c and 20c. Scale bar: 200 µm.

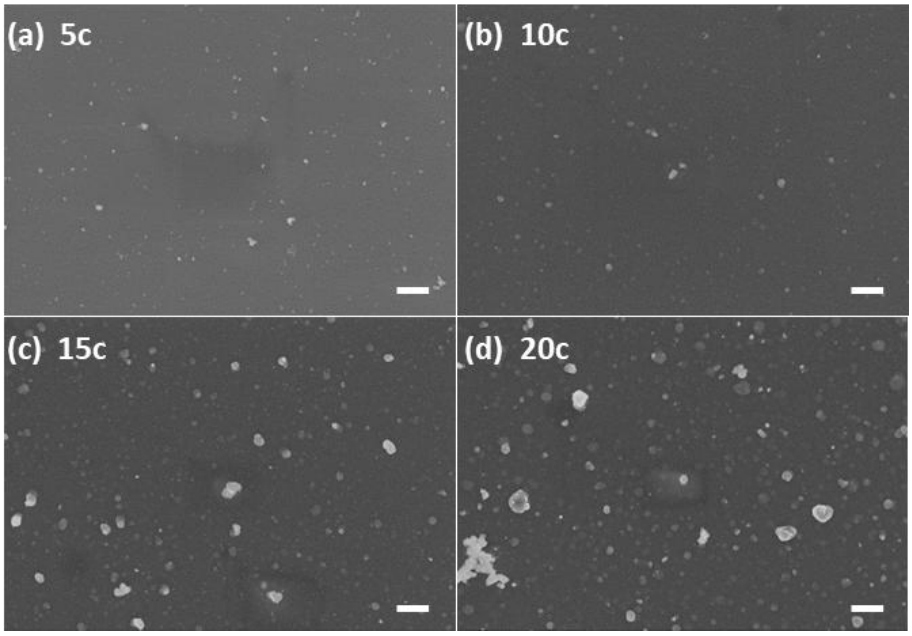

Figure 2.19: High-resolution SEM images of $Cu_3(HHTP)_2$ thin films prepared using dip coating at room temperature with different LbL cycles, 5c, 10c, 15c and 20c. Scale bar: 1 µm.

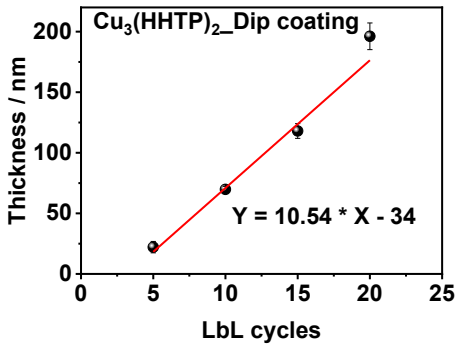

Figure 2.20: Plot of $Cu_3(HHTP)_2$ thin-film thickness against LbL cycles with corresponding linear fitting.

2.6 Summary

In this chapter, two automated platforms for the LbL-LPE growth of MOF thin films were introduced, using Ni-(BDC-NH_2) as a case study. Each platform offers distinct advantages. The microfluidics platform allows for the precise investigation of the effects of initial parameters on the growth of MOF thin films at a relatively small scale while minimizing the consumption of chemicals and solvents. In contrast, the dip coating method facilitates the production of large-scale MOF thin films with superior homogeneity, making it more suitable for device integration. Additionally, the insights gained from the microfluidics platform have the potential to guide and optimize the dip-coating process, although further systematic investigation is required. Beyond the study of Ni-(BDC-NH_2) thin films, the growth of $Cu_3(HHTP)_2$ thin films was also explored on both platforms, demonstrating the versatility of these methods for producing MOF thin films at various scales.

3 Lithographic patterning and optical contrast of MOF thin films

This chapter initially describes three lithographic methodologies for patterning MOF thin films. These methodologies utilize (1) a PaC coating, (2) an ultraviolet (UV) photoresist (e.g., AZ5214), or (3) a polymethyl methacrylate (PMMA)/SU-8 bilayer stack as sacrificial layers, respectively. These methodologies are summarized in **Table 3-1**. The applicability of these approaches is dependent upon the growth conditions of MOF thin films, particularly the solvents utilized and their stability during the subsequent lift-off process. Following the successful patterning of MOF thin films, an analytical method based on the optical contrast of MOF thin films on a Si/SiO_2 substrate was developed and employed to evaluate the thickness and relative surface roughness of the MOF thin films.

Table 3-1: Technological development for the patterning of MOF thin films.

Sacrificial layers	Removal methods
PaC coating	THF striping
UV photoresist	lift off
PMMA/SU-8 bilayer stack	lift off

3.1 Lithographic patterning

3.1.1 Approach A: Parylene C coating as a sacrificial layer

PaC polymers are a common material used in the semiconductor industry as a passivation layer, demonstrating exceptional resistance to a wide range of organic solvents. [159] The deposition of PaC is a conformal process that can be achieved through the polymerization of monomer via chemical vapor deposition at room temperature. Typically, an adhesion promoter (saline A-174) is applied to improve the attachment of PaC on Si/SiO_2 wafers prior to the deposition of PaC with a thickness of 1 µm for the patterning of MOF thin films. The requisite structures can be transferred onto Si/SiO_2 wafers by means of UV photolithography, development, and reactive oxygen plasma etching. The fabrication process is illustrated in **Figure 3.1a**. Subsequently, the growth of MOF thin films is accomplished through dip coating. The formation of structured

MOF thin films is accomplished by the removal of the PaC layer through immersion in tetrahydrofuran (THF) for a period exceeding two hours. Eventually, the structured samples are rinsed with isopropanol, dried with N_2 gas, and stored in an N_2 chamber for further characterization.

3.1.2 Approach B: UV photoresist as a sacrificial layer

UV photoresist is a commonly utilized material in microfabrication processes, facilitating the transfer of designed structures onto substrates. For example, processes such as metallization and lift-off, wet etching, and dry etching may be employed. These photoresists can be readily removed by organic solvents, including acetone, isopropanol, DMSO, and even ethanol. However, they are insoluble in water. Consequently, these photoresists can be employed as a mask layer for the growth of MOF thin films in aqueous conditions. The desired patterns are typically transferred to substrates by spin-coating photoresist, prebaking, photolithography, and development, as illustrated in **Figure 3.1b**. Subsequently, the growth of MOF thin films is accomplished through dip coating in deionized water. The formation of structured MOF thin films can be achieved through the removal of the photoresist in an organic solvent.

3.1.3 Approach C: PMMA/SU-8 stack as a sacrificial layer

PMMA is a common polymer employed in electron-beam lithography in lieu of conventional UV lithography due to its reduced sensitivity to UV radiation. SU-8 is selected as a hard mask for dry etching PMMA due to its favorable solvent stability. [160] Typically, a thin layer of PMMA with a thickness of approximately 500 nm was initially spin-coated and baked at 180°C for 90 seconds. This was followed by spin-coating and prebaking of a layer of SU-8 3005 with a thickness of approximately 5 µm. Subsequently, the SU-8 layer was structured through the application of UV exposure, post-baking, and development. Then, the PMMA layer was opened for the growth of MOF thin films through the application of short reactive oxygen plasma etching, as illustrated in **Figure 3.1c**. Subsequently, the growth of MOF thin films is accomplished through dip coating. The structured MOF thin films can be obtained through the lift-off process, which involves the use of solvents such as acetone or DMF.

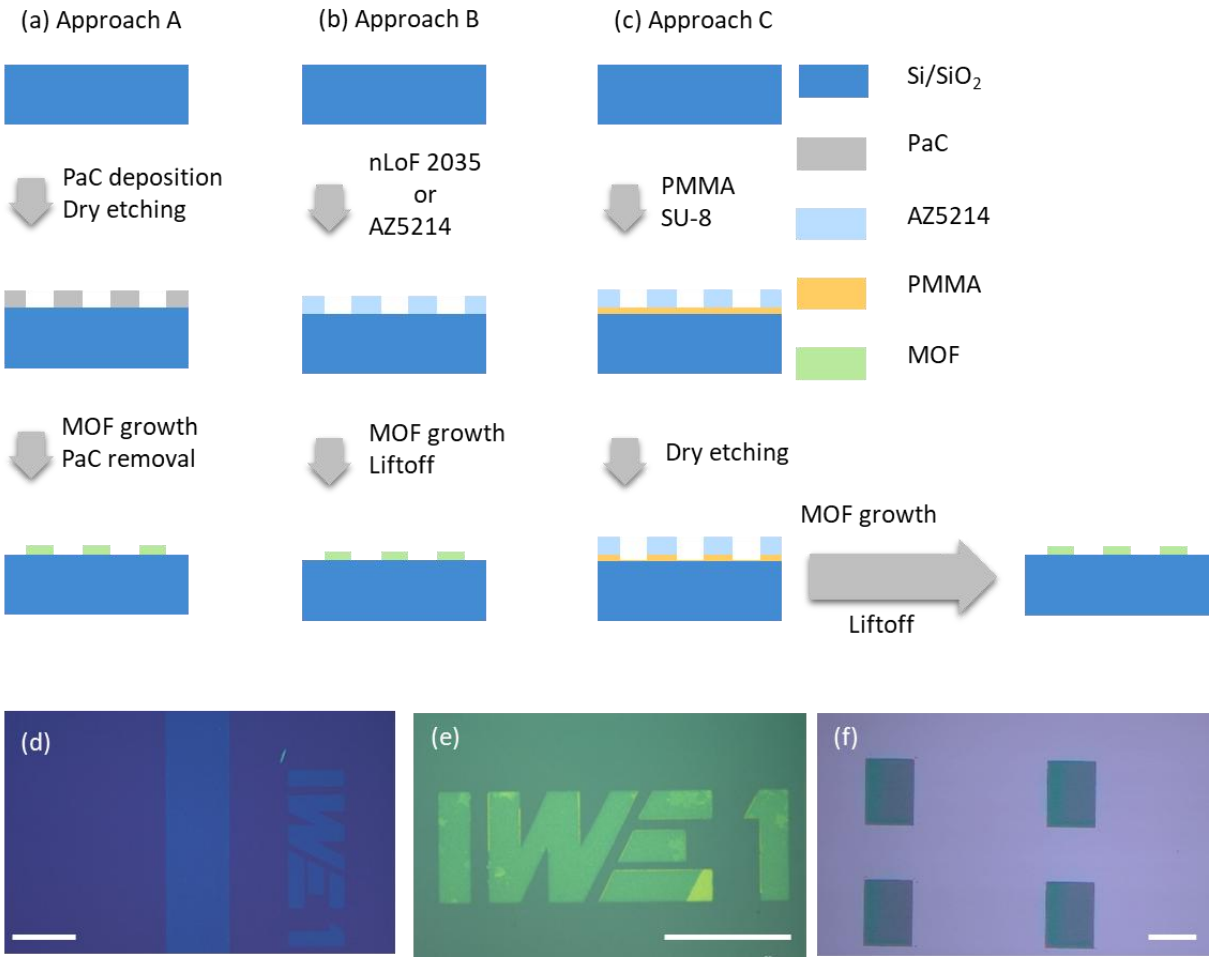

Figure 3.1: Three lithographic approaches for structuring MOF thin films. (a- c) PaC coating, UV photoresist, and PMMA/SU-8 stack as a sacrificial layer, respectively. (d) Optical image of Ni-(BDC-NH_2)-20c thin films patterned by approach A. (e) Optical image of Fe-(BDC-NH_2)-25c thin films patterned by approach B. (f) Optical image of Cu_3(HHTP)$_2$-20c thin films patterned by approach C. Scale bar: 200 µm.

3.2 Optical contrast of MOF thin films on Si/SiO_2 substrates

This section outlines an optical methodology that was devised for the expeditious analysis and characterization of MOF thin films. This method is based on the optical contrast (OC) of a thin layer of MOF thin film on Si/SiO_2 substrates, which has been previously employed for the characterization of 2-D materials, including graphene, transition metal dichalcogenides, and hexagonal BN. [161-163] For example, the use of monochromatic optical filters allows for the clear distinction of monolayer, bilayer, and trilayer graphene flakes on a Si substrate with an approximate oxide thickness of 300 nm. The addition of layers on a Si/SiO_2 substrate affects the light path, resulting in a variation of OC. [161] This phenomenon can be explained by a mathematical model based on Fresnel's law. In this study, a trilayer optical model is implemented and illustrated in **Figure 3.2**. The OC values of MOF thin films on Si/SiO_2 substrates are calculated in accordance with the formula presented in **Equation 3-1**.

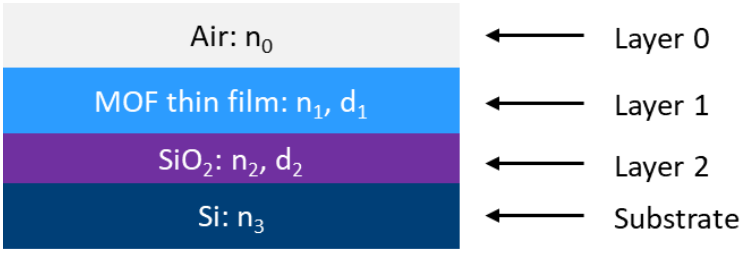

Figure 3.2: Schematic illustration of a trilayer optical model for MOF thin-film analysis based on optical contrast.

In this optical model, five critical parameters have an impact on the eventual OC, as shown in **Equation 4-1**: the thicknesses (d_1 and d_2) and refractive indices (RI: n_1 and n_2) of the MOF thin-film layer and SiO_2 layer, and the incidence wavelength (λ). In this particular instance, only the RI (n_1) and thickness (d_1) of the MOF thin films are taken into consideration, while the other parameters (n_0, n_2 and d_2) are maintained at a constant value. As previously stated, to predict the OC of the MOF thin film on the SiO_2/Si substrate, AFM measurements were conducted to characterize the thickness of the MOF thin films. Furthermore, spectroscopic ellipsometry (SE) measurements were conducted to ascertain the thickness of the SiO_2 layer and the RI (n_1) of the MOF thin films.

$$OC = \frac{I_{SiO_2} - I_{MOF}}{I_{SiO_2}} \tag{3-1}$$

$$I_{n1} = \Big|\left(r_1 * e^{i*(\emptyset_1+\emptyset_2)} + r_2 * e^{-i*(\emptyset_1-\emptyset_2)} + r_3 * e^{-i*(\emptyset_1+\emptyset_2)} + r_1 * r_2 * r_3 * e^{i*(\emptyset_1-\emptyset_2)}\right) * \left(e^{i*(\emptyset_1+\emptyset_2)} + r_1 * r_2 * e^{-i*(\emptyset_1-\emptyset_2)} + r_1 * r_3 * e^{-i*(\emptyset_1+\emptyset_2)} + r_2 * r_3 * e^{i*(\emptyset_1-\emptyset_2)}\right)^{-1}\Big|^2$$

$$r_1 = \frac{n_0-n_1}{n_0+n_1},\ r_2 = \frac{n_1-n_2}{n_1+n_2},\ r_3 = \frac{n_2-n_3}{n_2+n_3},\ \emptyset_1 = \frac{2\pi*n_1*d_1}{\lambda},\ \emptyset_2 = \frac{2\pi*n_2*d_2}{\lambda}$$

Where I_{SiO_2} and I_{MOF} stand for the intensities of reflected light on SiO_2 and MOF thin film, respectively. n_0 and n_3 represent the RI of air and Si substrate, respectively.

3.2.1 Theoretical prediction of OC of MOF thin films

In order to establish an optical analysis method for the characterization of MOF thin films, Ni-(BDC-NH_2) thin films were utilized as examples. These were prepared by automated dip coating, which was selected due to the good homogeneity observed over a large scale and the ease of patterning. Initially, Ni-(BDC-NH_2) thin films with varying thicknesses were fabricated and

are illustrated in **Figure 3.3**. Subsequently, SE measurements were performed at varying incidence angles to ascertain the RI of the Ni-(BDC-NH_2) thin films. The data were then fitted using the Cauchy model, as illustrated in **Figure 3.4**. The RI (n_1) of the Ni-(BDC-NH_2) thin film is presented in **Equation 4-2**, showing the wavelength dependency. The theoretical OC prediction for a 9 nm thick Ni-(BDC-NH_2) thin film is plotted in **Figure 3.5**, with the requisite thickness (d_1) and n_1 values incorporated. Two peaks with the highest OC values were observed in the vicinity of approximately 525 nm and 600 nm.

$$n_{1(\lambda)} = 1.54 + \frac{1102}{\lambda^2} + 0.005i \tag{3-2}$$

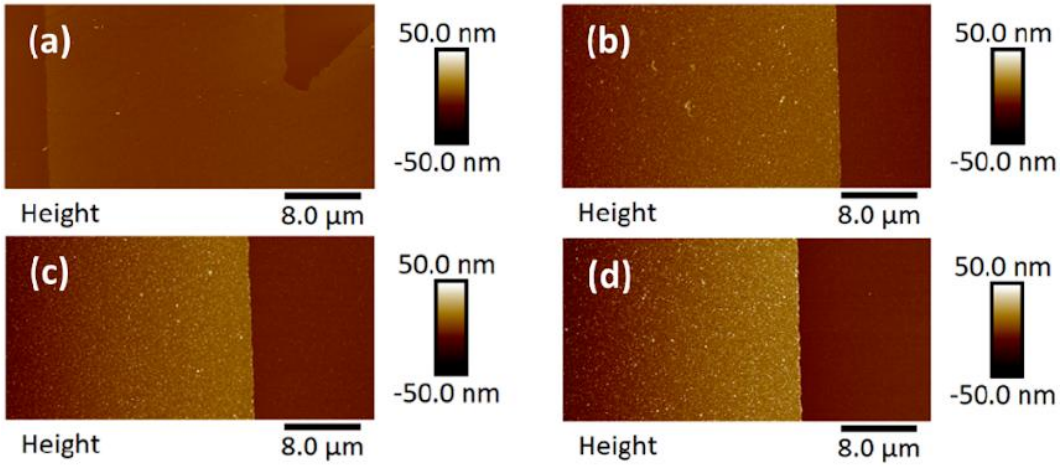

Figure 3.3: AFM images of structured Ni-(BDC-NH_2) thin films. (a) 4.5 nm; (b) 12.0 nm; (c) 16.0 nm and (d) 25.0 nm.

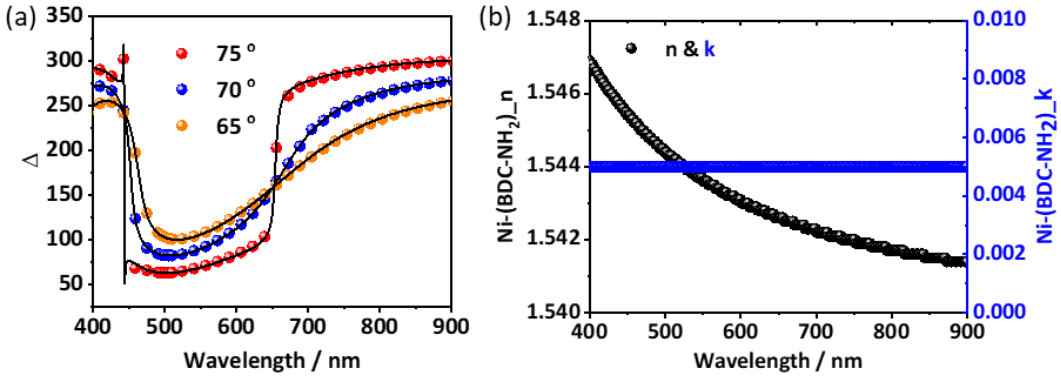

Figure 3.4: (a) SE measurements of Ni-(BDC-NH_2) thin film with a thickness of 9.0 nm and corresponding fitting using Cauchy model. (b) Calculated refractive index and permittivity.

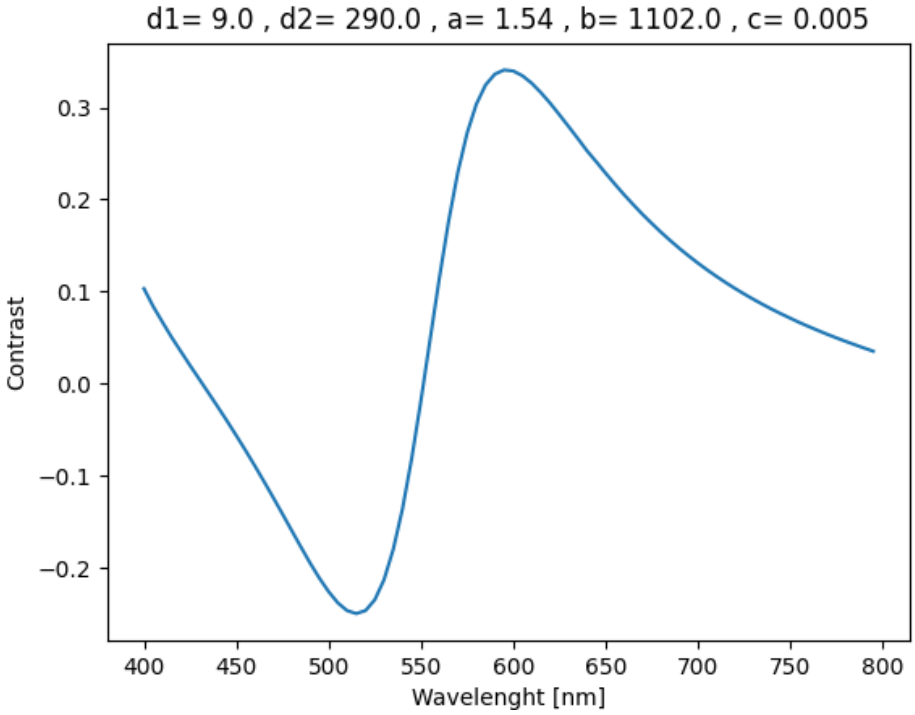

Figure 3.5: Theoretical OC prediction of a 9 nm thick Ni-(BDC-NH_2) thin film on Si/SiO_2 with an oxide thickness of 290 nm.

3.2.2 Experimental OC of MOF thin films

In order to evaluate the experimental OC of Ni-(BDC-NH_2) thin films, the same samples were utilized with the implementation of monochromatic optical filters with wavelengths of 405, 450, 532, 589, 632, and 660 nm, which cover the entire visible spectrum. As shown in **Figure 3.6**, the monochromatic images demonstrate the variation in OC value across different wavelengths. The corresponding OC value at a specific wavelength was calculated using **Equation 4-1** and is presented in **Figure 3.7**. As anticipated, the highest OC values were observed at approximately 525 nm and 600 nm.

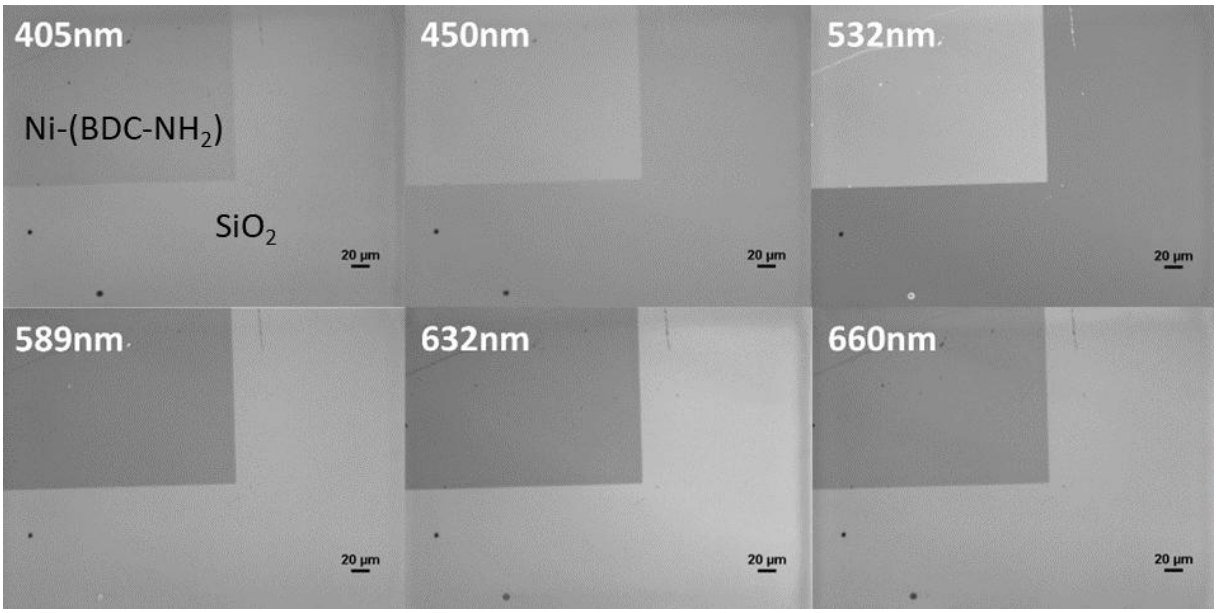

Figure 3.6: Monochromatic images of 9 nm thick Ni-(BDC-NH_2) thin film captured at different wavelengths.

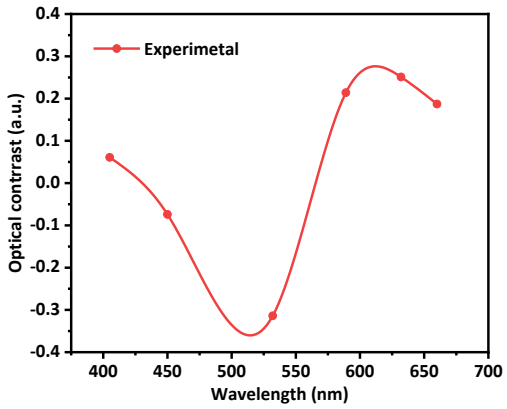

Figure 3.7: Experimental OC values of 9 nm thick Ni-(BDC-NH_2) thin film at different wavelengths.

3.2.3 Theoretical OC *vs* experimental OC

In order to facilitate a comparison between the OC values predicted theoretically and those obtained experimentally, the OC values at the same wavelength are extracted and plotted together with the experimental OC values in **Figure 3.8**. It can be observed that the same wavelength dependence of OC is evident, which serves to confirm the applicability of the mathematical model based on Fresnel's law for MOF thin films. A minor discrepancy was also identified, which is likely attributable to the light source, optical microscope, and image processing software.

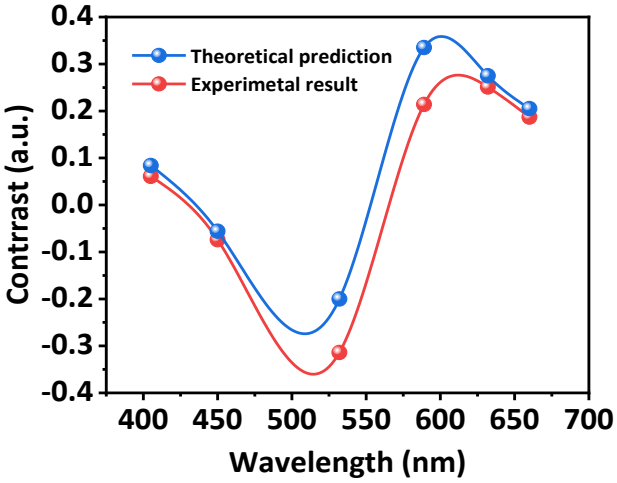

Figure 3.8: Comparison of theoretically predicted OC and experimental OC obtained from a 9 nm thick Ni-(BDC-NH_2) thin film.

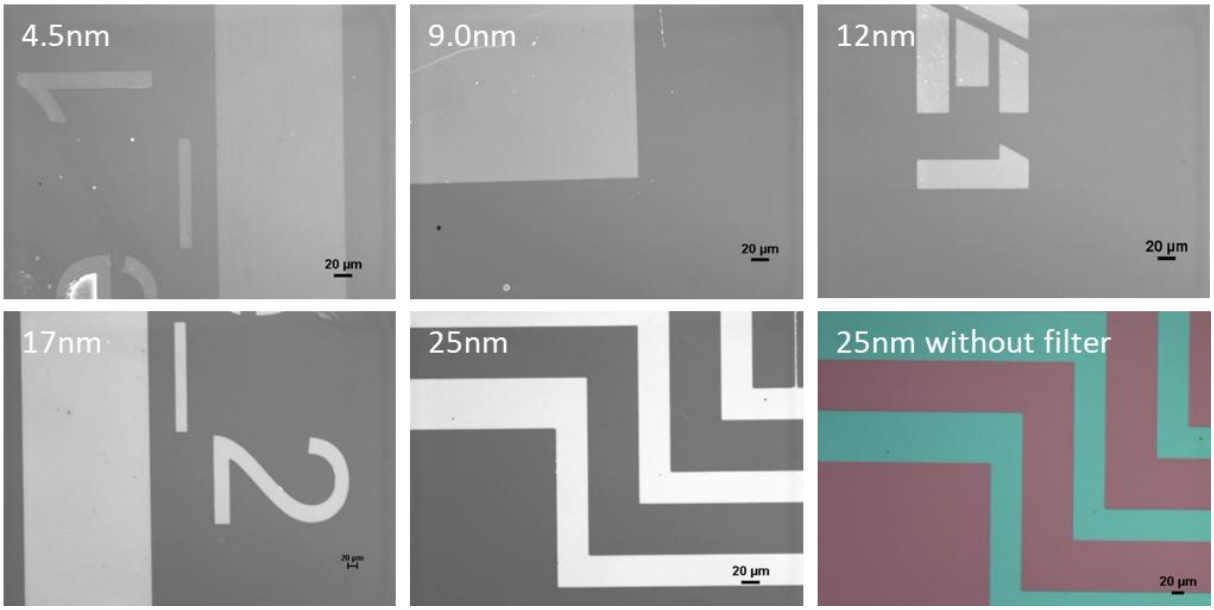

Figure 3.9: Monochromatic images of 4.5, 9.0, 12.0, 17.0, and 25.0 nm thick Ni-(BDC-NH_2) thin films, respectively. And one colored image of 25.0 nm thick Ni-(BDC-NH_2) thin film.

3.2.4 Thickness dependency of OC

As illustrated in **Figure 3.8**, the highest experimental OC value is observed at 532 nm. Subsequently, monochromatic images of Ni-(BDC-NH_2) thin films with varying thicknesses were captured at a fixed wavelength of 532 nm, as illustrated in **Figure 3.9**. From these images, it is evident that the OC is higher in thicker Ni-(BDC-NH_2) thin films, as illustrated in **Figure 3.10**. Consequently, this calibration curve may be utilized to assess the homogeneity of deposited MOF thin films and thickness.

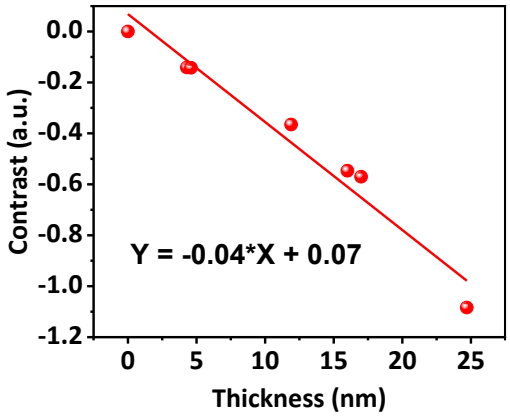

Figure 3.10: Thickness dependency of experimental OC values of Ni-(BDC-NH_2) thin films.

3.3 Discussion

As illustrated in Figure **3.1d-f**, the patterned MOF thin films exhibit exceptionally clean and sharp edges, which substantiates the remarkable efficacy of the developed lithographic techniques. **Figure 3.1d** depicts one of the optical images of structured Ni-(BDC-NH_2) thin films utilizing EtOH as the growth solvent. In this instance, a PaC coating was employed as a sacrificial layer, subsequently removed through immersion in THF for a period exceeding two hours following the growth of the Ni-(BDC-NH_2) thin films with 20 LbL cycles. Moreover, the patterned Ni-(BDC-NH_2) thin films illustrated in **Figures 3.3**, **3.6**, and **3.9** were all produced using approach A. **Figure 3.1e** depicts one of the optical images of Fe-(BDC-NH_2) thin films using DI H_2O as the synthetic solvent, where UV photoresist was utilized as a soft mask and can be removed by acetone or other organic solvents. Following the lift-off process in acetone, the Fe-(BDC-NH_2) thin films with 25 LbL cycles remained intact due to their excellent solvent stability. Further structural and morphological characterizations are presented in Chapter 6. **Figure 3.1f** depicts one of the optical images of $Cu_3(HHTP)_2$-20c thin films using ethanol as a growth solvent. In this case, a PMMA/SU-8 bilayer was employed as a sacrificial layer, which was subsequently removed by acetone or other strong organic solvents, such as DMF. Further structural and morphological characterization can be found in Chapter 4.

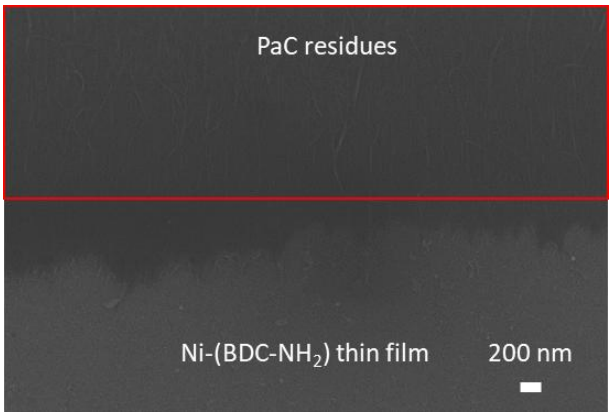

Figure 3.11: High-resolution SEM image of patterned Ni-(BDC-NH_2) thin film using approach A. PaC residues are marked.

Approach A is a relatively generic method due to the low polarity of THF, which is less aggressive to the grown MOF thin films. While the removal of PaC by soaking the samples in THF is not particularly effective, resulting in the residual presence of adhesion promoters, as illustrated in **Figure 3.11**. Approach B is only applicable to MOFs that are capable of growth in aqueous solutions, and which retain their structural integrity when exposed to strong organic solvents. Both approaches B and C can ensure the highest degree of cleanliness for the substrates and edges. The application of approach C is more expansive than that of approach B. Approach C may be applied to MOFs that can be grown in weak organic solvents, such as ethanol. Ethanol is one of the most commonly used solvents for the growth of MOF thin films through LbL-LPE, indicating that approach C has significant potential for the on-chip integration of MOF thin films in microelectronic sensor applications, which are discussed in more detail in Chapters 5 and 6.

The developed optical method, based on optical contrast, is also applicable to other MOF thin films, including those of Fe-(BDC-NH_2). Initially, four Fe-(BDC-NH_2) thin films with 10, 15, 20, and 25 LbL cycles were deposited on Si/SiO_2 substrates with an oxide thickness of approximately 290 nm. The corresponding thickness was characterized by AFM and plotted in **Figure 3.12a** against LbL cycles with a growth rate of 1 nm per cycle after 10 LbL cycles. Similarly, the Fe-(BDC-NH_2)-25c thin films display a range of optical contrasts when subjected to the optical filters, as illustrated in **Figures 3.12b-e**. The experimental contrast and theoretical contrast are plotted together in **Figure 3.13**, which demonstrates that the highest contrast occurs at 405 nm and 589 nm. Moreover, the optical contrast spectrum obtained from reflectometry measurements (**Figure 3.14**) also exhibits the highest contrast around 575 nm, which is in close proximity to 589 nm. The measurements were conducted at wavelengths between 425 and 675 nm, due to the limitations of the light source. These results demonstrate the applicability of the

optical contrast-based method. Subsequently, the thickness dependency of the optical contrast of Fe-(BDC-NH_2) thin films was investigated by fixing the wavelengths at 405 nm and 589 nm, respectively. As illustrated in **Figures 3.15** and **3.16**, a linear correlation was evident at both wavelengths, suggesting the potential for evaluating the thickness of Fe-(BDC-NH_2) thin films.

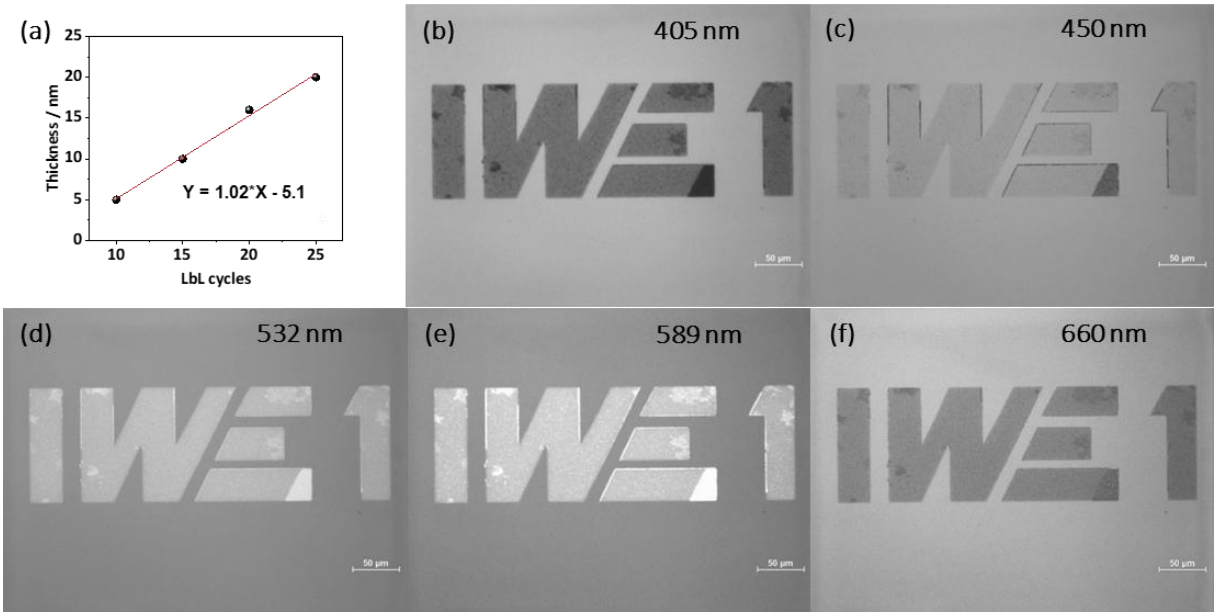

Figure 3.12: Fe-(BDC-NH_2) thin films on Si/SiO_2 substrates with an oxide thickness of approximately 290 nm. (a) A linear plot of thin-film thicknesses against LbL cycles. (b-f) Monochromatic images of patterned Fe-(BDC-NH_2)-25c thin films captured using the optical filters with varying wavelengths.

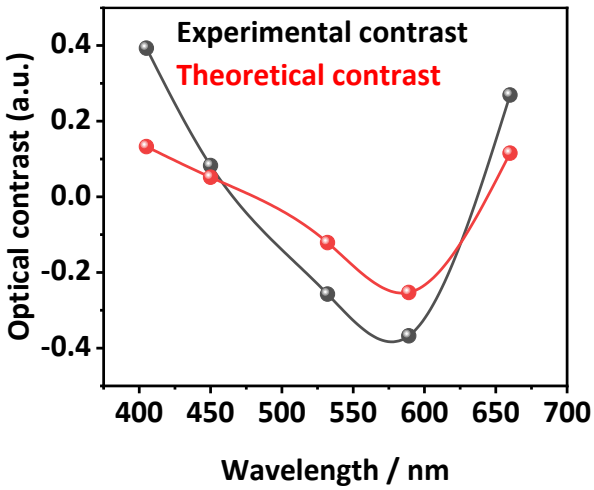

Figure 3.13: A comparison of experimental contrast and theoretical contrast of Fe-(BDC-NH_2)-25c thin films.

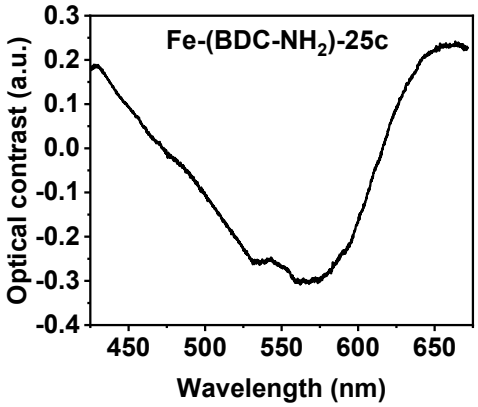

Figure 3.14: Optical contrast spectrum of Fe-(BDC-NH_2)-25c thin film.

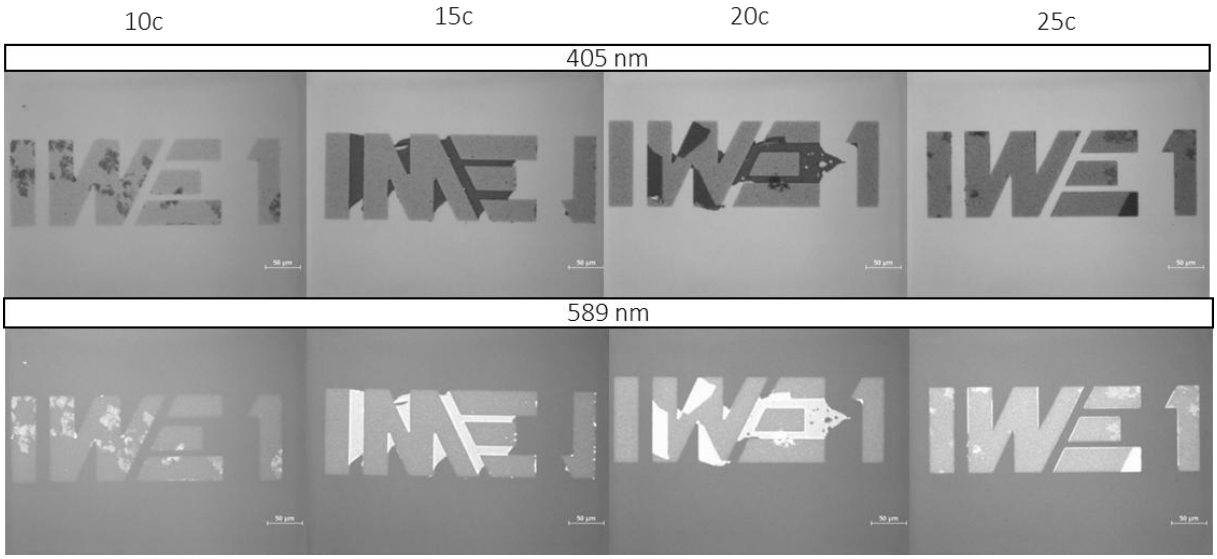

Figure 3.15: Monochromatic images of Fe-(BDC-NH_2) thin films with 10, 15, 20 and 25 LbL cycles captured at 405 nm and 589 nm, respectively.

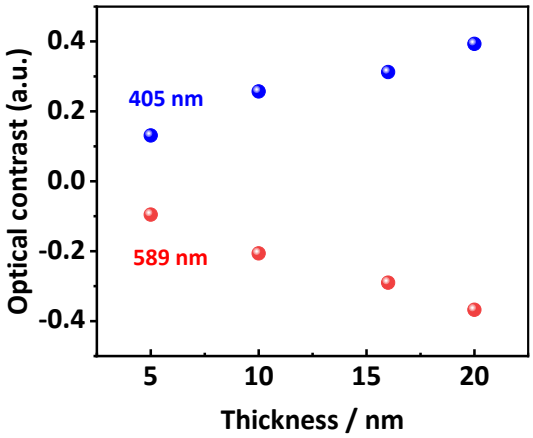

Figure 3.16: Thickness dependency of optical contrast of Fe-(BDC-NH_2) thin films at 405 nm and 589 nm.

A graphical user interface was developed to facilitate the prediction of MOF thin-film thickness and relative surface roughness. This was achieved through the implementation of a calibration curve, as illustrated in **Figure 3.10**. As illustrated in **Figure 3.17**, by selecting the regions of interest (e.g., the substrate and the MOF thin-film pattern), the thickness and relative thickness can be readily obtained. Furthermore, a 3-D representation of the height profile is generated.

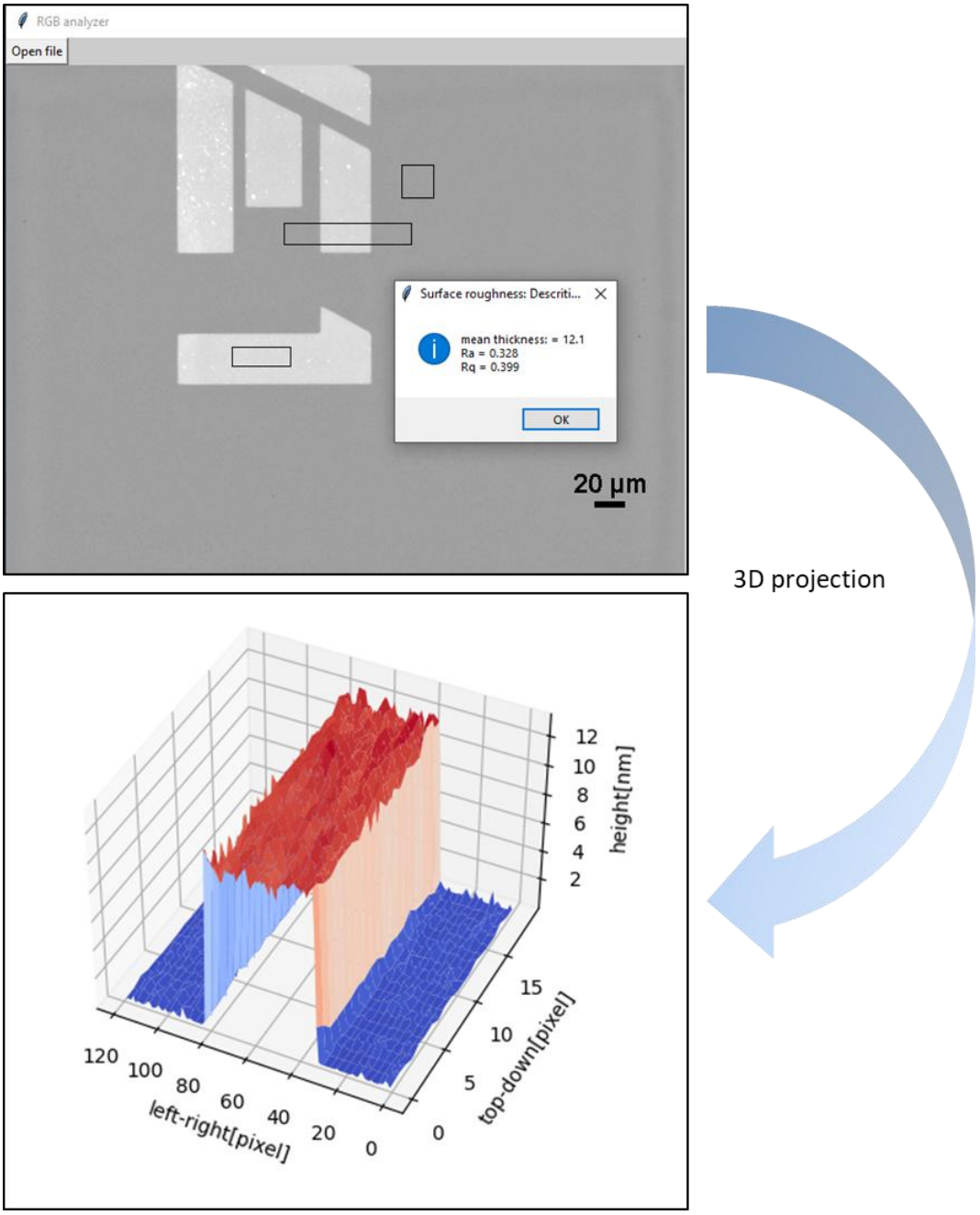

Figure 3.17: A Graphic user interface for the quick evaluation of MOF thin films and 3-D projection for height profile demonstration.

3.4 Summary

This chapter provides an overview of three lithographic techniques for patterning MOF thin films, which hold significant promise for both the characterization and on-chip integration of these films. The application of these methods was explored in detail, focusing on how growth conditions and solvent stability influence the targeted MOFs. Compared to other reported techniques, these lithographic methods can be implemented using UV lithography, eliminating the need for more complex approaches like electron-beam lithography, microcontact printing, or nanoimprinting. Additionally, a novel optical contrast-based analytical method is introduced, which allows for the rapid evaluation of MOF thin films, including assessments of film homogeneity and surface roughness. Film thickness can also be determined using a calibration curve. This optical method is versatile and can be applied to other MOF systems, such as Fe-(BDC-NH_2).

4 On-chip integration of MOF thin films and device characterization

This chapter details the on-chip integration of $Cu_3(HHTP)_2$ thin films, characterizes their electrical conductivity and contact resistivity, and investigates the effects of post-thermal treatment *via* rapid thermal processing (RTP) on their electrical properties. In addition to employing fundamental electrical characterization techniques, including the Van der Pauw (VdP) method, the collinear four-probe contact method, and the transfer length method (TLM), the chapter also evaluates the electrical characteristics of electrolyte-gated field-effect transistors (EG-FETs) fabricated using $Cu_3(HHTP)_2$ thin films as channel materials.

4.1 On-chip integration of $Cu_3(HHTP)_2$ thin films

Figure 4.1 illustrates the standard on-chip integration route for $Cu_3(HHTP)_2$ thin films, developed and implemented for the first time. The process typically begins with glass wafers being treated with a piranha solution to remove organic contaminants. For Si/SiO_2 wafers, acetone and IPA are used as cleaning agents.

Step 1: Prior to spin-coating the imaging reversal photoresist AZ5214, the wafers are placed on a hotplate at 120°C for over ten minutes to eliminate absorbed moisture. This is followed by a 3-minute oxygen plasma treatment (300W, 300 sccm O_2 flow). The wafers then undergo a 15-minute Hexamethyldisilane (HMDS) treatment at 120°C. A layer of AZ5214 photoresist, approximately 1.4 µm thick, is then coated onto the wafers and prebaked at 100°C for three minutes. The required structures are transferred onto the wafers via UV lithography on a mask aligner (MA/BA6). This is followed by a reversal bake at 115°C for 2.5 minutes and a flood exposure. After 45 to 60 seconds of development in AZ726MIF, the substrate is rinsed with deionized water and dried at 70°C. Subsequently, 30 nm of Ti and 100 nm of Au are deposited by electron-beam evaporation, followed by a lift-off process in DMSO for 24 hours at 80°C.

Step 2: A PaC coating is applied as a passivation layer. Prior to this, the wafers are treated with an A-174 silane solution (100 mL deionized water, 100 mL isopropanol, and 1 mL A-174 silane pre-aged for two hours) for 20 minutes to ensure optimal adhesion of the PaC coating. The wafers are then dried in a laminar airflow for 20 minutes, rinsed with isopropanol for 15 seconds,

and dried with nitrogen. A PaC film approximately 3.5 µm thick is deposited by chemical vapor deposition at room temperature to ensure optimal passivation, including the absence of pinholes.

Step 3: The contact pads and regions of the interdigital electrodes (IDEs) are opened by reactive ion etching (RIE) with oxygen plasma. A thick negative photoresist layer (nLoF 2070) of approximately 7 µm is coated and prebaked at 100°C for seven minutes. Patterns for opening contact pads and IDE regions are aligned and transferred onto the wafers using UV lithography, followed by a post-exposure bake (30 seconds at 60°C, 2 minutes at 110°C, and 2 minutes at 60°C) and development in AZ826MIF for 3.5 minutes. The contact pads are opened for wire bonding, while the IDE regions are intended for the growth of MOF thin films.

Step 4 & step 5: Spin-coating PMMA/SU-8 bilayer stack and opening IDE regions for MOF thin-film growth were discussed in **Section 3.1.3**.

Step 6: $Cu_3(HHTP)_2$ thin films, approximately 50 nm thick, are deposited using 10 LbL cycles, as depicted in **Figure 4.2**.

Step 7: The fabrication of $Cu_3(HHTP)_2$ thin-film chips is finalized by performing a lift-off process in acetone overnight to remove the PMMA and SU-8 bilayer stack.

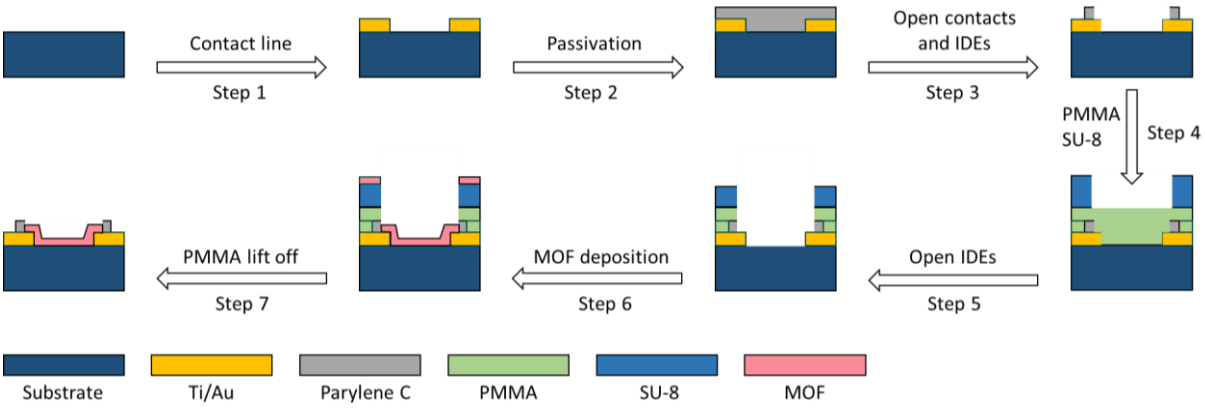

Figure 4.1: Standard fabrication of $Cu_3(HHTP)_2$ thin-film chips.

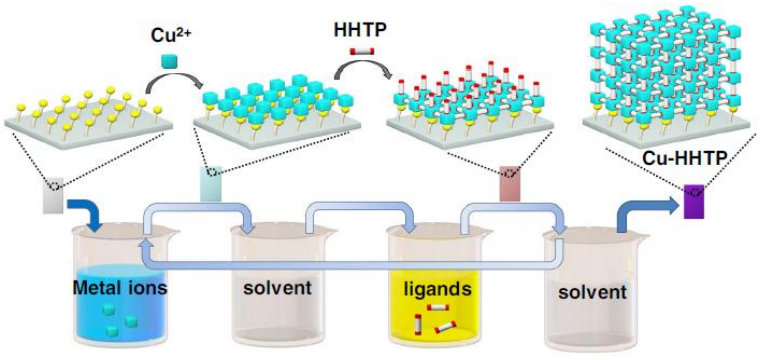

Figure 4.2: On-chip integration of $Cu_3(HHTP)_2$ thin films through dip coating assisted LbL-LPE. [164]

4.2 Rapid thermal processing

Rapid thermal processing (RTP) is a material treatment technique that involves subjecting a material to a specific temperature for a defined period, followed by a controlled cooling phase. [165] This process is designed to enhance the material's intrinsic properties and microstructure by eliminating or mitigating defects, stresses, crystal imperfections, or non-uniformities, thereby improving its overall performance. Thermal annealing, a critical aspect of RTP, holds significant implications in the field of materials science and engineering, influencing several key areas:

Control of Crystal Growth and Grain Size: Thermal annealing can promote crystal growth, enhance crystal order, and improve the mechanical and electrical properties of materials. The process allows for the regulation of grain size and configuration, leading to better-controlled material characteristics.

Stress Relief: Thermal annealing is effective in reducing or eliminating internal stresses within materials, thereby minimizing the risk of stress-induced fractures or deformations. This is crucial for enhancing the durability and reliability of materials.

Defect Repair: Thermal annealing facilitates the repair of material defects, including crystalline defects, dislocations, and impurities. This process significantly enhances the quality and performance of the treated material.

Control of Phase Transitions and Crystal Structure: Thermal annealing can induce phase transitions in materials, leading to changes in their crystal structure. This capability allows for the preparation of materials with specific structures tailored to meet the requirements of various applications.

Modification of Material Properties: Thermal annealing can be used to modify material properties such as hardness, elastic modulus, and conductivity. This makes it a valuable technique for tailoring materials to achieve specific performance characteristics.

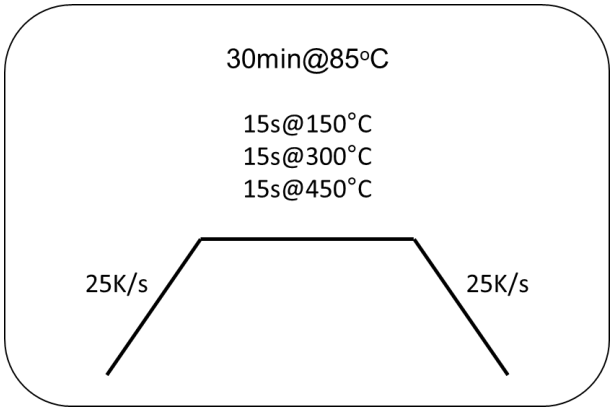

Figure 4.3: Parameters for annealing $Cu_3(HHTP)_2$ thin films.

In this study, RTP is employed for two primary purposes: (i) to reduce grain-boundary resistance and (ii) to enhance the electrical contact between the MOF thin film and metal electrodes. The annealing parameters for $Cu_3(HHTP)_2$ thin films are schematically illustrated in **Figure 4.3**. Initially, all $Cu_3(HHTP)_2$ thin films are annealed at 85°C in an argon (Ar) atmosphere for 30 minutes. This initial step has been shown to significantly improve the adhesion of $Cu_3(HHTP)_2$ thin films to various substrates, including glass. Following this pre-treatment, the chips are subjected to a secondary annealing process at 150°C, 300°C, and 450°C in Ar, each for 15 seconds. In all experiments, both the heating and cooling ramps are controlled at a rate of 25 K/s.

4.3 Morphological and structural characterizations

To characterize the changes in thickness, surface morphology, and crystallographic structures, AFM and GIXRD measurements were conducted. As illustrated in **Figure 4.4**, the AFM height profile image shows that the $Cu_3(HHTP)_2$ thin film maintains a consistent thickness of approximately 50 nm after annealing at various temperatures. **Figure 4.5** presents AFM surface scans (scan size: 2 x 2 μm^2) of the $Cu_3(HHTP)_2$ thin-film chip annealed at different temperatures. These scans indicate that the annealing process does not significantly affect the surface roughness of the thin film. These findings suggest that post-thermal treatment does not impact the observed thickness or surface roughness. However, significant changes were observed in the GIXRD patterns of $Cu_3(HHTP)_2$ thin films annealed at different temperatures (**Figure 4.6**). At lower temperatures (85°C and 150°C), two primary peaks are observed at 8° and 27.5°. After annealing at 300°C, the peak at 8° shifts to 9.3°, while the peak at 27.5° remains unchanged. Additionally, a new peak emerges at 5.3°. At 450°C, the peak at 9.3° shifts to 43.5°, indicating the degradation of the $Cu_3(HHTP)_2$ structure, though the framework appears to remain largely intact.

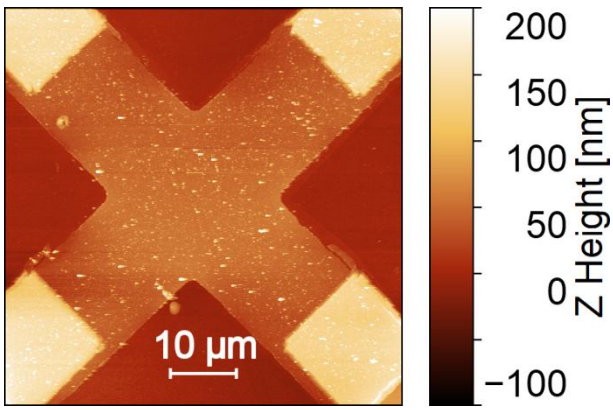

Figure 4.4: AFM height image of a $Cu_3(HHTP)_2$ thin-film device annealed at 85°C for 30 minutes in Ar atmosphere.

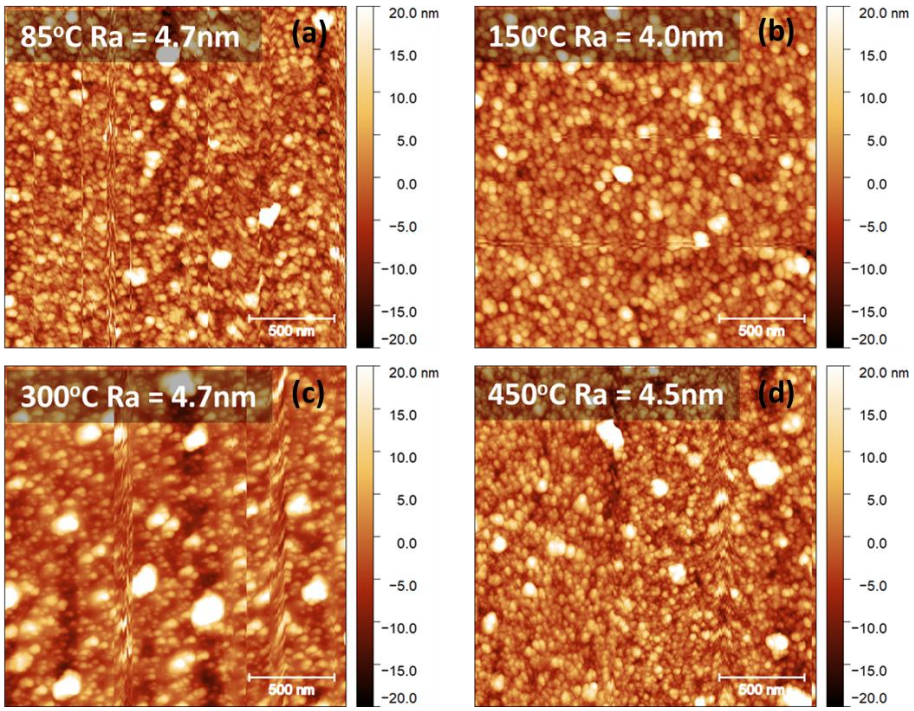

Figure 4.5: AFM images of surface scans on the position of $Cu_3(HHTP)_2$ thin-film device annealed at (a) 85°C, (b) 150°C, (c) 300°C and (d) 450°C.

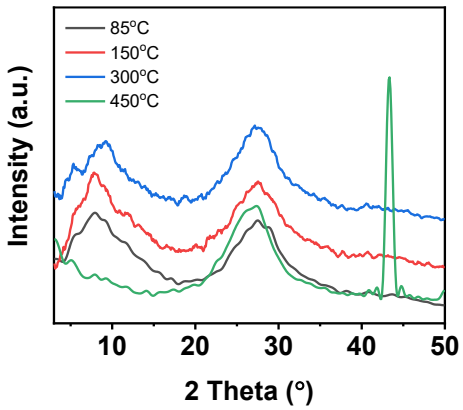

Figure 4.6: GIXRD patterns of $Cu_3(HHTP)_2$ thin films are annealed at 85°C, 150°C, 300°C and 450°C, respectively.

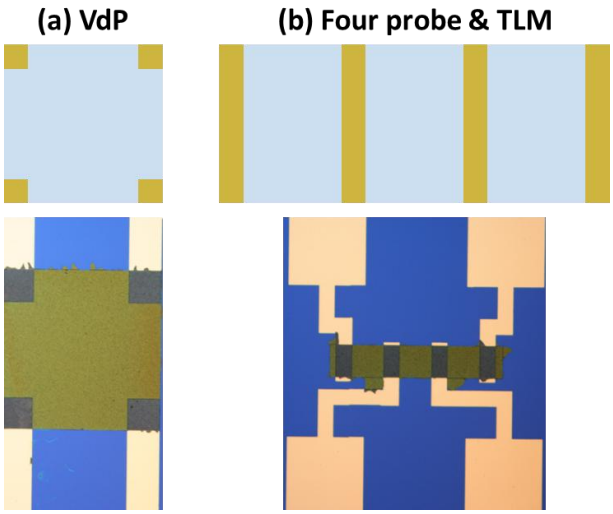

Figure 4.7: Device configurations and corresponding optical images. (a) VdP structure. (b) Collinear four-electrode structure.

4.4 Basic electrical characterizations

This section outlines three methods used to study the electrical properties of $Cu_3(HHTP)_2$ thin films. VdP method is widely employed to characterize the sheet resistance or conductivity of thin films, as well as the volume conductivity when the film's thickness is known. The collinear 4-probe contact method is considered the optimal approach for determining intrinsic conductivity, particularly in situations where the contact resistance is higher than the material's resistance. This method effectively eliminates the influence of contact resistance during I-V measurements. Additionally, TLM is utilized to assess the impact of contact resistance between $Cu_3(HHTP)_2$ thin films and gold microelectrodes. In this study, two key parameters are of interest: (i) conductivity (S/cm) and (ii) contact resistivity ($\Omega \cdot cm^2$). To characterize these parameters, a range of techniques and device configurations are employed, including the collinear 4-probe contact method, VdP method, and TLM. The corresponding device structures are illustrated in **Figure 4.7**.

4.4.1 Conductivity

This study employs three methods to characterize the electrical conductivity of $Cu_3(HHTP)_2$ thin films, which were subjected to various thermal treatments as detailed in **Section 4.2**. All devices were fabricated in accordance with the technology described in **Section 4.1**. Initially, the electrical conductivity of $Cu_3(HHTP)_2$ thin films was characterized through the implementation of VdP measurements. As illustrated in **Figure 4.8**, the conductivity of the three chips exhibits a similar correlation with annealing temperature. The highest conductivity was observed in $Cu_3(HHTP)_2$ thin films that had been annealed at 300°C. Moreover, a comparable

conductivity of 85°C-annealed devices was reported by Rubio-Giménez et al, exhibiting a value of 10^{-4} S·cm^{-1}. [166] A slight decrease in conductivity was observed following annealing at 150°C for 15 seconds in Ar. Subsequently, the observed decline in conductivity was attributed to thermal annealing at 450°C, which resulted in the formation of an oxide, as illustrated in **Figure 4.6**.

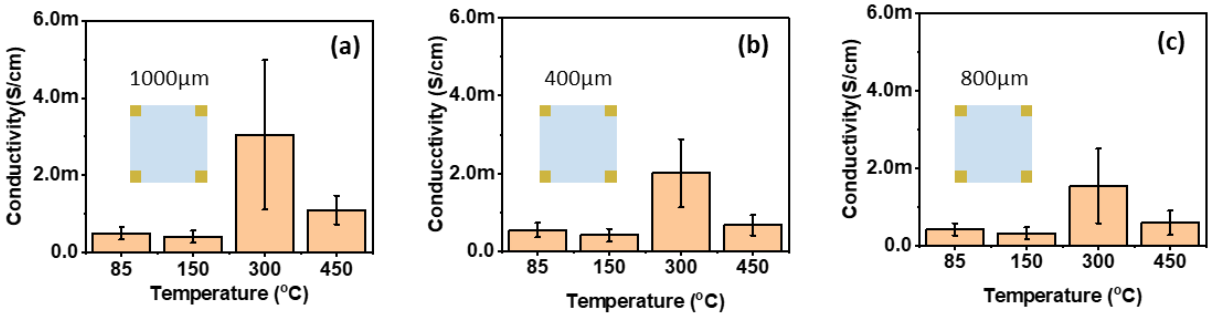

Figure 4.8: Conductivity of $Cu_3(HHTP)_2$ thin films annealed at 85, 150, 300, and 450°C characterized through VdP measurements with different dimensions. (a) 1000 µm, (b) 400 µm, (c) 800 µm.

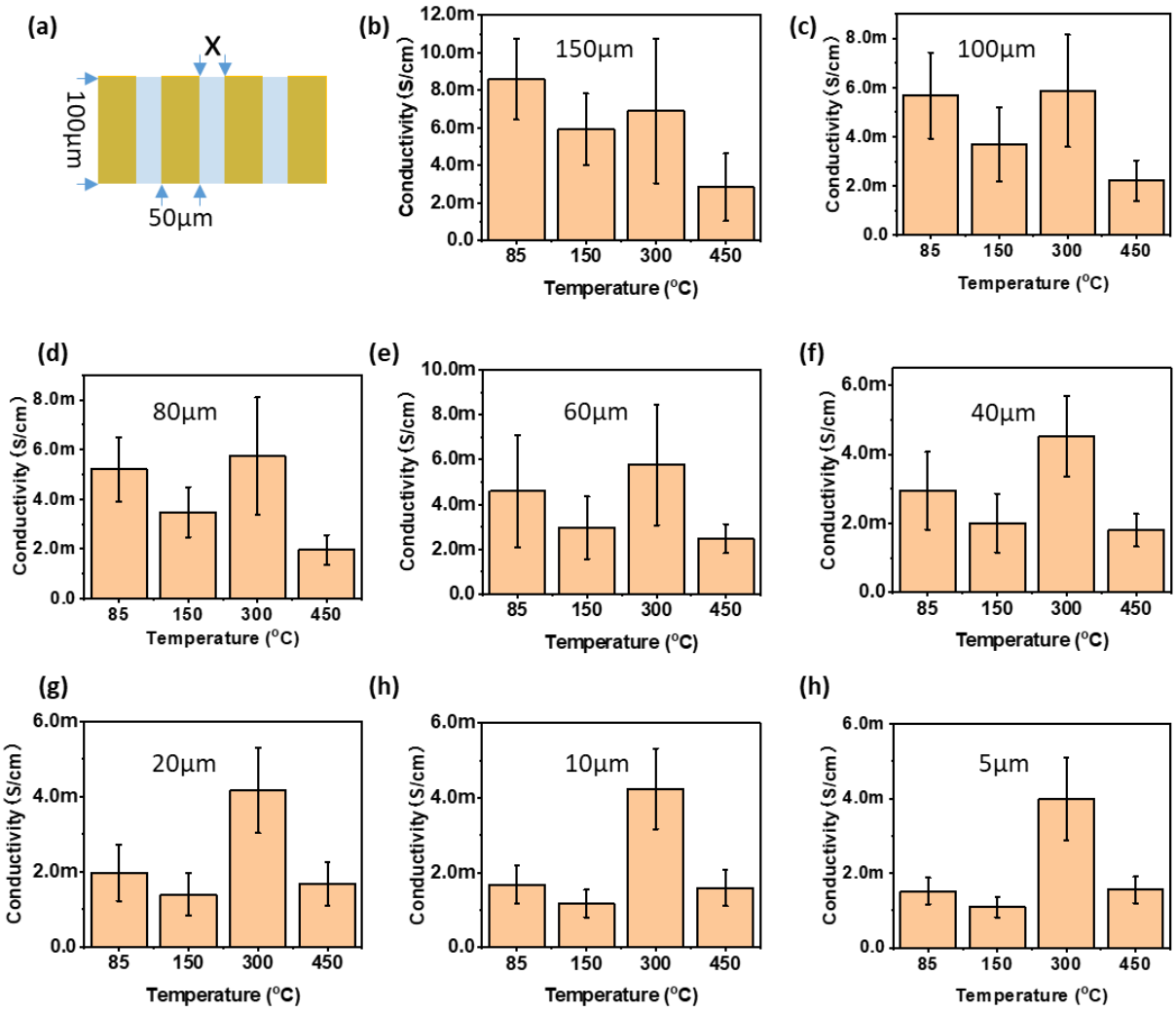

Figure 4.9: Conductivity of $Cu_3(HHTP)_2$ thin films annealed at 85, 150, 300, and 450°C characterized through collinear 4-probe contact measurements with different dimensions. (a) device structure, (b) 150 µm, (c) 100 µm, (d) 80 µm, (e) 60 µm, (f) 40 µm, (g) 20 µm, (h) 10 µm, and (h) 5 µm.

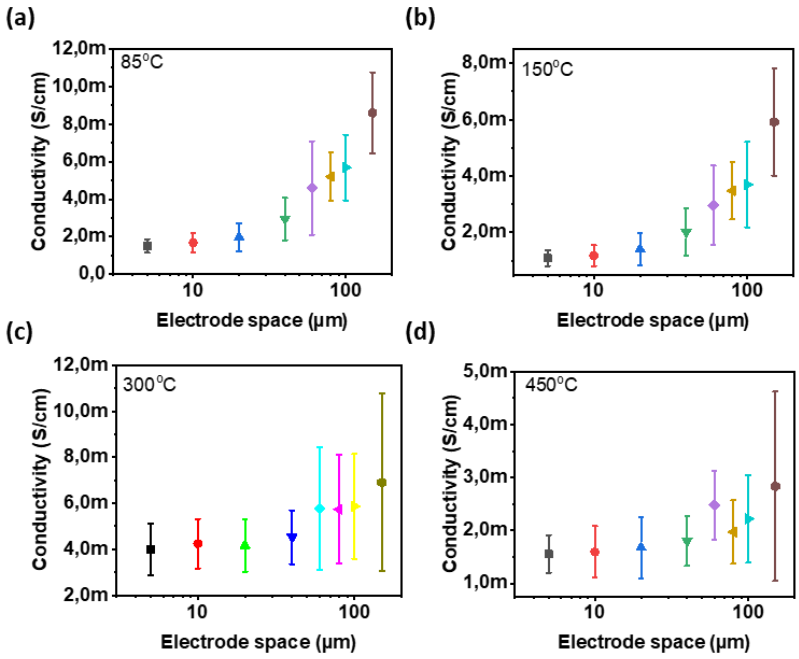

Figure 4.10: $Cu_3(HHTP)_2$ thin-film conductivity dependency on electrode space. (a) 85°C, (b) 150°C, (c) 300°C, and (d) 450°C.

To further investigate the influence of thermal treatment on the conductivity of $Cu_3(HHTP)_2$ thin films, the collinear 4-probe contact method was employed. This technique allows for the accurate measurement of conductivity by minimizing the impact of contact resistance. Additionally, TLM was used to assess the contact resistance between $Cu_3(HHTP)_2$ thin films and gold microelectrodes. The configuration for the collinear 4-probe contact measurements is shown in **Figure 4.9a**, with electrodes measuring 100 µm in length and 50 µm in width. In this study, we examined the effect of electrode spacing (X) on the uniformity of $Cu_3(HHTP)_2$ thin films. The results for devices with a 150 µm electrode spacing differed from those with other spacings, which displayed a similar trend to the VdP measurements. Notably, the devices with a 150 µm spacing exhibited slightly higher conductivity, suggesting that thermal treatment influences the material properties of $Cu_3(HHTP)_2$ thin films. As depicted in **Figure 4.6**, the peak observed at 8° shifts to 9.3° after annealing at 300°C, and a new peak appears at 5.3°, indicating improved crystallinity. Conversely, the disappearance of the 5.3° peak and the appearance of a peak at 43.5° after annealing at 450°C suggest a degradation in thin-film crystallinity. Additionally, the effect of device dimensions on the conductivity of $Cu_3(HHTP)_2$ thin films annealed at various temperatures was analysed, with results shown in **Figure 4.10**. Generally, an increase in conductivity was observed with larger electrode spacings across all annealing temperatures. However, it is important to note that device-to-device variability also increased, likely due to

the inhomogeneity of larger thin films. Therefore, smaller electrode spacings, such as 40 µm, 20 µm, 10 µm, and 5 µm, are recommended, as illustrated in **Figure 4.11**.

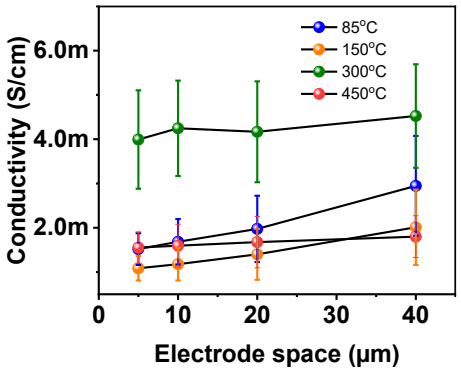

Figure 4.11: Comparison of the conductivity of $Cu_3(HHTP)_2$ thin films with small electrode space, annealed at 85, 150, 300, and 450°C, respectively.

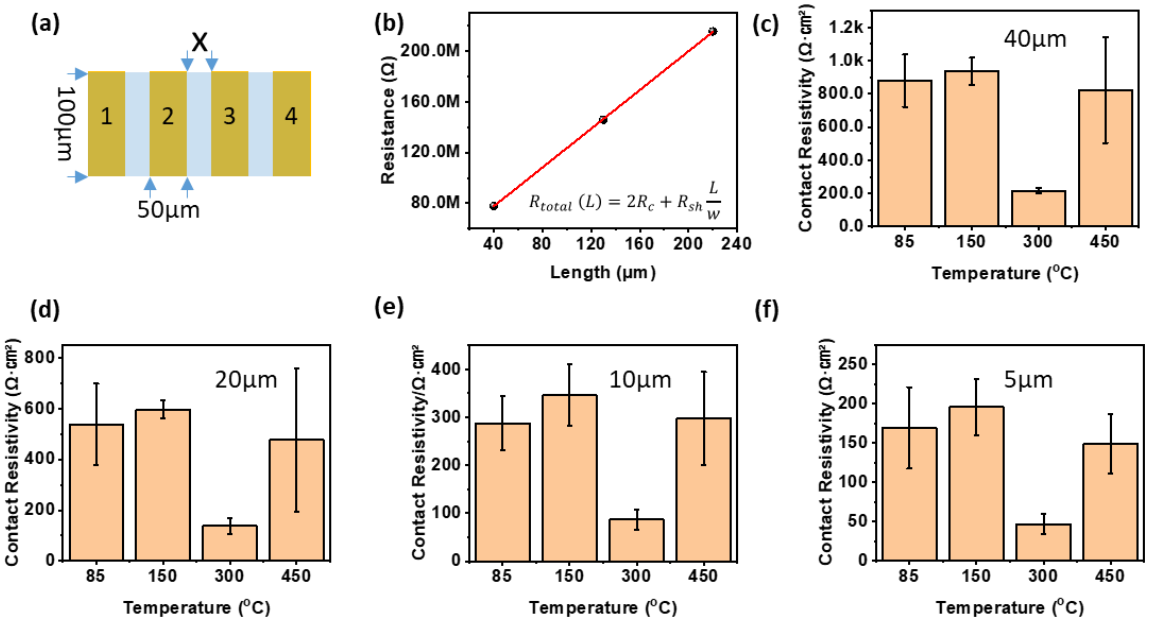

Figure 4.12: Contact resistivity. (a) Device structure, (b) exemplary plot for determination of contact resistance. (c) 40 µm, (e) 20 µm, (e) 10 µm, and (f) 5 µm.

4.4.2 Contact resistivity

The same device structures were employed to determine the contact resistance and contact resistivity between $Cu_3(HHTP)_2$ thin films and gold microelectrodes using TLM. In this context, only the electrode spacing is of relevance. **Figure 4.12a** shows that three I-V measurements were performed using the two-probe contact method between electrode 1 and electrodes 2, 3, and 4, respectively. The resulting resistances were then plotted against the electrode spacing. **Figure 4.12b** presents an example of the plot used to determine contact resistance. **Figures 4.12c-f** illustrate the contact resistivity between $Cu_3(HHTP)_2$ thin films and Au microelectrodes

after thermal annealing at various temperatures. It is clear that there is an inverse relationship between contact resistivity and electrode spacing. Devices annealed at 300°C display the lowest contact resistivity, consistent with the previously observed conductivity results. Based on these findings, it can be concluded that annealing at 300°C is optimal for improving both the crystallinity and the electrical contact between $Cu_3(HHTP)_2$ thin films and Au microelectrodes.

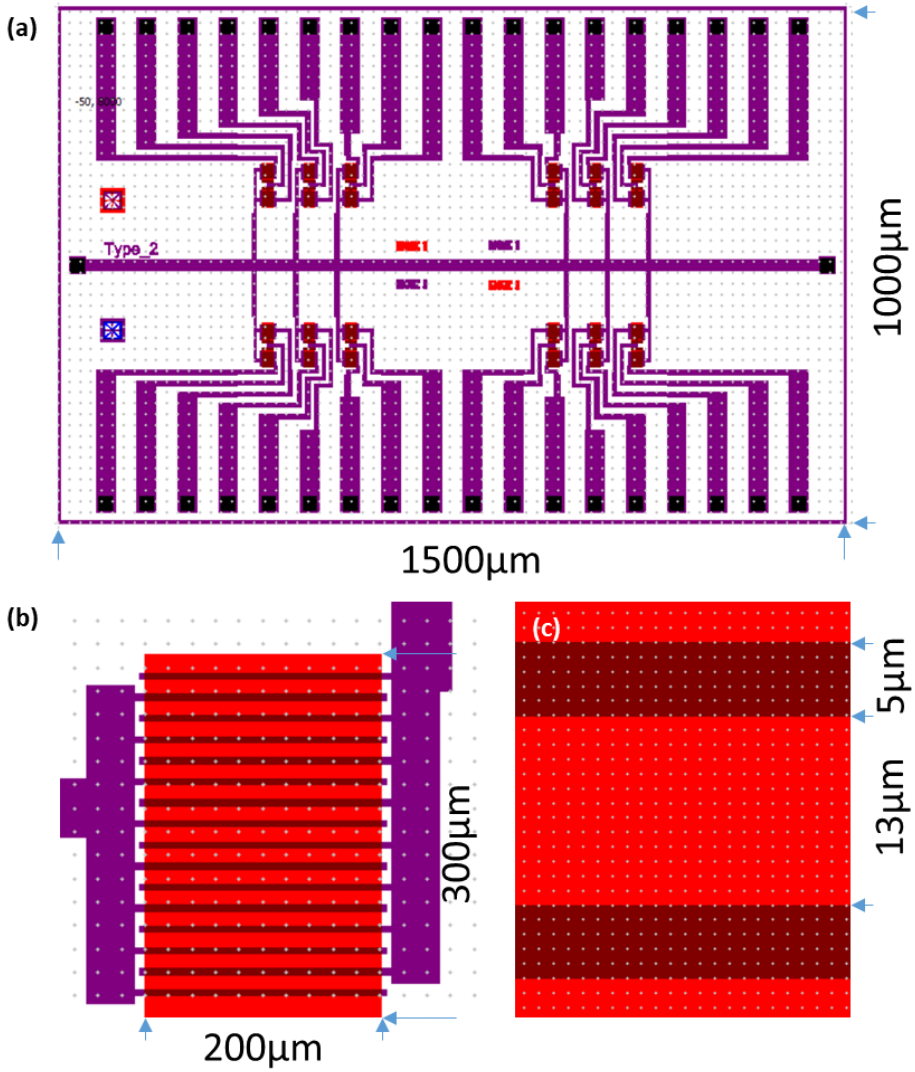

Figure 4.13: Mask design. (a) Layout of chip design, (b and c) dimension parameters of interdigital electrodes.

4.5 Electrolyte-gated field-effect transistors

To assess the characteristics of EG-FETs based on $Cu_3(HHTP)_2$ thin films, a new chip layout incorporating IDEs has been adopted. This revised layout is designed to reduce resistance by increasing the number of electrode pairs. **Figure 4.13** illustrates the chip layout along with the associated dimensional parameters. The chip fabrication and integration of the $Cu_3(HHTP)_2$ thin film follow the procedures detailed in **Section 4.1**. An optical image of one of the blocks is shown in **Figure 4.14**. The $Cu_3(HHTP)_2$ thin-film chips were subjected to thermal treatments

at both 85°C and 300°C. **Figure 4.15a** presents I-V plots for devices annealed at 85°C and 300°C. As expected, the current increased after annealing at 300°C compared to 85°C, aligning with the results discussed in **Section 4.4**. **Figures 4.15b** and **4.15c** display the average I-V plots of 24 devices on the same chip, annealed at 85°C and 300°C, respectively. The data reveal a slight variation between individual devices, which is beneficial for evaluating the performance of each device.

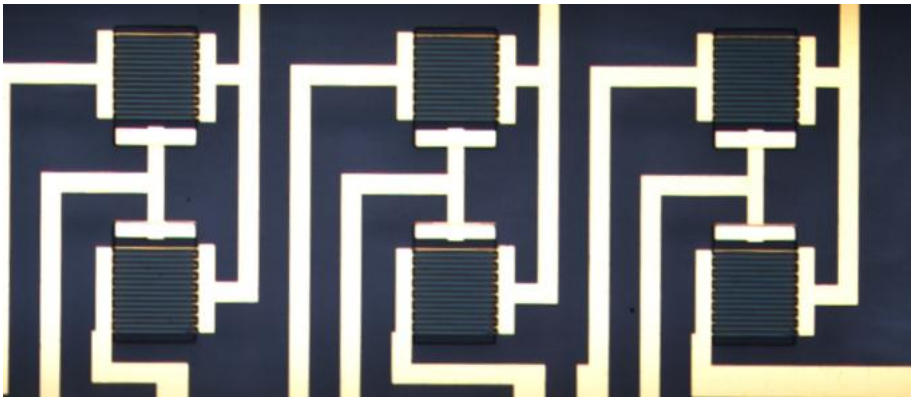

Figure 4.14: Optical image of $Cu_3(HHTP)_2$ thin film on chip with IDEs.

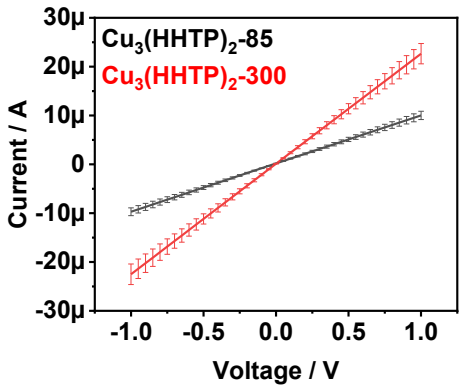

Figure 4.15: Averaged I-V plots of 24 devices on the same chip annealed at 85°C and 300°C, respectively.

The electrical characteristics of EG-FETs based on $Cu_3(HHTP)_2$ thin films were evaluated using a three-electrode configuration (source, drain, and gate electrodes) in various electrolytes: 1, 5, and 10 mM phosphate buffer solutions with a pH of 7.4. **Figure 4.16a** shows the device configuration of EG-FETs, while **Figure 4.16b** represents the wire-bonded and encapsulated chip. The chip was mounted on a custom-built measurement board, as illustrated in **Figure 4.17**. In these experiments, an Ag/AgCl pellet was used as the gate electrode. Measurements were carried out on a Keithley 4200 semiconductor characterization system. The drain-source voltage (V_{ds}) was kept constant at 0.1 V, while the gate-source voltage (V_{gs}) was varied from -0.2 V to 0.2 V and then from 0.2 V back to -0.2 V, with a step size of 2 mV. Two types of chips were

characterized: (i) those annealed at 85°C, referred to as EG-FET-85, and (ii) those annealed at 300°C, referred to as EG-FET-300.

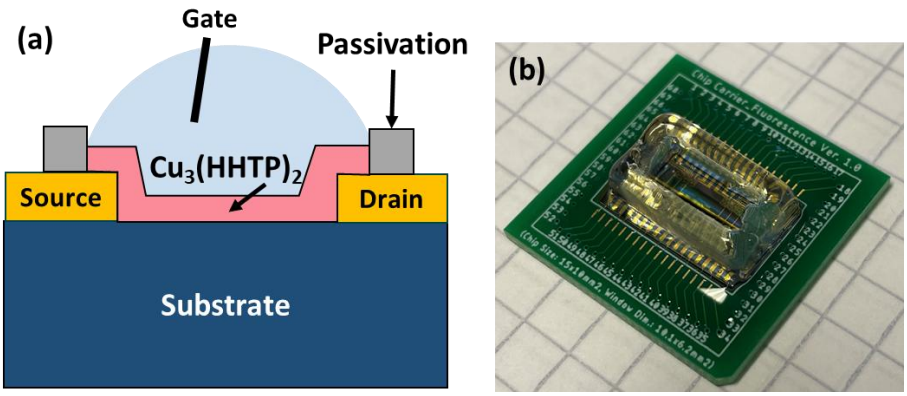

Figure 4.16: (a) Schematic illustration of device configuration of electrolyte-gated field-effect transistor using $Cu_3(HHTP)_2$ thin film as channel material. (b)Wire-bonded and encapsulated $Cu_3(HHTP)_2$ thin-film chip on a printed circuit board (PCB) for the measurements in liquid environments.

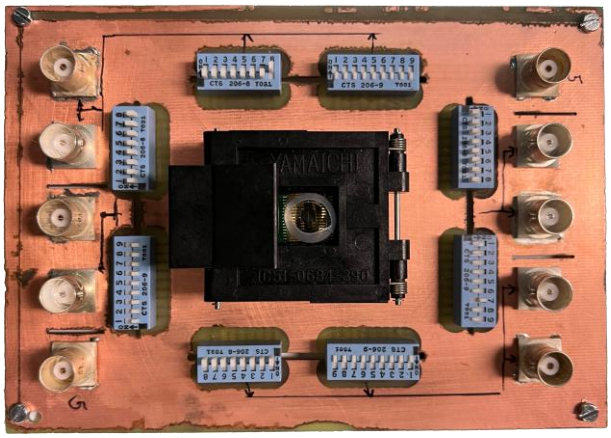

Figure 4.17: Custom-built measurement board.

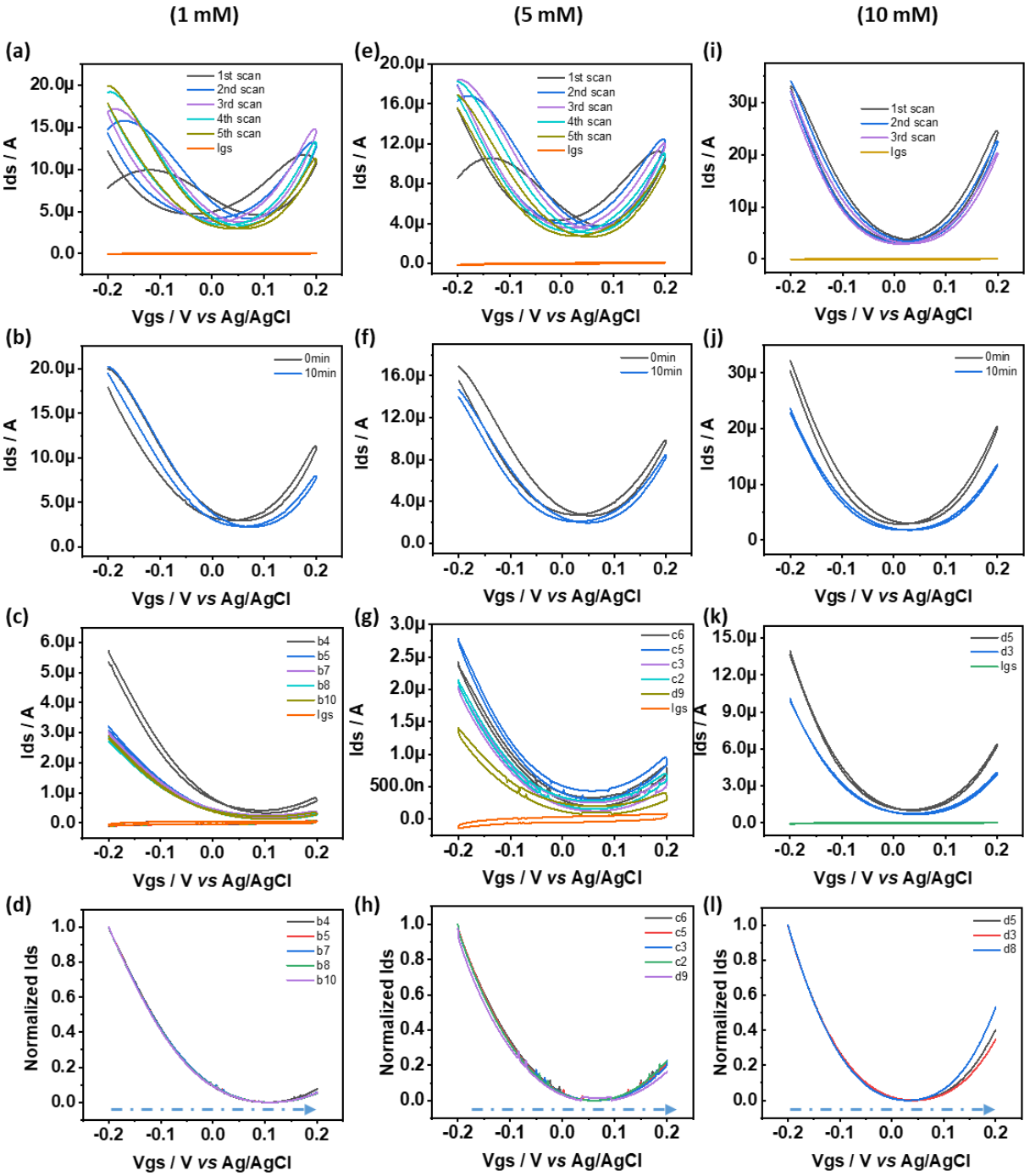

Figure 4.18: Transfer characteristics of EG-FET-85 in 1, 5 and 10 mM phosphate buffer solutions. (a, e, and i) Consecutive dual scans after the addition of electrolytes, (b, f, j) comparison of transfer curves at 0 and 10 minutes, (c, g and k) transfer characteristics of other devices on the same chip, (d, h and l) normalized forward transfer characteristics.

4.5.1 EG-FET-85

In the initial phase of the experiment, the EG-FET-85 devices were tested in a 1 mM phosphate buffer solution. Following the introduction of the electrolyte, five consecutive scans were performed. As shown in **Figure 4.18a**, the first scan displayed significant hysteresis, but by the third scan, the system reached equilibrium with only minimal hysteresis. The leakage current

(I_{gs}) remained below 100 nA across all measurements. **Figure 4.18b** highlights a positive shift in the charge neutrality point (CNP), which is the potential where the current is minimal. This shift is likely due to the low concentration of the electrolyte, requiring a longer diffusion time for ion movement. Further investigation of additional devices on the same chip (**Figure 4.18c**) confirmed similar characteristics, although with relatively lower drain-source currents (I_{ds}). These observations are more pronounced in the normalized plots of the forward scans (from -0.2 to 0.2 V), which show perfect overlap, as seen in **Figure 4.18d**. The same characterizations were also performed using 5 and 10 mM phosphate buffer solutions, with results displayed in **Figures 4.18e-h** and **Figures 4.18i-l**, respectively. **Figures 4.19a** and **4.19b** compare the initial I_{ds}-V_{gs} scans after introducing the 1, 5, and 10 mM phosphate buffer solutions. The transfer characteristics in low-concentration electrolytes (1 and 5 mM) show similar behaviour, marked by significant hysteresis. In contrast, in the 10 mM electrolyte, a nearly perfect ambipolar transfer characteristic is observed. [125] After twenty minutes, the final I_{ds}-V_{gs} scans (**Figures 4.19c** and **4.19d**) show that all devices exhibit typical ambipolar behaviour, with steeper slopes at higher ionic strengths. **Figure 4.20** illustrates the hysteresis behaviour of $Cu_3(HHTP)_2$ thin film-based EG-FET-85 devices in 1, 5, and 10 mM sodium phosphate electrolytes. These results suggest that the observed effects are consistent with typical capacitive gating. Additionally, **Figures 4.18b**, **18f**, and **18j** demonstrate that the CNP potential shifts positively in 1 and 5 mM electrolytes, while no significant shift is observed in the 10 mM electrolyte, except for a current drift to a lower amplitude, which is also apparent in the lower concentration electrolytes. This indicates that a stable gate potential distribution can be achieved more rapidly at higher ionic strengths. Finally, **Figures 4.18d**, **18h**, and **18l** show the normalized transfer characteristics obtained in 1 mM, 5 mM, and 10 mM electrolytes, respectively. As depicted in **Figure 4.21**, the negative potential shift of the CNP becomes more evident at higher electrolyte concentrations.

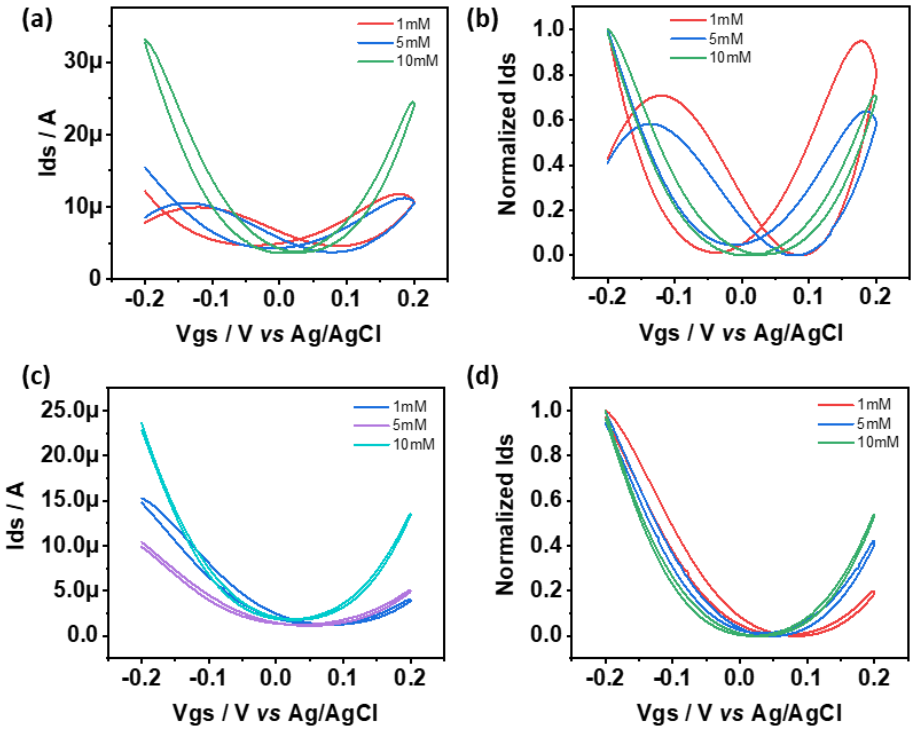

Figure 4.19: Comparison of transfer characteristics after the addition of phosphate buffer solution with different concentrations. Initial scans: (a) normal plots and (b) normalized plots. After 10 minutes: (c) normal plots and (d) normalized plots.

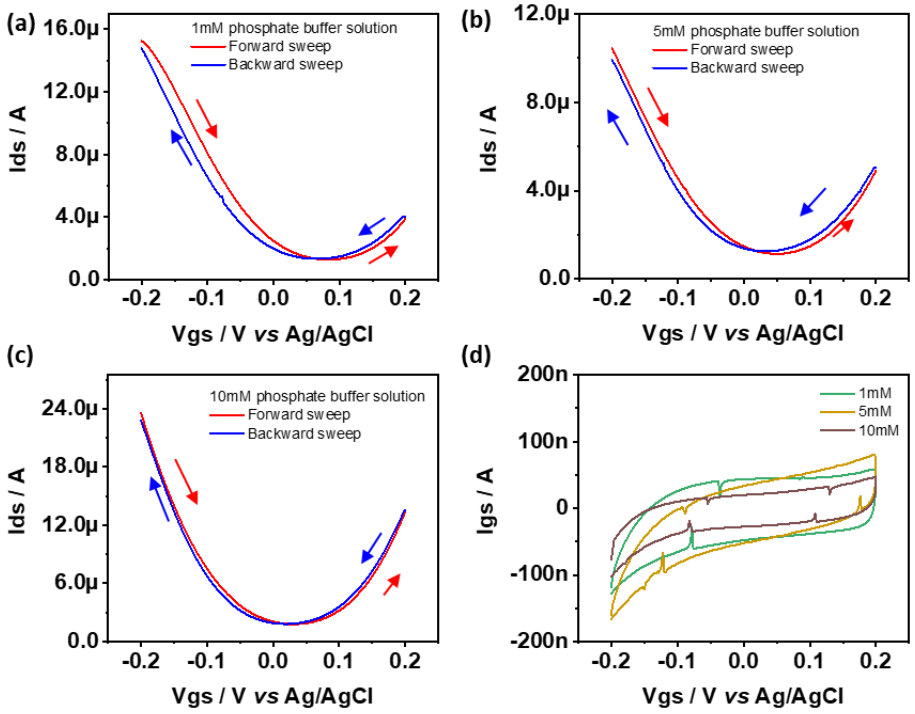

Figure 4.20: Hysteresis behaviors of EG-FET-85 devices stabilized for 10 minutes in phosphate buffer solutions (a) 1 mM, (b) 5 mM and (c) 10 mM. (d) Leakage current in 1, 5 and 10 mM, respectively.

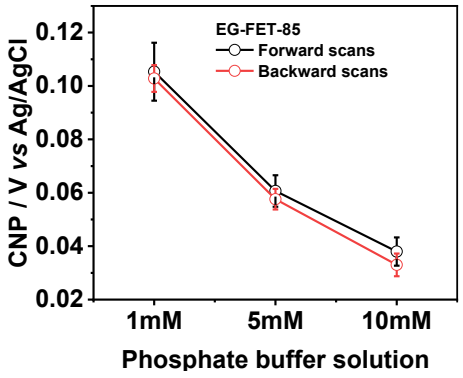

Figure 4.21: Comparison of CNP of EG-FET-85 devices stabilized for 10 minutes in 1, 5 and 10 mM phosphate buffer solutions, respectively.

4.5.2 EG-FET-300

To assess the impact of RTP on the performance of EG-FETs, a similar characterization was carried out on EG-FET-300 devices, which had undergone thermal annealing at 300°C. The transfer curves obtained from these devices were compared across 1, 5, and 10 mM phosphate buffer solutions, as shown in **Figures 4.22a** and **4.22b**. The results mirrored those observed in EG-FET-85 devices, with more pronounced ambipolar behaviour and reduced hysteresis at higher electrolyte concentrations. After a 20-minute stabilization period, further measurements revealed a decrease in hysteresis, especially at higher phosphate buffer concentrations, along with a negative shift in CNP, as illustrated in **Figures 4.22c** and **4.22d**. The comparison of CNP potentials in **Figure 4.23** highlights that the EG-FET-300 devices exhibited a lower CNP potential (83 mV) in 1 mM phosphate buffer solution compared to the EG-FET-85 devices (105 mV) under the same conditions. At higher concentrations (5 mM and 10 mM), the CNP potentials for both EG-FET-85 and EG-FET-300 devices were nearly identical, with only minor differences observed. Importantly, the device-to-device variation in CNP potentials was significantly reduced in EG-FET-300 devices, indicating enhanced reproducibility, as shown **in Figure 4.24**. This improved consistency is a key benefit of RTP in stabilizing the performance of these devices. Additionally, the reduction in hysteresis with increasing phosphate buffer concentration is detailed in **Figures 4.25a-c**. Moreover, the I_{gs} *vs* V_{gs} characteristics for the EG-FET-300 devices displayed quasi-rectangular curves typical of electrical double-layer (ECL) capacitors, as seen in **Figure 4.25d**. These curves were accompanied by a relatively low leakage current, particularly at higher concentrations, further supporting the conclusion that capacitive gating is the primary mechanism driving the ambipolar behaviour of $Cu_3(HHTP)_2$-based EG-FETs. These findings demonstrate that RTP enhances the electrical performance and consistency of EG-FET devices by improving the crystallinity and electrical contact of the

$Cu_3(HHTP)_2$ thin films. Nevertheless, the hysteresis is more pronounced in EG-FET-300 devices as increased CNP difference between forward scans and backward scans shown in **Figures 4.21** and **4.23**.

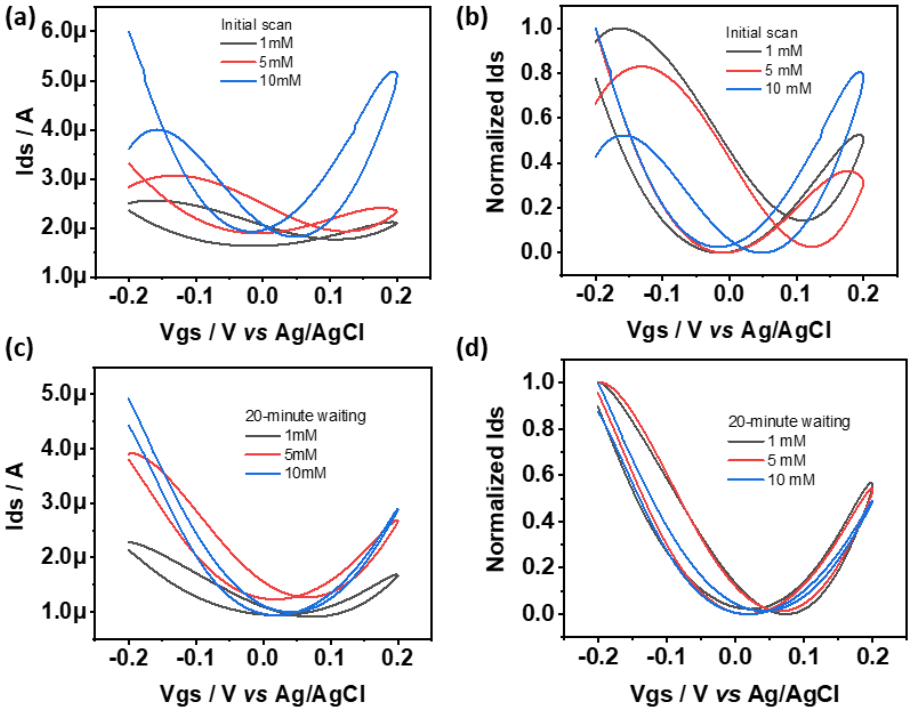

Figure 4.22: Transfer characteristics of EG-FET-300 chips. (a) Transfer characteristics of the initial scans in 1, 5 and 10 mM phosphate buffer solutions, respectively. (b) Corresponding normalized plots for comparison. (c) Transfer characteristics after 20-minute waiting in 1, 5 and 10 mM phosphate buffer solutions, respectively. (d) Corresponding normalized plots for comparison.

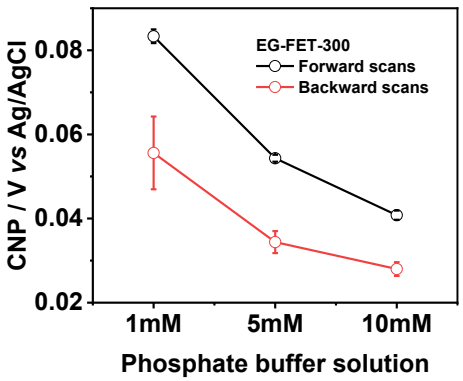

Figure 4.23: Comparison of CNP of EG-FET-300 in 1, 5 and 10 mM phosphate buffer solutions, respectively.

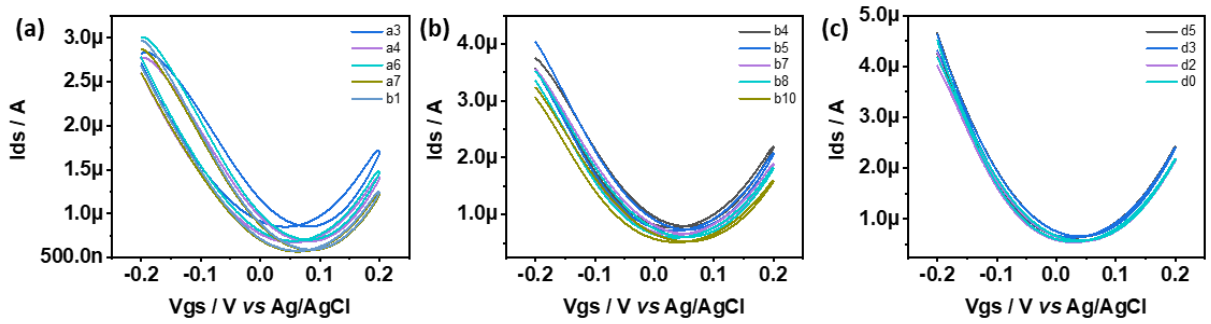

Figure 4.24: Device-to-device variation of EG-FET-300 chips in (a) 1mM, (b) 5mM and (c) 10mM phosphate buffer solutions, respectively.

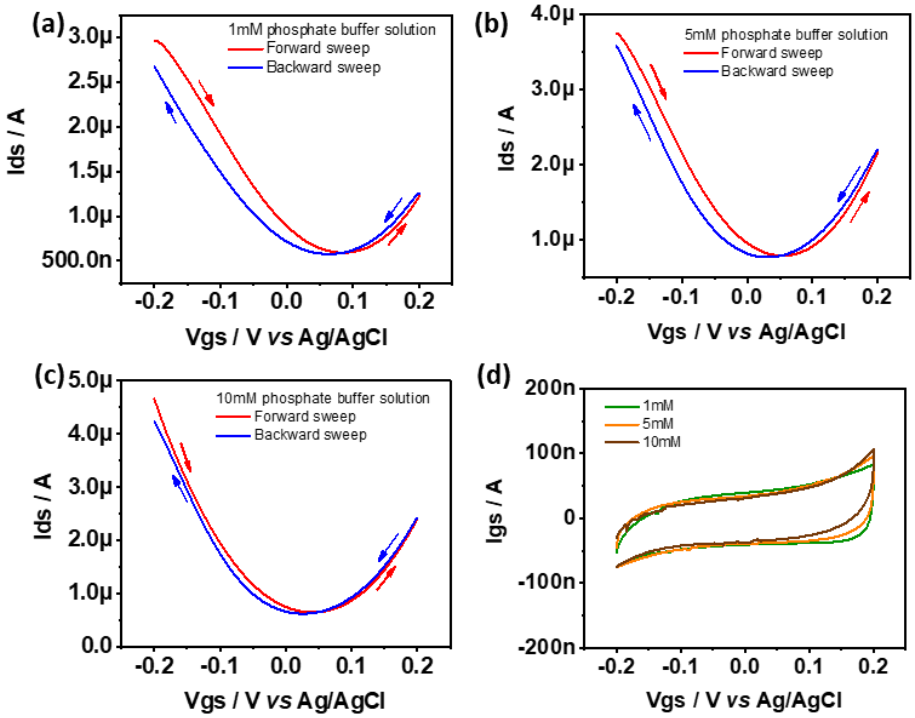

Figure 4.25: Hysteresis behaviors of EG-FET-300 chips in phosphate buffer solutions (a) 1 mM, (b) 5 mM and (c) 10 mM. (d) Leakage current in 1, 5 and 10 mM, respectively.

4.6 Discussion

To further explain the transfer characteristics of $Cu_3(HHTP)_2$ thin film-based EG-FETs in phosphate buffer solutions with varying concentrations, the corresponding ionic strength, Debye length and ECL capacitance are calculated using **Equations 4-1**, **4-2** and **4-3**, respectively. The results are summarized in **Table 4-1**.

$$c_0 = \frac{1}{2}\Sigma_i c_i z_i^2 \qquad 4\text{-}1$$

$$\lambda_D = k^{-1} = \sqrt{\frac{\varepsilon\varepsilon_0 k_B T}{2c_0 e^2}} \quad 4\text{-}2$$

$$C = \frac{\varepsilon\varepsilon_0}{\lambda_D} A \quad 4\text{-}3$$

Where c_i is the concentration of the ions. z_i is the corresponding charge. c_0 is ionic strength. ε is the dielectric constant of H_2O at 20ºC. ε_0 is the vacuum permittivity. k_B is the Bolzmann constant. T is the temperature in Kelvin. e is the elemental charge. λ_D is the Debye length. A is the gating area. C is the electrical double layer capacitance.

Table 4-1: Ionic strength, Debye length and EDL capacitance of 1, 5 and 10 mM phosphate buffer solutions, respectively.

Concentration (mM)	Ionic strength ($mol \cdot m^{-3}$)	Debye length (nm)	EDL capacitance (nF)
1	2.51	6.1	7.0
5	12.54	2.7	15.6
10	25.08	1.9	22.3

The ionic strength of a phosphate buffer solution is directly proportional to the concentration of ions present, as depicted in **Figure 4.26a**. As the concentration of ions increases, so does the ionic strength, leading to significant changes in the electrochemical properties of the system. One key consequence of this increased ionic strength is a reduction in the Debye length, which occurs due to the enhanced screening effect provided by the larger EDL capacitance, as illustrated in **Figure 4.26b. Figure 4.26c** provides a visual representation of the EDLs formed at the electrolyte-solid interfaces in 1, 5, and 10 mM phosphate buffer solutions. The thickness of the EDL, which includes both the compact layer and the diffuse layer, decreases with increasing ionic strength. [167] This behaviour is consistent with the Debye-Hückel model, which describes how higher ionic concentrations lead to a more compact and thinner EDL. A thinner and more compact EDL results in a more effective potential drop across the electrolyte-solid interface. This, in turn, leads to a negative shift in CNP observed in EG-FET devices. Additionally, the increase in ionic strength contributes to a reduction in hysteresis. This reduction occurs because a more concentrated electrolyte allows for faster redistribution of charges and potential, resulting in a more stable and efficient response from the EG-FETs. These observations underscore the critical role of ionic strength in tuning the electrical characteristics of EG-FETs, particularly

in terms of controlling the CNP and minimizing hysteresis, which are crucial for optimizing device performance.

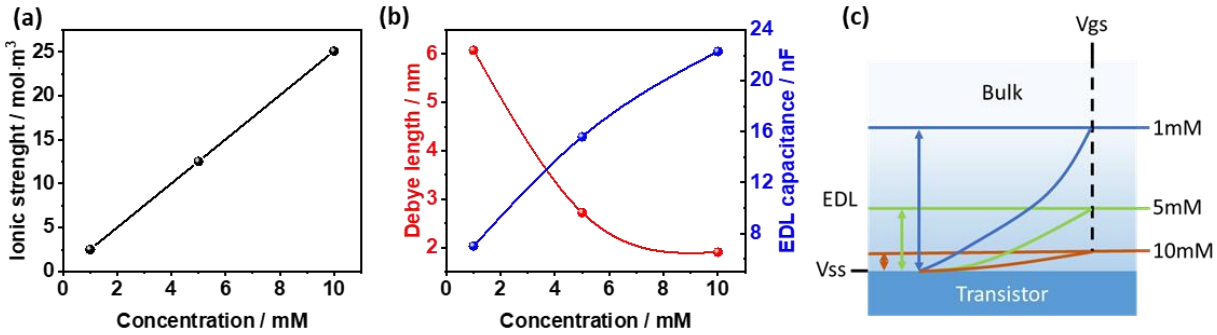

Figure 4.26: (a) Plot of Ionic strength against concentration of phosphate buffer solution. (b) Plots of Debye length and EDL capacitance against the concentration of phosphate buffer solution. (c) Schematic illustration of EDLs at electrolyte-solid interfaces and corresponding surface potential distribution.

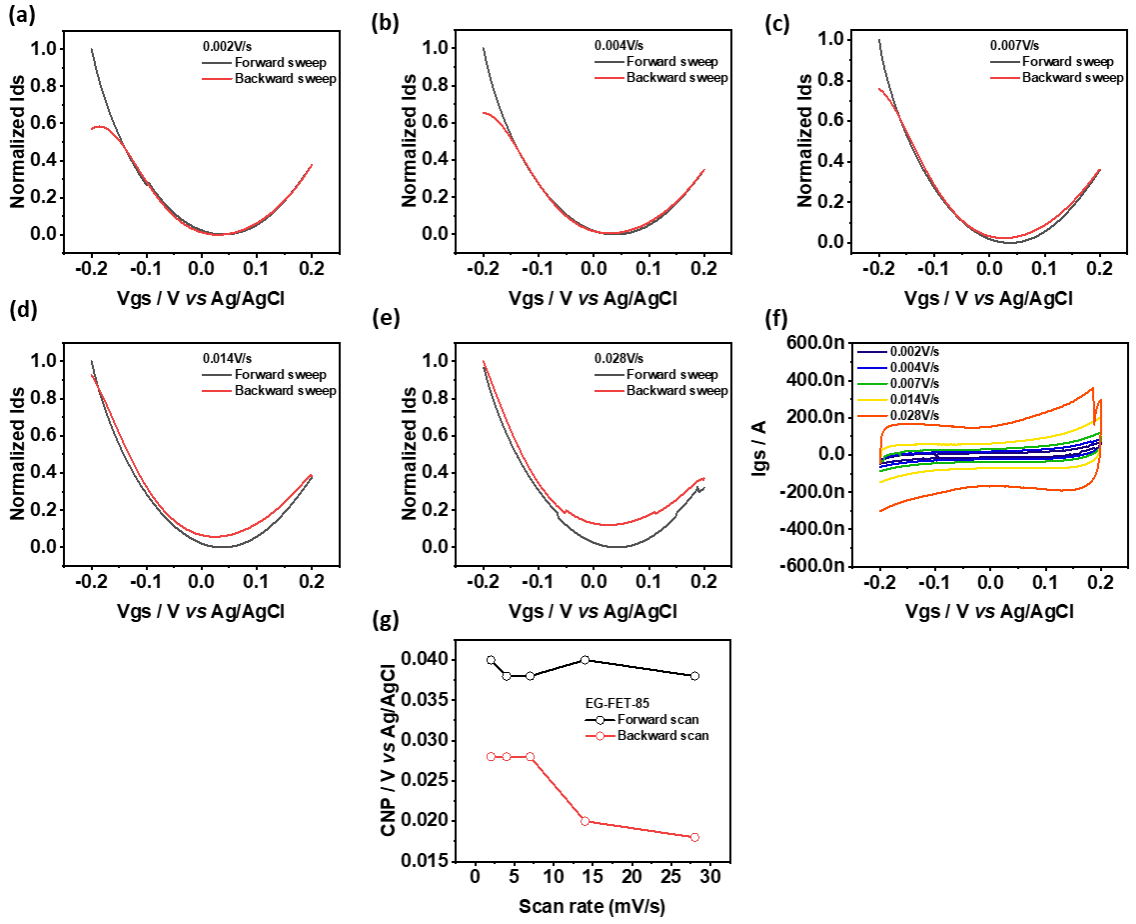

Figure 4.27: Hysteresis study of EG-FET-85 devices at varying scan rates. (a-e) I_{ds}-V_{gs} plots, (f) I_{gs}-V_{gs} plots, (g) Hysteresis.

To further validate our hypothesis regarding the capacitive gating mechanism, we investigated the transfer characteristics of EG-FET-85 devices across a range of scan rates. Specifically, the scan rates varied from 0.002 V/s to 0.028 V/s, as illustrated in **Figures 4.27a-e**. The results

reveal a clear trend: as the scan rate increases, the hysteresis in the transfer characteristics becomes more pronounced, particularly at higher rates like 0.014 and 0.028 V/s. This enhanced hysteresis can be attributed to the limited time available for the redistribution of the gate potential at faster scan rates, which further supports the notion of a capacitive gating mechanism governing the device behaviour. **Figure 4.27g** provides a plot of CNP extracted from both the forward and backward scans at each scan rate. The observed increase in hysteresis with higher scan rates corroborates the hypothesis that capacitive effects are at play, as the device struggles to maintain equilibrium at faster voltage sweeps. In addition to this, the response of EG-FET-85 devices to a 10 mM phosphate buffer solution with varying pH levels was examined, as shown in **Figure 4.28**. The results demonstrate a continuous negative shift in the CNP as the pH decreases, suggesting that the EG-FET-85 device has the potential to function as a pH sensor. This pH sensitivity is likely due to the protonation or deprotonation of functional groups on the $Cu_3(HHTP)_2$ thin film, which alters the surface potential and, consequently, the CNP. These findings not only reinforce the role of capacitive gating in the operation of EG-FETs based on $Cu_3(HHTP)_2$ thin films but also highlight the potential application of these devices in pH sensing, expanding their utility in electrochemical sensing technologies.

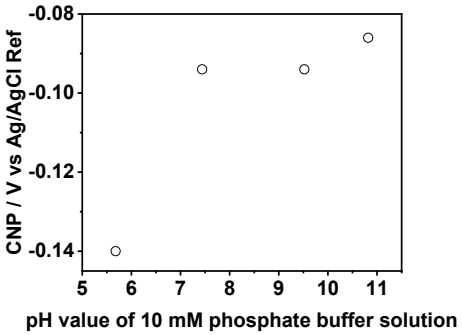

Figure 4.28: Shift of CNP of EG-FET-85 devices responding to varying pH values of 10 mM phosphate buffer solutions.

4.7 Summary

This chapter outlines the development of a standardized fabrication process for the on-chip integration of $Cu_3(HHTP)_2$ thin films, achieved through a combination of microfabrication techniques and LPE growth. Fundamental electrical characterizations revealed that the highest intrinsic conductivity and lowest contact resistance were attained after annealing at 300°C for 15 seconds in an Ar atmosphere. EG-FET-300 chips demonstrated superior reproducibility compared to those annealed at 85°C. Additionally, hysteresis behaviour was analyzed in phosphate buffer solutions of varying concentrations and scan rates, which indicate a capacitive gating

mechanism predominantly governs the ambipolar transport in $Cu_3(HHTP)_2$ thin-film-based EG-FETs.

5 Phthalates detection

This chapter introduces two impedimetric sensors based on MOF thin-film electronics designed for the detection of phthalates in liquid environments using EIS. Initially, the detection capability is demonstrated with a Ni-(BDC-NH_2) thin film as the transducer, though its sensitivity is limited to concentrations no higher than 1 $mg \cdot L^{-1}$ due to its poor conductivity. To enhance sensing performance, a semiconducting transducer using a $Cu_3(HHTP)_2$ thin film is employed, showing significant improvement. To systematically assess the sensor's performance and elucidate the detection mechanisms, the responses of $Cu_3(HHTP)_2$ thin film-based impedimetric sensors were studied against 11 different phthalates and their metabolites.

5.1 Background

Phthalates, also known as phthalic acid esters, are a family of plasticizers widely used in both consumer and industrial products. The general molecular structure of phthalates, along with the 11 targeted analytes, is illustrated in **Figure 5.1**. These phthalates share a common structural feature: a single aromatic ring with two adjacent ester groups. The variation among them lies in the side groups (R and R'), which can differ, resulting in either symmetrical or asymmetrical configurations.

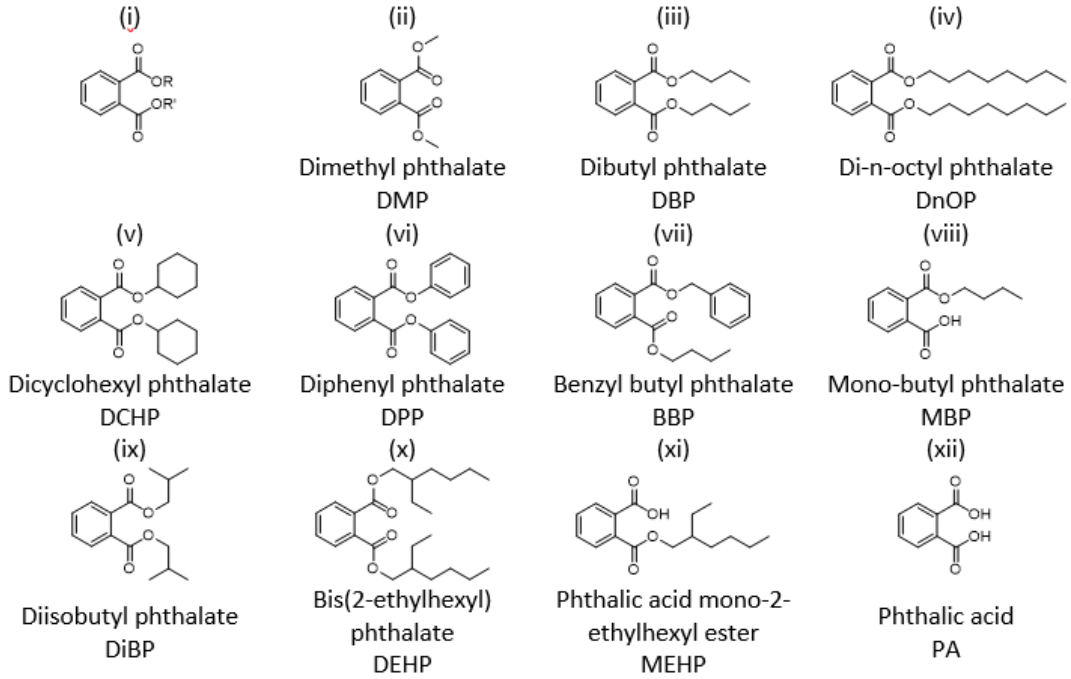

Figure 5.1: (i) General molecular structure of phthalates. (ii-xii) Targeted analytes.

Chapter 5: Phthalates detection

Despite growing awareness of the environmental impacts associated with extensive plastic use, such as white pollution and the proliferation of micro- and nano-plastics, global plastic production continues to rise. According to estimates from Conversio Market & Strategy GmbH and nova-Institute, global plastic production increased from 370.5 million tons in 2018 to 400.3 million tons in 2022, contributing to an accumulation of 4900 million tons of plastic waste in the environment. [167] Two major types of plastic waste, plasticizers and micro-/nano-plastics, pose severe environmental pollution risks and threaten both human and ecological health. [168, 169] Notably, phthalates, which constitute about 65% of plasticizers, are particularly concerning. [170] Phthalates are often not chemically bonded to the polymer matrix, making them prone to leaching into the environment. They have been detected in air, surface and groundwater, soil, and sediments. [171, 172] Exposure to phthalates, whether through inhalation or direct contact, has been linked to a range of adverse health effects. Chang et al. reviewed these potential impacts, noting that chronic exposure to phthalates can lead to significant environmental and health issues, particularly affecting the reproductive system. Phthalates are classified as endocrine-disrupting chemicals (EDCs) due to their interference with the endocrine system. Toxicological studies have highlighted their detrimental effects on various biological processes, including estrogen metabolism, reproductive function, fetal development, carcinogenesis, liver function, nervous system development, and immune system suppression. [170, 173] In response to these concerns, many countries, including those in the EU, US, and China, have enacted regulations to limit the use of certain phthalates as plasticizers. The maximum contamination levels (MCLs) for phthalates in drinking water vary by region, with limits set at 8 $\mu g \cdot L^{-1}$ (EU), 6 $\mu g \cdot L^{-1}$ (US), 8 $\mu g \cdot L^{-1}$ (China), and 6 $\mu g \cdot L^{-1}$ (WHO). [174]

MOFs, known for their porous crystalline structures, have been extensively studied for the removal and detection of phthalates due to their high specific surface area, porosity, and tuneable structures and functionalities. [175, 176] For instance, Khan et al. reported the pioneering application of ZIF-8 in the removal of phthalic acid (PA) and diethyl phthalate (DEP) from aqueous solutions. [175] ZIF-8 demonstrated a significantly higher adsorption capacity (> 500 $mg \cdot g^{-1}$) for PA compared to commercial sorbents like activated carbon and other MOFs such as MIL-53(Cr), MIL-101(Cr), MIL-100(Fe), MIL-100(Cr), NH_2-MIL-100(Cr), UiO-66, and NH_2-UiO-66. This enhanced performance is attributed to the stronger electrostatic interactions between the positively charged ZIF-8 and the negatively charged PA anions in aqueous solutions. However, the adsorption capacity of ZIF-8 for DEP (< 50 $mg \cdot g^{-1}$) is considerably lower than for PA, due to DEP's minimal charge in water. Li et al. synthesized three aluminium-based MOFs, MIL-

53AIO, MIL-53AIOH, and MIL-53BM, using water-insoluble metal sources (alumina, aluminium hydroxide, and boehmite) for the removal of dimethyl phthalate (DMP) from aqueous solutions. [176] These MOFs exhibited significantly higher adsorption capacities (MIL-53AIO: 206.2 $mg \cdot g^{-1}$; MIL-53AIOH: 192.1 $mg \cdot g^{-1}$; MIL-53BM: 189.9 $mg \cdot g^{-1}$) compared to MIL-53AIN synthesized from water-soluble aluminium nitrate (120.2 $mg \cdot g^{-1}$). This improvement is attributed to the enhanced stability of the MOFs. The adsorption capacity of these MIL-53(Al) variants for DMP is due to π-π stacking interactions between the aromatic rings of the host and guest molecules and the size-matching effect of DMP (7.8 x 6.0 $Å^2$) with the pore size (8.5 Å) of MIL-53(Al). Additionally, defective MOFs have been explored for phthalate adsorption and removal. For example, Qiao et al. investigated a series of defective MOFs. [177, 178] By controlling the number of defects in UiO-67 through the addition of a benzoic acid (BA) regulator, they found that UiO-67-30BA (with 30 times the molar number of ligands) exhibited the highest number of missing linkages and specific surface area, resulting in the highest adsorption capacity (228.1 $mg \cdot g^{-1}$) for DMP.

In addition to their direct applications for phthalate adsorption, MOFs have been extensively explored as absorbents for chromatographic analysis techniques, such as gas chromatography (GC) and high-performance liquid chromatography (HPLC). Their ability to preconcentrate or enrich phthalates from environmental samples can extend the limit of detection in chromatography. [179-184] This section focuses specifically on novel techniques for phthalate detection using MOFs, excluding their use as chromatographic sorbents or carriers for fluorophores. Wu et al. pioneered the application of MOFs for phthalate detection by employing a luminescent 3-D zinc-MOF as an indicator for various phthalates. [185] In this study, linear responses were observed for diethyl phthalate (DEP), dibutyl phthalate (DBP), and di-n-octyl phthalate (DnOP) within the concentration ranges of 1 mM to 10 mM, 0.7 mM to 2.1 mM, and 0.5 mM to 2 mM, respectively. However, the study did not address the sensitivity, selectivity, or limit of detection. Recently, Surface-Enhanced Raman Scattering (SERS) methods have been utilized with MOF composites, such as UIO-66@Ag nanoparticles, ZIF-67@Ag nanowires, and AuNSs@ZIF-67, for phthalate detection. [186-188] For instance, Xu et al. demonstrated the recognition and quantitative analysis of six types of phthalates using functionalized ZIF-67@Ag nanowires as a SERS substrate. The Raman signals for phthalate detection were enhanced by the "sharp tip effect" of the rough Ag nanowires and the exceptional adsorption capacity of ZIF-67, which captures targeted molecules into the electromagnetic field. The SERS spectra revealed characteristic peaks for different phthalates, facilitating their recognition and differentiation. ZIF-67@Ag nanowires

successfully detected six phthalate esters with wide linear ranges, low detection limits, and excellent repeatability and stability. Despite these advancements, electrochemical sensors based on MOFs for phthalate detection have not yet been reported. This represents a promising area for future research, leveraging the unique structural advantages of MOFs, such as tuneable pore sizes and functionalities, alongside the benefits of electrochemical sensors, including high sensitivity, good selectivity, simple sample preparation, portability, and cost-effective real-time analysis.

5.2 Methods

5.2.1 Fabrication of Ni-(BDC-NH_2) thin-film devices

Ni-(BDC-NH_2) thin-film devices were fabricated using LbL-LPE combined with an automated microfluidics platform at room temperature, employing ethanol as the solvent, as described in **Section 2.3**. In this process, Ni-(BDC-NH_2) thin films were deposited onto prefabricated microelectrode chips with interdigitated electrodes (IDEs) through twenty LbL cycles, as outlined in **Section 4.1**. The chips were then annealed at 85°C in an argon atmosphere for 30 minutes and subsequently stored in a nitrogen chamber. Prior to conducting detection experiments, the chips were wire-bonded and encapsulated.

5.2.2 Fabrication of $Cu_3(HHTP)_2$ thin-film devices

$Cu_3(HHTP)_2$ thin-film chips were fabricated using LbL-LPE combined with an automated dip coater at room temperature, utilizing ethanol as the solvent, as discussed in **Section 2.4**. In this process, $Cu_3(HHTP)_2$ thin films were deposited onto the same chips described in **Section 4.1**, through ten LbL cycles. The chips were then subjected to a sequential annealing process: first at 85°C in an argon atmosphere for 30 minutes, followed by 15 seconds at 300°C. After annealing, the chips were stored in a nitrogen chamber. Prior to conducting detection experiments, the chips were wire-bonded and encapsulated.

5.2.3 Preparation of Phthalates solutions

Considering the stability of MOFs in different solvents. Phthalates solutions were prepared in two different solvents: (i) pure ethanol, denoted as control solution 1 and (ii) 1% (v) ethanol spiked distilled H_2O, denoted as control solution 2.

Control solution 1 as a solvent

DiBP (DiBP = diisobutyl phthalate) solutions were prepared with a series of concentrations ranging from 100 $\mu g \cdot L^{-1}$ to 1000, 5000, 10000 and 20000 $\mu g \cdot L^{-1}$. The sensing performance of Ni-(BDC-NH_2) thin-film devices was evaluated using these solutions.

Control solution 2 as a solvent

Analyte solutions of the chemicals presented in **Figure 5.1** were prepared with concentrations ranging from 0.01 $\mu g \cdot L^{-1}$ to 0.1, 1, 10, 100, and 1000 $\mu g \cdot L^{-1}$. The sensing performance of $Cu_3(HHTP)_2$ thin-film devices were assessed with these solutions.

5.2.4 Electrochemical impedance spectroscopy

Ni-(BDC-NH_2) thin-film sensors

EIS measurements were conducted on a portable potentiostat (Pico Emstat, PalmSens) from 1 KHz to 200 KHz with an AC potential of 50 mV.

$Cu_3(HHTP)_2$ thin-film sensors

EIS spectra were collected on an Impedance Analyzer (SI 1840) from 100 Hz to 1 MHz with an AC potential of 50 mV.

5.3 Results and discussion

5.3.1 Ni-(BDC-NH_2) thin-film sensor

To demonstrate the capabilities of Ni-(BDC-NH_2) thin-film sensors for phthalates detection, DiBP was selected as the target for performance evaluation using ethanol as solvent. **Figure 5.2a** presents the flow direction and layout of four blocks on a single chip. Ni-(BDC-NH_2) thin films with 20 LbL cycles were deposited using liquid-phase epitaxy. Initially, the homogeneity of the grown Ni-(BDC-NH_2)-20c thin films were characterized. **Figure 5.2b** shows four optical images captured on each block. The comparable optical contrast (or color) of the regions with IDEs indicates a uniform growth of Ni-(BDC-NH_2)-20c thin films along the confined micro-fluidic channel, which is further approved by a zoomed-in optical image shown in **Figure 5.2c**. Furthermore, as shown in **Figure 5.3**, high-resolution SEM images demonstrate the successful growth of Ni-(BDC-NH_2)-20c thin films on Au microelectrodes, which is favorable of good electrical contact between IDEs and Ni-(BDC-NH_2)-20c thin films.

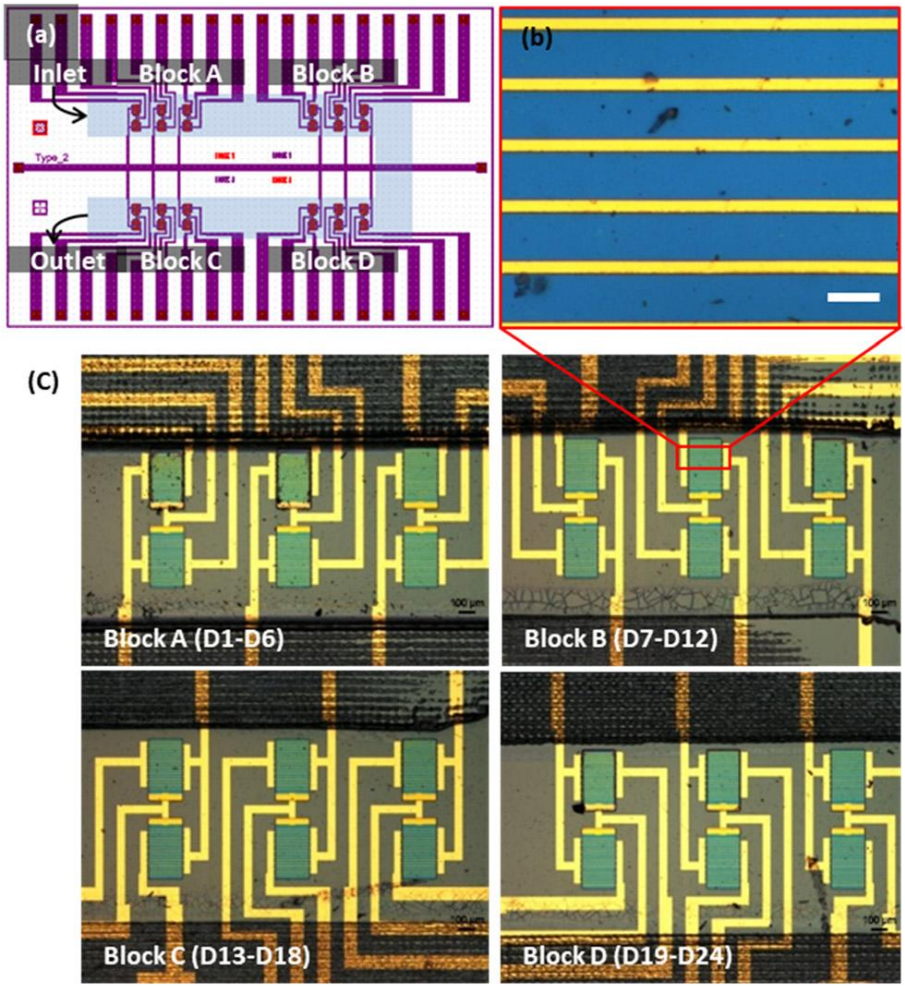

Figure 5.2: Ni-(BDC-NH_2)-20c thin-film sensors. (a) Schematic illustration of four blocks on a single chip. (b) Optical images of four blocks coated with Ni-(BDC-NH_2)-20c thin films in the same microfluidic channel. (c) A zoomed-in optical image of block B. Scale bar: 10 µm.

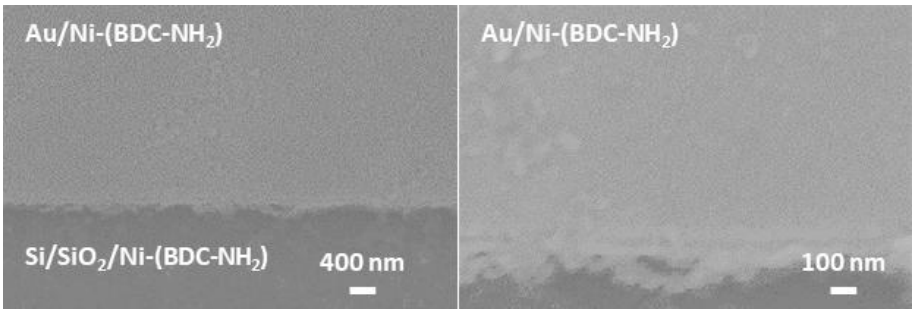

Figure 5.3: High-resolution SEM images of Ni-(BDC-NH_2)-20c thin films grown on Si/SiO_2 substrate and Au microelectrode.

Following, EIS technique with a two-electrode configuration was employed to characterize the impedance amplitude of all 24 devices on the same chip in a dry condition, shown in **Figure 5.4**. 21 of the 24 devices exhibited a close impedance amplitude within the range of a few MΩ, which can be attributed to the insulating properties of Ni-(BDC-NH_2). This illustrates a minimal

inter-device variability, which is advantageous for applications in sensors, including gas sensors, chemical sensors, and biosensors.

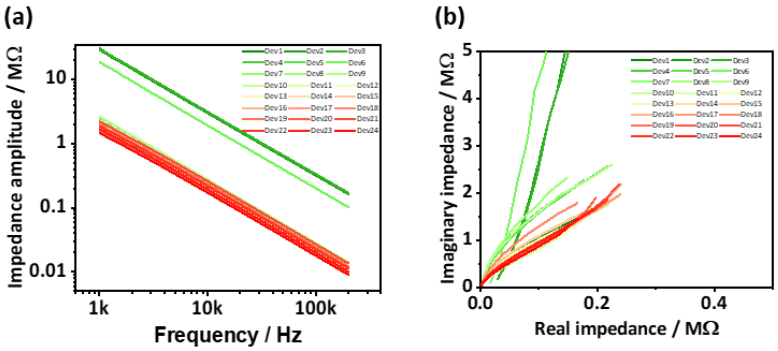

Figure 5.4: Electrochemical impedance spectroscopy characterization of a Ni-(BDC-NH_2)-20c thin-film chip. (a) Bode plots and (b) Nyquist plots of 24 devices.

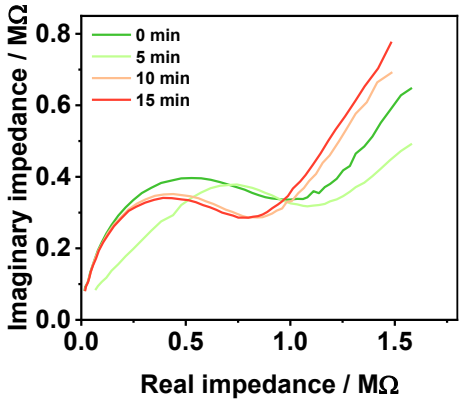

Figure 5.5: EIS spectra collected from one of the Ni-(BDC-NH_2)-20c thin-film devices after incubating in 20 $\mu g \cdot mL^{-1}$ DiBP solution for 5, 10, and 15 minutes, respectively.

After evaluating the homogeneity of Ni-(BDC-NH_2) thin-film chips morphologically and electrically, the sensing performance to DiBP was studied. First of all, the incubation time was studied in 20000 $\mu g \cdot L^{-1}$ DiBP solution, shown in **Figure 5.5.** Only a slight decline in impedance amplitude was observed from 10 to 15 minutes, indicating 15-minute incubation time is optimal, which was kept the same for all the following experiments. Then, the EIS spectra of the responding to DiBP with varying concentrations were recorded. As shown in **Figure 5.6a**, a noteworthy decline in impedance amplitude was observed following exposure to DiBP over a 15-minute period, with a decrease from 1 to 20000 $\mu g \cdot L^{-1}$. This illustrates the effective capacity of Ni-(BDC-NH_2) thin-film devices for the detection of DiBP at the ppm level. Although there is no discernible alteration in impedance amplitude at 100 $\mu g \cdot L^{-1}$ DiBP, this may be indicative of a superior actual limit of detection that surpasses this threshold. Subsequently, the electrical equivalent circuits were simulated and presented in **Figures 5.6b** and **Figures 5.6c**. The electrical circuit comprises four elements: electrical double layer capacitance (C_{dl}), charge transfer

resistance (R_{ct}), constant phase element (*CPE*), and series resistance (R_s). The fitted values for four distinct concentrations on a single Ni-(BDC-NH_2)-20c thin-film device are presented in **Table 5-1**. As R_s, R_{ct}, and C_{dl} demonstrate no notable trend or variation, it can be inferred that the sensing is dependent on the alteration of the *CPE*, which is represented by two parameters: Q (μT) and n. When n equals 1, the system is described by an ideal capacitor; when n equals 0, it is described by a pure resistor. As illustrated in **Figure 5.6d**, a linear correlation between the Q value and DiBP concentration is evident, indicating that this relationship could be exploited for the detection of DiBP. It can be postulated that the observed decrease in impedance following exposure to DiBP is likely due to electron donation from DiBP molecules to Ni-(BDC-NH_2), facilitated by pi-pi interactions and hydrogen bonding between Ni-(BDC-NH_2) and DiBP molecules. This process results in Ni-(BDC-NH_2) becoming more resistive, rather than capacitive, as indicated by the n values listed in **Table 5-1**. [189, 190] Furthermore, the fabricated 2D Ni-(BDC-NH_2) sensor arrays chip exhibited a minor discrepancy in performance between individual devices. **Figure 5.7** presents the EIS spectra of six devices situated at disparate locations on the chip, each exposed to varying concentrations of DiBP.

Table 5-1: Fitted values for four different concentrations of DiBP on the same Ni-(BDC-NH_2) thin-film sensor device.

Concentrations ($\mu g \cdot L^{-1}$)	R_s (Ω)	R_{ct} (Ω)	C_{dl} (nF)	Q (μT)	n
1000	9042	2.97E5	0.013	0.0004	0.682
5000	9069	4.44E5	0.013	0.006	0.498
10000	7062	2.89E5	0.014	0.010	0.488
20000	8014	3.78E5	0.015	0.028	0.464

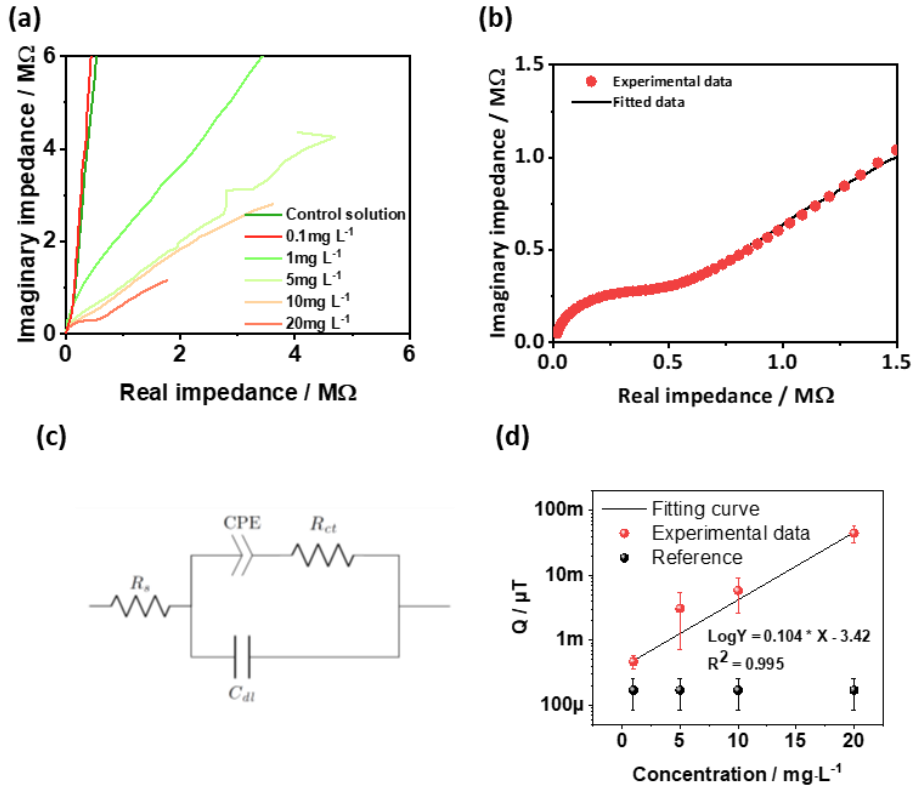

Figure 5.6: Performance of Ni-(BDC-NH_2) thin-film sensor to DiBP. (a) Dose reponse from 0 to 20 µg·mL^{-1}. (b, c) Fitted EIS spectrum and corresponding equivalent electrical circuit. (d) Plot of Q versus the concentration of DiBP.

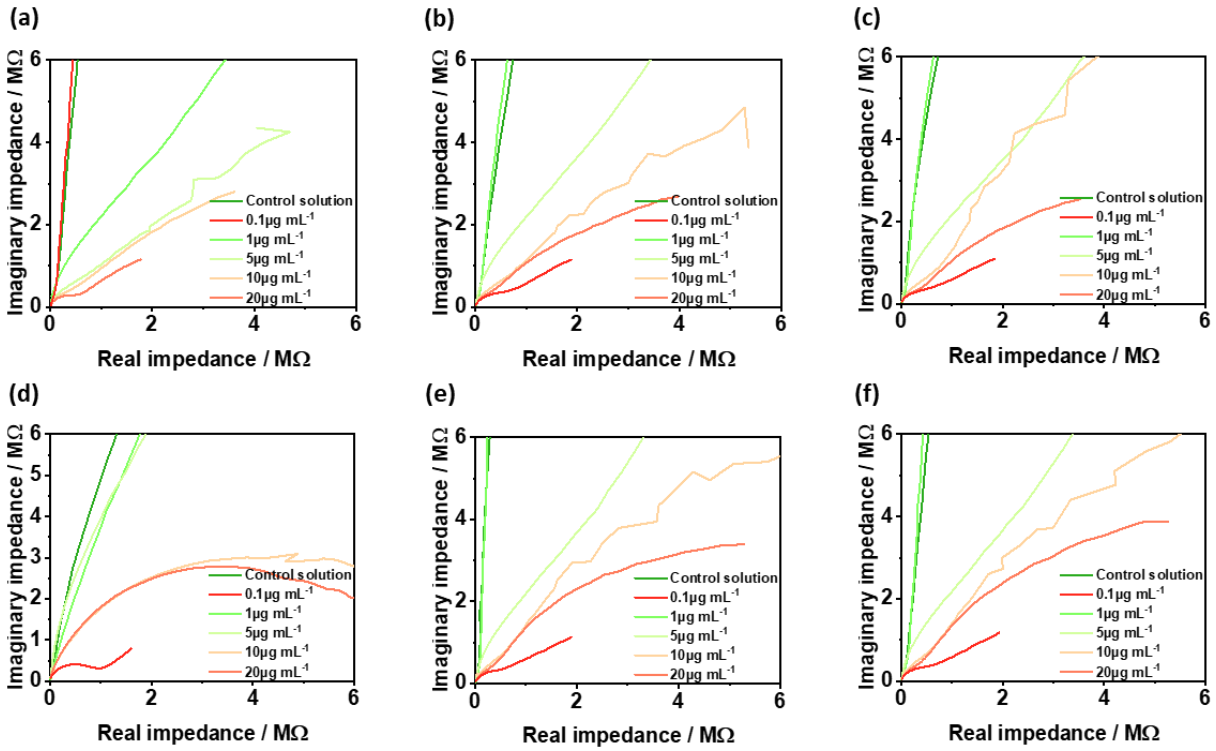

Figure 5.7: Sensor response reproducibility of Ni-(BDC-NH_2)-20c thin-film devices for the detection of DiBP in ethanol. Nyquist plots of 6 different individual devices on a sensor chip are shown here in the graphs.

5.3.2 $Cu_3(HHTP)_2$ thin-film sensor

The fabrication and characterization of $Cu_3(HHTP)_2$-10c thin-film chips were systematically discussed in **Chapter 4**. Thus, this section only focuses on the evaluation of sensing performance of $Cu_3(HHTP)_2$-10c thin-film devices to phthalates. In order to gain a deeper comprehension of the sensing mechanism and to facilitate the design of optimal materials for future studies, 11 types of phthalates and phthalate metabolites were studied, illustrated in **Figure 5.1**. Considering the good stability of $Cu_3(HHTP)_2$ thin films in water and the low solubility of phthalates in water, in this case, a mixed solvent (H_2O:EtOH = 99%:1% (v:v)) was utilized to prepare phthalate solutions. First of all, the drift of impedance of a $Cu_3(HHTP)_2$-10c thin-film device was studied in control solution for 60 minutes. The EIS spectra were collected every 5 minutes. As shown in **Figure 5.8**, a dramatic increase of impedance amplitude was observed after the addition of the control solution. While the increment is getting smaller, and the impedance amplitude reaches a relative equilibrium up to one hour.

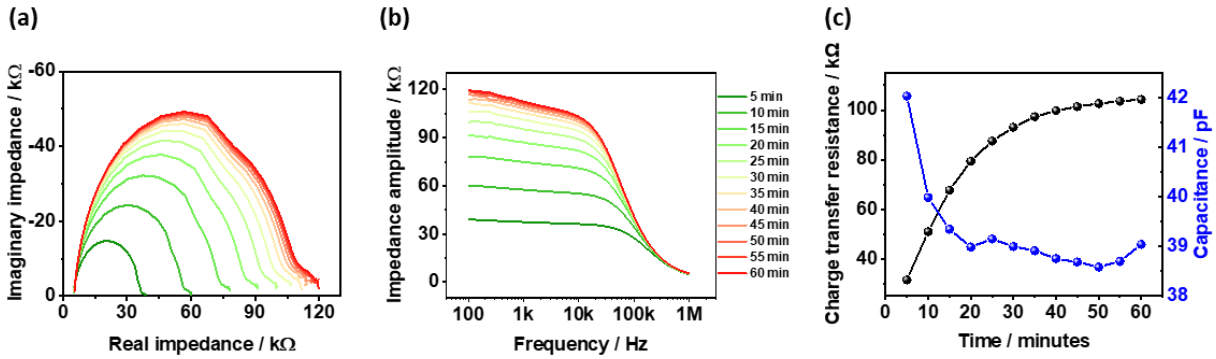

Figure 5.8: Impedance drift of a $Cu_3(HHTP)_2$-10c thin-film device in a control solution (H_2O:EtOH = 99%:1% (v:v)). (a) Nyquist plots. (b) Bode plots. (c) Extracted charge transfer impedance and electrical double layer capacitance.

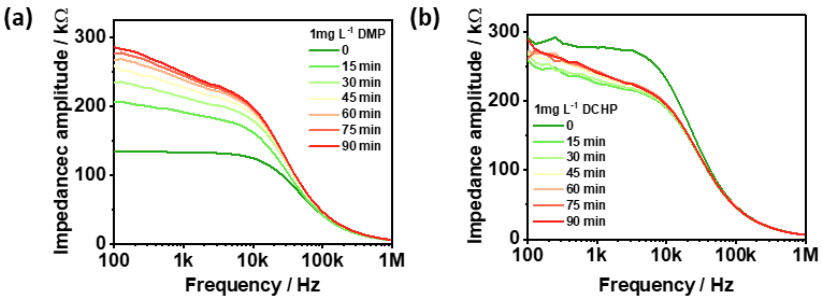

Figure 5.9: Transient EIS analyses of $Cu_3(HHTP)_2$-10c thin-film devices responding to phthalates. (a) 1 mg·L^{-1} DMP. (b) 1 mg·L^{-1} DCHP.

Then, two thirds of the control solution was replaced with phthalate solution with a concentration of 1 mg·L^{-1} or new control solution to avoid the drying effect or the influences caused by solution exchange. EIS spectra were collected every 15 minutes with an incubation time of 90

minutes. **Figure 5.9** presents two representative plots of EIS spectra while $Cu_3(HHTP)_2$-10c thin-film devices responding to phthalates. Some of the phthalates cause an increase of impedance, such as DMP (**Figure 5.9a**). While the others show the opposite impact, such as DCHP (**Figure 5.9b**). Nevertheless, impedance drift was observed on the devices despite the types of phthalates. To better understand the contribution of the adsorption of phthalate molecules, the impedance amplitude of $Cu_3(HHTP)_2$-10c thin-film devices toward phthalate solutions is normalized to the impedance amplitude of $Cu_3(HHTP)_2$-10c thin-film devices to control solution, shown in **Figure 5.10**. **Figure 5.11** presents a change of impedance over time (90 minutes) at selected frequencies (Black: 100 Hz, red: 3162.3 Hz, blue: 10 kHz Hz, green: 79422 Hz and purple: 1 MHz), which could provide the overall information. The responses of $Cu_3(HHTP)_2$-10c thin-film devices reach stable within 60 minutes for most of the phthalates, except MEHP and BBP. Therefore, the incubation was fixed at 60 minutes for comparison. Clearly, we could see the positive responses of $Cu_3(HHTP)_2$-10c thin-film devices to DMP, PA, MEHP, BBP, MBP, DEHP and DiBP, while negative responses to DnOP, DCHP, DPP and DBP at lower frequencies (100, 3162.3 and 10000 Hz). At higher frequencies (79433 and 1000000 Hz), no considerable change is observed, except DMP.

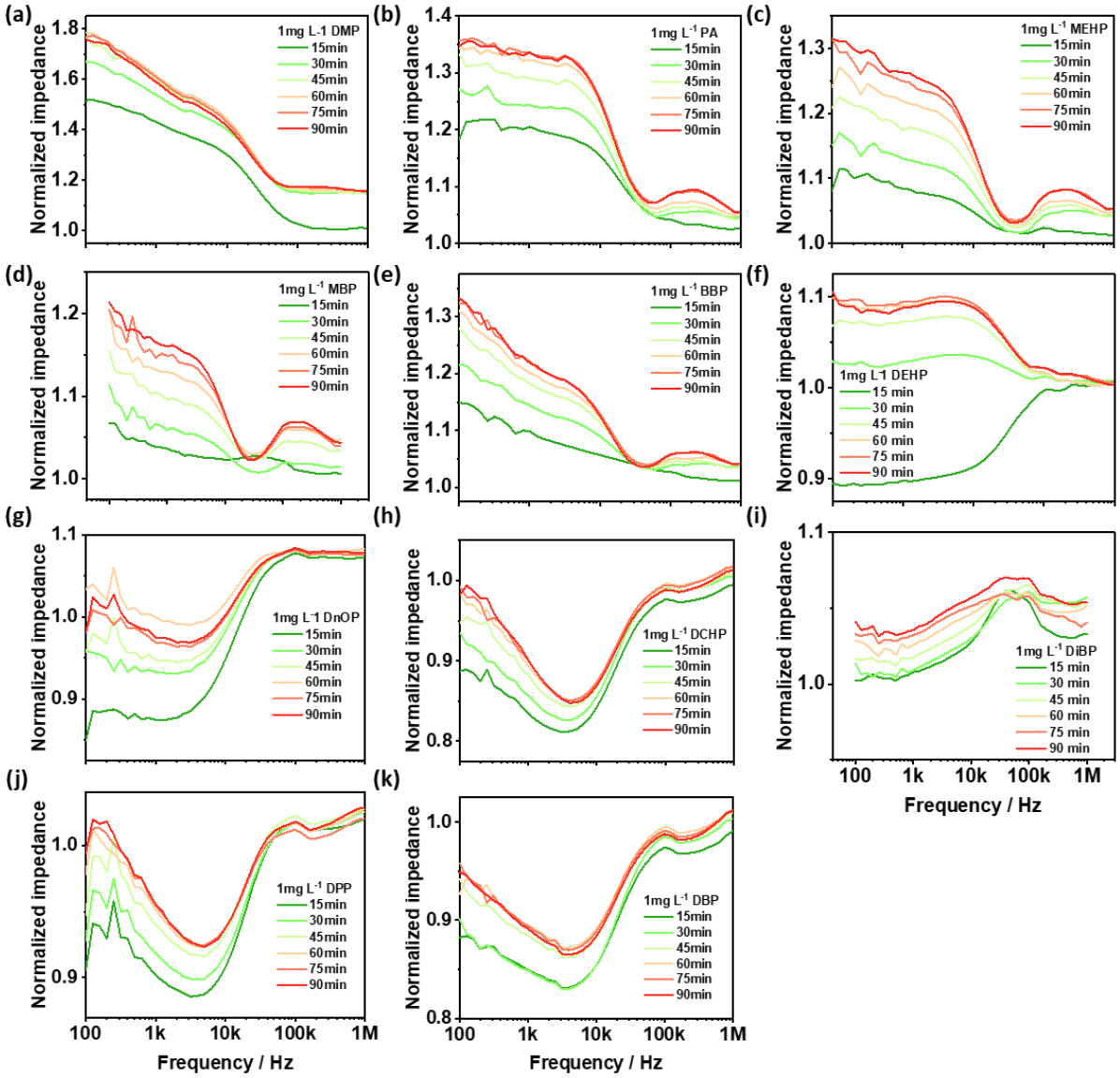

Figure 5.10: Normalized impedance amplitudes of $Cu_3(HHTP)_2$-10c thin-film devices responding to various phthalates using impedance amplitudes of $Cu_3(HHTP)_2$-10c thin-film responding to control solution as references.

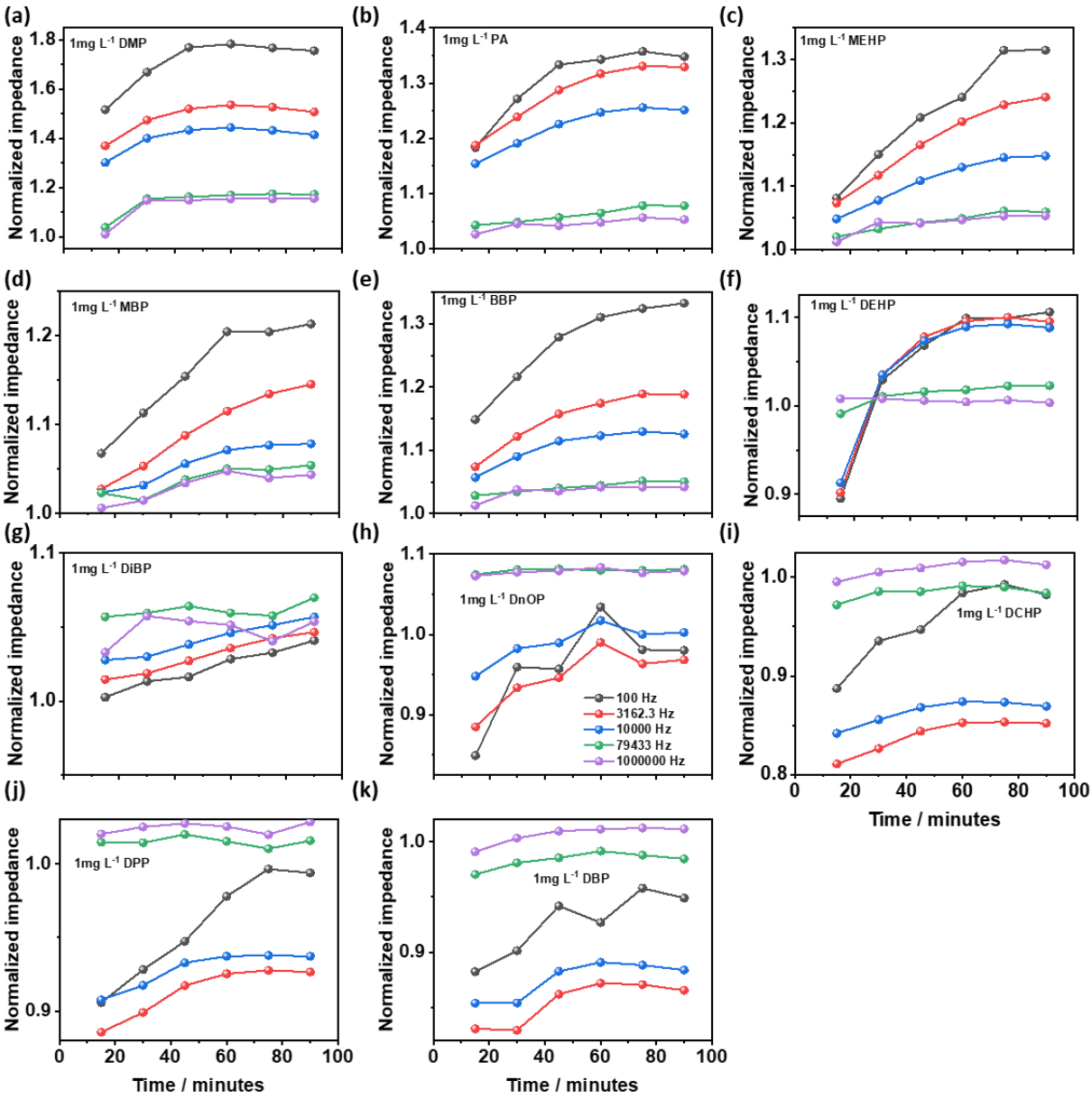

Figure 5.11: Transient analyses of the impedance amplitudes of $Cu_3(HHTP)_2$-10c thin-film devices at selected frequencies (Black: 100 Hz, read: 3162.3 Hz, blue: 10 kHz, green: 79422 Hz and purple: 1 MHz) responding to various phthalates using impedance amplitudes of $Cu_3(HHTP)_2$-10c thin-film responding to control solution as references.

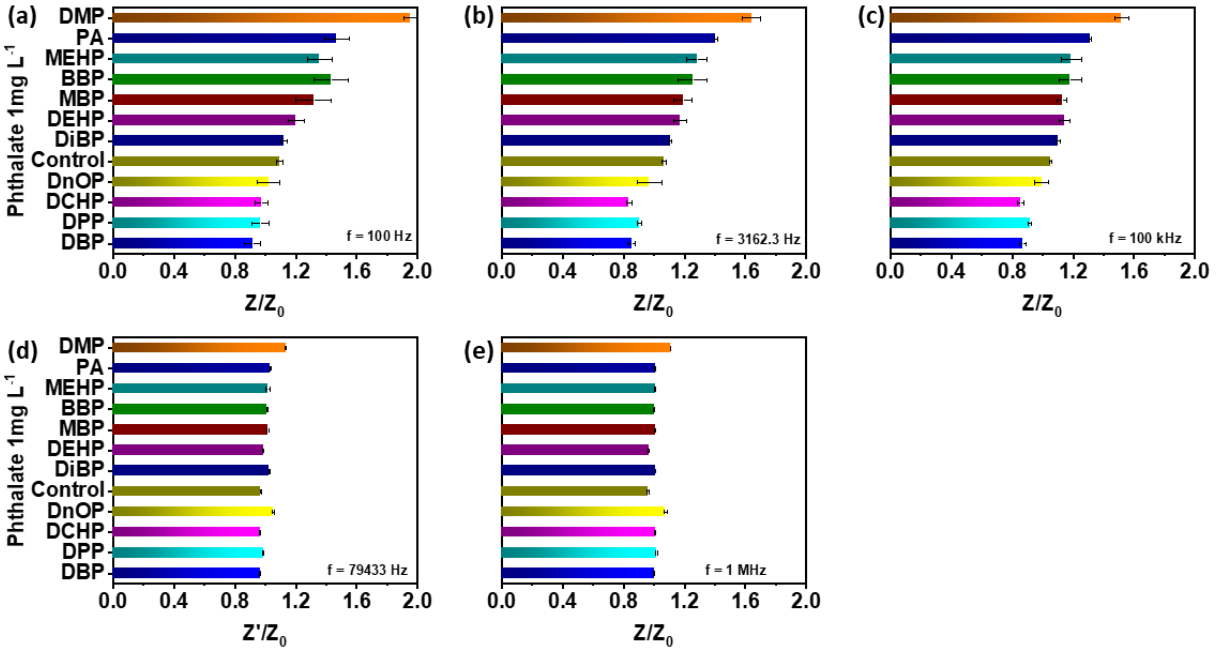

Figure 5.12: Change of impedance amplitudes of $Cu_3(HHTP)_2$-10c thin-film devices while responding to 1 mg·L^{-1} phthalate solutions at varying frequencies (a) 100 Hz, (b) 3162.3 Hz, (c) 10 kHz, (d) 79433 Hz and (e) 1 MHz.

To look into more details, the corresponding charge transfer resistance *(R_{ct})* and electrical double layer capacitance (C_{dl}) values are extracted, shown in **Figure 5.13** and **Figure 5.14**, respectively. Particularly, the change of R_{ct} is plotted in **Figure 5.15** with an incubation time of 60 minutes. Similarly, positive responses of $Cu_3(HHTP)_2$-10c thin-film devices to DMP, PA, MEHP, BBP, MBP, DEHP and DiBP, and negative responses to DnOP, DCHP, DPP and DBP were observed. While the change of capacitance caused by the adsorption of phthalates is irregular and neglectable. From all these results, we could conclude that the change of impedance amplitude of $Cu_3(HHTP)_2$-10c thin-film devices is mainly contributed by the change of charge transfer resistance due to the adsorption of phthalate molecules. **Figure 5.16** compares the molecular structures of different phthalates and corresponding response sequences. Where N and P stand for negative responses and positive responses, respectively. For instance, the R_{ct} of $Cu_3(HHTP)_2$-10c thin-film devices after DEHP adsorption is 1.19±0.05 (P) times higher, which increases to 1.33±0.07 (P, MEHP) and 1.47±0.02 (P, PA) due to the replacement of the side chains by –OH groups. The same trend is also observed in DBP (N, 0.85±0.02), MBP (P, 1.22±0.07) and PA (P, 1.47±0.02). With the increase of number of –COOH groups, the host-guest interaction is dominant by electrostatic interaction, resulting in the increase of impedance. In addition, we also observed that the responses are lower to phthalates with more molecular weight probably due to the size effect. For instance, the response of $Cu_3(HHTP)_2$-10c thin-film devices to DBP (N, 0.85±0.02) is higher than that of DPP (N, 0.85±0.02), DCHP (N, 0.91±0.02) and DnOP (N, 0.93±0.05). Very close responses were observed to DPP and DCHP due to the

close molecular weight. Such negative responses could be ascribed to weak van der Waals interactions between phthalate molecules and $Cu_3(HHTP)_2$ thin films. The last finding might help us distinguish the structural isomers, such as DEHP (P) and DnOP (N), as well as DBP (N) and DiBP (P). The underlying mechanisms can be further elucidated by performing molecular dynamics simulation.

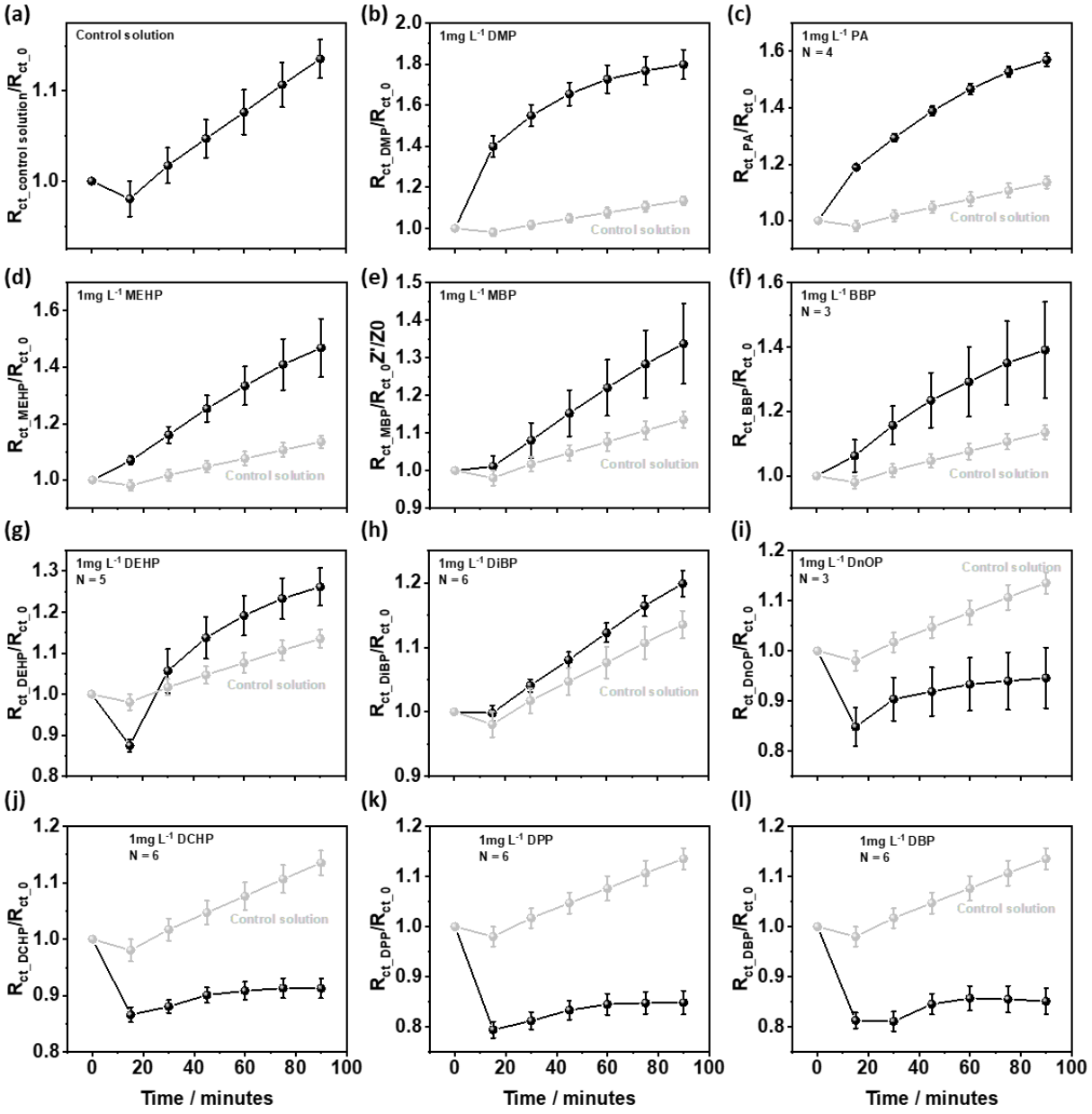

Figure 5.13: Change of charge transfer resistance (R_{ct}) while $Cu_3(HHTP)_2$-10c thin-film devices respond to different phthalates.

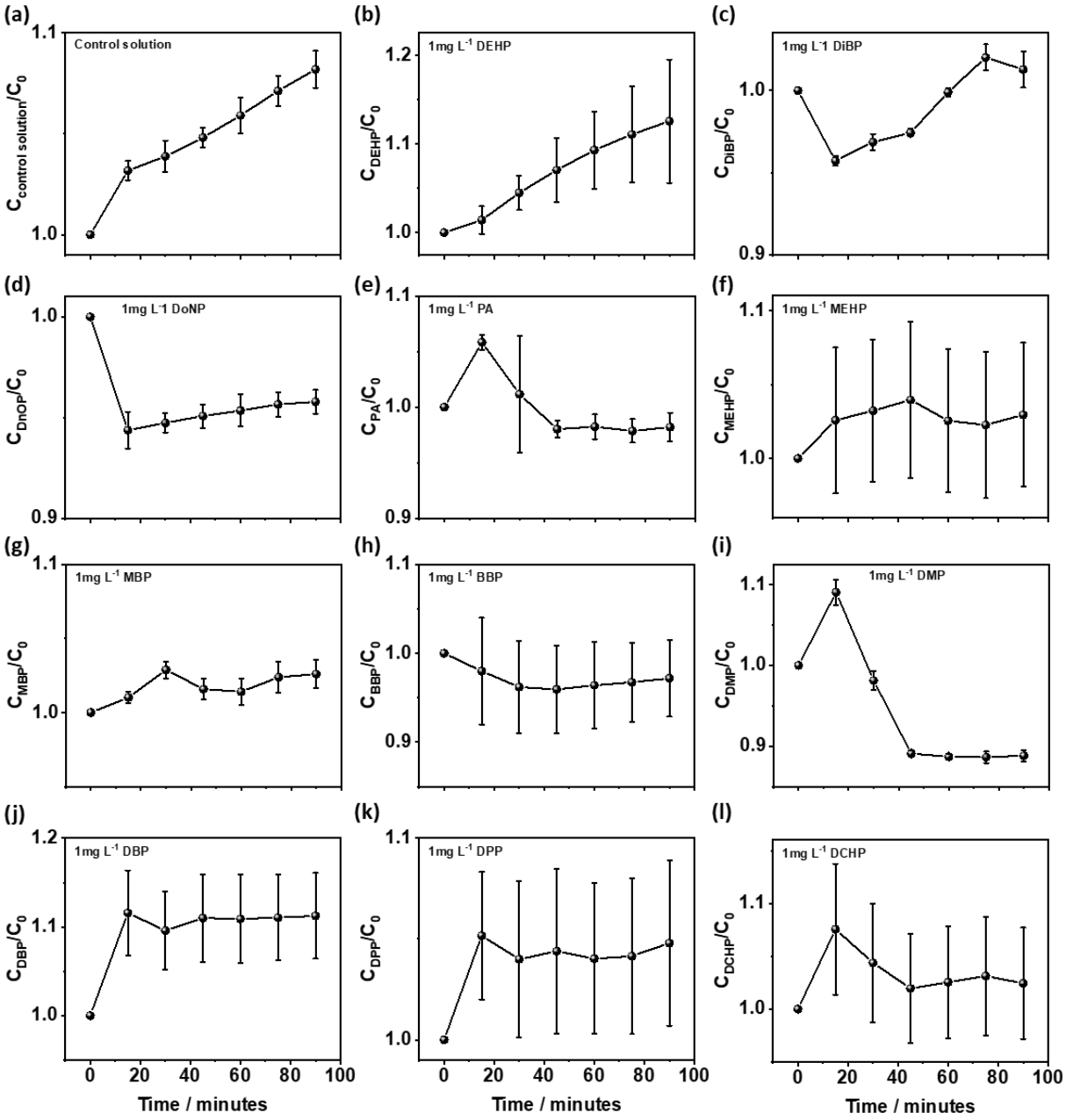

Figure 5.14: Change of electrical double layer capacitance while $Cu_3(HHTP)_2$-10c thin-film devices respond to different phthalates.

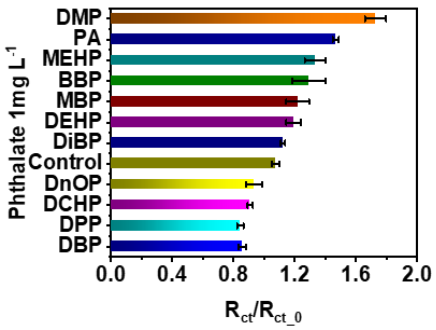

Figure 5.15: Change of charge transfer resistance of $Cu_3(HHTP)_2$-10c thin-film devices to 1 mg·L^{-1} phthalates with an incubation time of 60 minutes.

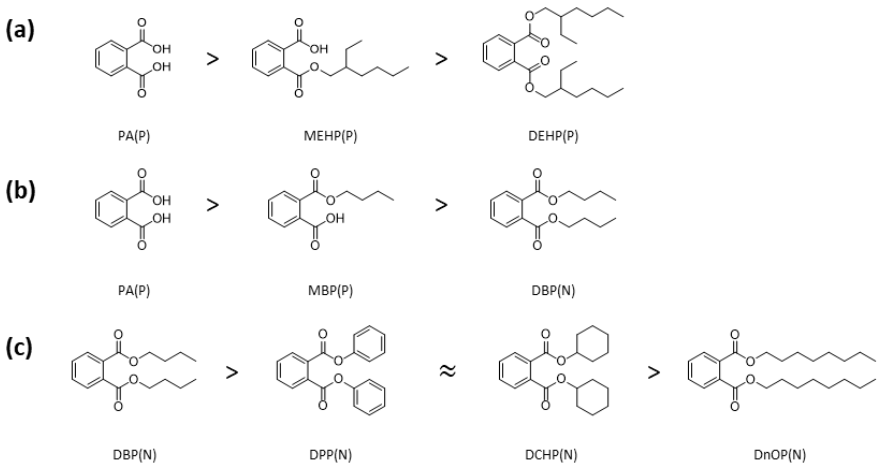

Figure 5.16: Schematic comparison of molecular structures and the corresponding contribution to the impedance of $Cu_3(HHTP)_2$-10c thin-film devices.

5.4 Summary

This chapter evaluates the sensing performance of two MOF thin-film-based sensor chips in liquid environments at room temperature. The Ni-(BDC-NH_2) thin-film sensor chips demonstrated linear detection of DiBP using Q values (a component of the CPE) as the criterion. However, the actual detection limit remains above 0.1 $mg \cdot L^{-1}$ due to the material's poor electrical conductivity, a limitation that could be addressed by employing electrically conductive MOFs as transducers. In contrast, the $Cu_3(HHTP)_2$ thin-film sensor chips exhibited varying responses to different phthalates and phthalate derivatives, with responses being either positive or negative depending on the molecular structure, molecular weight, and the number of –COOH groups present. The underlying interaction mechanisms could be further explored through molecular dynamics simulations. Overall, these findings provide valuable insights for designing optimized MOF-based transducers for sensor applications.

6 Cell-substrate interaction studies

This chapter explores the application of MOF thin films as active substrates for studying cell-substrate interactions using ECIS. Two MOF candidates, Ni-(BDC-NH_2) and Fe-(BDC-NH_2), were initially selected. To assess the biocompatibility of these MOF substrates, MTT cell proliferation and reactive oxygen species (ROS) assays were conducted using PC-12 cells as models. Additionally, immunostaining and morphological analyses of PC-12 cells on the MOF substrates were conducted to evaluate cell-substrate interactions. As a proof of concept, the ECIS technique was employed to investigate cell attachment, spreading, and proliferation on Fe-(BDC-NH_2) thin-film substrates. The findings have been published in Biosensors and Bioelectronics: X. [158] The research background and key results are presented in the following sections.

6.1 Background

Living systems, such as cells, actively engage with their environment, which plays a critical role in their sustenance and growth. [191] Growth substrates or templates are vital external factors that significantly influence cell growth, survival, and overall behaviour. As a result, cell-substrate interactions have garnered substantial interest in cell biology and are central to the development of various cell-based assays. Research in this area is particularly crucial for future applications in bioelectronics, biological implants, and tissue regeneration. [192-194] For example, studying these interactions provides valuable insights into designing novel materials or substrates that enhance cell adhesion, growth, and differentiation. [192, 193, 195] Thus, designing optimal cell substrates is essential not only for advancing our understanding of cellular processes but also for developing or improving techniques for such studies. One well-established method for examining cell-substrate interactions is ECIS, which enables non-invasive, real-time, and long-term monitoring of cell dynamics. [196-202] Over the past few decades, ECIS has advanced significantly alongside developments in the microfabrication of specialized device platforms using metal or semiconductor materials as active substrates. [197, 201] Beyond the development of planar metal electrodes and advanced microelectrode arrays with sophisticated materials and geometries, the application of standard silicon technology to create dedicated semiconductor chips for cell-based bioassays, stimulation, and recording represents a significant milestone in ECIS. [203-205] Consequently, the physical properties of active substrates and related transduction

mechanisms are crucial in designing advanced cell substrates and remain an active area of exploration.

The development of MOFs has traditionally focused on optimizing their unique characteristics for chemistry-related applications, particularly where high surface areas, porosity, customized topography, and highly accessible functional groups are of key interest. However, MOFs have also shown great promise in cell biology, particularly in drug delivery, bioimaging, and other biomedical studies. [47, 206-208] Recent research has demonstrated the potential of MOFs as scaffolds for cell growth. For example, Al-based MIL-53 thin films deposited onto polymeric substrates have been used as scaffolds for the growth of the C2C12 cell line (an immortalized mouse myoblast cell line), exhibiting superior serum protein adsorption, retention, and replenishment capabilities compared to conventional cell-culture scaffold. [209] Specifically, C2C12 cells cultured on MIL-53(Al) thin films loaded with serum proteins demonstrated exceptional adhesion, morphology, and proliferation, even in the absence of serum protein in the medium. Additionally, ZIF-8 modified polypropylene membranes have been employed as biomimetic cell-culture platforms to enhance guided bone regeneration. [210] Thus, MOFs are emerging as potential material systems for advanced cell-related studies. However, this requires careful examination of their varying stability in complex extracellular matrix environments and thorough analyses of their biocompatibility with different cell lines. [211]

6.2 Methods

6.2.1 Realization of MOF substrates on gold electrodes

$FeCl_3 \cdot 6H_2O$, $NiCl_2 \cdot 6H_2O$, and BDC-NH_2 were used for the synthesis of Fe-(BDC-NH_2) and Ni-(BDC-NH_2), respectively. $FeCl_3 \cdot 6H_2O$ was dissolved in deionized water at a concentration of 1 mM, while BDC-NH_2 was prepared by dissolving it in a 10 mM aqueous KOH solution. The preparation of the precursor solution for Ni-(BDC-NH_2) is detailed in Section 2.1. Prior to depositing Fe-(BDC-NH_2) or Ni-(BDC-NH_2) on gold substrates, a 10 nm Ti layer and a 100 nm Au layer were thermally evaporated onto 4-inch glass wafers, which were then diced into 1.5 × 1.0 cm^2 chips. These gold-coated chips were cleaned using acetone and isopropyl alcohol in an ultrasonication bath, followed by surface functionalization with a 1 mM 11-Mercapto-1-undecanol (11-MUD) ethanolic solution for 24 hours. [212] The epitaxial growth of Fe-(BDC-NH_2) on gold substrates was carried out using the LbL-LPE technique on an automated dip coater, as described in **Section 2.4**. During the LbL-LPE process, the 11-MUD-functionalized gold substrates were submerged in the $FeCl_3$ solution for 10 minutes, followed by rinsing to remove unreacted precursors. Subsequently, these substrates were dipped into the BDC-NH_2 solution

for another 10 minutes, followed by a second rinsing step to remove organic precursor residues. After twenty deposition cycles, the resulting Fe-(BDC-NH_2)-20c substrates were dried at 85°C and stored in a nitrogen chamber for further characterization and experiments.

6.2.2 PC-12 cell culture on MOF substrates

PC-12 Adh cells were used for both biocompatibility and ECIS experiments. The cells were cultured in Gibco RPMI-1640 medium, supplemented with 2 mM L-glutamine, 10% (v/v) inactivated horse serum, 5% (v/v) fetal bovine serum, and 1% (v/v) penicillin-streptomycin. For culturing PC-12 cells on the MOF substrates, all samples were either sterilized under UV light for one hour or rinsed with 70% ethanol. Following sterilization, the MOF substrates were coated with poly-L-lysine (PLL) to enhance cell adhesion. A 0.1 $mg \cdot mL^{-1}$ PLL aqueous solution was applied to functionalize the MOF substrates at room temperature for one hour, followed by thorough washing with sterile distilled water. Finally, PC-12 cells were seeded onto the Fe-(BDC-NH_2) thin-film substrates and incubated at 37°C for 24 hours in a humidified atmosphere (5% CO_2, 95% humidity).

6.2.3 Immunostaining experiments

All samples used for immunostaining were first coated with PLL. Immunostaining experiments were performed after 24 hours of cell culture. To fix the cells, the culture medium was removed, and the samples were rinsed three times with PBS. The cells were then fixed by covering the sample surfaces with 4% (w/v) paraformaldehyde for 15 minutes at room temperature, followed by another three PBS washes to remove any residual paraformaldehyde. Next, the cell membranes were permeabilized with 0.1% (w/v) Triton X-100 for 15 minutes at room temperature. After another three PBS washes, nonspecific protein binding sites were blocked using a blocking buffer for one hour. For focal adhesion staining, the samples were incubated with paxillin for one hour and then washed with the blocking buffer. This was followed by a one-hour incubation with anti-rabbit Alexa Fluor 488. Actin filaments were stained with phalloidin-iFluor 647 reagent for 40 minutes, followed by three PBS washes. Nuclei were visualized using Hoechst 33342 for 10 minutes, followed by another three PBS washes. All staining procedures were carried out at room temperature. Finally, the immunostained samples were mounted with fluorescence mounting medium and stored at 2–8°C until microscopy.

6.2.4 Morphological analysis

After immunostaining, the samples were visualized using a laser scanning confocal microscope. Fluorescence excitation was performed with lasers at 405 nm for the nucleus, 488 nm for paxillin, and 633 nm for F-actin. Images were captured at room temperature using a 40x oil immersion objective. Cellular morphology was analyzed using Fiji software (ImageJ). The final data were plotted and presented by analyzing various parameters, including cell area, circularity, roundness, perimeter, and aspect ratio. A circularity value of 1.0 indicates a perfect circle, while decreasing values indicate increasingly elongated polygons. The roundness value is directly related to the aspect ratio. Circularity and roundness were calculated using the following equations:

$$Circularity = \frac{4\pi * Area}{Perimeter^2} \tag{6-1}$$

$$Roundness = \frac{4 * Area}{\pi * Major\ Axis^2} \tag{6-2}$$

6.2.5 Biocompatibility assay

An MTT cell proliferation assay kit was used to evaluate cell viability on MOF thin-film substrates. To define the cell culture areas, MOF substrates were attached to a customized, bottomless 48-well plate with a 1.0 cm^2 growth area per well. PC-12 cells were then detached from petri dishes and seeded onto the PLL-coated MOF samples at a density of 71,500 cells/cm^2. The cell number was counted using a Countess 3 Cell Counter. After 24 hours of culture, the medium was replaced with 150 µL of serum-free media and 150 µL of MTT reagent in each sample well. For the background control, 150 µL of serum-free media and 150 µL of MTT reagent were added to a blank well. The plates were incubated at 37°C in a 5% CO_2 incubator for 3 hours. Following incubation, 450 µL of MTT solvent was added to each well, including the control well, and the plates were incubated for an additional 15 minutes at 37°C in the dark. The medium containing the MTT reagent was then transferred to a new 96-well plate for absorbance reading. The absorbance at 590 nm was recorded using a microplate reader. The acquired data were normalized to either bare glass (for MOFs on glass) or bare gold (for MOFs on Au) substrates and presented as percentages.

6.2.6 Cellular reactive oxygen species evaluation

The DCFDA/H2DCFDA Cellular Reactive Oxygen Species (ROS) Assay Kit was used to assess ROS levels in live PC-12 cells. Briefly, small vials from the assay kit were centrifuged at

low speed prior to opening. To prepare a 1x buffer for use, the 10x buffer provided in the kit was diluted with deionized water. The 1x buffer was stored in the refrigerator and equilibrated to 37°C before use. A working DCFDA solution was prepared by freshly diluting 20 mM DCFDA to a final concentration of 20 µM using the 1x buffer. To define the cell culture areas, MOF substrates were attached to customized, bottomless 48-well plates, providing a final growth area of 1.0 cm² per well. PC-12 cells were seeded into each well at a final density of 71,500 cells/cm². After 24 hours of incubation, the medium was removed, and the wells were rinsed with 300 µL of the 1x buffer per well. The cells were then stained with 300 µL of the DCFDA working solution per well and incubated for one hour at 37°C. Following incubation, the DCFDA solution was replaced with 300 µL of the 1x buffer per well. The plates were immediately analyzed using a microplate reader at excitation/emission wavelengths of 485/535 nm in end-point mode, with cells and medium present. The acquired data were normalized to either bare glass (for MOFs on glass) or bare gold (for MOFs on Au) control substrates and presented as percentages.

6.2.7 Focused Ion Beam - Scanning Electron Microscopy

The samples were prepared following the ultra-thin plasticization procedure described by Santoro et al. (2017) and Wrobel et al. (2008). Initially, the biological samples were chemically fixed using 4% (v/v) paraformaldehyde dissolved in Milli-Q water. This was followed by overnight incubation at 4°C in 2.5% (v/v) glutaraldehyde (Electron Microscopy Sciences) diluted in 0.1M cacodylate buffer. The samples were then rinsed with 0.1M cacodylate buffer while kept on ice throughout the procedures. Next, the buffer solution was replaced with a 20 mM glycine solution prepared in 0.1M sodium cacodylate, and the samples were incubated for 20 minutes. Following this, the specimens were placed in a solution containing 4% (v/v) aqueous osmium tetroxide (Electron Microscopy Sciences) and 2% potassium ferrocyanide (Electron Microscopy Sciences) for 1 hour at 4°C, protected from direct light. The samples were then washed three times with 0.1M cacodylate buffer. A final incubation was performed using a 2% (v/v) aqueous osmium tetroxide solution (Electron Microscopy Sciences) at room temperature for 30 minutes. The specimens were rinsed with deionized (DI) water at room temperature and then immersed in a 1% filtered thiocarbohydrazide (TCH) solution (Electron Microscopy Sciences, USA) in DI water for 20 minutes at room temperature. Following this, the samples underwent three rounds of rinsing with DI water. The samples were then immersed overnight at 4°C in an En bloc staining solution containing 4% (v/v) uranyl acetate. After rinsing three times with DI water, the samples were briefly incubated for 3 minutes at 4°C in a 0.15% (v/v) tannic acid solution (Sigma-Aldrich). Dehydration was carried out through a series of ethanol dilutions

(30%, 50%, 75%, 2×95%, and 100% v/v ethanol in water), with each step lasting 10 minutes at 4°C. The samples were further dehydrated with two changes of 100% ethanol at room temperature. Finally, the samples were gradually embedded in resin (comprising 25 mL NSA, 8 mL D.E.R. 736, 10 mL ERL 4221, and 301 µL DMAE, obtained from Electron Microscopy Sciences) using varying ethanol-to-resin ratios. The initial embedding involved a 1:3 ethanol-to-resin ratio for 2 hours, followed by a 1:2 ratio for another 2 hours. The final embedding was done with pure resin, which was left overnight and throughout the following day. Afterwards, the specimens were positioned vertically for 2 hours and then polymerized at 70°C for 24 hours. For electron microscopy imaging, the samples were affixed to 3.2 mm diameter aluminium stubs using silver conductive paste and coated with a 15 nm thick layer of gold. The specimens were then loaded into the dual-beam vacuum chamber. The region of interest was identified, and the stage was tilted to 52°. One deposition layer was applied using ion beam deposition (0.3 µm thickness of platinum, with a beam current of 0.43 nA and 30 kV acceleration voltage). Cross-sections were created by trenching the material with an ion beam (cutting thickness: 5 µm; current: 0.79 nA; acceleration voltage: 30 kV). The ion beam was also used to polish the interface (current: 0.23–0.43 nA; acceleration voltage: 30 kV). Scanning electron micrographs were acquired in backscattering mode at high resolution, with a dwell time of 20 µs, an electron beam acceleration voltage of 3 kV, and a beam current of 0.17 nA.

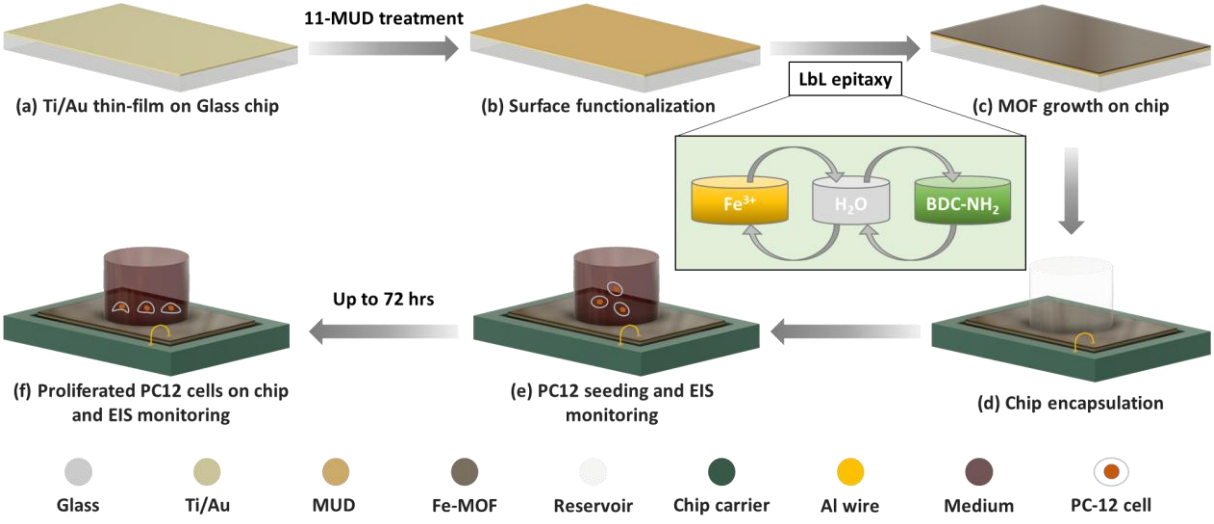

Figure 6.1: Schematic illustration representing the integration of Fe-(BDC-NH_2) thin films on Au electrodes for performing ECIS with PC-12 cells.

6.3 Results and Discussion

6.3.1 Morphological and structural characterizations of MOF substrates

As illustrated in **Figure 6.1** and described in **Section 6.2**, Fe-(BDC-NH_2) thin films were synthesized on Au substrates functionalized with hydroxyl groups by performing twenty LbL-LPE cycles using an automated dip coater. These samples are referred to as Fe-(BDC-NH_2)-20c. The successful growth of homogeneous Fe-(BDC-NH_2) thin films was initially confirmed using confocal laser microscopy. In **Figure 6.2a**, distinct regions of Au substrate and Fe-(BDC-NH_2) thin film are clearly visible. To determine the thickness of the LPE-grown MOF thin films, a photolithography process was developed to pattern the MOFs on various substrates. The protocol for micro-patterning of Fe-(BDC-NH_2) thin films is detailed in **Section 3.1**. Once micro-patterned, the thickness of Fe-(BDC-NH_2)-20c was measured using AFM. As shown in **Figure 6.2b**, the thickness is approximately 20 nm, resulting in an ultra-thin functional thin film on Au substrate, which can also serve as an electrode for the EIS measurements. The low surface roughness value of R_a = 3.9 nm indicates the smoothness of Fe-(BDC-NH_2)/Au substrate (**Figure 6.2c**). As expected for the LPE-grown Fe-(BDC-NH_2) thin film, the surface roughness after growth is notably higher compared to the Au electrode, which has an average roughness value R_a = ~1.0nm and the MUD functionalized Au electrode measured at R_a = ~1.0nm, shown in **Figure 6.3.** The corresponding amplitude image displays a consistent tip-deflection, suggesting a high degree of homogeneity in the Fe-(BDC-NH_2) coating on the Au electrodes (**Figure 6.2d**). Additionally, the successful growth of the Fe-(BDC-NH_2) on Au was further confirmed by comparative analysis of water contact angle measurements on bare Au substrates, MUD functionalized Au substrates, and Fe-MOF-20c on Au, as shown in **Figure 6.4a-c**. The significant decrease in contact angle from 84.8° to 55.4° indicates the successful introduction of hydroxyl groups on Au substrates. Then, the subsequent increase in contact angle from 55.4° to 61.5° implies the growth of Fe-(BDC-NH_2) on the functionalized Au substrate. Moreover, the contact angle of 61.5° for Fe-(BDC-NH_2)-20c suggests these novel substrates exhibit hydrophilic characteristics, with wettability properties conducive to live cell attachment and spreading, potentially due to the interactions between Fe-(BDC-NH_2) and membrane proteins. [213]

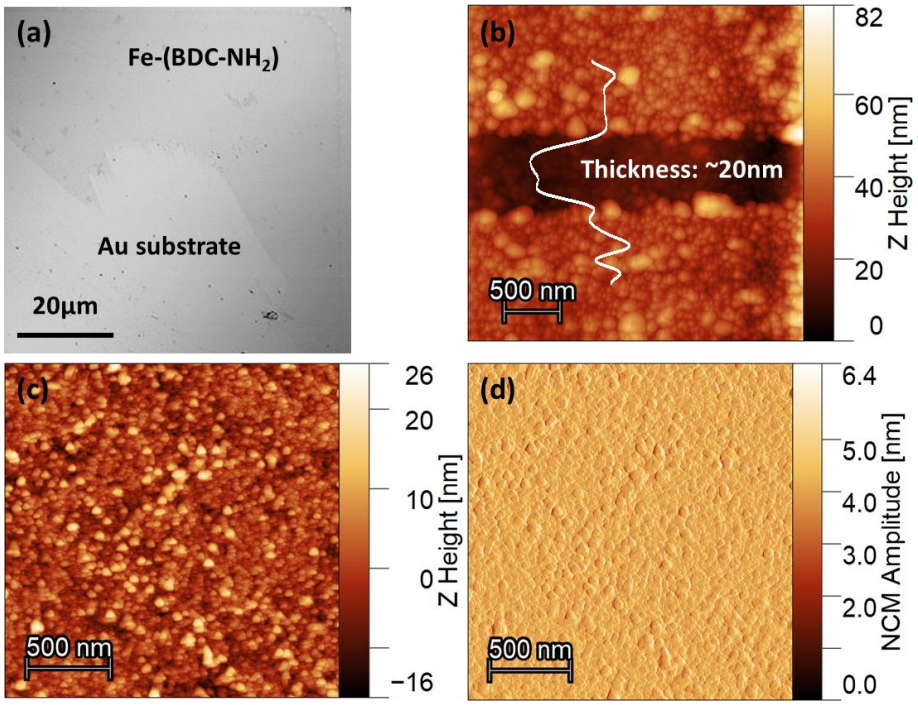

Figure 6.2: Surface characterizations of a typical Fe-(BDC-NH_2)/Au sample. (a) A confocal microscope image. (b) An AFM height profile image. (c) An AFM surface image. (d) An AFM amplitude image.

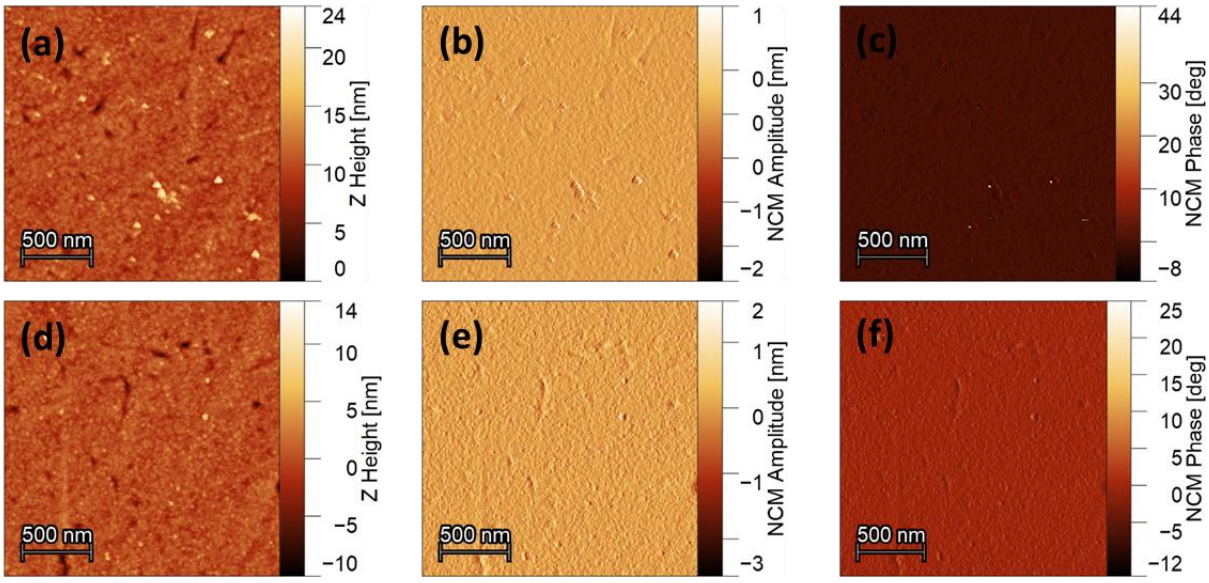

Figure 6.3: Surface characterizations. (a-c) Topography image and corresponding amplitude as well as phase images of a bare Au substrate. (d-f) Topography image and corresponding amplitude as well as phase images of an 11-MUD modified Au substrates.

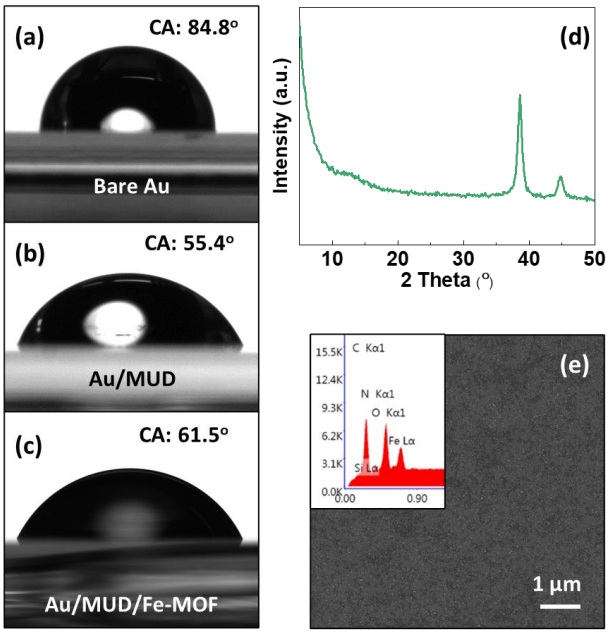

Figure 6.4: Water contact angle and structural characterizations. (a-c) Images showing water contact angle at bare Au, MUD-functionalized Au, and Fe-(BDC-NH_2)/Au substrate (d) GIXRD pattern of Fe-(BDC-NH_2) thin film on an Au substrate. (e) SEM image of the Fe-(BDC-NH_2)/Au substrate and the corresponding Energy Dispersive X-ray Spectroscopy (EDAX) spectrum.

The crystallographic structure of the Fe-(BDC-NH_2) thin film was evaluated using GIXRD measurements, as shown in **Figure 6.4d**. Two sharp peaks at 38.6° and 44.8° are observable, which can be attributed to the Au substrate. Additionally, two weaker peaks at 8.94° and 10.02°, along with a broad peak around 12.5°, are associated with Fe-(BDC-NH_2), indicating a relatively low crystallinity characteristic of the developed Fe-(BDC-NH_2) films. [214] The GIXRD measurements also confirmed the absence of elemental impurities, whether foreign or from the precursors used in the growth process. The SEM image presented in **Figure 6.4e** further corroborates the homogeneous growth of a typical Fe-(BDC-NH_2) layer on the Au substrates. The insert EDAX spectrum reveals the presence of C, O, N, and Fe elements, confirming the formation of coordination frameworks between Fe^{3+} ions and BDC-NH_2 linkers albeit with a short-range order.

6.3.2 Biocompatibility evaluation of MOF substrates

After confirming the stable and reliable growth of MOF thin films, we assessed the biocompatibility of these MOF substrates. Fe-(BDC-NH_2) and Ni-(BDC-NH_2) thin films were prepared on glass and gold substrates and subsequently evaluated using PC-12 cells after 24 hours of incubation, as shown in **Figure 6.5**. Cell viability determined through MTT assays, was individually normalized to bare glass (for MOF thin films on glass) and bare gold (for MOF thin films on Au) to assess the compact of the MOF thin films on the different substrates. After 24 hours, an increase in PC-12 cell viability was observed for both Fe-(BDC-NH_2)/glass

(108.3±42.8 %) and Ni-(BDC-NH_2)/glass (123.1±42.9 %) substrates compared to bare glass (95.4±24.2 %) substrates. These results indicate the biocompatibility of both MOF thin films realized on glass substrates. In contrast, for Fe-(BDC-NH_2)/Au (69.9±18.9 %) substrates, a decrease in cell viability was noted compared to bare Au substrate (100.0±15.0 %), while Ni-(BDC-NH_2)/Au (107.7±28.3 %) showed a statistically significant difference, as illustrated in **Figure 6.5a**. The varying viability results on Au substrates suggest potential surface interaction between Fe-(BDC-NH_2) and PC-12 cells, highlighting opportunities to regulate the bioactivity on these MOF substrates.

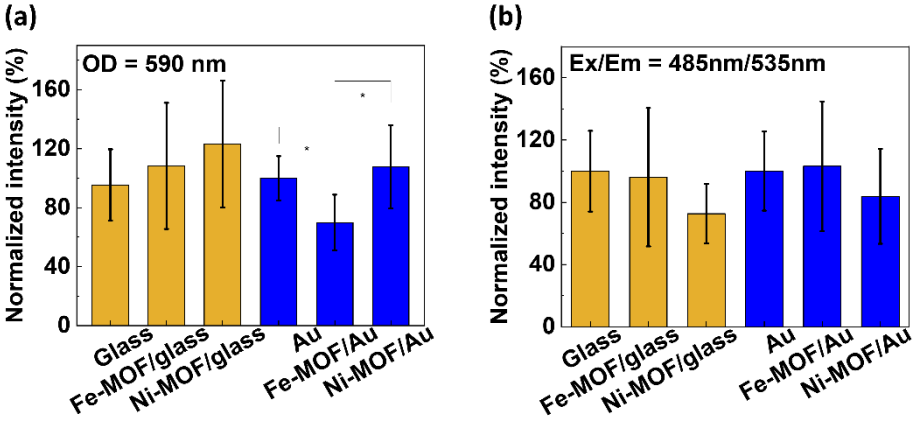

Figure 6.5: Biocompatibility characterizations of LbL-LPE grown MOF substrates with the PC-12 cell line. (a) Fluorescence absorbance recorded from the PC-12 cell cultures. (b) Evaluation of cellular reactive oxygen species (ROS).

To further explore the potential of Fe- and Ni- based MOFs in regulating cellular activity, ROS generation of PC-12 cells was measured after 24 hours of incubation to evaluate the cellular oxidative stress. The corresponding datasets, presented in percentage (%) after normalization to bare glass (for MOF thin films on glass) and bare gold (for MOF thin films on Au), are shown in **Figure 6.5b**, where higher values indicate increased ROS levels. Similar ROS generation was recorded for bare glass (100.0±25.9 %) and Fe-(BDC-NH_2)/glass (96.2±44.5 %), while lower ROS was observed with Ni-(BDC-NH_2)/glass (72.2±19.2 %). Comparatively, Fe-(BDC-NH_2)/Au (103.1±41.7 %) exhibited ROS levels similar to bare Au (100.0±25.4 %), whereas a reduction in ROS was noted for Ni-(BDC-NH_2)/Au (83.8±30.5 %). These results suggest the ROS-reducing capability of Ni-(BDC-NH_2) on both glass and Au substrates, aligning with the biocompatibility evaluation. Considering the redox behaviors of Fe and Ni as transition metals, these findings supported the role of Fe- and Ni-chelated MOFs in regulating oxidative stress and thereby improving cell viability, presenting opportunities for development of redox active biosensors. [206, 215]

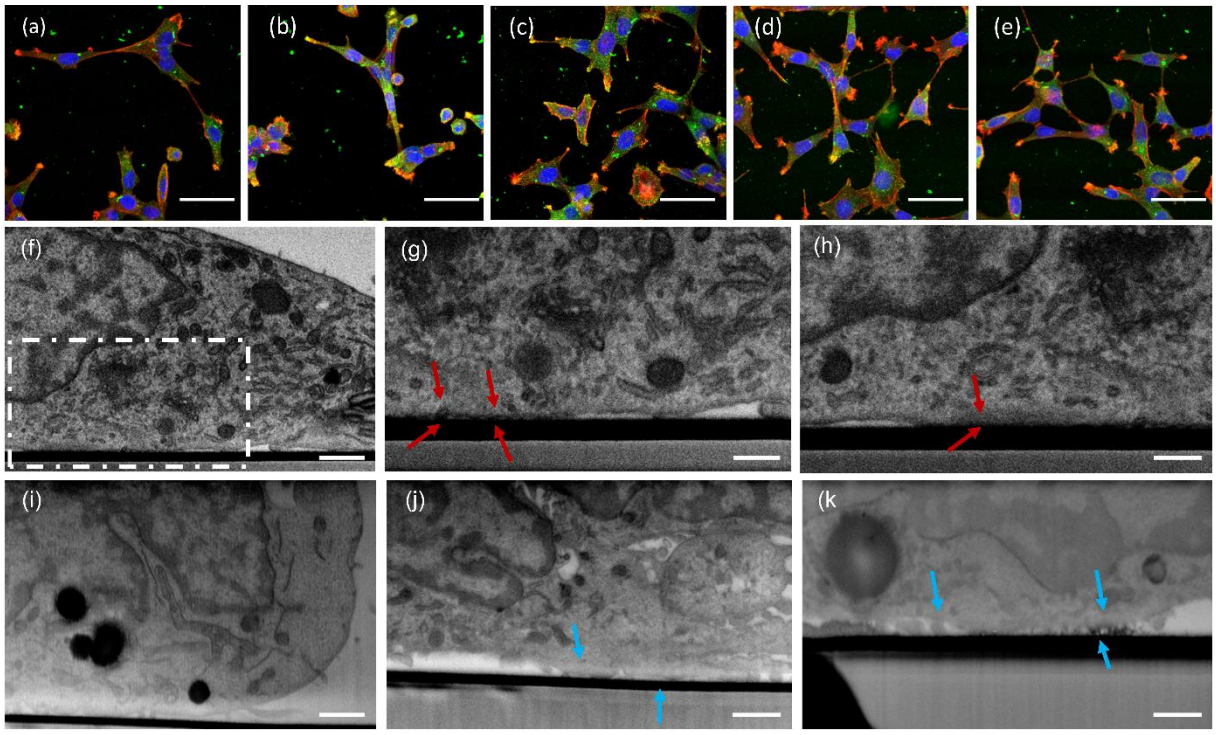

Figure 6.6: Morphological analyses of PC-12 cells on LbL-LPE grown MOF substrates. Exemplary fluorescence microscopy images of PC-12 cells after immunostaining on (a) cover glass, (b) Ni-(BDC-NH_2)/glass, (c) Fe-(BDC-NH_2)/glass, (d) Ni-(BDC-NH_2)/Au, (e) Fe-(BDC-NH_2)/Au. Scale bar: 50 µm. Actin cytoskeleton (red), focal adhesion (green), nuclei (blue). SEM-FIB analysis of PC-12 cell adhesion on different surfaces: (f-h) Ni-(BDC-NH_2)/Au substrate, (i-k) Fe-(BDC-NH_2)/Au substrate. The black line indicates the original electrode surfaces and arrows point towards the focal adhesion sites. The scale bar is 500 nm.

6.3.3 Morphological analysis of PC-12 cells on MOF substrates

Morphological analyses were performed following immunostaining F-actin (red), paxillin (green) and nuclei (blue), as shown in **Figure 6.6a-e**. When comparing MOF layers to standard glass substrates, PC-12 cells exhibited smaller aspect ratios (AR) on both Fe-(BDC-NH_2) and Ni- (BDC-NH_2) substrates, with a larger cell coverage area observed on Ni-(BDC-NH_2)/Au. The smaller AR is also evident from the roundness parameter, which is related to AR, as presented in **Figure 6.7**. Further comparison between Fe-(BDC-NH_2) and Ni-(BDC-NH_2) revealed no differences in AR and roundness. Overall, the cells appeared more elongated on Ni-(BDC-NH_2)/Au with lower circularity value compared to those on Fe-(BDC-NH_2)/glass surfaces. In terms of coverage area, Ni-(BDC-NH_2)/Au substrates showed a higher cell coverage area and perimeter compared to Fe-(BDC-NH_2)/Au and other substrates, as shown in **Figure 6.7**. This suggests that Fe-(BDC-NH_2) and Ni-(BDC-NH_2) effectively regulate cytoskeleton structures compared to non-functionalized bare substrates, which could be attributed to the lower ROS concentrations at these cell-chip interfaces.

The contact area between PC-12 cells and the imposed topography was visualized using SEM and *in-situ* cross-section imaging by FIB milling. On both Ni-(BDC-NH_2)/Au and Fe-(BDC-

NH_2)/Au, the plasma membrane follows the surface profiles, shown in **Figures 6.6f-k**. Micrographs depicting the interaction between PC-12 cells and Ni-(BDC-NH_2)/Au (**Figures 6.7f-h**) indicate active cell engagement with the imposed magnetic metal topography (highlighted by red arrows). Conversely, in **Figures 6.7i-k**, PC-12 cells on Fe-MOF/Au show that the high magnetic properties of Fe lead to the formation of the white halo and detaching phases (highlighted by blue arrows). FIB-SEM micrographs further reveal that as cells explore the substrate, the cross-section images display membrane invagination (highlighted by red arrows).

6.3.4 Electric cell-substrate impedance sensing

Before investigating cell-substrate interactions using the ECIS technique, the long-term electrochemical stability of Fe-(BDC-NH_2) thin film in cell culture medium was assessed through EIS measurements. These measurements were conducted with a small AC potential of 50 mV across a frequency range of 5 Hz to 200 kHz. As shown in **Figure 6.8**, a significant decrease in impedance amplitudes was observed after 24 hours of incubation in PC-12 cell culture medium, likely due to ion intercalation into the porous Fe-(BDC-NH_2) matrix. In addition, changes in phase suggest that the culture medium affects the Fe-(BDC-NH_2) matrix. Furthermore, the impedance amplitude of the Fe-(BDC-NH_2)/Au substrate was monitored and analyzed at a fixed frequency of 200 kHz over 24 hours, as depicted in **Figure 6.9**. The impedance amplitude initially decreased sharply and then gradually increased, reaching a quasi-equilibrium state after sixteen hours, which was maintained for over twenty hours. This stable response is crucial for the ECIS measurements with cells, as it ensures that changes in impedance are not due to the Fe-(BDC-NH_2) itself, from the Fe-(BDC-NH_2) itself, a conclusion further supported by AFM characterizations presented in **Table 6-1**.

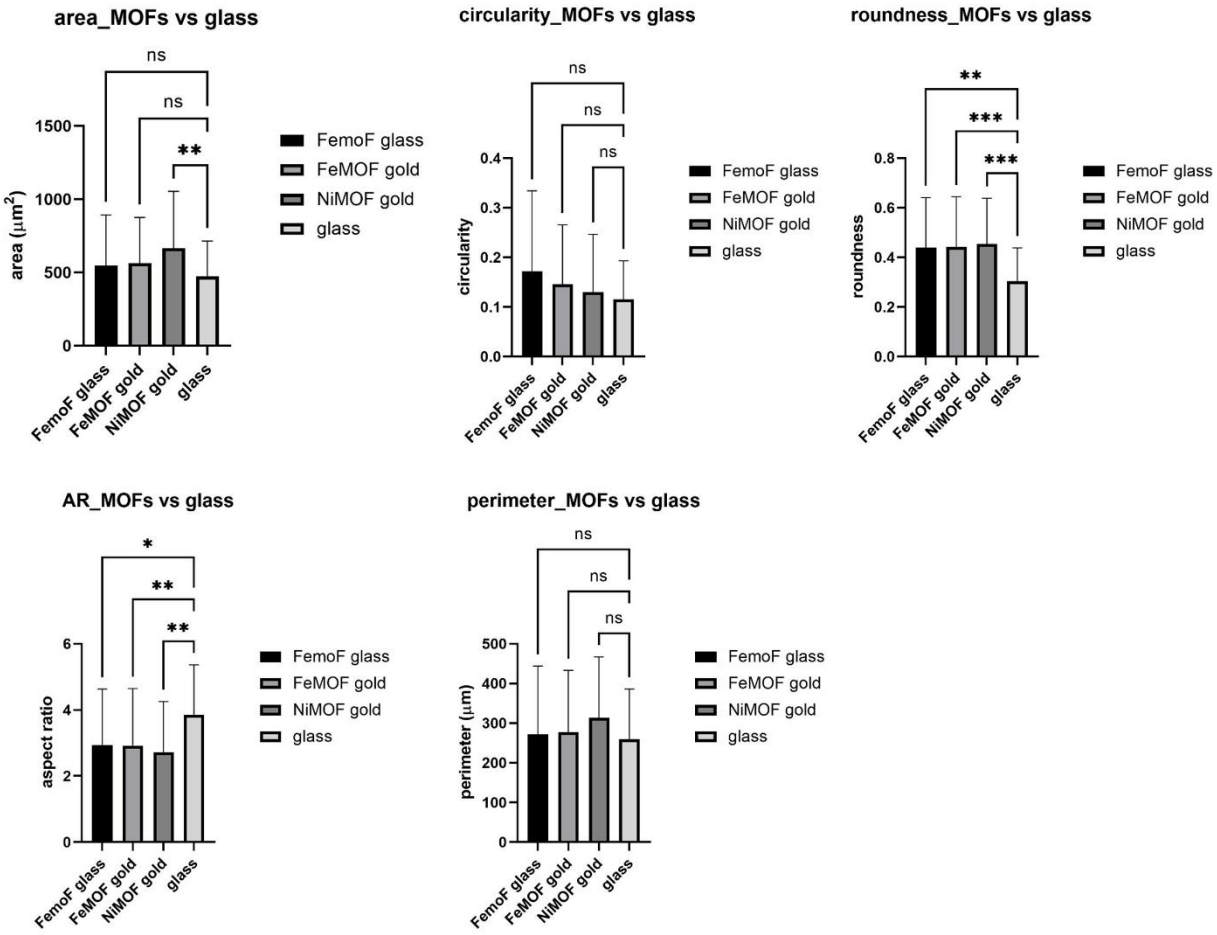

Figure 6.7: Morphological analysis of PC-12 cells grown on MOF substrates and comparison with standard glass substrates.

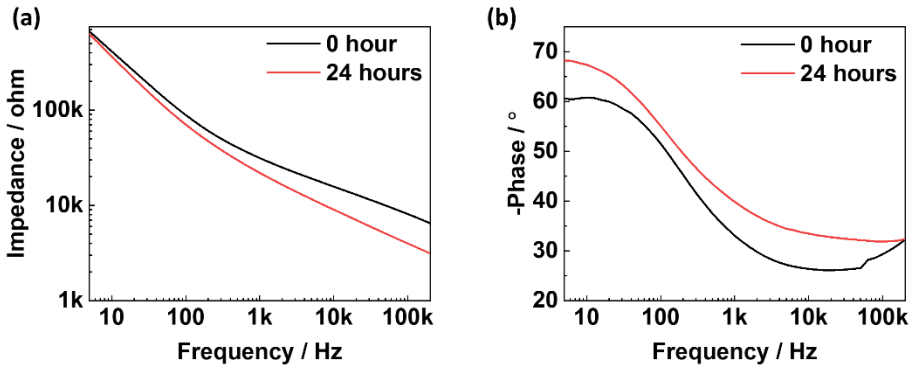

Figure 6.8: Comparison of impedance amplitude and phase of Fe-(BDC-NH_2)/Au electrode over 24 hours in PC-12 cell culture medium.

Table 6-1: Stability of Fe-(BDC-NH_2)/Au substrates in PC-12 cell culture medium over 24 hours.

	Thickness (nm)	Roughness R_a (nm)
Before	~14	5.7
After	~12	4.2

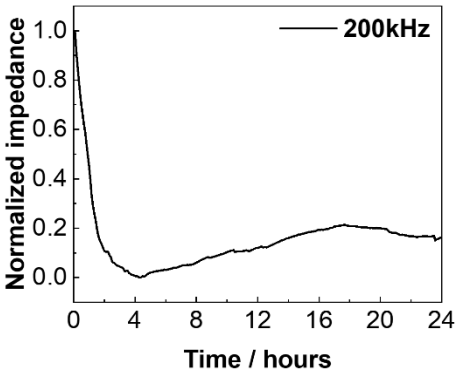

Figure 6.9: Real-time monitoring. Normalized impedance amplitude of a bare Fe-(BDC-NH_2)/Au substrate at 200 kHz in PC-12 cell culture medium.

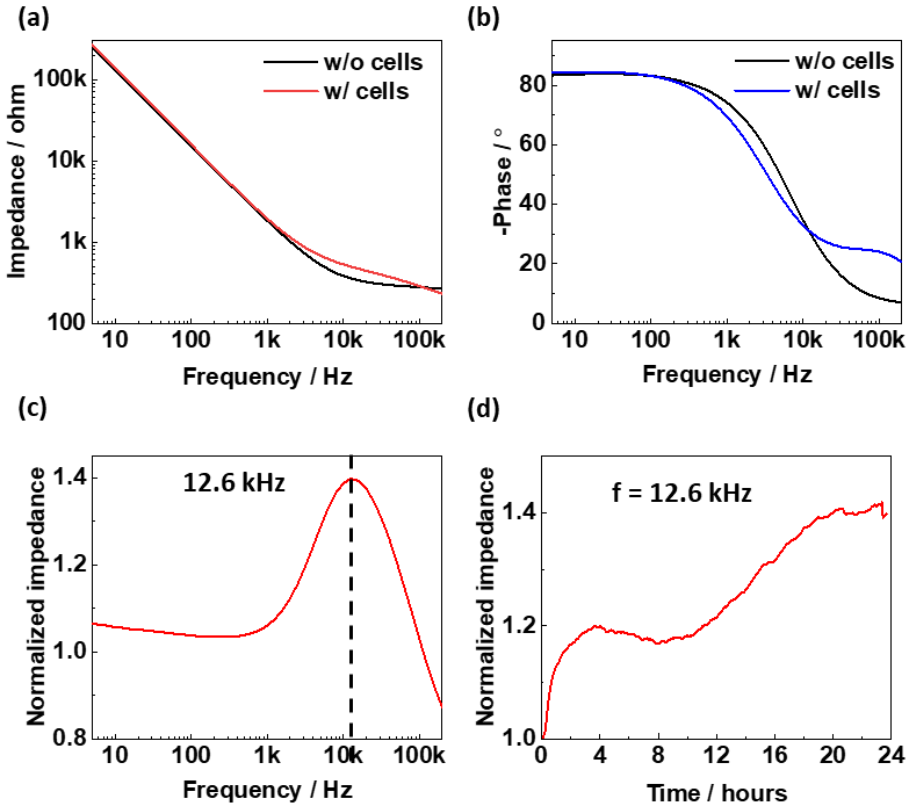

Figure 6.10: Long-term EIS characterization of the PC-12 cell culture on Fe-(BDC-NH_2)/Au electrodes. (a) Impedance spectrum of a typical Fe-(BDC-NH_2)/Au electrode without cell (black curve) compared with impedance spectrum (red curve) after 24 hours of cell culture. (b) Characteristic phase change recorded without (black curve) and with the cells (blue curve) after 24 hours of cell culture. (c) Normalized impedance spectral response without and with cells. (d) Real-time EIS response of the Fe-(BDC-NH_2)/Au electrode over 24 hours after the seeding of PC-12 cells recorded at 12.6 kHz inside an incubator.

The EIS characterization of cell cultures entailed the seeding of PC-12 cells onto the Fe-(BDC-NH_2)/Au electrodes. A notable rise in impedance was discerned at the frequencies approximately 10 kHz over the course of 24 hours, while no discernible alteration was observed at

lower frequencies (e.g., < 1 kHz), shown in **Figure 6.10a**. Furthermore, the phase change observed in the frequency range over 24 hours is illustrated in **Figure 6.10b,** which suggests successful cell attachment. In order to identify the optimal frequency for monitoring cell behaviors (e. g., attachment, spreading, and proliferation) on Fe-(BDC-NH_2)/Au substrates, the impedance was normalized according to: $Z_{w/\ cells}/Z_{w/o\ cells}$ (w/ = with, w/o = without). As illustrated in **Figure 6.10c**, the impedance amplitude exhibits the greatest variation at a frequency of 12.6 kHz. Subsequently, the growth and spreading of PC-12 cells were monitored and studied at this fixed frequency for a period of 24 hours. A rapid increase in impedance amplitude was observed following cell seeding within four hours, as illustrated in **Figure 6.10d**. A slight decrease in the impedance amplitude was observed from the fourth to the eighth hour, which is indicative of the cells spreading on the Fe-(BDC-NH_2)/Au substrate. Subsequently, the PC-12 cells commenced growth and proliferation over the subsequent ten hours, resulting in a continue increase in impedance due to the rising coverage of the Fe-(BDC-NH_2)/Au electrode with cells. [200] As indicated in **Figure 6.10d**, a confluent cell layer was formed after 20 hours due to impedance saturation from the 20^{th} – 24^{th} hour. This finding was corroborated by an optical microscopy image captured after 24 hours, as shown in **Figure 6.11**. Finally, to gain insight into the influence of attached cells onto Fe-(BDC-NH_2)/Au electrode, electrically equivalent circuits were simulated as illustrated in **Figure 6.12**, presenting the circuit before and after cell attachment. In this study, three components were included in the model to account for the contribution of the PC-12 cells: $R_{Junction}$, R_{Cell}, and $C_{Membrane}$. There were included due to the formation of a confluent layer. The fitted curves and parameters before and after cell attachment are shown in **Figure 6.13** and **Table 6-2,** respectively. The experimental and modelling results are in good agreement, thus validating the electrical model.

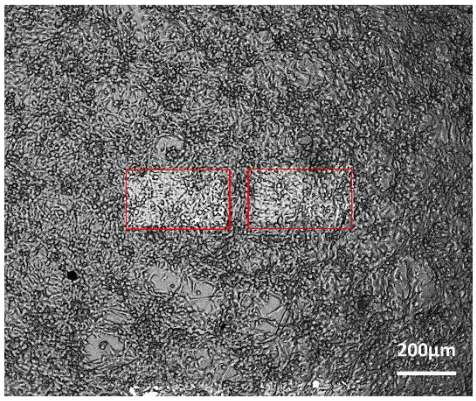

Figure 6.11: Confluent PC-12 cell layer on Fe-(BDC-NH_2)/Au electrode (highlighted in red, 2 out of 12 patterns) after 24 hours.

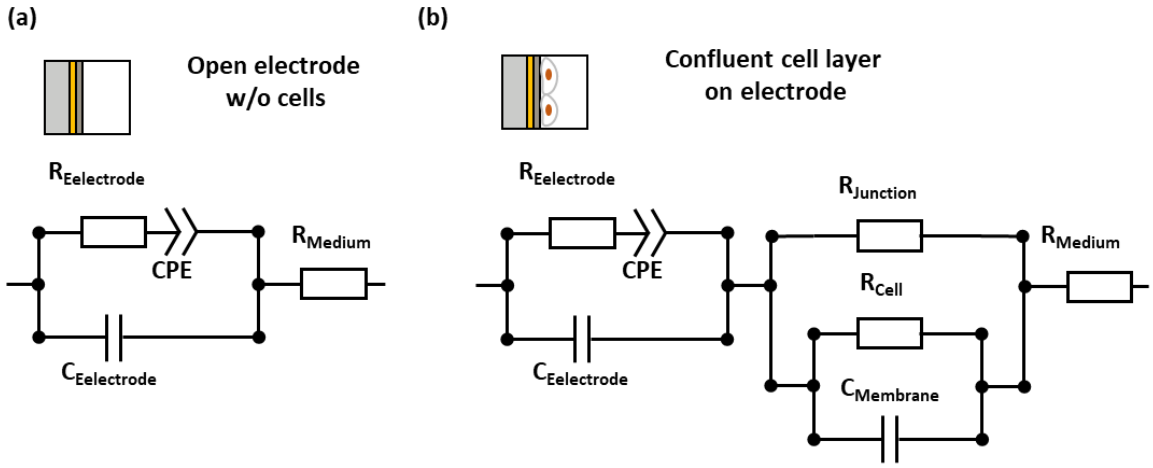

Figure 6.12: Illustrations show the equivalent electrical circuits for the EIS measurement set-up without and with cells. [216]

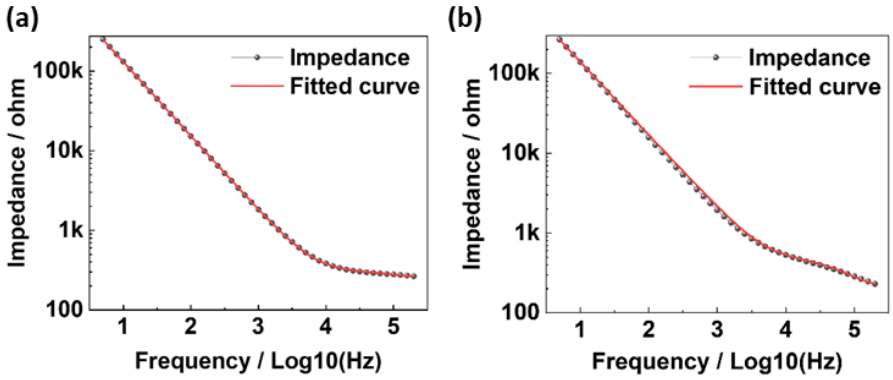

Figure 6.13: Equivalent electrical circuit fitting. (a) Before cell attachment, (b) after cell attachment.

Table 6-2: Summary of the electrical parameters derived from the EIS measurements using the equivalent circuit as shown in Figure 6.12.

		Without cells	With cells
R_{Medium} (Ω)		252.6	192.4
$R_{Electrode}$ (Ω)		88.87	232.9
$C_{Electrode}$ (nF)		23.68	9.847
CPE	Q (μT)	0.141	0.137
	n	0.913	0.936
$R_{Junction}$ (Ω)		NA	209.7
R_{Cell} (Ω)		NA	310.4
$C_{Membrane}$ (nF)		NA	129.4

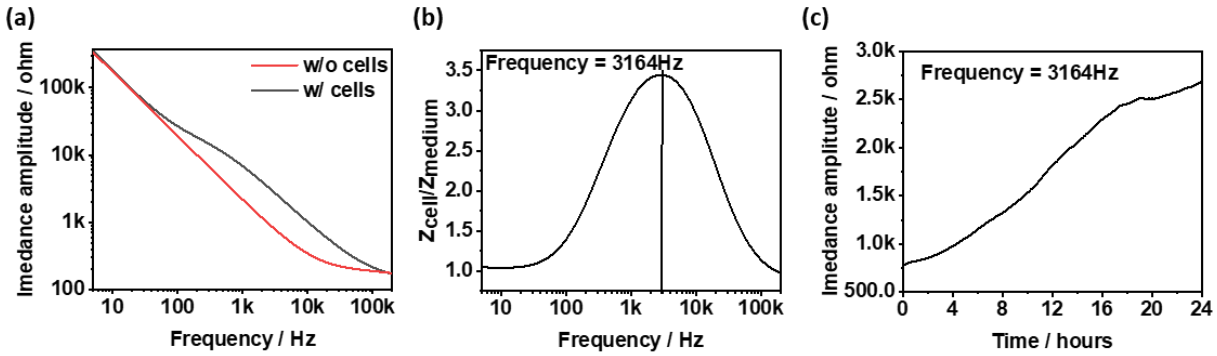

Figure 6.14: ECIS study of MDCK cells on Fe-(BDC-NH_2)/Au electrodes.

6.4 Summary

MOF thin films based on Fe-(BDC-NH_2) and Ni-(BDC-NH_2) were successfully synthesized and deposited onto glass and Au substrates. To assess their biocompatibility, metabolic and ROS assays were conducted using the PC-12 neuroblastoma cell line, which demonstrated that the cells not only survived but also proliferated. This evidence supports the classification of MOFs as a novel class of porous, crystalline, and electrically tunable functional materials, presenting new opportunities for the development of bioelectronics and biosensors. The processes of cell attachment, spreading, and proliferation were studied in real-time using ECIS with Fe-(BDC-NH_2)/Au electrodes, allowing the continuous monitoring of distinct stages of cell behavior. To the best of our knowledge, this is the first demonstration of MOF substrates being used to investigate cell-substrate interactions through ECIS technology. In addition to PC-12 cells, Fe-(BDC-NH_2)/Au electrodes were also employed to study MDCK cells, as illustrated in **Figure 6.14**. The development of MOF-based surface coatings could significantly enhance the study of living system dynamics, supporting the emerging use of MOFs in applications such as biological scaffolds and implants. Furthermore, the routine integration of novel MOF thin films, as demonstrated in this work, offers an opportunity for fundamental studies of the mechanisms that regulate biological activity. This is expected to be highly beneficial in the design of future solutions for stimulating and recording biological signals.

7 Conclusions and Outlook

The primary objective of the dissertation was to develop microelectronic devices based on MOF thin films for applications in chemical sensing and biosensing. Three distinct MOF candidates were selected for specific purposes: Ni-(BDC-NH_2), Fe-(BDC-NH_2), and $Cu_3(HHTP)_2$. The first two are electrically insulating with good biocompatibility, whereas the latter exhibiting semiconducting properties. The successful fabrication of MOF thin-film microelectronic devices necessitated several significant technological advancements.

(1) Automated growth platforms: Two automated systems, a microfluidics platform and a dip coater, were established to perform LbL-LPE growth of MOF thin films. Both platforms possess the capability of producing high-quality thin films with precise control over thickness and minimal surface roughness. The microfluidics system offers versatility for investigating the growth parameters of MOF thin films, including temperature, solvents, precursor concentrations, and flow rates. Insights derived from microfluidic deposition can guide the dip-coating process, which is more scalable and enables the growth of MOF thin films on substrates ranging from small chips to entire wafers. Moreover, the microfluidics platform minimizes the consumption of chemicals and solvents, although it is limited by a smaller growth area.

(2) Lithographic patterning: Three lithographic techniques were developed for the patterning MOF thin films using sacrificial layers composed of PaC coatings, UV photoresists, or PMMA/SU-8 stacks. These methods are adaptable to diverse growth conditions of MOFs and their stability in solvents like acetone and DMSO.

(3) Optical quality assessment: An innovative optical method based on optical contrast differences between MOF thin films on Si/SiO_2 substrates was developed for rapid assessment of film quality, including homogeneity and thickness. This non-contact technique is particularly suitable for MOF thin-film development within cleanroom environments.

Through the integration of these techniques: combining microfabrication in cleanrooms (e.g., lithography, metallization, passivation, etching), MOF thin-film growth *via* LbL-LPE, and lithographic patterning, on-chip integration of MOF thin films was successfully achieved. Structural, morphological, and electrical characterizations indicated that the MOF thin films exhibited high quality and low variability across devices. A comprehensive investigation of the rapid

thermal annealing treatment of semiconducting $Cu_3(HHTP)_2$ thin films was conducted at various annealing temperatures (85, 150, 300, and 450°C) in an Ar atmosphere. The results demonstrated that the optimal annealing condition - 85°C for 30 minutes followed by 300°C for 15 seconds, resulting in a doubling of electrical conductivity compared to samples annealed only at 85°C. This process also minimized contact resistance. $Cu_3(HHTP)_2$ thin-film EG-FETs showed ambipolar transport behaviour in phosphate buffer solutions. Hysteresis studies suggested that a capacitive gating mechanism dominated the ambipolar transport, and the shift of CNP indicated potential pH-sensing capabilities.

The potential applications of MOF thin-film microelectronic device in chemical and biosensing were further explored. Ni-(BDC-NH_2) thin-film sensors exhibited linear detection of DiBP across a concentration range of 1 - 20 $mg \cdot L^{-1}$. However, sensitivity could be improved with the implementation of more conductive MOFs as transducers. $Cu_3(HHTP)_2$ thin-film sensors demonstrated varied responses to different phthalates and phthalate derivatives, likely influenced by molecular structure, weight, and the presence of carboxyl (–COOH) groups. The underlying sensing mechanisms, which may involve electrostatic or weak van der Waals interactions, offer insights for future sensor design. Fe-(BDC-NH_2) thin-film devices were utilized to investigate cellular dynamics, including attachment, spreading, and proliferation, on MOF substrates due to their biocompatibility. Real-time monitoring of PC-12 and MDCK cells enabled distinct observations of cell behaviour over extended periods.

Several promising avenues for future research have emerged from this study:

(1) Automated platforms for MOF heterostructures: The microfluidics platform and the dip coater have significant potential for constructing MOF-on-MOF heterostructures. For instance, by combining insulating MOFs with conductive MOFs, novel devices could be developed in which the insulating layer serves as a functional component, while the conductive layer serves as a transducer to convert stimuli into electrical signals.

(2) Expansion to other materials: In addition to MOFs, other materials, such as perovskites, can also be synthesized using these platforms, thereby providing further opportunities for device development.

(3) Optical sensing platforms: The optical method developed based on the contrast of MOF thin films on Si/SiO_2 substrates can be expanded by incorporating the effects of refractive index changes, which occur upon the adsorption of external speciesby the MOF. This provides a basis for developing MOF-based optical sensors and sensor arrays.

(3) Chemical/Bio-Sensing and Artificial Intelligence: The integration of artificial intelligence and molecular dynamics simulations has the potential to optimizethe selection of MOFs for detecting various pollutants and analysing different cell lines. This approach would minimize the need for trial-and-error methods, thereby accelerating the development of more effective sensors.

Appendix

List of Figures

Appendix

Appendix

Appendix

List of Tables

Abbreviations

MOFs	Metal-organic frameworks
EIS	Electrochemical impedance spectroscopy
LbL	Layer by layer
LPE	Liquid-phase epitaxy
HHTP	2,3,6,7,10,11-hexahydroxytriphenylene
EG-FETs	Electrolyte-gated field-effect transistors
BDC-NH_2	2-aminoterephthalic acid
DiBP	Diisobutyl phthalate
ECIS	Electric Cell-substrate Impedance Sensing
DNA	Deoxyribonucleic acid
Si	Silicon
Ge	Germanium
Te	Tellurium
GaN	Gallium nitride
GaAs	Gallium arsenide
GaP	Gallium phosphide
SiC	Silicon carbide
ZnO	Zinc oxide
CdS	Cadmium sulfide
COFs	Covalent-organic frameworks
c-MOFs	Conductive metal-organic frameworks
SBUs	Secondary building blocks
IRMOFs	Isoreticular metal-organic framework
MIL	Matériaux de l′Institut Lavoisier
1-D	One dimensional
2-D	Two dimensional
3-D	Three dimensional

Appendix

SMNs	Single-metal nodes
MMNs	Multiple-metal nodes
CN	Coordination numbers
CG	Coordination geometry
0-D	Zero dimensional
ZIFs	Zeolitic imidazolate frameworks
im	Imidazolate
BTC	1,3,5-benzenetricarboxylate
DEF	N,N-Dimethylformamide
BDC	Terephthalic acid
CPO	Coordination polymer of Oslo
H_4BTEC	Benzene-1,2,4,5-tetracarboxylic acid
HTTP	Hexathiotriphenylene
HITP	Hexaiminotriphenylene
PSM	Post-synthetic modification
DFT	Density Functional Theory
GCMC	Grand Canonical Monte Carlo
CUS	Coordination unsaturated sites
ML	Machine learning
TTFTB	Tetrathiafulvalene tetrabenzoate
HIB	Hexaiminobenzene
DSBDC	2,5-disulfhydrylbenzene-1,4-dicarboxylic acid
DOBC	2,5-dihydroxybenzene-1,4-dicarboxylic acid
H_2BDT	5,5′-(1,4-phenylene)bis(1H-tetrazole))
VdP	Van der Pauw
TLM	Transfer length method
BTC	1,3,5-benzenetricarboxylate
SAM	Self-assembly monolayer

MUD	11-Mercapto-1-undecanol
MUDA	11-mercaptoundecanoic acid
HDT	1-hexadecanethiol
HmIM	2-methylimidazole
DMSO	Dimethylsulfoxide
PDMS	Polydimethylsiloxane
PaC	Parylene C
GIXRD	Grazing-incidence X-ray diffraction
SEM	Scanning electron microscopy
AFM	Atomic force microscopy
DMF	N,N-Dimethylformamide
UV	Ultraviolet
PMMA	Polymethyl methacrylate
OC	Optical contrast
RI	Refractive index
SE	Spectroscopic ellipsometry
RTP	Rapid thermal processing
HMDS	Hexamethyldisilane
MA	Mask aligner
IDEs	Interdigital electrodes
RIE	Reactive ion etching
$\mathbf{V_{gs}}$	Gate-source voltage
$\mathbf{I_{ds}}$	Drain-source current
$\mathbf{V_{ds}}$	Drain-source voltage
PCB	Printed circuit board
CNP	Charge neutrality point
ECL	Electrical double layer
DMP	Dimethyl phthalate

Appendix

DBP	Dibutyl phthalate
DnOP	Di-n-octyl phthalate
DCHP	Dicyclohexyl phthalate
DPP	Diphenyl phthalate
BBP	Benzyl butyl phthalate
MBP	Mono-butyl phthalate
DiBP	Diisobutyl phthalate
DEHP	Bis(2-ethylhexyl) phthalate
MEHP	Phthalic acid mono-2-ethylhexyl ester
PA	Phthalic acid
EDCs	Endocrine-disrupting chemicals
MCLs	Maximum contamination levels
BA	Benzoic acid
GC	Gas chromatography
HPLC	High-performance liquid chromatography
SERS	Surface-Enhanced Raman Scattering
PAEs	Phthalate esters
LoD	Limit of detection
C_{dl}	Double-layer capacitance
R_{ct}	Charge transfer resistance
CPE	Constant phase element
R_s	Series resistance
ROS	Reactive oxygen species
PLL	Poly-L-lysine
FIB	Focused ion beam
EDAX	Energy Dispersive X-ray Spectroscopy

Curriculum Vitae

01.2021 - current	PhD student
	RWTH Aachen University, Aachen, Germany
09.2017 – 07.2020	Master of Sciences
	University of Chinese Academy of Sciences, Beijing, China
08.2013 –07.2017	Bachelor of Engineering
	East China University of Science and Technology, Shanghai, China
11.1995	Born in Shangqiu, China

Publications and Conferences

Publications

1. **H. Jiang**, Z. Gao, C. Lubrano, C. L. Bovio, H. Bommes, A. Kauth, L. Baumann, B. Cheng, D. Murugan, J. Knoch, R. Waser, S. Ingebrandt, F. Santoro, V. Pachauri, Metal-organic frameworks as an active substrate for cell-interaction studies and cell-on-a-chip platforms, *Biosensors and Bioelectronics: X*, 2024, **19**,100487.
2. **H. Jiang,** B. Cheng, J. Knoch, S. Kumar, N. Dilbaghi, A. Deep, S. Ingebrandt, V. Pachauri, Programming layer-by-layer liquid phase epitaxy in microfluidics for realizing two-dimensional metal-organic framework sensor arrays, *Environmental Science: Nano*, 2025, **12**, 1849 - 1857.
3. A. Kauth, J. Wegener, **H. Jiang**, V. Pachauri, S. Ingebrandt, PEDOT:PSS electropolymerization protocol for microelectrodes enabling low-cost impedance-based cellular assays, *Applied Research*, 2025, **4**: e202400087.
4. **H. Jiang**, D. Murugan, B. Cheng, H. Amiri, A. Deep, J. Knoch, S. Ingebrandt, V. Pachauri, An on-chip accelerator for rational design of metal-organic frameworks, *in preparation*
5. L. Yuan, **H. Jiang**, G. Liang, W. Deng, Q. Li, W. Li, G. Xu, The exceptionally high moisture responsiveness of a new conductive-coordination-polymer based chemiresistive sensor, *CrystEngComm*, 2021, **23**, 3549-3556.

Supervised student works

1. B. Cheng. (B.Sc. Faculty of Electrical Engineering and Information Technology) Development of MOF thin-film sensors using localized layer-by-layer epitaxy via automated microfluidics. 2021
2. T. Wei. (B.Sc. Faculty of Electrical Engineering and Information Technology) Basic electrical characterizations of conductive 2D MOFs. 2022
3. S. Zhang. (B.Sc. Faculty of Electrical Engineering and Information Technology) Two-dimensional conductive metal-organic framework electrochemical transistors. 2022
4. I. B. Sönmez. (B.Sc. Faculty of Electrical Engineering and Information Technology) Temperature and solvent effect on the transistor behaviours of two-dimensional metal-organic frameworks. 2023

Conferences

1. **H. Jiang**, I. B. Sönmez, S. Ingebrandt, V. Pachauri, Temperature and solvent effect on the electrical characteristics of two-dimensional metal-organic frameworks. In: Engineering of Functional Interfaces, 2024, Linz, Australia
2. **H. Jiang**, B. Cheng, S. Ingebrandt, V. Pachauri, Cell-substrate impedance spectroscopy with system-integrated ion-sensing field-effect transistors based on metal-organic frameworks. In: Biosensor, 2023, Busan, South Korea
3. **H. Jiang**, S. Zhang, H. Bommes, B. Cheng, S. Ingebrandt, V. Pachauri, System-integrated metal-organic frameworks as novel device platforms for studies of cell-substrate interactions. In: 5th Conference on Impedance-Based Cellular Assays, 2023, Aachen, Germany
4. **H. Jiang**, B. Cheng, S. Ingebrandt, V. Pachauri, Revisiting Fresnel's law with 2D metal-organic frameworks for rapid detection of phthalates in the environment. In: Engineering of Functional Interfaces, 2022, Maastricht, The Netherlands
5. **H. Jiang**, B. Cheng, S. Scholz, J. Knoch, S. Ingebrandt, V. Pachauri, A novel optical approach to high-resolution thickness and roughness analysis of two-dimensional metal-organic frameworks. In: 12th edition of the largest European Event in Graphene and 2D Materials, 2022, Aachen, Germany
6. **H. Jiang**, B. Cheng, S. Ingebrandt, V. Pachauri, System integration of two-dimensional metal-organic frameworks for ion-sensitive field-effect transistors. In: 8th International Conference on Metal-Organic Frameworks and Open Framework Compounds, 2022, Dresden, Germany

References

1. A. P. Dorey, Semiconductor and microelectronic sensors, *Physics in Technology*, 1981, **12**, 24-28.
2. M. R. Haskard, Microelectronic sensor technology, *Journal of Physics E: Scientific Instruments*, 1986, **19**, 891-896.
3. A. Hierlemann, CMOS-based bio/chemosensor and bioelectronic microsystems, *Procedia Chemistry*, 2009, **1**, 5-8.
4. W. Henning, in *Festkörperprobleme 22: Plenary Lectures of the 46th Annual Meeting of the German Physical Society (DPG) and of the Divisions "Semiconductor Physics" "Metal Physics" "Low Temperature Physics" "Thermodynamics and Statistical Physics" "Thin Films" "Surface Physics" "Magnetism" Münster, March 29 - April 2, 1982*, ed. P. Grosse Aachen, Springer Berlin Heidelberg, Berlin, Heidelberg, 1982, DOI: 10.1007/BFb0107940, pp. 189-200.
5. T. He, F. Wen, Y. Yang, X. Le, W. Liu and C. Lee, Emerging wearable chemical sensors enabling advanced integrated systems toward personalized and preventive medicine, *Analytical Chemistry*, 2023, **95**, 490-514.
6. H. J. N. P. D. Mello and M. Mulato, Well-established materials in microelectronic devices systems for differential-mode extended-gate field effect transistor chemical sensors, *Microelectronic Engineering*, 2016, **160**, 73-80.
7. S. Joo and R. B. Brown, Chemical sensors with integrated electronics, *Chemical Reviews*, 2008, **108**, 638-651.
8. M. Mirzaei and M. Sawan, Microelectronics-based biosensors dedicated to the detection of neurotransmitters: a review, *Sensors*, 2014, **14**, 17981-18008.
9. M. Gronow and M. Boutelle, in *Biotechnology-The Science and the Business*, CRC Press, 2020, pp. 367-385.
10. B. G. Yacobi, in *Semiconductor Materials: An Introduction to Basic Principles*, ed. B. G. Yacobi, Springer US, Boston, MA, 2003, DOI: 10.1007/0-306-47942-7_6, pp. 135-170.
11. M. A. Berding, A. Sher and M. Van Schilfgaarde, Group-IV semiconductor compounds, *Physical Review B*, 1997, **56**, 3885.
12. X. Blase, E. Bustarret, C. Chapelier, T. Klein and C. Marcenat, Superconducting group-IV semiconductors, *Nature Materials*, 2009, **8**, 375-382.
13. J. A. del Alamo, Nanometre-scale electronics with III-V compound semiconductors, *Nature*, 2011, **479**, 317-323.
14. T. F. Kuech, III-V compound semiconductors: Growth and structures, *Progress in Crystal Growth and Characterization of Materials*, 2016, **62**, 352-370.
15. G. Iannaccone, C. Sbrana, I. Morelli and S. Strangio, Power electronics based on wide-bandgap semiconductors: Opportunities and challenges, *IEEE Access*, 2021, **9**, 139446-139456.
16. K. Takahashi, A. Yoshikawa and A. Sandhu, in *Verlag Berlin Heidelberg*, Springer, 2007.
17. K. Takimiya, S. Shinamura, I. Osaka and E. Miyazaki, Thienoacene-based organic semiconductors, *Advanced Materials*, 2011, **23**, 4347-4370.
18. Q. Zhang, W. Hu, H. Sirringhaus and K. Müllen, Recent progress in emerging organic semiconductors, *Advanced Materials*, 2022, **34**, e2108701.

19. M. H. Chuang, K. C. Chiu, Y. T. Lin, G. Tulevski, P. H. Chen, A. Pezeshki, C. J. Chen, P. Y. Chen, L. J. Chen and S. J. Han, Integrated low-dimensional semiconductors for scalable low-power CMOS Logic, *Advanced Functional Materials*, 2023, **33**, 2212722.
20. J. Fang, Z. Zhou, M. Xiao, Z. Lou, Z. Wei and G. Shen, Recent advances in low-dimensional semiconductor nanomaterials and their applications in high-performance photodetectors, *InfoMat*, 2020, **2**, 291-317.
21. R. K. Parashar, P. Jash, M. Zharnikov and P. C. Mondal, Metal-organic frameworks in semiconductor devices, *Angewandte Chemie International Edition*, 2024, **63**, e202317413.
22. M. Usman, S. Mendiratta and K. L. Lu, Semiconductor metal-organic frameworks: future low-bandgap materials, *Advanced Materials*, 2017, **29**, 1605071.
23. L. Yang and D.-C. Wei, Semiconducting covalent organic frameworks: a type of two-dimensional conducting polymers, *Chinese Chemical Letters*, 2016, **27**, 1395-1404.
24. Y. Zhu, S. Jiang, X. Jing and X. Feng, Electrically conductive 2D covalent organic frameworks, *Trends in Chemistry*, 2022, **4**, 128-141.
25. J. P. Chambers, B. P. Arulanandam, L. L. Matta, A. Weis and J. J. Valdes, Biosensor recognition elements, *Current issues in molecular biology*, 2008, **10**, 1-12.
26. D. S. Dkhar, R. Kumari, S. Mahapatra, R. Kumar, T. Tripathi and P. Chandra, Antibody-receptor bioengineering and its implications in designing bioelectronic devices, *International Journal of Biological Macromolecules*, 2022, **218**, 225-242.
27. A. Gupta, S. Sharma and R. Goswami, Review-Silicon based ISFETs: Architecture, fabrication process, sensing membrane, and spatial variation, *ECS Journal of Solid State Science and Technology*, 2024, **13**, 047006.
28. A. Chieng, Z. Wan and S. Wang, Recent advances in real-time label-free detection of small molecules, *Biosensors*, 2024, **14**, 80.
29. R. Peltomaa, B. Glahn-Martínez, E. Benito-Peña and M. C. Moreno-Bondi, Optical biosensors for label-free detection of small molecules, *Sensors*, 2018, **18**, 4126.
30. A. Vilan and D. Cahen, Chemical modification of semiconductor surfaces for molecular electronics, *Chemical reviews*, 2017, **117**, 4624-4666.
31. R. Freund, S. Canossa, S. M. Cohen, W. Yan, H. Deng, V. Guillerm, M. Eddaoudi, D. G. Madden, D. Fairen-Jimenez and H. Lyu, 25 years of reticular chemistry, *Angewandte Chemie International Edition*, 2021, **60**, 23946-23974.
32. H. Jiang, D. Alezi and M. Eddaoudi, A reticular chemistry guide for the design of periodic solids, *Nature Reviews Materials*, 2021, **6**, 466-487.
33. S. Kitagawa, Metal-organic frameworks (MOFs), *Chemical Society Reviews*, 2014, **43**, 5415-5418.
34. N. Stock and S. Biswas, Synthesis of metal-organic frameworks (MOFs): routes to various MOF topologies, morphologies, and composites, *Chemical reviews*, 2012, **112**, 933-969.
35. K. A. Adegoke and N. W. Maxakato, Porous metal-organic framework (MOF)-based and MOF-derived electrocatalytic materials for energy conversion, *Materials Today Energy*, 2021, **21**, 100816.
36. M. Daniel, G. Mathew, M. Anpo and B. Neppolian, MOF based electrochemical sensors for the detection of physiologically relevant biomolecules: An overview, *Coordination Chemistry Reviews*, 2022, **468**, 214627.
37. R. Du, Y. Wu, Y. Yang, T. Zhai, T. Zhou, Q. Shang, L. Zhu, C. Shang and Z. Guo, Porosity engineering of MOF-based materials for electrochemical energy storage, *Advanced Energy Materials*, 2021, **11**, 2100154.
38. W. Fan, X. Zhang, Z. Kang, X. Liu and D. Sun, Isoreticular chemistry within metal-organic frameworks for gas storage and separation, *Coordination Chemistry Reviews*, 2021, **443**, 213968.

References

39. Y.-M. Jo, Y. K. Jo, J.-H. Lee, H. W. Jang, I.-S. Hwang and D. J. Yoo, MOF-based chemiresistive gas sensors: toward new functionalities, *Advanced Materials*, 2023, **35**, 2206842.
40. J. Liu, Y. Chen, X. Feng and R. Dong, Conductive 2D conjugated metal-organic framework thin films: synthesis and functions for (opto-)electronics, *Small Structures*, 2022, **3**, 2100210.
41. X. Mu, W. Wang, C. Sun, J. Wang, C. Wang and M. Knez, Recent progress on conductive metal-organic framework films, *Advanced Materials Interfaces*, 2021, **8**, 2002151.
42. Q. Qian, P. A. Asinger, M. J. Lee, G. Han, K. Mizrahi Rodriguez, S. Lin, F. M. Benedetti, A. X. Wu, W. S. Chi and Z. P. Smith, MOF-based membranes for gas separations, *Chemical Reviews*, 2020, **120**, 8161-8266.
43. M. M. Sabzehmeidani, S. Gafari, S. jamali and M. Kazemzad, Concepts, fabrication and applications of MOF thin films in optoelectronics: A review, *Applied Materials Today*, 2024, **38**, 102153.
44. Y. Shen, T. Pan, L. Wang, Z. Ren, W. Zhang and F. Huo, Programmable logic in metal-organic frameworks for catalysis, *Advanced Materials*, 2021, **33**, 2007442.
45. Y. Shen, A. Tissot and C. Serre, Recent progress on MOF-based optical sensors for VOC sensing, *Chemical Science*, 2022, **13**, 13978-14007.
46. M. d. J. Velásquez-Hernández, M. Linares-Moreau, E. Astria, F. Carraro, M. Z. Alyami, N. M. Khashab, C. J. Sumby, C. J. Doonan and P. Falcaro, Towards applications of bioentities@MOFs in biomedicine, *Coordination Chemistry Reviews*, 2021, **429**, 213651.
47. A. A. Vodyashkin, A. V. Sergorodceva, P. Kezimana and Y. M. Stanishevskiy, Metal-organic framework (MOF) - a universal material for biomedicine, *International Journal of Molecular Sciences*, 2023, **24**. 7819.
48. M. Wang, R. Dong and X. Feng, Two-dimensional conjugated metal-organic frameworks (2D c-MOFs): chemistry and function for MOFtronics, *Chemical Society Reviews*, 2021, **50**, 2764-2793.
49. A. Felix Sahayaraj, H. Joy Prabu, J. Maniraj, M. Kannan, M. Bharathi, P. Diwahar and J. Salamon, Metal-organic frameworks (MOFs): the next generation of materials for catalysis, gas storage, and separation, *Journal of Inorganic and Organometallic Polymers and Materials*, 2023, **33**, 1757-1781.
50. T. Irshad, M. Saeed, V. Aiman, M. Ali, H. Ahsan, S. Ameen and M. Munir, Metal-organic frameworks for energy storage applications: Recent advances, *Journal of the Chinese Chemical Society*, 2023, **70**, 1692-1714.
51. L. Liu, Q. Xu and Q. L. Zhu, Electrically conductive metal-organic frameworks for electrocatalytic applications, *Advanced Energy and Sustainability Research*, 2021, **2**, 2100100.
52. T. Xia, Y. Lin, W. Li and M. Ju, Photocatalytic degradation of organic pollutants by MOFs based materials: A review, *Chinese Chemical Letters*, 2021, **32**, 2975-2984.
53. J. Yan, T. Liu, X. Liu, Y. Yan and Y. Huang, Metal-organic framework-based materials for flexible supercapacitor application, *Coordination Chemistry Reviews*, 2022, **452**, 214300.
54. X. Fang, B. Zong and S. Mao, Metal-organic framework-based sensors for environmental contaminant sensing, *Nano-micro letters*, 2018, **10**, 1-19.
55. Y. M. Jo, Y. K. Jo, J. H. Lee, H. W. Jang, I. S. Hwang and D. J. Yoo, MOF-based chemiresistive gas sensors: toward new functionalities, *Advanced Materials*, 2023, **35**, 2206842.

56. X. Mu, W. Wang, C. Sun, J. Wang, C. Wang and M. Knez, Recent progress on conductive metal-organic framework films, *Advanced Materials Interfaces*, 2021, **8**, 2002151.
57. H. Furukawa, K. E. Cordova, M. O'Keeffe and O. M. Yaghi, The chemistry and applications of metal-organic frameworks, *Science*, 2013, **341**, 1230444.
58. S. Kitagawa, R. Kitaura and S. i. Noro, Functional porous coordination polymers, *Angewandte Chemie International Edition*, 2004, **43**, 2334-2375.
59. H.-C. Z. J. R. L. O. M. Yaghi, Introduction to metal-organic frameworks, *Chemical Reviews*, 2012, **112**, 673-674.
60. A. I. Inamdar, S. Kamal, M. Usman, M.-H. Chiang and K.-L. Lu, Design strategies for dielectric metal-organic frameworks and their applications in microelectronic devices, *Coordination Chemistry Reviews*, 2024, **502**, 215596.
61. P. Thanasekaran, C.-H. Su, Y.-H. Liu and K.-L. Lu, Hydrophobic Metal-organic frameworks and derived composites for microelectronics applications, *Chemistry – A European Journal*, 2021, **27**, 16543-16563.
62. R. Masoudifar, N. Pouyanfar, D. Liu, M. Ahmadi, B. Landi, M. Akbari, S. Moayeri-Jolandan, F. Ghorbani-Bidkorpeh, E. Asadian and M.-A. Shahbazi, Surface engineered metal-organic frameworks as active targeting nanomedicines for mono- and multi-therapy, *Applied Materials Today*, 2022, **29**, 101646.
63. W. Xu, B. Tu, Q. Liu, Y. Shu, C.-C. Liang, C. S. Diercks, O. M. Yaghi, Y.-B. Zhang, H. Deng and Q. Li, Anisotropic reticular chemistry, *Nature Reviews Materials*, 2020, **5**, 764-779.
64. O. M. Yaghi, M. O'Keeffe, N. W. Ockwig, H. K. Chae, M. Eddaoudi and J. Kim, Reticular synthesis and the design of new materials, *Nature*, 2003, **423**, 705-714.
65. R. Freund, S. Canossa, S. M. Cohen, W. Yan, H. Deng, V. Guillerm, M. Eddaoudi, D. G. Madden, D. Fairen-Jimenez, H. Lyu, L. K. Macreadie, Z. Ji, Y. Zhang, B. Wang, F. Haase, C. Wöll, O. Zaremba, J. Andreo, S. Wuttke and C. S. Diercks, 25 Years of reticular chemistry, *Angewandte Chemie International Edition*, 2021, **60**, 23946-23974.
66. E. Ploetz, H. Engelke, U. Lächelt and S. Wuttke, The chemistry of reticular framework nanoparticles: MOF, ZIF, and COF materials, *Advanced Functional Materials*, 2020, **30**, 1909062.
67. A. Dutta, Y. Pan, J.-Q. Liu and A. Kumar, Multicomponent isoreticular metal-organic frameworks: Principles, current status and challenges, *Coordination Chemistry Reviews*, 2021, **445**, 214074.
68. H. Zhang, X. Hu, T. Li, Y. Zhang, H. Xu, Y. Sun, X. Gu, C. Gu, J. Luo and B. Gao, MIL series of metal organic frameworks (MOFs) as novel adsorbents for heavy metals in water: A review, *Journal of Hazardous Materials*, 2022, **429**, 128271.
69. H. Kim and C. S. Hong, MOF-74-type frameworks: tunable pore environment and functionality through metal and ligand modification, *CrystEngComm*, 2021, **23**, 1377-1387.
70. B. Chen, Z. Yang, Y. Zhu and Y. Xia, Zeolitic imidazolate framework materials: recent progress in synthesis and applications, *Journal of Materials Chemistry A*, 2014, **2**, 16811-16831.
71. S. Wang, L. Luo, A. Wu, D. Wang, L. Wang, Y. Jiao and C. Tian, Recent advances in tailoring zeolitic imidazolate frameworks (ZIFs) and their derived materials based on hard template strategy for multifunctional applications, *Coordination Chemistry Reviews*, 2024, **498**, 215464.
72. S. A. Hodgson, J. Adamson, S. J. Hunt, M. J. Cliffe, A. B. Cairns, A. L. Thompson, M. G. Tucker, N. P. Funnell and A. L. Goodwin, Negative area compressibility in silver(I) tricyanomethanide, *Chemical Communications*, 2014, **50**, 5264-5266.

References

73. M. Hmadeh, Z. Lu, Z. Liu, F. Gándara, H. Furukawa, S. Wan, V. Augustyn, R. Chang, L. Liao, F. Zhou, E. Perre, V. Ozolins, K. Suenaga, X. Duan, B. Dunn, Y. Yamamto, O. Terasaki and O. M. Yaghi, New porous crystals of extended metal-catecholates, *Chemistry of Materials*, 2012, **24**, 3511-3513.
74. S. K. Elsaidi, M. H. Mohamed, C. M. Simon, E. Braun, T. Pham, K. A. Forrest, W. Xu, D. Banerjee, B. Space, M. J. Zaworotko and P. K. Thallapally, Effect of ring rotation upon gas adsorption in SIFSIX-3-M (M = Fe, Ni) pillared square grid networks, *Chemical Science*, 2017, **8**, 2373-2380.
75. W. G. Guimarães and G. F. de Lima, Investigating greenhouse gas adsorption in MOFs SIFSIX-2-Cu, SIFSIX-2-Cu-i, and SIFSIX-3-Cu through computational studies, *Journal of Molecular Modeling*, 2020, **26**, 188.
76. S. A. Younis, N. Bhardwaj, S. K. Bhardwaj, K.-H. Kim and A. Deep, Rare earth metal-organic frameworks (RE-MOFs): Synthesis, properties, and biomedical applications, *Coordination Chemistry Reviews*, 2021, **429**, 213620.
77. L. Öhrström and K. Larsson, *Molecule-based materials: The structural network approach*, Elsevier, 2005.
78. S. Vagin, A. K. Ott and B. Rieger, Paddle-wheel zinc carboxylate clusters as building units for metal-organic frameworks, *Chemie Ingenieur Technik*, 2007, **79**, 767-780.
79. S. S. Y. Chui, S. M. F. Lo, J. P. H. Charmant, A. G. Orpen and I. D. Williams, A chemically functionalizable nanoporous material $[Cu_3(TMA)_2(H_2O)_3]_n$, *Science*, 1999, **283**, 1148-1150.
80. H. Li, M. Eddaoudi, T. L. Groy and O. M. Yaghi, Establishing microporosity in open metal−organic frameworks: gas sorption isotherms for Zn(BDC) (BDC = 1,4-Benzenedicarboxylate), *Journal of the American Chemical Society*, 1998, **120**, 8571-8572.
81. G. Zhan, L. Fan, F. Zhao, Z. Huang, B. Chen, X. Yang and S.-f. Zhou, Fabrication of ultrathin 2D Cu-BDC nanosheets and the derived integrated MOF nanocomposites, *Advanced Functional Materials*, 2019, **29**, 1806720.
82. C. A. Williams, A. J. Blake, P. Hubberstey and M. Schröder, A unique example of a 36 tessellated 2-D net based on a tri-nuclear zinc(II)-1,4-benzenedicarboxylate framework, *Chemical Communications*, 2005, DOI: 10.1039/B509929C, 5435-5437.
83. H. Deng, S. Grunder, K. E. Cordova, C. Valente, H. Furukawa, M. Hmadeh, F. Gándara, A. C. Whalley, Z. Liu, S. Asahina, H. Kazumori, M. O'Keeffe, O. Terasaki, J. F. Stoddart and O. M. Yaghi, Large-pore apertures in a series of metal-organic frameworks, *Science*, 2012, **336**, 1018-1023.
84. Y.-W. Li, J.-P. Zhao, L.-F. Wang and X.-H. Bu, An Fe-based MOF constructed from paddle-wheel and rod-shaped SBUs involved in situ generated acetate, *CrystEngComm*, 2011, **13**, 6002-6006.
85. T. Pham, K. A. Forrest, R. Banerjee, G. Orcajo, J. Eckert and B. Space, Understanding the H_2 sorption trends in the M-MOF-74 series (M = Mg, Ni, Co, Zn), *The Journal of Physical Chemistry C*, 2015, **119**, 1078-1090.
86. F. M. Amombo Noa, M. Abrahamsson, E. Ahlberg, O. Cheung, C. R. Göb, C. J. McKenzie and L. Öhrström, A unified topology approach to dot-, rod-, and sheet-MOFs, *Chem*, 2021, **7**, 2491-2512.
87. D. Banerjee, S. J. Kim and J. B. Parise, Lithium based metal-organic framework with exceptional stability, *Crystal Growth & Design*, 2009, **9**, 2500-2503.
88. W. Lu, Z. Wei, Z.-Y. Gu, T.-F. Liu, J. Park, J. Park, J. Tian, M. Zhang, Q. Zhang, T. Gentle Iii, M. Bosch and H.-C. Zhou, Tuning the structure and function of metal-organic frameworks via linker design, *Chemical Society Reviews*, 2014, **43**, 5561-5593.

89. H. Ghasempour, K.-Y. Wang, J. A. Powell, F. ZareKarizi, X.-L. Lv, A. Morsali and H.-C. Zhou, Metal-organic frameworks based on multicarboxylate linkers, *Coordination Chemistry Reviews*, 2021, **426**, 213542.
90. H. Li, M. Eddaoudi, M. O'Keeffe and O. M. Yaghi, Design and synthesis of an exceptionally stable and highly porous metal-organic framework, *Nature*, 1999, **402**, 276-279.
91. D. Sheberla, L. Sun, M. A. Blood-Forsythe, S. Er, C. R. Wade, C. K. Brozek, A. Aspuru-Guzik and M. Dincă, High Electrical Conductivity in Ni_3(2,3,6,7,10,11-hexaiminotriphenylene)$_2$, a Semiconducting metal-organic graphene analogue, *Journal of the American Chemical Society*, 2014, **136**, 8859-8862.
92. W. Morris, C. J. Doonan, H. Furukawa, R. Banerjee and O. M. Yaghi, Crystals as molecules: postsynthesis covalent functionalization of zeolitic imidazolate frameworks, *Journal of the American Chemical Society*, 2008, **130**, 12626-12627.
93. K. S. Park, Z. Ni, A. P. Côté, J. Y. Choi, R. Huang, F. J. Uribe-Romo, H. K. Chae, M. O'Keeffe and O. M. Yaghi, Exceptional chemical and thermal stability of zeolitic imidazolate frameworks, *Proceedings of the National Academy of Sciences*, 2006, **103**, 10186-10191.
94. S. Mandal, S. Natarajan, P. Mani and A. Pankajakshan, Post-synthetic modification of metal-organic frameworks toward applications, *Advanced Functional Materials*, 2021, **31**, 2006291.
95. M.-L. Hu, M. Y. Masoomi and A. Morsali, Template strategies with MOFs, *Coordination Chemistry Reviews*, 2019, **387**, 415-435.
96. N. Zhao, K. Cai and H. He, The synthesis of metal-organic frameworks with template strategies, *Dalton Transactions*, 2020, **49**, 11467-11479.
97. K. Mukherjee and Y. J. Colón, Machine learning and descriptor selection for the computational discovery of metal-organic frameworks, *Molecular Simulation*, 2021, **47**, 857-877.
98. H. Demir, H. Daglar, H. C. Gulbalkan, G. O. Aksu and S. Keskin, Recent advances in computational modeling of MOFs: From molecular simulations to machine learning, *Coordination Chemistry Reviews*, 2023, **484**, 215112.
99. L. Jiao, J. Y. R. Seow, W. S. Skinner, Z. U. Wang and H.-L. Jiang, Metal-organic frameworks: Structures and functional applications, *Materials Today*, 2019, **27**, 43-68.
100. L. Song, J. Zhang, L. Sun, F. Xu, F. Li, H. Zhang, X. Si, C. Jiao, Z. Li, S. Liu, Y. Liu, H. Zhou, D. Sun, Y. Du, Z. Cao and Z. Gabelica, Mesoporous metal-organic frameworks: design and applications, *Energy & Environmental Science*, 2012, **5**, 7508-7520.
101. L. S. Xie, G. Skorupskii and M. Dinca, Electrically conductive metal-organic frameworks, *Chemical Reviews*, 2020, **120**, 8536-8580.
102. M. L. Aubrey, B. M. Wiers, S. C. Andrews, T. Sakurai, S. E. Reyes-Lillo, S. M. Hamed, C.-J. Yu, L. E. Darago, J. A. Mason, J.-O. Baeg, F. Grandjean, G. J. Long, S. Seki, J. B. Neaton, P. Yang and J. R. Long, Electron delocalization and charge mobility as a function of reduction in a metal-organic framework, *Nature Materials*, 2018, **17**, 625-632.
103. L. Sun, C. H. Hendon, M. A. Minier, A. Walsh and M. Dincă, Million-fold electrical conductivity enhancement in Fe_2(DEBDC) versus Mn_2(DEBDC) (E = S, O), *Journal of the American Chemical Society*, 2015, **137**, 6164-6167.
104. L. Sun, T. Miyakai, S. Seki and M. Dincă, Mn_2(2,5-disulfhydrylbenzene-1,4-dicarboxylate): A microporous metal-organic framework with infinite $(-Mn-S-)_\infty$ chains and high intrinsic charge mobility, *Journal of the American Chemical Society*, 2013, **135**, 8185-8188.
105. L. S. Xie, L. Sun, R. Wan, S. S. Park, J. A. DeGayner, C. H. Hendon and M. Dincă, Tunable mixed-valence doping toward record electrical conductivity in a three-

dimensional metal-organic framework, *Journal of the American Chemical Society*, 2018, **140**, 7411-7414.

106. G. Skorupskii, B. A. Trump, T. W. Kasel, C. M. Brown, C. H. Hendon and M. Dincă, Efficient and tunable one-dimensional charge transport in layered lanthanide metal-organic frameworks, *Nature Chemistry*, 2020, **12**, 131-136.
107. L. S. Xie, S. S. Park, M. J. Chmielewski, H. Liu, R. A. Kharod, L. Yang, M. G. Campbell and M. Dincă, Isoreticular linker substitution in conductive metal-organic frameworks with through-space transport pathways, *Angewandte Chemie International Edition*, 2020, **59**, 19623-19626.
108. R. Dong, Z. Zhang, D. C. Tranca, S. Zhou, M. Wang, P. Adler, Z. Liao, F. Liu, Y. Sun, W. Shi, Z. Zhang, E. Zschech, S. C. B. Mannsfeld, C. Felser and X. Feng, A coronene-based semiconducting two-dimensional metal-organic framework with ferromagnetic behavior, *Nature Communications*, 2018, **9**, 2637.
109. H. Jia, Y. Yao, J. Zhao, Y. Gao, Z. Luo and P. Du, A novel two-dimensional nickel phthalocyanine-based metal-organic framework for highly efficient water oxidation catalysis, *Journal of Materials Chemistry A*, 2018, **6**, 1188-1195.
110. M. Wang, H. Shi, P. Zhang, Z. Liao, M. Wang, H. Zhong, F. Schwotzer, A. S. Nia, E. Zschech, S. Zhou, S. Kaskel, R. Dong and X. Feng, Phthalocyanine-based 2D conjugated metal-organic framework nanosheets for high-performance micro-supercapacitors, *Advanced Functional Materials*, 2020, **30**, 2002664.
111. C. Yang, R. Dong, M. Wang, P. S. Petkov, Z. Zhang, M. Wang, P. Han, M. Ballabio, S. A. Bräuninger, Z. Liao, J. Zhang, F. Schwotzer, E. Zschech, H.-H. Klauss, E. Cánovas, S. Kaskel, M. Bonn, S. Zhou, T. Heine and X. Feng, A semiconducting layered metal-organic framework magnet, *Nature Communications*, 2019, **10**, 3260.
112. R. Dong, P. Han, H. Arora, M. Ballabio, M. Karakus, Z. Zhang, C. Shekhar, P. Adler, P. S. Petkov, A. Erbe, S. C. B. Mannsfeld, C. Felser, T. Heine, M. Bonn, X. Feng and E. Cánovas, High-mobility band-like charge transport in a semiconducting two-dimensional metal-organic framework, *Nature Materials*, 2018, **17**, 1027-1032.
113. K. W. Nam, S. S. Park, R. dos Reis, V. P. Dravid, H. Kim, C. A. Mirkin and J. F. Stoddart, Conductive 2D metal-organic framework for high-performance cathodes in aqueous rechargeable zinc batteries, *Nature Communications*, 2019, **10**, 4948.
114. A. Chandresh, C. Wöll and L. Heinke, Metal-organic framework thin films grown on functionalized graphene as solid-state ion-gated FETs, *Advanced Functional Materials*, 2023, **33**, 2211880.
115. G. Ding, B. Yang, K. Zhou, C. Zhang, Y. Wang, J.-Q. Yang, S.-T. Han, Y. Zhai, V. A. L. Roy and Y. Zhou, Synaptic plasticity and filtering emulated in metal-organic frameworks nanosheets based transistors, *Advanced Electronic Materials*, 2020, **6**, 1900978.
116. S. Kumar, Y. Pramudya, K. Müller, A. Chandresh, S. Dehm, S. Heidrich, A. Fediai, D. Parmar, D. Perera, M. Rommel, L. Heinke, W. Wenzel, C. Wöll and R. Krupke, Sensing molecules with metal-organic framework functionalized graphene transistors, *Advanced Materials*, 2021, **33**, 2103316.
117. E. H. Kwon, M. Kim, C. Y. Lee, M. Kim and Y. D. Park, Meta-organic-framework-decorated carbon nanofibers with enhanced gas sensitivity when incorporated into an organic semiconductor-based gas sensor, *ACS Applied Materials & Interfaces*, 2022, **14**, 10637-10647.
118. S. Mallik, S. Chand Pal, S. Acharyya, S. P. Verma, A. Mandal, P. K. Guha, M. C. Das and D. K. Goswami, MOF-assimilated high-sensitive organic field-effect transistors for rapid detection of a chemical warfare agent, *ACS Applied Materials & Interfaces*, 2023, **15**, 30580-30590.

119. B. Wang, H. Li, H. Tan, Y. Gu, L. Chen, L. Ji, Z. Sun, Q. Sun, S. Ding, D. W. Zhang and H. Zhu, Gate-modulated high-response field-effect transistor-type gas sensor based on the MoS_2/metal-organic framework heterostructure, *ACS Applied Materials & Interfaces*, 2022, **14**, 42356-42364.
120. S. Yuvaraja, S. G. Surya, V. Chernikova, M. T. Vijjapu, O. Shekhah, P. M. Bhatt, S. Chandra, M. Eddaoudi and K. N. Salama, Realization of an ultrasensitive and highly selective ofet no2 sensor: the synergistic combination of PDVT-10 polymer and porphyrin-MOF, *ACS Applied Materials & Interfaces*, 2020, **12**, 18748-18760.
121. G. Lu, B. Zong, T. Tao, Y. Yang, Q. Li and S. Mao, High-performance $Ni_3(HHTP)_2$ film-based flexible field-effect transistor gas sensors, *ACS Sensors*, 2024, **9**, 1916-1926.
122. P. W. Sayyad, A. A. Farooqui, N. N. Ingle, T. Al-Gahouari, G. A. Bodkhe, M. M. Mahadik, S. M. Shirsat and M. D. Shirsat, High carrier mobility and environmentally stable microporous zeolite imidazolate framework (ZIF-67): A field-effect transistor (FET) approach, *Chemical Physics Letters*, 2021, **776**, 138690.
123. G. Wu, J. Huang, Y. Zang, J. He and G. Xu, Porous field-effect transistors based on a semiconductive metal-organic framework, *Journal of the American Chemical Society*, 2017, **139**, 1360-1363.
124. S. Shen, P. Tan, Y. Tang, G. Duan and Y. Luo, Adjustable synthesis of ni-based metal-organic framework membranes and their field-effect transistor sensors for mercury detection, *ACS Applied Electronic Materials*, 2022, **4**, 622-630.
125. J. Song, H. Liu, Z. Zhao, X. Guo, C.-k. Liu, S. Griggs, A. Marks, Y. Zhu, H. K.-w. Law, I. McCulloch and F. Yan, 2D metal-organic frameworks for ultraflexible electrochemical transistors with high transconductance and fast response speeds, *Science Advances*, 2023, **9**, eadd9627.
126. J. Song, J. Zheng, A. Yang, H. Liu, Z. Zhao, N. Wang and F. Yan, Metal-organic framework transistors for dopamine sensing, *Materials Chemistry Frontiers*, 2021, **5**, 3422-3427.
127. B. Wang, Y. Luo, L. Gao, B. Liu and G. Duan, High-performance field-effect transistor glucose biosensors based on bimetallic Ni/Cu metal-organic frameworks, *Biosensors and Bioelectronics*, 2021, **171**, 112736.
128. J. E. Ellis, S. E. Crawford and K.-J. Kim, Metal-organic framework thin films as versatile chemical sensing materials, *Materials Advances*, 2021, **2**, 6169-6196.
129. O. Shekhah, H. Wang, S. Kowarik, F. Schreiber, M. Paulus, M. Tolan, C. Sternemann, F. Evers, D. Zacher, R. A. Fischer and C. Wöll, Step-by-step route for the synthesis of metal-organic frameworks, *Journal of the American Chemical Society*, 2007, **129**, 15118-15119.
130. A. L. Semrau, Z. Zhou, S. Mukherjee, M. Tu, W. Li and R. A. Fischer, Surface-mounted metal-organic frameworks: past, present, and future perspectives, *Langmuir*, 2021, **37**, 6847-6863.
131. Z.-G. Gu, A. Pfriem, S. Hamsch, H. Breitwieser, J. Wohlgemuth, L. Heinke, H. Gliemann and C. Wöll, Transparent films of metal-organic frameworks for optical applications, *Microporous and Mesoporous Materials*, 2015, **211**, 82-87.
132. H. K. Arslan, O. Shekhah, D. C. F. Wieland, M. Paulus, C. Sternemann, M. A. Schroer, S. Tiemeyer, M. Tolan, R. A. Fischer and C. Wöll, Intercalation in layered metal-organic frameworks: reversible inclusion of an extended π-system, *Journal of the American Chemical Society*, 2011, **133**, 8158-8161.
133. H. K. Arslan, O. Shekhah, J. Wohlgemuth, M. Franzreb, R. A. Fischer and C. Wöll, High-throughput fabrication of uniform and homogenous MOF coatings, *Advanced Functional Materials*, 2011, **21**, 4228-4231.

References

134. V. Chernikova, O. Shekhah and M. Eddaoudi, Advanced fabrication method for the preparation of mof thin films: liquid-phase epitaxy approach meets spin coating method, *ACS Applied Materials & Interfaces*, 2016, **8**, 20459-20464.
135. Y. Zhang and C.-H. Chang, Metal-organic framework thin films: fabrication, modification, and patterning, *Processes*, 2020, **8**, 377.
136. P. Falcaro, D. Buso, A. J. Hill and C. M. Doherty, Patterning techniques for metal organic frameworks, *Advanced Materials*, 2012, **24**, 3153-3168.
137. J. Aizenberg, A. J. Black and G. M. Whitesides, Control of crystal nucleation by patterned self-assembled monolayers, *Nature*, 1999, **398**, 495-498.
138. J. A. Liddle and G. M. Gallatin, Nanomanufacturing: A Perspective, *ACS Nano*, 2016, **10**, 2995-3014.
139. I. Stassen, M. Styles, G. Grenci, Hans V. Gorp, W. Vanderlinden, Steven D. Feyter, P. Falcaro, D. D. Vos, P. Vereecken and R. Ameloot, Chemical vapour deposition of zeolitic imidazolate framework thin films, *Nature Materials*, 2016, **15**, 304-310.
140. K. Okada, R. Ricco, Y. Tokudome, M. J. Styles, A. J. Hill, M. Takahashi and P. Falcaro, Copper conversion into $Cu(OH)_2$ nanotubes for positioning $Cu_3(BTC)_2$ MOF crystals: controlling the growth on flat plates, 3D architectures, and as patterns, *Advanced Functional Materials*, 2014, **24**, 1969-1977.
141. I. Stassen, N. Campagnol, J. Fransaer, P. Vereecken, D. De Vos and R. Ameloot, Solvent-free synthesis of supported ZIF-8 films and patterns through transformation of deposited zinc oxide precursors, *CrystEngComm*, 2013, **15**, 9308-9311.
142. T. Ladnorg, A. Welle, S. Heißler, C. Wöll and H. Gliemann, Site-selective growth of surface-anchored metal-organic frameworks on self-assembled monolayer patterns prepared by AFM nanografting, *Beilstein Journal of Nanotechnology*, 2013, **4**, 638-648.
143. S. Li, W. Shi, G. Lu, S. Li, S. C. J. Loo and F. Huo, Unconventional nucleation and oriented growth of ZIF-8 crystals on non-polar surface, *Advanced Materials*, 2012, **24**, 5954-5958.
144. J.-L. Zhuang, D. Ceglarek, S. Pethuraj and A. Terfort, Rapid room-temperature synthesis of metal-organic framework HKUST-1 crystals in bulk and as oriented and patterned thin films, *Advanced Functional Materials*, 2011, **21**, 1442-1447.
145. R. Ameloot, E. Gobechiya, H. Uji-i, J. A. Martens, J. Hofkens, L. Alaerts, B. F. Sels and D. E. De Vos, Direct patterning of oriented metal-organic framework crystals via control over crystallization kinetics in clear precursor solutions, *Advanced Materials*, 2010, **22**, 2685-2688.
146. R. Ameloot, L. Stappers, J. Fransaer, L. Alaerts, B. F. Sels and D. E. De Vos, Patterned growth of metal-organic framework coatings by electrochemical synthesis, *Chemistry of Materials*, 2009, **21**, 2580-2582.
147. M. Tu, B. Xia, D. E. Kravchenko, M. L. Tietze, A. J. Cruz, I. Stassen, T. Hauffman, J. Teyssandier, S. De Feyter, Z. Wang, R. A. Fischer, B. Marmiroli, H. Amenitsch, A. Torvisco, M. d. J. Velásquez-Hernández, P. Falcaro and R. Ameloot, Direct X-ray and electron-beam lithography of halogenated zeolitic imidazolate frameworks, *Nature Materials*, 2021, **20**, 93-99.
148. G. Lu, O. K. Farha, W. Zhang, F. Huo and J. T. Hupp, Engineering ZIF-8 thin films for hybrid MOF-based devices, *Advanced Materials*, 2012, **24**, 3970-3974.
149. C. Dimitrakakis, B. Marmiroli, H. Amenitsch, L. Malfatti, P. Innocenzi, G. Grenci, L. Vaccari, A. J. Hill, B. P. Ladewig, M. R. Hill and P. Falcaro, Top-down patterning of Zeolitic Imidazolate Framework composite thin films by deep X-ray lithography, *Chemical Communications*, 2012, **48**, 7483-7485.
150. G. M. Whitesides, The origins and the future of microfluidics, *Nature*, 2006, **442**, 368-373.

151. C. Echaide-Górriz, C. Clément, F. Cacho-Bailo, C. Téllez and J. Coronas, New strategies based on microfluidics for the synthesis of metal-organic frameworks and their membranes, *Journal of Materials Chemistry A*, 2018, **6**, 5485-5506.
152. J. Puigmartí-Luis, Microfluidic platforms: a mainstream technology for the preparation of crystals, *Chemical Society Reviews*, 2014, **43**, 2253-2271.
153. S. Sevim, C. Franco, H. Liu, H. Roussel, L. Rapenne, J. Rubio-Zuazo, X.-Z. Chen, S. Pané, D. Muñoz-Rojas, A. J. deMello and J. Puigmartí-Luis, In-flow MOF lithography, *Advanced Materials Technologies*, 2019, **4**, 1800666.
154. K. Raj M and S. Chakraborty, PDMS microfluidics: A mini review, *Journal of Applied Polymer Science*, 2020, **137**, 48958.
155. N. K. Gupta, S. Kim, J. Bae and K. Soo Kim, Fabrication of $Cu(BDC)_{0.5}(BDC\text{-}NH_2)_{0.5}$ metal-organic framework for superior H_2S removal at room temperature, *Chemical Engineering Journal*, 2021, **411**, 128536.
156. R. Zheng, Z.-H. Fu, W.-H. Deng, Y. Wen, A.-Q. Wu, X.-L. Ye and G. Xu, The growth mechanism of a conductive MOF thin film in spray-based layer-by-layer liquid phase epitaxy, *Angewandte Chemie International Edition*, 2022, **61**, e202212797.
157. Q. Li, J. Gies, X.-J. Yu, Y. Gu, A. Terfort and M. Kind, Concentration-dependent seeding as a strategy for fabrication of densely packed surface-mounted metal-organic frameworks (SURMOF) layers, *Chemistry - A European Journal*, 2020, **26**, 5185-5189.
158. H. Jiang, Z. Gao, C. Lubrano, C. L. Bovio, H. Bommes, A. Kauth, L. Baumann, B. Cheng, D. Murugan, J. Knoch, R. Waser, S. Ingebrandt, F. Santoro and V. Pachauri, Metal-organic frameworks as an active substrate for cell-interaction studies and cell-on-a-chip platforms, *Biosensors and Bioelectronics: X*, 2024, **19**, 100487.
159. B. J. Kim and E. Meng, Micromachining of parylene C for bioMEMS, *Polymers for Advanced Technologies*, 2016, **27**, 564-576.
160. K. Scholten and E. Meng, Electron-beam lithography for polymer bioMEMS with submicron features, *Microsystems & Nanoengineering*, 2016, **2**, 16053.
161. P. Blake, E. W. Hill, A. H. Castro Neto, K. S. Novoselov, D. Jiang, R. Yang, T. J. Booth and A. K. Geim, Making graphene visible, *Applied physics letters*, 2007, **91**, 063124.
162. Y. Wang, V. Zhou, Y. Xie, X.-Q. Zheng and P. X. L. Feng, Optical contrast signatures of hexagonal boron nitride on a device platform, *Optical Materials Express*, 2019, **9**, 1223-1232.
163. X. Zhang, H. Kawai, J. Yang and K. E. J. Goh, Detecting MoS_2 and $MoSe_2$ with optical contrast simulation, *Progress in Natural Science: Materials International*, 2019, **29**, 667-671.
164. Z.-Z. Ma, Q.-H. Li, Z. Wang, Z.-G. Gu and J. Zhang, Electrically regulating nonlinear optical limiting of metal-organic framework film, *Nature Communications*, 2022, **13**, 6347.
165. A. T. Fiory, Recent developments in rapid thermal processing, *Journal of Electronic Materials*, 2002, **31**, 981-987.
166. V. Rubio-Giménez, M. Galbiati, J. Castells-Gil, N. Almora-Barrios, J. Navarro-Sánchez, G. Escorcia-Ariza, M. Mattera, T. Arnold, J. Rawle and S. Tatay, Bottom-up fabrication of semiconductive metal-organic framework ultrathin films, *Advanced materials*, 2018, **30**, 1704291.
167. B. Chu, D. Biriukov, M. Bischoff, M. Předota, S. Roke and A. Marchioro, Evolution of the electrical double layer with electrolyte concentration probed by second harmonic scattering, *Faraday Discussions*, 2023, **246**, 407-425.
168. D.-W. Lee, M.-S. Kim, Y.-H. Lim, N. Lee and Y.-C. Hong, Prenatal and postnatal exposure to di-(2-ethylhexyl) phthalate and neurodevelopmental outcomes: A systematic review and meta-analysis, *Environmental Research*, 2018, **167**, 558-566.

References

169. R. Wang, M. Ji, H. Zhai and Y. Liu, Occurrence of phthalate esters and microplastics in urban secondary effluents, receiving water bodies and reclaimed water treatment processes, *Science of The Total Environment*, 2020, **737**, 140219.
170. Z.-M. Zhang, H.-H. Zhang, J. Zhang, Q.-W. Wang and G.-P. Yang, Occurrence, distribution, and ecological risks of phthalate esters in the seawater and sediment of Changjiang River Estuary and its adjacent area, *Science of the Total Environment*, 2018, **619**, 93-102.
171. G.-L. Wei, D.-Q. Li, M.-N. Zhuo, Y.-S. Liao, Z.-Y. Xie, T.-L. Guo, J.-J. Li, S.-Y. Zhang and Z.-Q. Liang, Organophosphorus flame retardants and plasticizers: sources, occurrence, toxicity and human exposure, *Environmental pollution*, 2015, **196**, 29-46.
172. H. Zhang, Q. Zhou, Z. Xie, Y. Zhou, C. Tu, C. Fu, W. Mi, R. Ebinghaus, P. Christie and Y. Luo, Occurrences of organophosphorus esters and phthalates in the microplastics from the coastal beaches in north China, *Science of the total environment*, 2018, **616**, 1505-1512.
173. H. Li, J. Li, X. Jiao, K. Li, Y. Sun, W. Zhou, Y. Shen, J. Qian, A. Chang and J. Wang, Characterization of the biosynthetic pathway of nucleotide sugar precursor UDP-glucose during sphingan WL gum production in Sphingomonas sp. WG, *Journal of biotechnology*, 2019, **302**, 1-9.
174. K. E. Okpara, K. Phoungthong, I. Agbozu, E. Edwin-Isotu and K. Techato, Phthalate esters in tap water, Southern Thailand: daily exposure and cumulative health risk in infants, lactating mothers, pregnant and nonpregnant women, *International Journal of Environmental Research and Public Health*, 2022, **19**, 2187.
175. N. A. Khan, B. K. Jung, Z. Hasan and S. H. Jhung, Adsorption and removal of phthalic acid and diethyl phthalate from water with zeolitic imidazolate and metal-organic frameworks, *Journal of hazardous materials*, 2015, **282**, 194-200.
176. Z. Li, Y. n. Wu, J. Li, Y. Zhang, X. Zou and F. Li, The Metal-organic framework MIL-53 (Al) Constructed from multiple metal sources: alumina, aluminum hydroxide, and boehmite, *Chemistry-A European Journal*, 2015, **21**, 6913-6920.
177. Q. Liu, J. Ye, Y. Han, P. Wang, Z. Fei, X. Chen, Z. Zhang, J. Tang, M. Cui and X. Qiao, Defective UiO-67 for enhanced adsorption of dimethyl phthalate and phthalic acid, *Journal of Molecular Liquids*, 2021, **321**, 114477.
178. P. Wang, L. Sun, J. Ye, Q. Liu, Z. Fei, X. Chen, Z. Zhang, J. Tang, M. Cui and X. Qiao, Construction of crystal defect sites in UiO-66 for adsorption of dimethyl phthalate and phthalic acid, *Microporous and Mesoporous Materials*, 2021, **312**, 110778.
179. R. Dargahi, H. Ebrahimzadeh, A. A. Asgharinezhad, A. Hashemzadeh and M. M. Amini, Dispersive magnetic solid-phase extraction of phthalate esters from water samples and human plasma based on a nanosorbent composed of MIL-101 (Cr) metal-organic framework and magnetite nanoparticles before their determination by GC-MS, *Journal of separation science*, 2018, **41**, 948-957.
180. L. Shu, S. Chen, W. W. Zhao, Y. Bai, X. C. Ma, X. X. Li, J. R. Li and P. Somsundaran, High-performance liquid chromatography separation of phthalate acid esters with a MIL-53 (Al)-packed column, *Journal of Separation Science*, 2016, **39**, 3163-3170.
181. E. Tahmasebi, M. Y. Masoomi, Y. Yamini and A. Morsali, Application of a Zn (II) based metal-organic framework as an efficient solid-phase extraction sorbent for preconcentration of plasticizer compounds, *RSC advances*, 2016, **6**, 40211-40218.
182. T. Wang, J. Wang, C. Zhang, Z. Yang, X. Dai, M. Cheng and X. Hou, Metal-organic framework MIL-101 (Cr) as a sorbent of porous membrane-protected micro-solid-phase extraction for the analysis of six phthalate esters from drinking water: a combination of experimental and computational study, *Analyst*, 2015, **140**, 5308-5316.

183. T. Wang, R. Zhang, D. Li, P. Su and Y. Yang, Application of magnetized MOF-74 to phthalate esters extraction from Chinese liquor, *Journal of separation science*, 2019, **42**, 1600-1609.
184. C. Wu, J. He, N. Chen, Y. Li, L. Yuan, D. Zhao, L. He, K. Gu and S. Zhang, Synthesis of cobalt-based magnetic nanoporous carbon core-shell molecularly imprinted polymers for the solid-phase extraction of phthalate plasticizers in edible oil, *Analytical and bioanalytical chemistry*, 2018, **410**, 6943-6954.
185. M. Z. Wu, Z. L. Ma, J. Y. Shi and L. Tian, A Zn (II) metal-organic framework based on bimetallic paddle wheels as a luminescence indicator for carcinogenic organic pollutants: phthalate esters, *RSC advances*, 2019, **9**, 37101-37108.
186. P. Hu, Y. Zhang, H. Wei, W. Zhang, L. Song, M. Zhang, X. Meng, M. Shang and C. Wang, Point-of-use SERS approach for efficient determination and removal of phthalic acid esters based on a metal-organic framework-coated melamine sponge, *ACS Applied Materials & Interfaces*, 2024, **16**, 11528-11536.
187. H. Xu, J. Zhu, Y. Cheng and D. Cai, Functionalized UIO-66@Ag nanoparticles substrate for rapid and ultrasensitive SERS detection of di-(2-ethylhexyl) phthalate in plastics, *Sensors and Actuators B: Chemical*, 2021, **349**, 130793.
188. H. Xu, J. Zhu, X. Wu, Y. Cheng, D. Wang and D. Cai, Recognition and quantitative analysis for six phthalate esters (PAEs) through functionalized ZIF-67@Ag nanowires as surface-enhanced Raman scattering substrate, *Spectrochimica Acta Part A: Molecular and Biomolecular Spectroscopy*, 2023, **284**, 121735.
189. P. Arroyo, F. Meléndez, J. I. Suárez, J. L. Herrero, S. Rodríguez and J. Lozano, Electronic nose with digital gas sensors connected via bluetooth to a smartphone for air quality measurements, *Sensors*, 2020, **20**, 786.
190. M. R. Awual, M. M. Hasan, J. Iqbal, M. A. Islam, A. Islam, S. Khandaker, A. M. Asiri and M. M. Rahman, Ligand based sustainable composite material for sensitive nickel(II) capturing in aqueous media, *Journal of Environmental Chemical Engineering*, 2020, **8**, 103591.
191. J. G. Miller, The nature of living systems, *The quarterly review of biology*, 1973, **48**, 63-91.
192. M. Ermis, E. Antmen and V. Hasirci, Micro and Nanofabrication methods to control cell-substrate interactions and cell behavior: A review from the tissue engineering perspective, *Bioactive Materials*, 2018, **3**, 355-369.
193. M. Vandrovcová and L. Bacakova, Adhesion, growth and differentiation of osteoblasts on surface-modified materials developed for bone implants, *Physiological Research*, 2011, **60**, 403.
194. L. Wang, H. Wang, L. Wang, K. Mitchelson, Z. Yu and J. Cheng, Analysis of the sensitivity and frequency characteristics of coplanar electrical cell-substrate impedance sensors, *Biosensors and Bioelectronics*, 2008, **24**, 14-21.
195. N. J. Sniadecki, R. A. Desai, S. A. Ruiz and C. S. Chen, Nanotechnology for cell-substrate interactions, *Annals of Biomedical Engineering*, 2006, **34**, 59-74.
196. A. Hedayatipour, S. Aslanzadeh and N. McFarlane, CMOS based whole cell impedance sensing: Challenges and future outlook, *Biosensors and Bioelectronics*, 2019, **143**, 111600.
197. F. Hempel, J. K. Y. Law, T. C. Nguyen, R. Lanche, A. Susloparova, X. T. Vu and S. Ingebrandt, PEDOT:PSS organic electrochemical transistors for electrical cell-substrate impedance sensing down to single cells, *Biosensors and Bioelectronics*, 2021, **180**, 113101.
198. J. Hong, K. Kandasamy, M. Marimuthu, C. S. Choi and S. Kim, Electrical cell-substrate impedance sensing as a non-invasive tool for cancer cell study, *Analyst*, 2011, **136**, 237-245.

References

199. F. Liu, A. N. Nordin, F. Li and I. Voiculescu, A lab-on-chip cell-based biosensor for label-free sensing of water toxicants, *Lab on a Chip*, 2014, **14**, 1270-1280.
200. R. Szulcek, H. J. Bogaard and G. P. van Nieuw Amerongen, Electric cell-substrate impedance sensing for the quantification of endothelial proliferation, barrier function, and motility, *Journal of Visualized Experiments*, 2014, e51300.
201. J. Wegener, C. R. Keese and I. Giaever, Electric cell–substrate impedance sensing (ECIS) as a noninvasive means to monitor the kinetics of cell spreading to artificial surfaces, *Experimental Cell Research*, 2000, **259**, 158-166.
202. Y. Xu, X. Xie, Y. Duan, L. Wang, Z. Cheng and J. Cheng, A review of impedance measurements of whole cells, *Biosensors and Bioelectronics*, 2016, **77**, 824-836.
203. E. Ghafar-Zadeh, M. Sawan, V. P. Chodavarapu and T. Hosseini-Nia, Bacteria growth monitoring through a differential CMOS capacitive sensor, *IEEE Transactions on Biomedical Circuits and Systems*, 2010, **4**, 232-238.
204. Q. Lin, J. ho Cheon, B. D. Gong, Y. J. Park, H. s. Min, D. won Kang, L. Kim and J. S. Suh, Capacitive measurements for a novel ECIS (electrolyte-carbon nanotubes-insulator-semiconductor) structure, *Semiconductor Science and Technology*, 2006, **21**, 686.
205. L. U. Vinzons, A. K. Gupta, T.-Y. Lai and S.-P. Lin, Interpretation of biosensing technology in cell-coupled silicon nanowire transistors via impedance spectra, *Materials Letters*, 2022, **308**, 131087.
206. Z. Gao, P. Carames-Mendez, D. Xia, C. M. Pask, P. C. McGowan, P. A. Bingham, A. Scrimshire, G. Tronci and P. D. Thornton, The facile and additive-free synthesis of a cell-friendly iron(iii)-glutathione complex, *Dalton Transactions*, 2020, **49**, 10574-10579.
207. P. Horcajada, R. Gref, T. Baati, P. K. Allan, G. Maurin, P. Couvreur, G. Férey, R. E. Morris and C. Serre, Metal-organic frameworks in biomedicine, *Chemical Reviews*, 2012, **112**, 1232-1268.
208. A. C. McKinlay, R. E. Morris, P. Horcajada, G. Férey, R. Gref, P. Couvreur and C. Serre, BioMOFs: Metal-organic frameworks for biological and medical applications, *Angewandte Chemie International Edition*, 2010, **49**, 6260-6266.
209. T. Katayama, S. Tanaka, T. Tsuruoka and K. Nagahama, Two-dimensional metal-organic framework-based cellular scaffolds with high protein adsorption, retention, and replenishment capabilities, *ACS Applied Materials & Interfaces*, 2022, **14**, 34443-34454.
210. F. Ejeian, A. Razmjou, M. H. Nasr-Esfahani, M. Mohammad, F. Karamali, M. Ebrahimi Warkiani, M. Asadnia and V. Chen, ZIF-8 modified polypropylene membrane: a biomimetic cell culture platform with a view to the improvement of guided bone regeneration, *International journal of nanomedicine*, 2020, **15**, 10029-10043.
211. M. Hanke, H. K. Arslan, S. Bauer, O. Zybaylo, C. Christophis, H. Gliemann, A. Rosenhahn and C. Wöll, The biocompatibility of metal-organic framework coatings: an investigation on the stability of SURMOFs with regard to water and selected cell culture media, *Langmuir*, 2012, **28**, 6877-6884.
212. B. D. Dhanapala, D. L. Maglich and M. E. Anderson, Impact of surface functionalization and deposition method on Cu-BDC surMOF formation, morphology, crystallinity, and stability, *Langmuir*, 2023, **39**, 12196-12205.
213. H. Cui, W. Wang, L. Shi, W. Song and S. Wang, Superwettable surface engineering in controlling cell adhesion for emerging bioapplications, *Small Methods*, 2020, **4**, 2000573.
214. P. Huang, L. Yao, Q. Chang, Y. Sha, G. Jiang, S. Zhang and Z. Li, Room-temperature preparation of highly efficient NH_2-MIL-101(Fe) catalyst: The important role of -NH_2 in accelerating Fe(III)/Fe(II) cycling, *Chemosphere*, 2022, **291**, 133026.

215. H. T. S. Boschker, P. L. M. Cook, L. Polerecky, R. T. Eachambadi, H. Lozano, S. Hidalgo-Martinez, D. Khalenkow, V. Spampinato, N. Claes, P. Kundu, D. Wang, S. Bals, K. K. Sand, F. Cavezza, T. Hauffman, J. T. Bjerg, A. G. Skirtach, K. Kochan, M. McKee, B. Wood, D. Bedolla, A. Gianoncelli, N. M. J. Geerlings, N. Van Gerven, H. Remaut, J. S. Geelhoed, R. Millan-Solsona, L. Fumagalli, L. P. Nielsen, A. Franquet, J. V. Manca, G. Gomila and F. J. R. Meysman, Efficient long-range conduction in cable bacteria through nickel protein wires, *Nature Communications*, 2021, **12**, 3996.

216. C. C. Chen, S. Y. Lin and J. T. Sheu, presented in part at the NEMS 2011 - 6th IEEE International Conference on Nano/Micro Engineered and Molecular Systems, 2011.

217. X. Shen, K. H. R. Yie, X. Wu, Z. Zhou, A. Sun, A. M. Al-bishari, K. Fang, M. A. Al-Baadani, Z. Deng and P. Ma, Improvement of aqueous stability and anti-osteoporosis properties of Zn-MOF coatings on titanium implants by hydrophobic raloxifene, *Chemical Engineering Journal*, 2022, **430**, 133094.

218. J. Wu, S. Jiang, W. Xie, Y. Xue, M. Qiao, X. Yang, X. Zhang, Q. Wan, J. Wang, J. Chen and X. Pei, Surface modification of the Ti surface with nanoscale bio-MOF-1 for improving biocompatibility and osteointegration in vitro and in vivo, *Journal of Materials Chemistry B*, 2022, **10**, 8535-8548.